Electronic Photodissociation Spectroscopy of Electrosprayed Anions

by

Jesse Cohen Marcum

B.S. University of New Hampshire, 2004

A thesis submitted to the Faculty of the Graduate School of the University of Colorado in partial fulfillment of the requirements for the degree of Doctor of Philosophy

Department of Chemistry and Biochemistry

2011

This thesis entitled:

Electronic Photodissociation Spectroscopy of Electrosprayed Anions

written by Jesse Cohen Marcum

has been approved for the Department of Chemistry and Biochemistry

_____

J. Mathias Weber

_____

Veronica Bierbaum

Date: _____

The final copy of this thesis has been examined by the signatories, and we find that both the content and the form meet acceptable presentation standards of scholarly work in the above mentioned discipline.

Marcum, Jesse Cohen (Ph.D., Chemistry, Department of Chemistry and Biochemistry)

Electronic Photodissociation Spectroscopy of Electrosprayed Anions

Thesis directed by Assistant Professor J. Mathias Weber

Ionic compounds are ubiquitous and play central roles in a variety of chemical, physical, and biological processes. Due to the incredible complexity of many of these processes, it is advantageous to develop a detailed molecular-level description of ions as isolated species. This approach provides the ability to study the *intrinsic* properties of ions in the absence of perturbing effects from solvent and/or counterions. Additionally, such studies can be used to perform experiments on model systems in which ions serve as "molecular laboratories" for developing new insight to fundamental physical and chemical phenomena.

This thesis is comprised of work I have carried out on a number of gas-phase anionic systems of both applied and fundamental interest. Early stages of my work focused on the development of instrumentation for performing electronic photodissociation spectroscopy on relatively large and/or fragile anionic species. A complete account of the resulting apparatus is provided, followed by an account of a number of experiments that employed photodissociation spectroscopy to extract intrinsic information on the electronic energy levels, photofragmentation mechanisms, and dissociation thresholds for a variety of ionic species. Experiments on gas-phase mononucleotides provided information necessary for understanding the complex sequence of events involved in the ultra-violet photodissociation of nucleotides, where initial excitation of the nucleobase chromophore is followed by rapid internal conversion, energy redistribution, nuclear rearrangement, and eventually fragmentation *via* a number of complex mechanisms. Studies on the prototypical gas-phase dianion, $IrBr_6^{2-}$, highlight the importance of repulsive Coulomb barriers in determining the overall stability and spectroscopy of multiply-charged anions, where a variety of potential dissociation mechanisms were identified to be highly dependent upon the nature of photoexcitation. Experiments on gas-phase $IrBr_5^-$ and $IrBr_4^-$ help to further characterize the complex potential energy surface of $IrBr_6^{2-}$ and provide direct spectroscopic information on under-coordinated transition metal

complexes that would be otherwise extremely difficult to obtain due to their transient, reactive nature. Work on two chloroaurate complexes, $AuCl_4^-$ and $AuCl_2(OH)_2^-$, provides insight into the photoreduction and speciation of gold(III) compounds. Finally, in a slight deviation from the above-themed work, infrared predissociation spectroscopy was used to elucidate the structure of water networks around the nitromethane anion and how solvation affects anion structure.

Dedication

To my teachers. For inspiring, encouraging, and challenging me and for providing guidance when I needed it most. But most of all to those teachers whose lessons I prize above all others, my parents.

Acknowledgements

Throughout the course of my graduate career I have been fortunate to have had the support of many amazing people whom I am thoroughly grateful for. Of course, this list must begin with my advisor, Mathias Weber, without whom none of this work would have been possible. I was provided with the unusual opportunity of joining Mathias' research group before he had even begun his position at the University of Colorado. Somehow, I managed to convince him to let me work in his lab after only a single, brief introduction while he was visiting from Germany. I can only hope that he has not regretted his decision. Being a part of transforming an empty room into a fully-functional, modern research lab has been a truly singular experience that has provided me with countless opportunities for intellectual and personal growth. Mathias has proven to be a great mentor and friend and I cannot thank him enough.

While working in lab I was lucky to have been surrounded by so many great colleagues and friends. Of these, I couldn't imagine a better person than Holger Schneider to introduce me to the laboratory. While he was only a graduate student a couple of years ahead of me, his advice was as good as any postdoc could have offered. His tireless ability to answer my incessant questions and lend a helping hand made building a new experiment an exceptionally enjoyable experience when it easily could have gone the other way. Over the last few years I have had the pleasure of getting to work with Chris Adams. I will be hard-pressed to find another person with whom I can have such fruitful scientific discussions as I have with Chris. Our long debates never failed to stretch my ability to think about science, both practically and philosophically. I hope that he has learned at least half as much from me as I have from him. Since the early stages of working on my experiment I have grown increasingly territorial and have dreaded the time that I would have to turn over my real estate in the lab. Fortunately, I had someone as patient and non-forgiving as Sydney Kaufman to take the helm of my instrument. She has put up with my all of my persnickety habits as well as my longwinded and verbose explanations of everything including the most trivial of details. I wish her the very best of luck and a fruitful scientific career. I must also thank two undergraduate students, Amit Halevi and Robert Warner, for their willingness to work with me and collect some of the data

that appear in this thesis. They never failed to keep me on my toes and offered me new perspectives on science. More recently, I have gotten to know the newer members of the research group, Eric Pozzi, Ben Knurr, and Casey Christopher. Despite our short overlap, I have learned much from each of them and wish them all much success.

I have also received the support of many people outside of our research group. In particular, very special thanks must go out to the Negative Ion Super Group. Professors Veronica Bierbaum, Barney Ellison, and Carl Lineberger and their research groups have been a treasure trove of formative insight, advice, and new ideas. Additionally, their willingness to lend us equipment during the early stages of putting together our lab helped us to get off the ground running far sooner than would have been otherwise possible. Very important thanks must also go to the JILA shops, without whom our lab would still be an empty room (or only contain a heap of scrap metal). I have had the good fortune of working with every member in the JILA Instrument Shop, each of whom provided me with invaluable guidance on designing and building scientific equipment. The JILA Electronics Shop designed and built most of the power supplies that are the life-blood of my experiment and taught me much about making measurements and eliminating noise. Members of JILA Computing provided me unconditional support of all things computer and never grew tired of my panic-laden requests to get me out of a jam. Thanks must also be given to the JILA Supply Office whose members keep JILA well-oiled and running smoothly and constantly remind us all not to take ourselves too seriously.

I would also like to acknowledge and thank the funding sources which financed my research and education. All of my research has been funded by grants from the National Science Foundation through either the JILA AMO Physics Frontier Center (PHY-0551010) or the Career Program (CHE-0845618). Further support was also provided by the University of Colorado Department of Chemistry and Biochemistry through Teaching Assistantships.

Finally, I would like to thank the many family members and friends who have supported me through their love and friendship. I could write an entire book praising you for everything you have given me. Most importantly, I would like to thank my wife, Kim, for her unwavering support and encouragement. She is a blessing that I don’t deserve.

Contents

List of Tables

List of Figures

1 Introduction

1.1 The chicken and the egg

When providing background and motivation for why we study ionic species, I am often challenged by the age-old question of the chicken and the egg. In my own opinion, ions are of interest for two primary reasons and it is easy to get caught up in trying to make up one's mind about which is the one that really got us started in this business anyway. On one hand (the chicken), ions are ubiquitous and developing a detailed understanding of how they behave is of interest for the many chemical phenomena in which they play important roles. On the other hand (the egg), ions provide certain experimental advantages over their neutral cousins that make them attractive for use as "molecular laboratories" where fundamental physical and chemical phenomena can be studied in detail without interference from the surrounding environment.

In defense of the first case, ions are everywhere. They exist in massive quantities in our planet's oceans and on its lands, in the plants and animals that we rely upon, and even in our own bodies. Farther from home, they are present in stars and galaxies and even the vast measures of space in between. They are not only spectators but actors as well, often with leading roles. In spite of their overwhelming abundance and importance, they are often less well understood than their neutral cousins and, in some cases, present formidable scientific challenges that have stood the test of time. At the root of these challenges are the strong Coulomb interactions that govern them. Because of these interactions, ions often exhibit substantial deviation from ideality, making many of the usual approaches of classical physical chemistry highly inaccurate.[1-3] Even when attempts to theoretically model these deviations are successful, they are often only accurate in the limit of extremely low concentrations, well below those at which neutral species would behave ideally.[1-3]

In order to better understand ionic compounds, obtaining species-specific information for intrinsic properties would be highly advantageous. However, the strong Coulomb interactions of ions present a problem here as well. Ideally, classical physical chemistry experiments would be made convenient by obtaining bulk quantities of a single ionic species. However, Coulomb

forces lead ions to be in cohorts with a wide variety of other species such as counterions or solvent. Obtaining bulk quantities would involve overcoming the stabilizing interactions with these other species as well as the repulsive forces between the ions themselves, both at substantial energetic costs. Even if these costs could be met, any properties measured would be overwhelmed by ion-ion interactions. As a result, a complete description of the intrinsic properties of many ionic species has long eluded classical physical chemistry.

The charged nature of ions forms the support for the second case. While it can be considered the bane of classical physical chemistry experiments, the charged nature can be viewed as a blessing for more modern gas-phase experiments, particularly those involving mass spectrometry. Mass spectrometric techniques can be used to produce, manipulate, and store gas-phase ions for long periods of time.[4-5] Perhaps more importantly, they can be used to easily isolate and identify a single ionic species of interest, a task that is considerably more difficult for neutral species. These abilities are particularly advantageous for reactive species. Such species often play important roles in chemical processes[6] but can be considerably difficult to study due to their transient nature. Mass spectrometry provides a practical approach for keeping reactive species isolated so that they do not interact with reaction partners that would otherwise lead to their destruction. Because ions in mass spectrometers are effectively isolated from the perturbing effects of counterions, solvent, and each other (usually), observed behaviors correspond to their *intrinsic* properties, thus providing a way to obtain the information necessary for testing and developing fundamental physical and chemical theories.

The two above-mentioned reasons demonstrate a strong case for being the primary motivation for studying ionic species. However, as it turns out, knowing which of the two reasons got us started in studying ions isn't so important after all. Both motivations continue to drive an active field of research that strives to obtain detailed information on ions of both applied and fundamental interest. Regardless of whether the chicken or the egg came first, both are here to stay. This thesis encompasses the work I have conducted on a number of gas-phase anionic systems of applied and/or fundamental interest. Chapter 2 describes the early phases of this work that entailed designing and building the experimental apparatus necessary

for obtaining electronic photodissociation spectra of gas-phase anions and the remaining chapters describe work on a number of anionic systems. Chapter 3 highlights work on eight different mononucleotides that revealed key information necessary for understanding the sequence of events that lead to ultraviolet photodissociation of nucleotides. Chapters 4 through 6 highlight work on a series of transition metal-containing complexes. Of these three chapters, Chapters 4 and 5 describe work on bromoiridates. Chapter 4 is an account of experiments on the prototypical dianion $IrBr_6^{2-}$ and Chapter 5 is an account of experiments on the under-coordinated species $IrBr_5^-$ and $IrBr_4^-$. Chapter 6 describes experiments on a series of mixed chloro-hydroxy gold complexes of the form $AuCl_n(OH)_{4-n}^-$ that are expected to play important roles in a number of chemical and geochemical processes. Finally, Chapter 7 highlights an experiment performed on the small molecule cluster system $CH_3NO_2^-\cdot(H_2O)_n$. This last system is an admitted departure from those discussed in previous chapters since it involved using a supersonic entrainment source rather than electrospray to produce ions and involved interrogation by infrared spectroscopy rather than electronic spectroscopy. This study was performed during the initial stages of my graduate career when the electrospray photodissociation spectrometer had been built but was not fully operational.

1.2 References for Chapter 1

1. McQuarrie, D.A. and Simon, J.D., *Physical Chemistry: A Molecular Approach*. 1997, Sausalito, CA: University Science Books.

2. Raff, L.M., *Principles of Physical Chemistry*. 2001, Upper Saddle River, NJ: Prentice-Hall.

3. Laidler, K.J., Meiser, J.H., and Sanctuary, B.C., *Physical Chemistry*. 4th ed. 2003, Boston, MA: Houghton Mifflin Company.

4. Grayson, M.A., ed. "Measuring Mass: From Positive Rays to Proteins." 2002, Chemical Heritage Foundation: Philadelphia, PA.

5. Hoffmann, E. and Stroobant, V., *Mass Spectrometry: Principles and Applications*. Second ed. 2006, West Sussex: John Wiley & Sons, Ltd.

6. Pilling, M.J. and Seakins, P.W., *Reaction Kinetics*. 2005, New York, NY: Oxford University Press.

2 Instrument Development and Operation

2.1 General concept

One of the primary experimental goals for the apparatus developed in this work is to obtain electronic spectra for ionic molecules as isolated species in the gas-phase. This approach is used to eliminate the perturbing effects of solvent and/or counterions, making interrogation of *intrinsic* electronic and molecular properties of ions possible. This turns out to be a non-trivial task since ions are generated in small quantities, precluding experiments based on the Beer-Lambert law. Such an approach relies on measuring the decrease in intensity of light across an absorbing sample. Because the number of absorbing species in our experiment is so small (at best on the order of about 10^5 ions per shot), the net reduction in light intensity is expected to be much less than 1 part in 10^{10}, far below our limits of detection. In fact, this reduction of light intensity would correspond to the upper limit of our experiment where every molecule present absorbs a photon, which is highly unlikely. To circumvent this problem, we turn to action spectroscopy where, rather than measuring the absorption of photons directly, we monitor a process that is the result of photon absorption. Action spectroscopy provides the advantage that signal is measured against an effectively zero background, providing significant enhancements in signal-to-noise levels. Although it is possible to study both anions and cations, only anions are studied in this work.

The form of action spectroscopy that we employ is photodissociation spectroscopy. A cartoon representation of the photodissociation process is depicted in Figure 2.1. Upon absorption of a photon, a molecule will be promoted into an excited state. This excess energy can then be used to induce molecular dissociation, leading to the formation of fragments. By monitoring the formation of fragment ions as a function of the excitation wavelength, it is possible to obtain a photodissociation action spectrum. Figure 2.2 depicts a block diagram of the general setup required for obtaining photodissociation spectra (more detailed information on the complete experimental setup can be found in the subsequent sections of this chapter). In the first step, ions are produced in a source region. Inevitably, most ionization sources produce a large number of different species, the majority of which are not of interest for a

particular experiment and could potentially complicate analysis. For this reason, primary mass analysis is performed on all parent ions to be able to filter out a single species. Once the ion of interest is isolated, it is irradiated with the output of a tunable light source. Following irradiation, parent ions may undergo dissociation into a number of neutral and ionic fragments. A second mass spectrometry step is then used to perform fragment ion mass analysis.

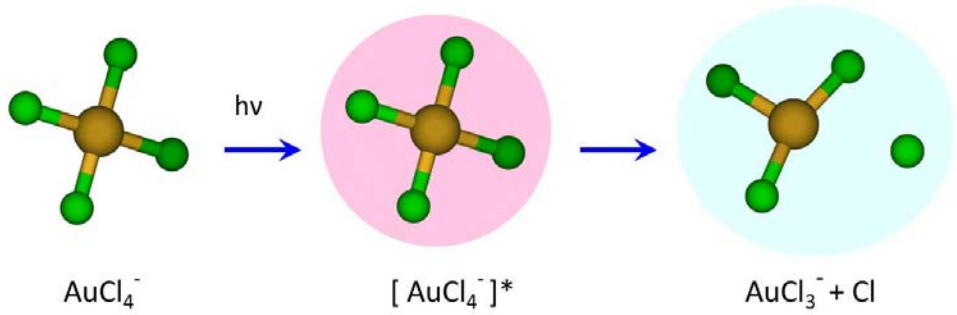

Figure 2.1. Cartoon diagram representing the photodissociation process using fragmentation of the tetrachloroaurate(III) ion as an example (see Chapter 6 for more information on the tetrachloroaurate ion).

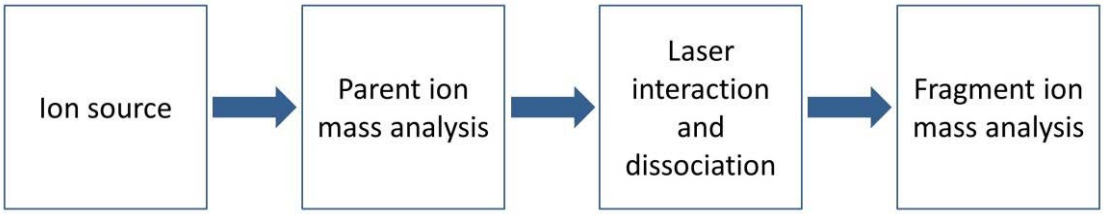

Figure 2.2. Block diagram representing the four main steps for obtaining photodissociation spectra.

A schematic diagram of the actual setup used for obtaining photodissociation spectra is shown in Figure 2.3. Ions are produced using an electrospray ionization (ESI) source and accumulated in a radiofrequency hexapole ion trap (see §2.2). The ions are then injected into the acceleration region of a Wiley-McLaren time-of-flight mass spectrometer where parent ion mass analysis is performed through a combination of perpendicular extraction and a pulsed mass gate (see §2.3 and §2.4). At the space focus of the mass spectrometer, ions are irradiated with the output of a tunable optical parametric converter (see §2.6). Upon dissociation, secondary mass analysis of parent and fragment ions is carried out using a two-stage reflectron at the end of the mass spectrometer (see §2.3). Ions are then detected on a microchannel plate

detector at the second space focus of the mass spectrometer (see §2.5 for more details on ion signal detection).

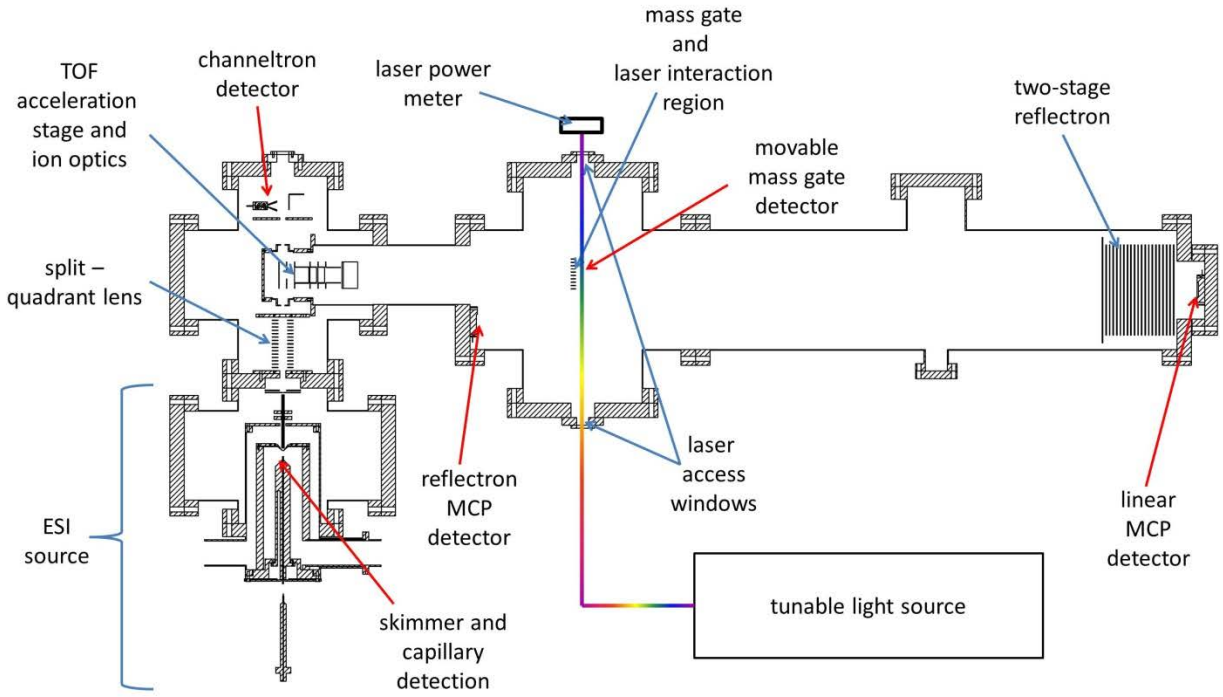

Figure 2.3. Schematic diagram of complete apparatus for acquiring photodissociation spectra with major components labeled. All five points where ion signal is routinely measured are pointed out in red.

In order for the photodissociation process to occur, several conditions must be met. First, the parent ion must absorb a photon. If no photon is absorbed then energy will not be deposited into the molecule and fragmentation cannot occur. This indicates that photodissociation will be dependent upon the absorption cross section for the parent ion. Because the absorption cross section varies as a function of photon energy, so should the photodissociation process. The second condition for photodissociation is that, upon absorption of a photon, the energy deposited into the parent ion must be enough to induce fragmentation. If the energy deposited is lower than all dissociation thresholds, fragmentation cannot occur. Finally, fragmentation must occur on the timescale of the experiment. If dissociation does not occur prior to fragment ion mass analysis, then no fragment ions will be detected and photodissociation action spectra cannot be obtained. If no photons are absorbed or no photo-fragmentation occurs, there will still be a background signal present that is comprised of fragment ions formed as a result of unimolecular decay induced by thermal energy imparted

while still in the source region. In our experiment, this background is considerably smaller than the intensity of fragments that result from photodissociation. An example of this is shown in Figure 2.4.

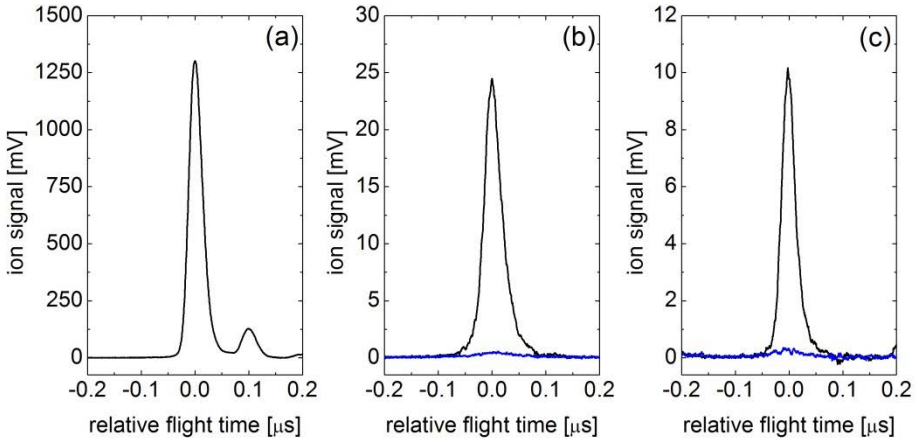

Figure 2.4. Representative time traces for parent and fragment ion mass peaks using a mononucleotide as an example. (See Chapter 3 for more information on nucleotide experiments.) Note the different intensity scales for the different peaks, showing the dynamic range of the experiment. (a) Parent ion mass peak for the mononucleotide $[dAMP\text{-}H]^-$. The smaller peak at relative flight time of +0.1 μs is due to isotopomers with one ^{13}C. (b) Peak corresponding to the PO_3^- fragment ion resulting from photodissociation of $[dAMP\text{-}H]^-$ at 4.77 eV photon energy (black) and from unimolecular decay in the ion source (blue). (c) Peak corresponding to the A^- fragment ion from photodissociation of $[dAMP\text{-}H]^-$ at 4.77 eV photon energy (black) and from unimolecular decay in the ion source (blue).

In addition to monitoring the production of fragment ions to obtain photodissociation action spectra, it is also possible to monitor the depletion of parent ions as a function of wavelength to obtain photodissociation depletion spectra. In this case, signal is not measured against a background of zero. Rather, it is measured relative to the number of undepleted parent ions and, consequently, is likely to result in lower signal-to-noise ratios than when using action spectroscopy. However, this problem is not nearly as severe as would be the case for direct absorption since reduction of light intensity is expected to be as low as 10^{-10} and therefore below detection limits. On the other hand, depletion of parent ion signal can be as high as a few percent and is thus a viable method for obtaining spectroscopic information.

Both photodissociation action and depletion depend on the absorption cross section of the parent molecule and, consequently, are able to provide *intrinsic* spectroscopic information about anionic species. However, both processes also depend upon the quantum yields for

dissociation. If the quantum yields are constant across the entire recorded spectral range, then photodissociation yields will be directly proportional to the absorption cross section. Alternatively, within a small spectral region where the absorption cross section is approximately constant or at least well-characterized, photodissociation spectra can provide information about the energy dependence of the quantum yield. Details on extracting information from experimental data can be found in §2.9.

2.2 Electrospray ionization source

One of the principal challenges of this experiment is promoting relatively large, fragile ions into the gas-phase. Typical ionization sources such as those that employ electrical discharge, laser ablation, or plasmas have been fruitful for small molecule and cluster studies but are too harsh for larger, more delicate species. In order to promote such ions into the gas-phase, we utilize electrospray ionization. A detailed discussion of the electrospray process is beyond the scope of this thesis,[1-11] but a general overview is provided so that the home-built ESI source can be completely described. A cartoon representation of the electrospray process is depicted in Figure 2.5 and a schematic diagram of the home-built source is depicted in Figure 2.6. This process is carried out at ambient temperature and pressure by pumping a solution that contains the ion of interest through a highly electrically charged needle that is typically positioned 2-20 mm away from a stainless steel capillary that is charged to a lower electrical potential. For experiments on anionic compounds typical operating potentials are between -1.5 and -3.0 kV for the needle and between -50 and -300 V for the capillary.[1] This voltage difference between the needle and capillary results in the formation of a plume of highly-charged liquid droplets containing the ion of interest. Since our experiment utilizes a microspray configuration, droplet formation is aided by the use of a nebulizing gas. These droplets will then move to the lower-potential capillary that also serves as the entrance aperture to the vacuum system. As the highly-charged droplets travel through the capillary, evaporation of solvent will occur until only the bare, gas-phase ions remain.

[1]Experiments on cationic compounds can be performed by switching the polarity of these and all subsequently mentioned voltages.

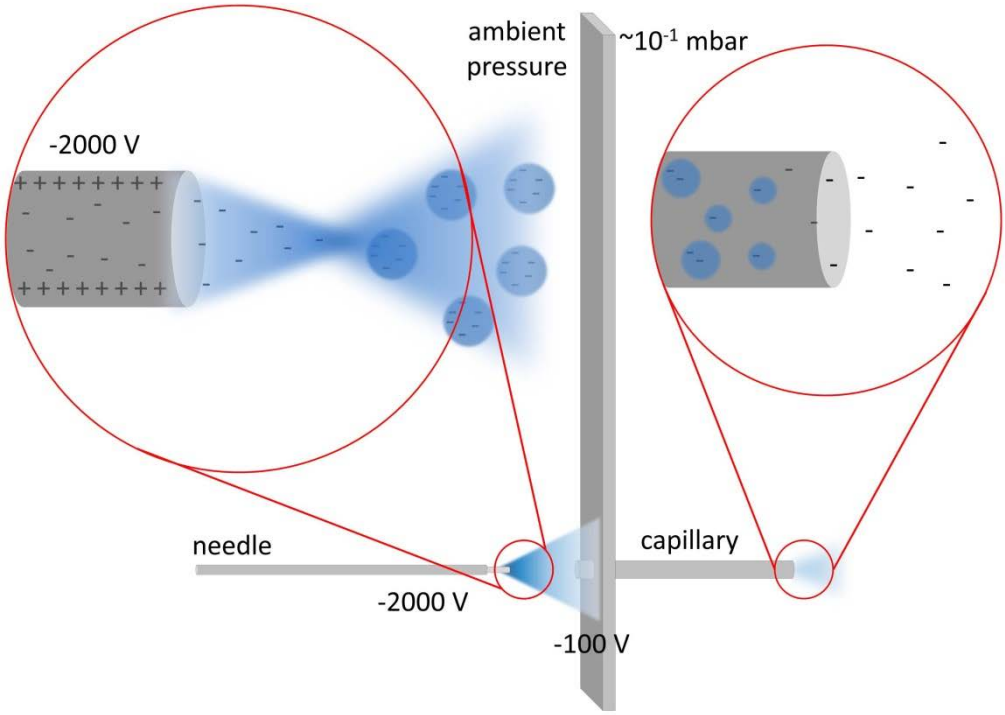

Figure 2.5. Cartoon representation of the electrospray ionization process. The needle and capillary voltages are only representative and meant to roughly convey the orders of magnitude typically used for experiments.

Following the desolvation process, ions pass through a series of differential pumping stages (JILA Instrument Shop, "differentially pumped chamber") that serve to both facilitate the remainder of the electrospray process and isolate the mass spectrometer from the ambient pressure conditions at which the spraying process is carried out. Generally, the setup consists of a modified 6-way cross (two of the arms have been shortened) with a pair of nested inner chambers (see Figure 2.6), each of which are pumped independently.

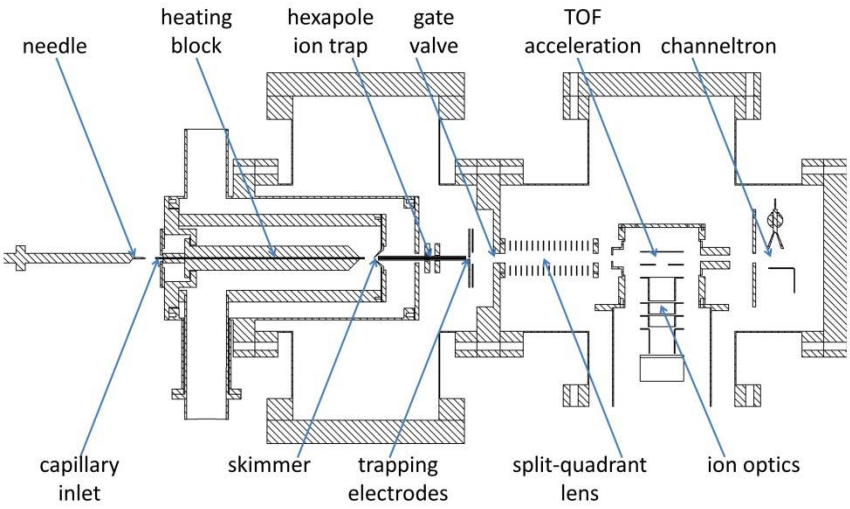

Figure 2.6. Electrospray ionization source region and acceleration region of the apparatus.

Because electrospray ionization is an inherently continuous ion source it is not directly compatible with the pulsed operation of a time-of-flight mass spectrometer. To couple the ion source to the mass spectrometer, we store and accumulate ions using a home-built, radiofrequency hexapole ion trap. Accumulation will also serve to increase the signal-to-noise level of the experiment. Following accumulation and ejection from the ion trap, it is necessary to focus and steer the ions so that optimal transmission into the mass spectrometer can be achieved. Both steering and focusing is performed using a home-built, split-quadrant ion lens.

2.2.1 Needle assembly

Electrospray ionization is carried out at ambient pressure using a microspray needle assembly (Analytica of Branford, model 103207-1) that consists of an inner spraying needle that extends approximately 2-3 mm from an outer needle (400 µm inner diameter). All fluid connections are made using standard high performance liquid chromatography connectors obtained from Upchurch Scientific (Scivex). The type of inner needle used depends on the system being studied and is either made of stainless steel with a 100 µm inner diameter and 200 µm outer diameter (Small Parts, B000RMS6OI) or made of fused silica with 75 µm inner diameter and 150 µm outer diameter (Polymicro, 2000133-10M). The outer needle is used to flow nebulizing gas (dry N_2, ~2.5 bar, ~1 L min^{-1}) around the inner spraying needle to aid the electrospray process. The entire assembly is mounted to an *x-y-z* translational stage so that the position of the needle can be optimized relative to entrance of the desolvation capillary.

Solutions containing ions of interest are pumped through the needle assembly using a syringe pump (Harvard Apparatus, Model 11 Plus). The electric potential of the assembly is provided using a high-voltage DC power supply (Bertan Associates, Series 225-05R).

2.2.2 Desolvation capillary and skimmer

Upon entry into the vacuum system, the highly-charged droplets formed at the spraying needle travel through a desolvation capillary where solvent is evaporated and they are reduced to bare, isolated ions (see Figure 2.6). The capillary consists of a 21.5 cm long piece of stainless steel tubing with a 0.0625" (1.5875 mm) outer diameter and 0.020" (0.508 mm) inner diameter and is surrounded by a copper block that can be heated from ambient temperature (~20°C) to ~130°C using a 100 W cartridge heater (Omega Engineering, model CSS-034100/120). The temperature of the copper block and desolvation capillary is monitored using a type K thermocouple and regulated using an autotuning temperature controller (Omega Engineering, model CN9000A). Upon leaving the capillary, ions enter the first differential pumping stage of the apparatus. This stage is pumped by a 65 m^3 h^{-1} rotary vane pump (Leybold, Trivac D65 B) and has a typical operating pressure of ~10^{-1} mbar.

Approximately 1 cm after the exit of the desolvation capillary is a skimmer that is used to separate the first and second differential pumping stages (see Figure 2.6). The skimmer is made of stainless steel and has an inner diameter of 1.5 mm (JILA instrument shop). The second differential pumping stage is pumped by a 65 m^3 hr^{-1} rotary vane pump (Leybold, Trivac D65 B) and has a typical operating background pressure of ~10^{-2} mbar (this pressure is likely to be slightly higher immediately before and after the skimmer).

The voltages of both the capillary and skimmer are supplied using a four-channel DC power supply that has a range of -100 to +100 V on two channels and -300 to + 300 V on the two others (JILA electronics shop, WM005-1, "ESI DC Supply"). Typical operating voltages for the capillary are between -50 and -300 V and for the skimmer are between -10 and -20 V. A key point to note is that the difference in voltage between the capillary and skimmer has a tremendous effect on the initial internal energy of the ions. As ions traverse this pumping region they will undergo a large number of collisions with background gas. The amount of

energy deposited into the ions during a collision will be dependent upon the translational kinetic energy of the ions prior to collision that is dependent upon the potential difference between the capillary and skimmer. As this potential difference is increased, ions will attain higher translational kinetic energies as they move from the capillary to the skimmer, resulting in more internal energy. If the internal energy is high enough, it can induce unimolecular fragmentation of ions. For particularly fragile ionic species (see Chapter 4), this potential difference is kept as low as possible. When fragmentation is desired (see Chapter 5), this potential difference is maximized.

2.2.3 Radiofrequency hexapole ion guide/trap

The radiofrequency (RF) hexapole ion trap is used to perform three important functions. First, it serves to guide ions through the second differential pumping stage where operating pressures (~10^{-2} mbar) are too high to utilize lens-type ion optics. Second, it is used as a linear trap for accumulation of ions to increase signal-to-noise as the continuous ESI source is coupled to the pulsed reflectron time-of-flight mass spectrometer. Third, trapping provides a way for the ions to reach thermal equilibrium after possibly gaining poorly-defined amounts of internal energy while in the first pumping stage. This final function is important since the internal energy distribution of the ions could have a significant effect on the photodissociation process.

The trap design is based on the linear multipole traps developed by Dieter Gerlich.[12-15] Briefly, it consists of an array of 6 stainless steel rods of alternating polarity with a set of electrodes at either end (Figure 2.6 and Figure 2.7). The polarity of the hexapole rods alternates at radio frequencies so that the time-varying hexapole field creates an effective potential that confines ions to the *z*-axis of the trap (in the center of the six rods). Ions are confined along the *z*-axis with the electrodes set at the ends of the hexapole rods. The skimmer serves as the entrance electrode in our experiment. Figure 2.8 shows a cartoon representation of how the ion trap is operated in it three main steps. In the first step (Figure 2.8a), the trap is filled by keeping the exit electrode at high potential. The second step (Figure 2.8b) involves pulsing the exit electrode to ground or slightly positive potentials so that ions drift out of the trap. The final step (Figure 2.8c) involves pulsing the exit electrode back to high potential and serves two functions; returning the trap to filling mode and providing an acceleration pulse to the

previously-ejected ions so that they are sent into the acceleration region of the mass spectrometer. Because ions undergo collisions with ambient-temperature background gas while in the trap, they are assumed to reach thermal equilibrium at a temperature of ~300 K.

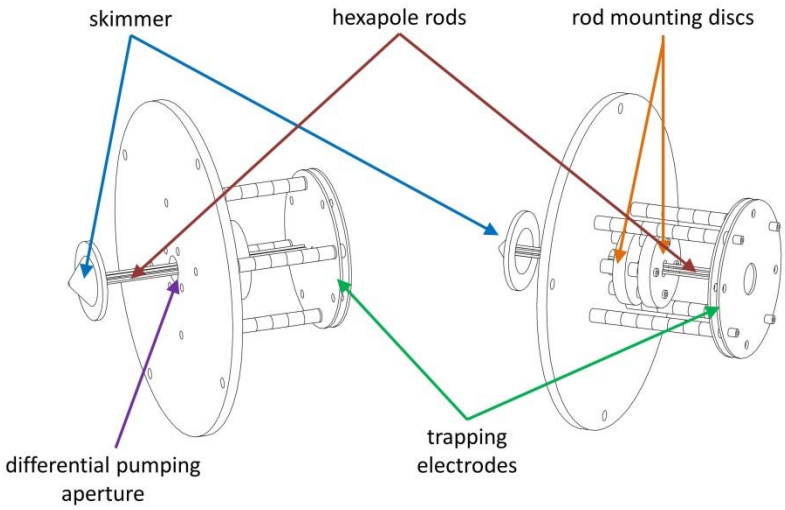

Figure 2.7. Schematic diagram for the hexapole ion trap from two different perspectives.

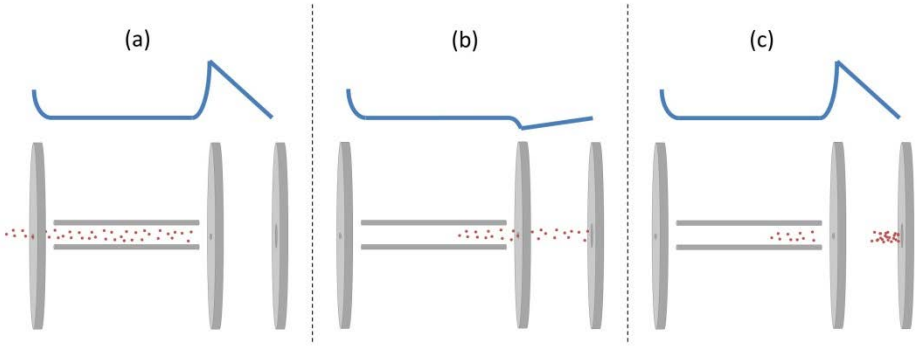

Figure 2.8. Cartoon representation of the steps involved in hexapole ion trap operation. Blue lines above trap diagrams represent the electric potential experienced by ions along the trapping axis. Potentials are not to scale. (a) Filling of the trap. (b) Passive ejection from the trap. (c) Active acceleration of ions that have already left the trap and return to filling mode.

The trap consists of an array of 6 stainless steel rods (0.04” (1.016 mm) diameter, 90 mm length) mounted such that the internal circumscribed diameter is 2.6 mm. Three rods are spot welded to each of two stainless steel mounting discs. This alternating configuration allows every second rod to be in electrical contact with one another but insulated from the other,

adjacent rods. The rods penetrate into the back of the skimmer with ~1 mm of space between the rods and the skimmer wall. The rods continue through the remainder of the second pumping region, through a 10 mm diameter orifice, and into the third pumping region, pumped by a 350 L s^{-1} turbomolecular pump (Leybold, Turbovac 361; backed by a Leybold D16 B, 16 m^3 hr^{-1} rotary vane pump) to a typical operating pressure of ~10^{-4} mbar. A set of two stainless steel trapping electrodes (1 mm thick, 60 mm diameter) are located directly behind the rods to facilitate trapping along the *z*-axis. The first electrode is mounted approximately 1 mm behind the rods and has a 1.5 mm orifice at the center. The second electrode is mounted 0.2" (5.08 mm) behind the first and has a 10 mm orifice at the center. Both the hexapole and the trapping electrodes are mounted to the chamber wall using insulating alumina rods (Kimball Physics, 0.124" (3.1496 mm) outer diameter) and an assortment of insulating alumina spacers (Kimball Physics, 0.125" (3.175 mm) inner diameter, variable length).

The hexapole trap is driven using a RF power supply tunable between 3 and 6 MHz and capable of voltages up to ±600 V on each rod (JILA Electronics Shop, WM004-01 and WM004-02). Trapping electrodes are powered using a 3-channel power supply capable of pulsing the electrodes anywhere between +100 and -100 V. Typical voltages used are -100 V for accumulating and 0 to +30 V for extracting ions. The ion trap is typically operated at a repetition rate of ~40 Hz, providing ions with an accumulation time of ~25 ms and allowing the ion source to be synchronized with the pulsed time-of-flight mass spectrometer and photodissociation laser. Triggering of the trapping electrodes is performed using a TTL pulse sent from a digital delay generator (see §2.8).

2.2.4 Split-quadrant ion lens

Upon extraction from the hexapole ion trap, ions pass through a gate valve into a fourth differential pumping stage, pumped by a 520 L s^{-1} turbomolecular pump (Pfeiffer TC600, backed by a Leybold D16 B, 16 m^3 hr^{-1} rotary vane pump) to operating pressures of ~10^{-6} mbar. Mounted to the low-pressure side of the gate valve is a split-quadrant, electrostatic ion lens designed to both steer and focus the ions so that optimal transmission to the mass spectrometer can be achieved. The location and positioning of the lens can be seen in Figure 2.3 and Figure 2.6 and a schematic diagram of the lens with an exploded view is shown in Figure

2.9. The lens consists of an array of 15 stainless steel electrodes (Kimball Physics, 0.025” (0.635 mm) thick, 1.4” (35.56 mm) wide, 1.4” (35.56 mm) high, 0.625” (15.875 mm) inner diameter, 0.125” (3.175 mm) mounting holes) mounted on insulating alumina rods (Kimball Physics, 0.124” (3.1496 mm) outer diameter) and separated by 0.2” (5.08 mm) insulating alumina spacers (Kimball Physics, 0.125” (3.175 mm) inner diameter). The electrodes are wired in several groups. The first and the last group of five are electrically connected to the vacuum chamber so that they maintain ground potential. The middle five electrodes are each divided into four quadrants (see Figure 2.9) where the voltage of each quadrant can be controlled independently. The voltages are set so that the center-point potential of the middle five electrodes are all the same and is typically between -60 and -85 V, depending on the settings of the ion trap. This potential serves to electrostatically focus the ions traveling through the lens. Minor steering of the beam is then accomplished by adding an additional bias on each of the four quadrants. The biases are controlled so that opposing quadrants have the same magnitude, but opposite polarity bias. For example, using the notation of Figure 2.9, a center-point voltage -70 V would be obtained by applying voltages of -71 V, -69 V, -74 V, and -66 V to quadrants (V+α), (V-α), (V+β), and (V-β) respectively. Because only minor corrections are needed, typical quadrant voltages deviate less than 0.5 V from the center point potential. All potentials are controlled by a DC power supply capable of center-point voltages of ±100 V and quadrant biasing of ±1 V (JILA Electronics Shop, WM014-1).

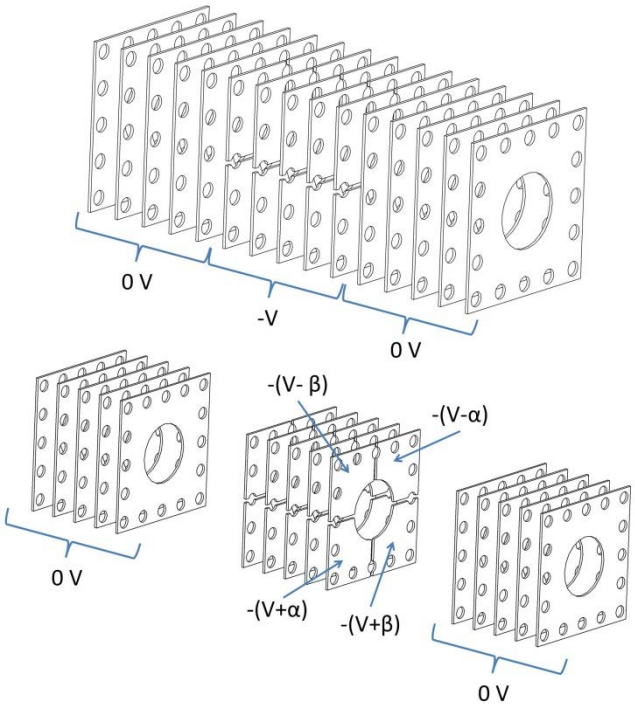

Figure 2.9. Schematic diagram of the entire split-quadrant lens (top) and an exploded view highlighting the three separate regions (bottom). The first and third regions are held at ground potential. Ions leaving the ESI source region are focused by applying a voltage, V, to the center region. Steering of ions is accomplished by applying small (0-1 V) biases (α and β) to each of the four quadrants of the center region.

2.3 Reflectron time-of-flight mass spectrometer

Upon extraction from the hexapole ion trap and passage through the split-quadrant ion lens, ions enter the acceleration region of a Wiley-McLaren, reflectron time-of-flight mass spectrometer (RETOF-MS). The RETOF-MS was purchased from Jordan TOF Products (Angular Reflectron Time of Flight D-850) and has been modified to fit the needs of the experiment (see Figure 2.3). The flight tube of the RETOF-MS (Jordan TOF, C-855 Flight Tube Assembly) is pumped by a 520 L s^{-1} turbomolecular pump (Pfeiffer TC600, backed by a Leybold D16 B, 16 m^3 hr^{-1} rotary vane pump) to operating pressures of ~10^{-7} mbar. Using a high-voltage pulse between the repeller, extractor, and ground acceleration electrodes (Figure 2.6), ions in the acceleration region undergo a perpendicular extraction into the flight tube with final kinetic energies of ~3.75 keV depending on the experiment. By controlling the relative potentials of the repeller and extractor, it is possible to select the point in which the space focus of the mass spectrometer occurs.[16] This point is selected to be at the center of the laser interaction chamber where the mass gate is located (see §2.4). Repeller and extractor voltages are

controlled using a pair of high-voltage DC power supplies (FuG, HCN 35-6 500) and pulsing is accomplished using a pair of fast high-voltage, push-pull switches (Behlke, GHTS 60) that are triggered using a TTL pulse (see §2.8).

Immediately following acceleration, the ions are focused with an electrostatic ion lens and steered using a set of deflector plates. Deflector plates for the *y*-direction were not part of the original setup as purchased from Jordan TOF Products (B-682 acceleration region with shroud for differential pumping; mounted to a C-854 Offset Adaptor Assembly) and had to be added. These deflectors consist of a pair of stainless steel electrodes mounted to the inside of the RETOF-MS acceleration shroud using insulating alumina rods (Kimball Physics, 0.124" (3.1496 mm) outer diameter) and separated using variable-length insulating alumina spacers (Kimball Physics, 0.125" (3.175 mm) inner diameter).

Upon leaving the acceleration region of the RETOF-MS, ions enter the laser interaction chamber (standard 6-way cross, with 10" (254 mm) conflat flanges) where they are mass selected using a home-built mass gate (see §2.4) and irradiated with the output of a tunable optical parametric converter (see §2.6) at the space focus of the mass spectrometer. Following irradiation, ions may undergo fragmentation. Photofragment ions (as well as undissociated parent ions) continue down the remainder of the flight tube where they are reflected and separated according to their mass-to-charge ratio (*m/z*) by a two-stage reflectron (Jordan TOF Products, C-852). The ions then travel back through the flight tube and are detected at a second space focus. The location of this space focus can be manipulated by controlling the relative voltages of the two reflectron stages. The reflectron is controlled by a two-channel, high-voltage, proportional-scaling power supply (JILA Electronics Shop, WM009-1, "photodissociation spectrometer H.V. DC supply"). The first channel is capable of supplying voltages of ±4.5 kV and the second channel is controlled to have a proportional output between 0 and 100 % of the first channel's output. By monitoring the detector output as a function of time after acceleration, we are able to obtain time-of-flight mass spectra. Calibration of mass spectra is performed by comparing the measured flight times for a series of well-characterized ions to their known masses. The ions typically used for calibration are derived from the dianion

$IrBr_6^{2-}$. This ion is known to undergo dissociation in the initial regions of the ESI source (see §2.2.2 as well as Chapters 4 and 5) into a number of fragment ions that include $IrBr_6^-$, $IrBr_5^-$, $IrBr_4^-$, $IrBr_3^-$, and $IrBr_2^-$. These ions allow for optimal calibration since they provide a wide mass range (m/z ≅ 348 – 672) as well as a number of peaks for the multiple isotopomers of each species.

In addition to increasing the resolving power of the mass spectrometer, the two-stage reflectron is also used to perform secondary mass analysis.[11] Any charged fragments that enter the reflectron incur changes in trajectory. Following dissociation, all fragments will continue to travel along the flight tube with the same velocity as the undissociated parent ions. Thus, the kinetic energy of all ions entering the reflectron will be directly proportional to their mass. Ions with higher m/z values will have higher kinetic energies and will be able to penetrate further into the reflectron than ions with lower m/z values (see Figure 2.10). Consequently, ions with higher m/z values will have longer trajectories and longer total flight times than those with lower m/z values. In principle, this behavior alone can be used to perform fragment ion mass analysis. However, trajectories within the mass spectrometer are configured for optimal transmission and detection of parent ions, not for the modified trajectories of fragment ions. However, it is possible to scale the reflectron voltage such that the fragment ion trajectories match those that have been configured for optimal transmission and detection.

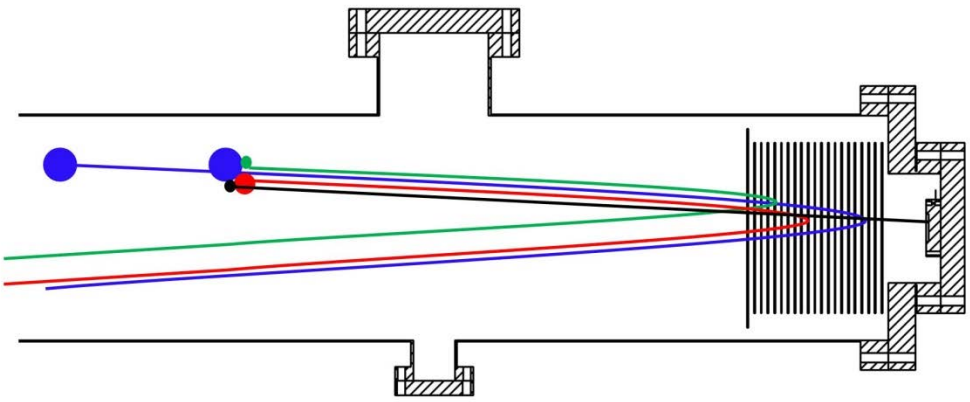

Figure 2.10. Diagram representing the differences in trajectories for parent ions (blue) ionic fragments (red and green) and neutral fragments (black) as they pass through the reflectron.

It can be shown[11] that the approximate length of the *parent* ion trajectory within a single-stage reflectron (the same arguments also apply qualitatively to two-stage reflectrons) is given by

Equation 2.1

$$x_p(V_1) = \frac{2E_p}{qV_1}$$

where $x_p(V_1)$ is the length of the trajectory for parent ions when the reflectron is set to a voltage of V_1, E_p is the kinetic energy of parent ions, q is the charge of the parent ions, and V_1 is the electric field in the reflectron. Using the equivalence of the parent and fragment ion velocities, it is then possible to obtain the approximate length of the *fragment* ion trajectory within the reflectron as

Equation 2.2

$$x_f(V_1) = \frac{2E_f}{qV_1} = \frac{2E_p\left(m_f/m_p\right)}{qV_1}$$

where $x_f(V_1)$ is the length of the trajectory for fragment ions when the reflectron is set to a voltage of V_1, E_p is the kinetic energy of parent ions, q is the charge of the parent ions, V_1 is the electric field in the reflectron, and m_p and m_f are the mass-to-charge ratios of the parent and fragment ions, respectively. It is then possible to reset the reflectron to have a new electric field, V_2, equal to

Equation 2.3

$$V_2 = V_1\left(m_f/m_p\right)$$

so that the fragment ion trajectory length within the reflectron at the new setting is

Equation 2.4

$$x_f(V_2) = \frac{2E_p\left(m_f/m_p\right)}{qV_1\left(m_f/m_p\right)} = x_p(V_1)$$

In other words, it is possible to scale the reflectron voltage by a ratio of the parent and fragment ion mass-to-charge ratios such that the fragment ion has the same trajectory within the reflectron as the parent ion had at the original settings. Furthermore, fragment ions will have the same total flight time at the new reflectron setting, V_2, as the parent ion had at the

initial reflectron setting of V_1. Thus, by appropriately scaling the reflectron, it is possible to selectively identify product ions and optimize trajectories through the mass spectrometer.

It is important to note that, for singly-charged ions, the reflectron will always be scaled down since $V_2 < V_1$. However, for multiply-charged ions, it is possible for fragment ions to have a higher m/z value than the parent ions. In such a case, the reflectron voltage will have to be scaled up since $V_2 > V_1$. This is not possible in our experiment since the typical reflectron operating voltage (V_1) is ±4.0 kV and the maximum voltage that can be applied on the reflectron is only ±4.5 kV. Consequently, it is necessary to scale down both the reflectron and acceleration stage when monitoring multiply-charged parent ions. An example of this situation is shown in Chapter 4.

2.4 Mass gate assembly

Despite the fact that a reasonable degree of mass-selection occurs due to the perpendicular configuration of the ions leaving the source and the flight axis of the RETOF-MS, a separate, independent mass gate was constructed to provide further mass-selection. A schematic diagram of the mass gate assembly is shown in Figure 2.11. The design used is a crude version of several previous devices for mass-selection ion time-of-flight experiments.[17] Our greatly simplified version lacks the resolution afforded by the earlier devices but was designed in such a manner that it can be easily upgraded if need be.

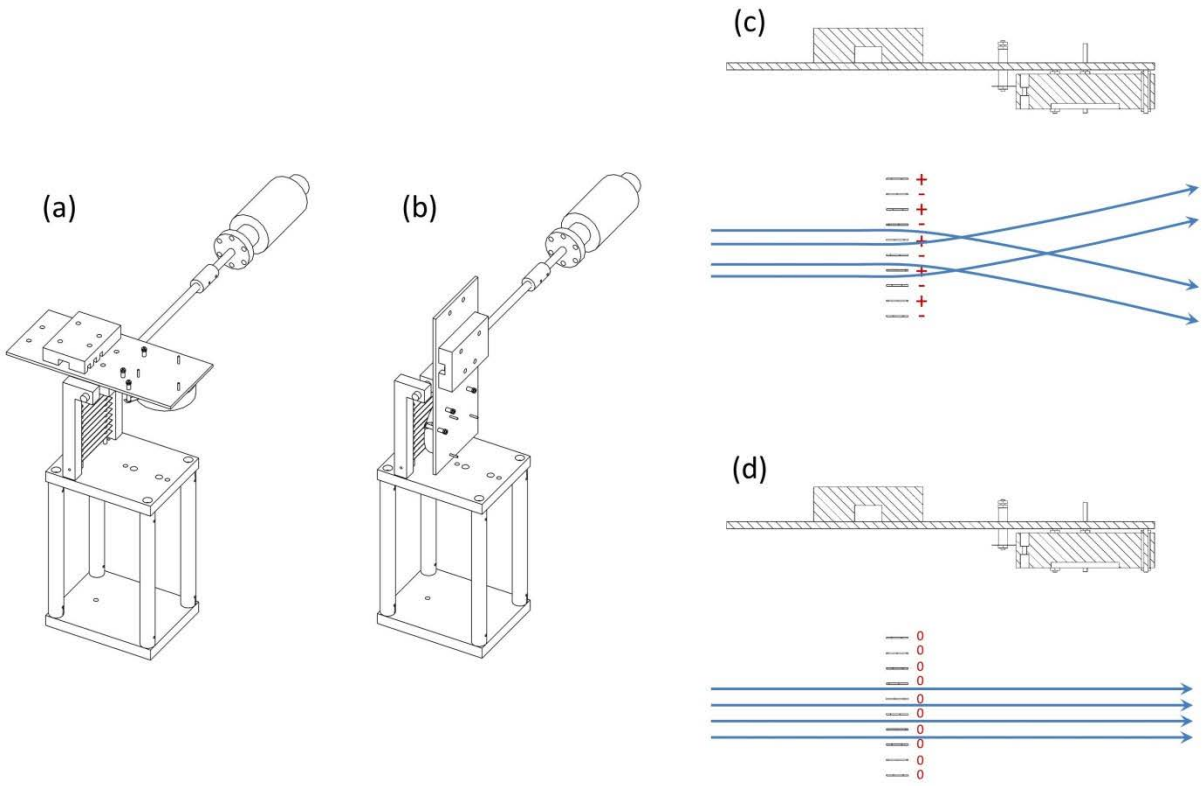

Figure 2.11. Schematic diagrams for the mass gate assembly. (a) Assembly with movable detector in the up position for normal operation of the mass gate. (b) Assembly with movable detector in the down position for optimizing the first space focus of the mass spectrometer. (c) Mass gate in "closed" mode where ions are deflected into the walls of the chamber. (d) Mass gate in "open" mode where ions pass through, unaffected.

The basic principle behind the mass gate is that a series of oppositely-charged, parallel plates can be used to deflect ions from their normal trajectories along the flight tube. When the mass gate is closed, alternating voltages are applied to the plates so that ions traveling down the flight tube experience a deflecting electric field and are directed toward the walls of chamber (see Figure 2.11c). When the mass gate is open, all plates are set to ground potential so that the ion trajectories remain unaffected (see Figure 2.11d). Through pulsing on and off, selective filtering of ions based on their flight times and mass-to-charge ratios can be accomplished. For example, to allow a small window of mass-to-charge ratios to be transmitted, the gate is operated in closed mode until the ions of interest reach the mass gate whereupon the gate is temporarily switched to open mode. Once the ions of interest pass the mass gate, the gate is returned to closed mode to prevent any ions with higher m/z from reaching the detector. Alternatively, the mass gate can be used to selectively block ions within a

narrow mass-to-charge range by operating it in a reverse fashion (open, closed, open). The typical resolving power of the mass gate is $\Delta m/m \approx 50$.

The plates are made of ~0.5 mm thick, 8 mm wide, and 50 mm long stainless steel and are separated by a distance of 0.2" (5.08 mm) with insulating alumina spacers (Kimball Physics, 0.2" (5.08 mm) long, 0.125" (3.175 mm) inner diameter). All plates are mounted on a pair of insulating alumina rods (Kimball Physics, 0.124" (3.1496 mm) outer diameter) that are in turn mounted on an aluminum support plate (see Figure 2.11). Electrical connections to plates were made by spot-welding stainless steel wire to each of the plates in alternating fashion. To prevent the ions from the possibility of interacting with the mass gate on their return trip toward the detector, ground shields (that also form the supports for the movable detector) have been placed on each end of the plates.

The mass gate is operated by a power supply built in-house by the JILA electronics shop (WM008-1, "mass gate pulse supply"). This power supply is capable of pulsing the mass gate plates between ground and operating potentials on a timescale of 0.5 to 2 μs, depending on the operating voltage. Typical operating voltages are around ±100 V but the power supply is capable of voltages up to ±400 V. Control of the open/closed state is obtained by means of a TTL pulse sent to the power supply from a digital delay generator (see §2.8).

In order for the mass gate to achieve optimal mass-resolution, its position must coincide with the space focus of the mass spectrometer. This is also the same point as the laser interaction region so that the laser beam and ions achieve maximum overlap. Because we are using a Wiley-McLaren setup for the TOF-MS[16] the specific location of the space focus is highly dependent upon and controlled by the conditions of the acceleration stage. To ensure that the space focus occurs where the mass gate and laser interaction region is located, a movable microchannel plate detector (Burle Electro-Optics, APD 3025MA) has been built into the mass gate assembly (Figure 2.11). The ground shields for the mass gate plates also serve as mounting brackets to hold the movable detector. The detector can be moved by means of a rotation stage/feedthrough (MDC vacuum, BRM-133) mounted on the side of the laser interaction chamber (see Figure 2.11). To adjust the space focus of the mass spectrometer, the

detector is rotated into the down position (Figure 2.11b) so that the plane of the detector is in roughly the same place as the laser interaction region. The acceleration voltages for the Wiley-McLaren RETOF-MS can then be optimized by minimizing the peak width of ions reaching the mass gate detector. More information on the power supply and operation of the detector is provided in §2.5.

2.5 Ion signal detection

Measuring ion signal in the various regions of the mass spectrometer is accomplished with five different detectors and configurations. These five points are labeled in Figure 2.3. Several of these are used primarily for diagnostic purposes when optimizing the settings of the mass spectrometer. The first way ions are monitored involves using a picoammeter (Keithley 6485) to measure the total ion current (without mass selection) on either the capillary or the skimmer in the ESI source chamber. During normal operation, these components have applied potentials but are disconnected from the nominal power supplies and kept at ground potential while ion currents are being measured. In principle, the picoammeter is capable of measuring ion currents on electrically charged components. However, this setup has not yet been utilized. Measuring ion currents on these two components is for purely diagnostic purposes to ensure that the front end of the ESI source (needle, capillary, and skimmer) is operating properly and that ions are being formed and transmitted.

The next place where ions can be detected is in the acceleration chamber, opposite the gate valve and behind the acceleration optics (see Figure 2.3). This detector is used to optimize the settings for the RF hexapole ion trap prior to mass analysis with the RETOF-MS. In choosing the type of detector for this location, several important points had to be considered. First, the translational kinetic energy of ions reaching this detector will be limited by what they obtain as they are ejected from the hexapole ion trap. For almost all experiments that have been conducted thus far, this energy has an upper limit of 100 eV. These low translational kinetic energies will result in exceedingly low detection efficiencies for most electron multiplier-based detectors. Second, this detector is directly in line with and unshielded from the desolvation capillary in the ESI source. This means that potentially large quantities of solvent and any other species present in the electrospray solution will have a direct path to the detector, running the

risk of damaging the detector. Taking these two points into consideration, the decision was made to use an off-axis channel electron multiplier (Sjuts Optotechnik, KBL15RS) with a repeller/conversion dynode. The complete assembly consists of a home-built, off-axis mount for the channeltron as well as a home-built repeller/conversion dynode (Figure 2.12). The repeller/conversion dynode is constructed of a piece of shaped stainless steel and can be used either as a repeller to deflect ions into the channeltron or as a conversion dynode by attracting the ions to itself, leading to the formation of secondary ions of opposite polarity that are then accelerated to the channeltron. When working with negative ions, operating the detector in conversion dynode mode tends to result in the best detection efficiencies. Power for the channeltron is supplied by a home-built voltage divider circuit (Figure 2.13) that is in turn supplied by a Bertan 225-05R high-voltage power supply. The voltage divider circuit has been designed so that it can be used to run the channeltron in both negative and positive ion modes, making it easier to not only switch between running experiments on negative or positive ions but also to switch between running the detector in either repeller or conversion dynode mode. The conversion dynode is powered by a high voltage, DC power supply built at the University of Karlsruhe.

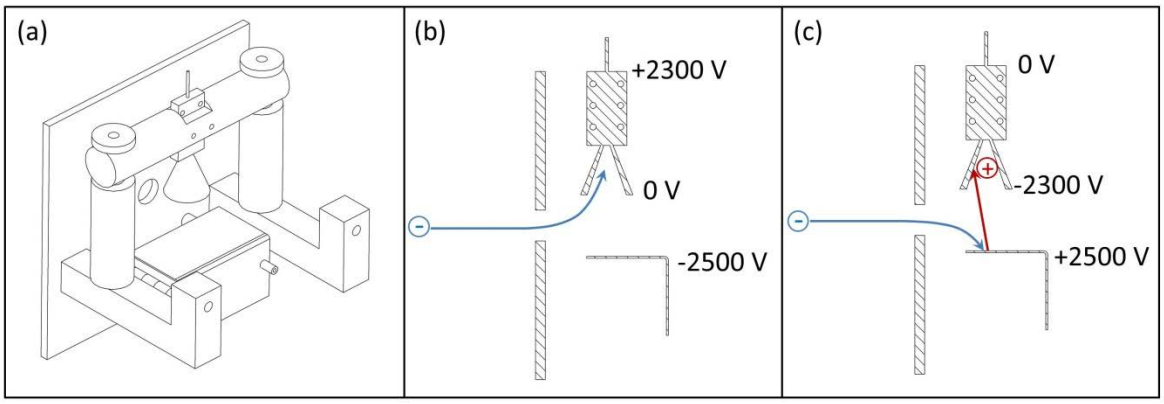

Figure 2.12. Schematic diagrams of the channeltron assembly. (a) Three-dimensional perspective. (b) Assembly being operated in repeller mode. (c) Assembly being operated in conversion dynode mode.

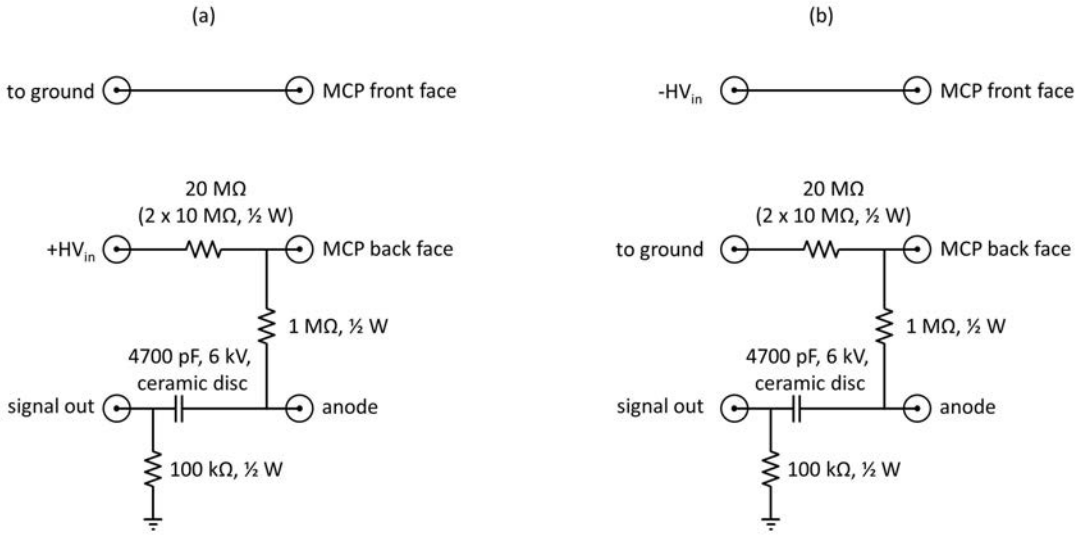

Figure 2.13. Voltage divider circuit for the mass gate MCP and the channeltron detectors. (a) Configuration for monitoring anions. (b) Configuration for monitoring cations.

Detection of ions at the mass gate is performed using a microchannel plate detector (MCP) that is mounted to a rotatable stage so that it can be moved in and out of the path of ions for optimization of the RETOF-MS space focus (see §2.4 for more detailed information). This detector consists of a set of two impedance-matched, 40 mm diameter microchannel plates assembled in a chevron configuration (Burle Electro-Optics, APD 3025MA). Power for the detector is supplied by a home-built voltage divider circuit (Figure 2.13) that is in turn supplied by a Bertan 225-05R high-voltage power supply. The voltage divider circuit has been designed so that it can be used to run the MCP detector in both negative and positive ion modes.

Detection of ions at the end of the linear TOF, behind the reflectron is performed using an MCP detector ("linear MCP", Figure 2.3). This detector is used to obtain linear time-of-flight mass spectra with the reflectron set to ground potential. Additionally, it can be used to monitor the production of neutral fragments following photodissociation. This is accomplished by applying a sufficient potential to the reflectron so that all parent and fragment ions are deflected while neutral fragments penetrate the field and are registered on the linear detector. This detector was included as part of the original RETOF-MS assembly as purchased from Jordan TOF Products (see §2.3 for more information) and consists of a set of two 18 mm diameter microchannel plates assembled in a chevron configuration (Jordan TOF C-701, MCP detector

assembly). Power for the detector is supplied by a home-built voltage divider circuit (Figure 2.14) that is in turn supplied by a Bertan 225-05R high-voltage power supply.

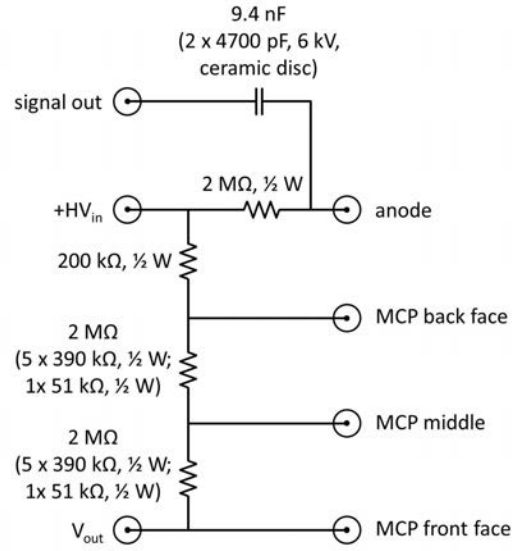

Figure 2.14. Voltage divider circuit for the linear and reflectron MCP detectors. For normal operation, V_{out} is set to ground potential. For information on pulsed operation, see §2.10.7.

Detection of ions at the end of the RETOF-MS (opposite the reflectron) is performed using an MCP detector ("reflectron MCP", Figure 2.3). This detector is used to obtain reflectron time-of-flight mass spectra as well as to monitor charged fragment ions following photodissociation. This detector was included as part of the original RETOF-MS assembly as purchased from Jordan TOF Products (see §2.3 for more information) and consists of a set of two 40 mm diameter microchannel plates assembled in a chevron configuration (Jordan TOF Products, C-726, Dual Microchannel Plate Detector). In principle, power for the detector can be supplied by the same voltage divider circuit and high-voltage power supply as was used for the linear TOF detector (Figure 2.14). However, due to difficulties associated with scattered UV light inside of the chamber, a modification was made to the voltage divider circuit so that the detector can be turned on and off in a pulsed manner (see §2.10.7 for more information).

2.6 Tunable light source

2.6.1 Overview

A schematic diagram of the light source for the experiment is shown in Figure 2.15. The system consists of three primary components: a solid-state pump laser, a visible/near-infrared optical parametric oscillator (OPO), and a stage capable of both second harmonic generation (SHG) and sum-frequency mixing (SFM). The entire system is capable of providing pulsed, tunable, coherent radiation from 220-2500 nm, with a bandwidth of ~4 cm^{-1} and ~5 ns pulse duration. The system operates at a repetition rate of 20 Hz and has output pulse energies between ~1 and 25 mJ, depending on the wavelength. Calibration is performed using a four channel, fiber-optic, diffraction grating-based, UV-Vis spectrometer (Avantes, AvaSpec-2048-USB2-DT) to measure the output wavelength. A five point polynomial fit of the OPO signal beam wavelength is performed within the preciScan software suite and is used for subsequent calibration of all other beams. Typical calibration error is ≤ 2 cm^{-1}, which is less than the ~4 cm^{-1} resolution of the system. While a detailed theoretical description of the entire system is beyond the scope of this thesis, a general operational overview is provided for each of the main components in the system.

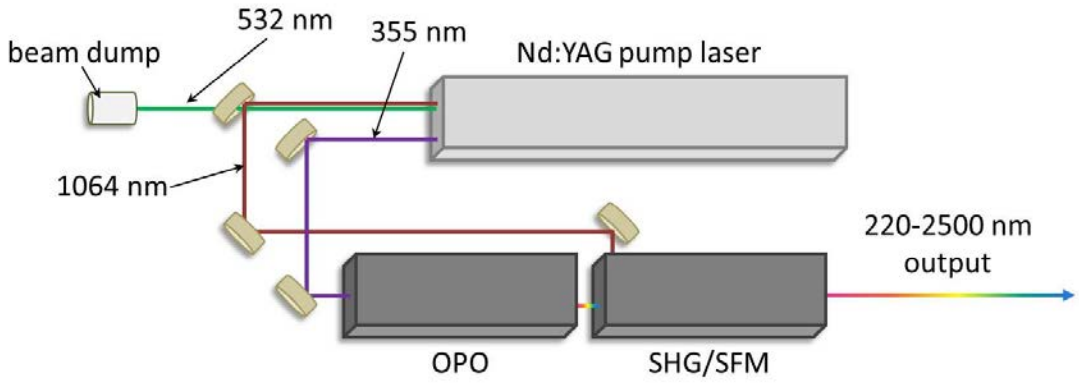

Figure 2.15. Overview of the entire tunable light source.

2.6.2 Pump laser

The primary source of light generation for our system is an Innolas Spitlight 600 pump laser. A schematic diagram of the pump laser is depicted in Figure 2.16. The resonator cavity consists of an output coupler, high reflector, and a neodymium-doped yttrium aluminum garnet

(Nd:YAG) rod as the lasing medium. Directly next to the Nd:YAG rod is a xenon arc lamp that is pulsed at a repetition rate of 20 Hz to electronically excite the lasing medium and create a population inversion. Also within the resonator cavity is a Pockels cell that, in combination with a polarizer, functions as a Q-switch. By controlling the voltage across the dielectric medium in the Pockels cell (holdoff), it is possible to control the amount of light that is allowed to build up in the resonator and thus the output power of the pump laser. Timed pulsing of the Pockels cell voltage is used to ensure that Q-switching occurs in synchronization with the kinetics of the population inversion. By changing the delay time between the flashlamp and Q-switch (delay), the output power of the pump laser can be varied. Additionally, it is possible to run the laser in "fixed-Q" mode by disabling the Pockels cell and placing a $^{\lambda}/_{4}$ waveplate between it and the high reflector.

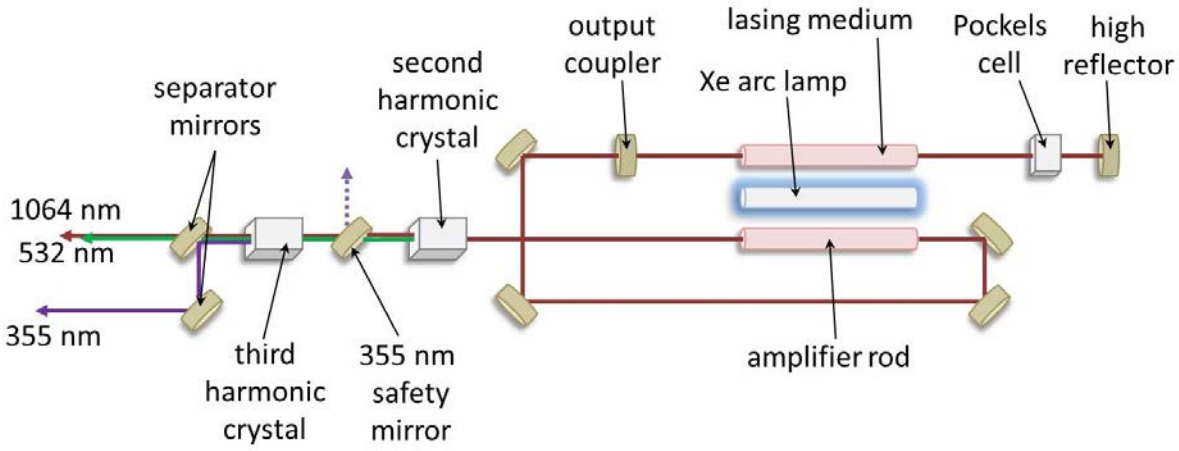

Figure 2.16. Overview of the Innolas Spitlight 600 pump laser with second and third harmonic crystals.

After a generated laser pulse leaves the resonator cavity, it is directed by a series of steering optics into a second Nd:YAG rod that is also excited by the xenon arc lamp at the same time as the first Nd:YAG rod. Because this second rod is not contained within the resonator cavity, it does not play a part in the buildup and lasing process and its population inversion will remain largely intact. This remaining population inversion provides a final amplification step for the laser pulse that was generated in the resonator cavity as it passes through the second rod. This amplified, Q-switched system produces radiation primarily at the fundamental wavelength of 1064 nm with typical pulse energies of □600 mJ.

In order to drive the OPO (§2.6.3), pump radiation with a wavelength of 355 nm is required. This is obtained by non-linear optical conversion of the 1064 nm fundamental radiation of the pump laser. Following amplification in the second Nd:YAG rod, 1064 nm fundamental radiation is frequency-doubled in a Type I KD*P non-linear optical crystal. This results in the generation of second-harmonic 532 nm radiation that propagates collinearly with any remaining unconverted 1064 nm fundamental radiation. Optimization of second harmonic generation is accomplished by angle-tuning of the crystal. Typical pulse energies are □200 mJ at 532 nm. Immediately following this stage, both the 1064 nm fundamental and 532 nm second-harmonic pass through a KD*P non-linear optical crystal in which sum-frequency mixing of the two incident beams is accomplished to produce third-harmonic radiation at 355 nm. Typical output pulse energies at 355 nm are between ~125 and ~160 mJ. Optimization of third harmonic generation is accomplished by angle-tuning of the crystal.

At this point, the fundamental, second-harmonic, and third-harmonic beams all propagate collinearly and must be separated so that the 355 nm radiation can be used to pump the OPO. This is accomplished through a series of dichroic separator mirrors located in the front of the laser head. Additionally, there is a third 355 nm turning mirror between the second- and third-harmonic crystals that is used to prevent any 355 nm radiation that may be reflected from the OPO (indicated by the dashed purple line in Figure 2.16) from reentering the resonator cavity.

2.6.3 Optical parametric oscillator

The tunable light for the experiment is generated using a GWU preciScan ULD optical parametric oscillator (OPO). A schematic diagram for the OPO is shown in Figure 2.17. Upon entering the OPO housing, the third harmonic of the pump laser (355 nm) is sent through a telescope to condition the beam. The type and focal length of the telescope is selected to ensure that the beam does not converge and is of the proper energy density for parametric conversion. If the characteristics of the pump laser beam change significantly, the telescope must be either adjusted or rebuilt according to the new input beam characteristics. The OPO cavity consists of an output coupler, a high reflector (combination of a Porro prism and $\lambda/4$ waveplate), and a Type II β-barium-borate (BBO) crystal where parametric conversion takes place. The 355 nm pump beam is injected into the OPO cavity by means of a periscope/pump-

injection mirror. The pump beam makes a single pass through the crystal, is reflected off of the output coupler, makes a second pass through the crystal, and is sent back toward the pump laser. To ensure that the back reflected pump beam does not reenter the pump resonator, a 355 nm turning mirror is placed in the beam between the second- and third-harmonic crystals in the pump laser head (see §2.6.2 and Figure 2.16). While in the cavity, the 355 nm pump beam is converted into two lower-energy beams (signal and idler) by optical parametric conversion within the BBO crystal. The relationship between the frequency of the signal, idler, and pump beams is given by

Equation 2.5

$$\omega_{sig} + \omega_{idl} = \omega_{pump}$$

where ω_{sig}, ω_{idl}, and ω_{pump} are the frequencies of the signal, idler, and pump beam, respectively and $\omega_{sig} > \omega_{idl}$. The relative frequencies of the signal and idler beams are adjusted by angle tuning of the BBO crystal, resulting in a tuning range of 400-710 nm for the signal beam and 710-2500 nm for the idler beam. In principle, a single BBO crystal could be used for the entire wavelength range. However, this OPO utilizes two separate BBO crystals (designated as “blue” and “red”), each of which is used to tune over a portion of the wavelength range. The “blue” crystal has a tuning range of ~415-515 nm for the signal beam and ~1140-2450 nm for the idler beam. The “red” crystal has a tuning range of ~505-710 nm for the signal beam and ~710-1190 nm for the idler beam. These tuning ranges are only approximate and are highly dependent upon the OPO calibration.

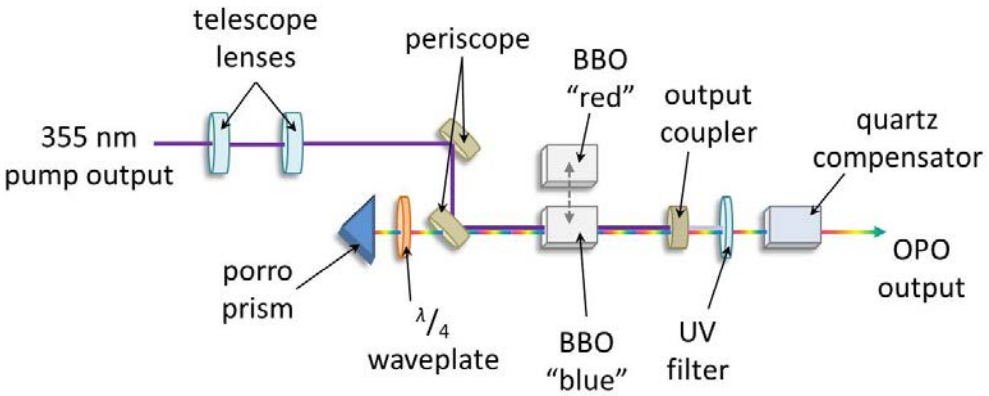

Figure 2.17. Overview of the GWU preciScan OPO setup.

In principle, the OPO resonator could use a broadband mirror for the high reflector. However, this would result in the OPO output beam having a high degree of divergence. To overcome this problem, the high reflector consists of a $\lambda/4$ waveplate and a Porro prism mounted at a 45° angle relative to the polarization of the pump beam. Two additional optics are present after the OPO output coupler. The first is a UV filter that absorbs any remaining unconverted pump radiation that is not reflected by the output coupler. Following this filter is a quartz compensator crystal that is used to correct for any beam walk that occurs as a result of angle tuning the BBO crystals. At this point, both signal and idler beams propagate collinearly. Separation of these two beams can be performed either by use of the Pellin-Broca prism in the SHG/SFM stage or by use of a polarizing beam-splitter cube (see §2.6.4 and §2.6.5 for more information).

Due to reoccurring problems with the quality of the output coupler, several modifications have been made to the OPO. First, a shim has been inserted to mount the output coupler in a manner such that the pump laser does not reflect from the center. This provides the ability to rotate the output coupler to a new position in the event that one area becomes damaged. Because of this modification, the original position of the UV filter (attached directly to the output coupler mount) blocks the outgoing beam. To overcome this problem, a new mount was made for the UV filter that fits in between the output coupler and the compensator crystal.

2.6.4 Second harmonic generation and sum frequency mixing stage

In order to extend the wavelength range of the experiment into the ultraviolet region, the output of the OPO is converted to higher frequencies in a GWU uvScan that utilizes a combination of both second harmonic generation and sum-frequency mixing. A schematic diagram of the GWU uvScan in SHG mode is shown in Figure 2.18. The output of the OPO is sent through two BBO crystals where frequency doubling takes place. Several BBO crystals are used to account for the various polarizations and wavelength regions of the OPO output. By frequency doubling the “blue” signal using the “UV1” crystal, radiation from ~220 – 257 nm is produced. Frequency doubling the “red” signal using the “UV2” crystal is used to produce radiation from ~257 – 354 nm. Frequency doubling of the “red” idler is performed using the “UV3” crystal for wavelengths from ~354 – 412 nm. Because the polarization of the OPO idler is

opposite that of the OPO signal, a $^{\lambda}/_{2}$ waveplate is used to rotate the idler polarization for use with the "UV3" crystal. Optimization of the SHG process is accomplished by adjusting the angle of the relevant BBO crystal. Since this will result in beam walk, two BBO crystals are always used at the same time and rotated in opposite directions from one another so that the second crystal acts as a beam-walk compensator. The produced SHG as well as the remaining unconverted OPO signal and idler beams are then directed using a right angle turning prism into a Pellin-Broca prism. The Pellin-Broca prism is used to separate the three beams and select a single wavelength output.

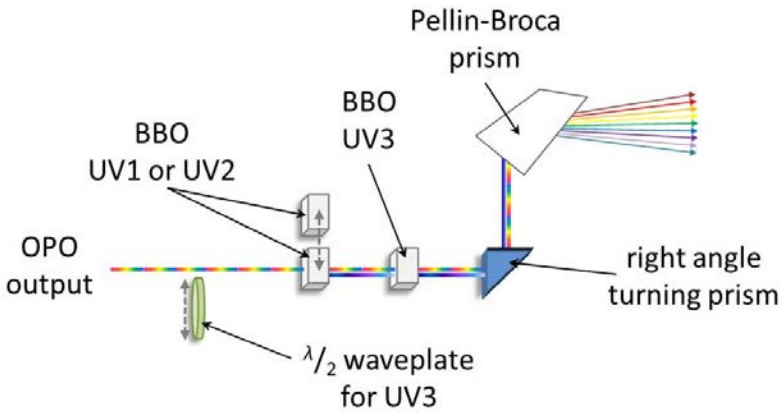

Figure 2.18. Overview of the GWU uvScan in SHG mode.

A schematic diagram of the GWU uvScan in SFM mode is shown in Figure 2.19. Prior to reaching the entrance of the SHG/SFM stage, residual 1064 nm output from the pump laser is conditioned by being sent through a telescope and a ceramic aperture to ensure that it has an appropriate energy density and beam diameter. This beam is then overlapped with the OPO output using a periscope/injection mirror. Both beams are then sent through a series of BBO crystals where sum frequency mixing of the OPO output beam with 1064 nm pump radiation is performed. Using the "UV1" crystal, SFM of the OPO "blue" signal is performed, resulting in radiation from ~299 – 350 nm. Using the "UV2" crystal, SFM of the OPO "red" signal is performed, resulting in radiation from ~350 – 404 nm. Similar to when the stage is used in SHG mode, a second BBO crystal is kept in place at all times to act as a compensator and wavelength selection is performed using a Pellin-Broca prism.

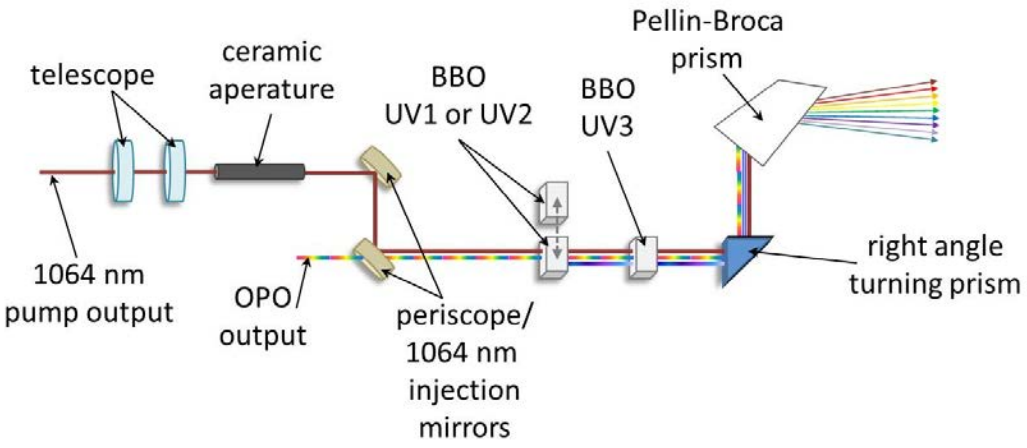

Figure 2.19. Overview of the GWU uvScan in SFM mode.

2.6.5 Beam selection, steering and measurement

In most situations, wavelength selection is performed using the Pellin-Broca prism located in the SHG/SFM stage. However, this is not possible when the output of the OPO is near the degeneracy point at ~710 nm since the difference in refraction for the signal and idler is far too small to separate the two beams using the Pellin-Broca prism. Whenever the OPO "red" crystal is being used, beam selection is performed using a pair of broadband polarizing beam-splitter cubes (CVI Laser, PBSH-450-1300-100). Two cubes are used to ensure that as much of the unwanted beam is attenuated as possible.

In order to steer the output beams into the interaction region within the mass spectrometer, a series of quartz right angle turning prisms are used. Prisms were chosen because they can be used for all wavelengths within the tuning range whereas several sets of broadband turning mirrors would be necessary for steering over the same range. The beam is sent into the interaction region of the mass spectrometer through a calcium fluoride window (see Figure 2.3). The beam leaves the mass spectrometer through a second calcium fluoride window. The beam pulse energy is measured immediately behind the exit window of the apparatus using a Coherent J8LP pyroelectric joulemeter.

2.7 Data acquisition

When ions strike electron multiplier detectors (channeltron and MCPs), electrons are emitted and then collected by the detector anode. The anode signal is measured using a series

of digital oscilloscopes equipped with 50 Ω terminators. Mass spectra are monitored and recorded using a LeCroy WaveSurfer 62Xs (2-channel, 600 MHz, 2.5 GS/s). In order to increase signal to noise, between 250 and 10,000 mass spectra may be averaged, depending on the system. Mass spectra are recorded and saved directly on the oscilloscope in text format. Parent and fragment ion signal is recorded for action and depletion spectra using a single channel on each of two Tektronix TDS 2022 oscilloscopes (2-channel, 200 MHz, 2GS/s). Peak areas are obtained by setting the measurement window to include only the peak corresponding to the ion of interest and obtaining a mean waveform voltage. To increase signal to noise, an average of 16 mean values is used per data point. Laser signal is also monitored in a similar way using the second available channel on each of the two ion peak measurement oscilloscopes. The direct output of the laser power meter (Coherent J8LP pyroelectric joulemeter) is measured so that normalization to photon flux can be performed (see §2.9). All data are relayed to a control computer using RS-232 serial communications ports (Tektronix, TDS2CMAX).

2.8 Experiment control and timing

Primary control of the experiment and synchronization of all components is performed using a digital delay generator (Quantum Composers, 9518 Plus). Table 2.1 outlines that experimental component each channel controls as well as typical pulse widths and delays for each channel and Figure 2.20 depicts a representative pulse scheme. The entire experiment is referenced to the internal clock of the delay generator (t_0). A large delay is used for the start of the experiment sequence (ejection from ion trap) to be sure that there is enough of a time buffer to trigger the flashlamp of the pump laser that needs to be triggered ~215 μs before the laser output pulse is triggered. Channel D serves to both trigger the laser pulse and turn on the ion detector. The pulse width of this channel determines the amount of time the detector is on. All mass spectra are initiated when the TOF acceleration trigger is sent. The mass spectrometer is run at twice the repetition rate of the laser, allowing mass spectra to be taken both with and without the laser being fired so that background and baseline subtraction can be performed for action spectra (see §2.10.1 for more information). This 40 Hz setup is also used to measure both the initial and undepleted fragment ion signals that are necessary to obtain depletion spectra (see §2.9.2 and §2.10.4).

Table 2.1. Setup for digital delay generator used to control instrument timing.

Channel	Referenced to:	Phase	Component	Width (μs)	Delay (μs)
A	t_0	1,2	Ion Trap	2 - 10	2000
B	A	1,2	TOF Acceleration	4 - 10	15 - 60
C	B	1,2	Mass Gate	0.5 - 2	8 - 15
D	B	1,2	Q-Switch and Detector	2000	8 - 15
E	D	1	Flashlamp	10	(-225) - (-210)
F	B	1	Signal Oscilloscope	10	0
G	B	2	Background Oscilloscope	10	0

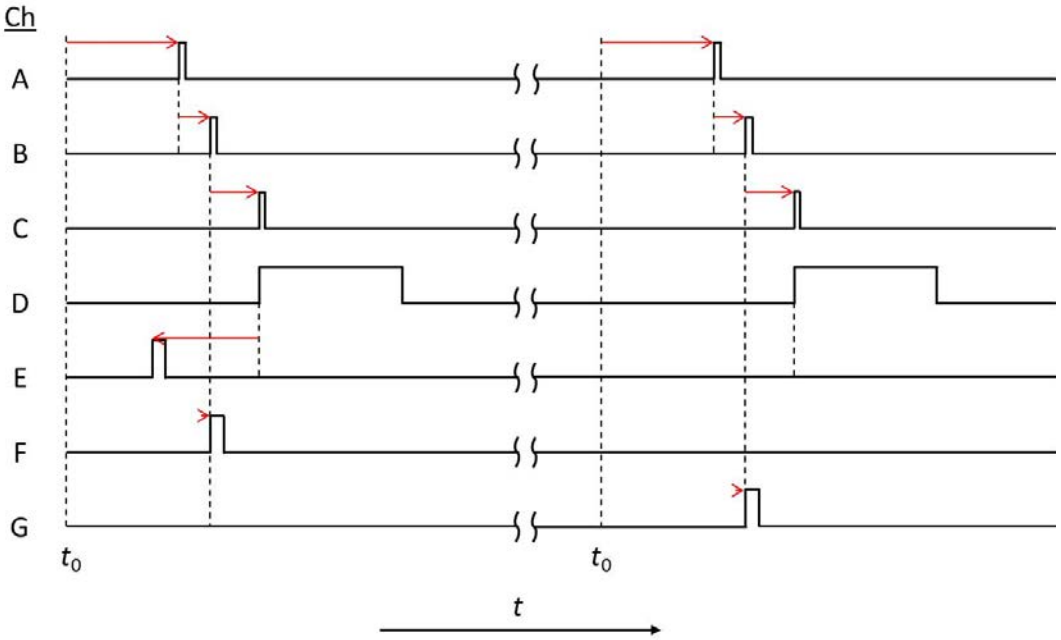

Figure 2.20. Pulse scheme for experimental timing. See Table 2.1 for a list of which experimental component each channel controls.

An important caveat of the timing system is the relationship between when the ions are ejected from the trap and when they are accelerated in the RETOF-MS. Because of the way ions are ejected from the trap (see §2.2.3), the most natural way to trigger the start of the RETOF-MS would be in reference to the end of the trap pulse. However, this is not possible with the current setup of the digital delay generator. Thus, modifying the trap pulse delay will necessitate modifying the relative starting time of the RETOF-MS as well. Currently, a firmware upgrade is pending from the manufacturer.

Secondary control of the experiment is performed using a LabVIEW control program. It communicates with the measurement oscilloscopes to control settings and obtain ion and laser signals. It also communicates with the laser control computer to control and monitor the output wavelength of the tunable optical parametric converter. Photodissociation spectra are typically recorded using a step size of 20 cm^{-1}. All raw data are stored in text files on the control computer as well as a remote data server. The program performs most necessary normalization steps (see §2.9 and §2.10) and stores the output to a separate text file in the same directories as the raw data.

2.9 Data processing

The primary pieces of information we wish to obtain from our experiment are the energy dependence of the absorption cross section and photodissociation quantum yield. As mentioned in §2.1, these cannot be measured directly but can be determined by monitoring either photodissociation action or depletion spectra for ions of interest. It is thus important to consider how these quantities are related and how data should be interpreted. This section provides a basic overview of how information is extracted from raw data. Further technical details specific to our instrument are covered in §2.10.

2.9.1 Action spectra

Taking into account the three conditions for photodissociation described in §2.1, the number of fragment ions formed following irradiation will be given by the equation

Equation 2.6

$$N_i(E,\tau) = P_0 \cdot \sigma(E) \cdot F \cdot Q_i(E,\tau)$$

where $N_i(E,\tau)$ is the number of fragment ions formed for the i^{th} dissociation channel, P_0 is the number of parent ions in the irradiation volume, $\sigma(E)$ is the absorption cross section for the parent ion molecule that is a function of the photon energy E, F is the photon flux within the irradiation volume, and $Q_i(E,\tau)$ is the quantum yield for the i^{th} fragmentation channel, which is given by

Equation 2.7

$$Q_i(E,\tau) = (1 - Q_r) \int_{\tau_0}^{\tau} k_i(E) e^{-k_T(E)t} dt$$

where $k_i(E)$ is the unimolecular dissociation rate at energy E for parent ions fragmenting into the i^{th} dissociation channel, $k_T(E)$ is the total unimolecular dissociation rate for parent ions fragmenting into all channels at energy E, and integration is performed for the time interval between irradiation ($\tau_0 = 0$) and fragment ion mass analysis (τ). The factor of $(1 - Q_r)$ is included to account for the possibility of radiative decay as a relaxation mechanism. Rearrangement of Equation 2.6 leads to

Equation 2.8

$$\sigma(E) \cdot Q_i(E,\tau) = \Omega_i(E,\tau) = \frac{N_i(E,\tau)}{P_0 \cdot F}$$

where the product $\sigma(E)\cdot Q_i(E,\tau)$ is denoted as the photodissociation cross section, $\Omega_i(E,\tau)$, for the i^{th} fragment channel of the parent ion of interest. Thus, by monitoring the number of fragment ions produced as a function of photon energy and normalizing to both the amount of parent ion and photon flux within the irradiation volume, it is possible to obtain a photodissociation action spectrum that will contain information pertaining to the gas-phase absorption cross section as well as the photodissociation quantum yield.

Implicit in these equations are several important assumptions that must be addressed. The first assumption is that the density of parent ions within the irradiation volume is low enough so that ions do not effectively shield one another from being irradiated. Given typical ion counts of ~10^5 in an irradiation volume of ~0.2 cm^3, this first assumption is quite reasonable. The second assumption is that all parent ions are located within the irradiation volume since it is not possible to directly measure the number of parent ions within the irradiation volume. This assumption makes possible the normalization to the total number of parent ions in the ion beam, a quantity that can be measured. If this assumption is not strictly true, then normalization to parent ion signal can still be performed as long as the number of parent ions within the irradiation volume is linearly proportional to the total number of parent ions both inside and outside. The third assumption is that the spatial distributions of both the parent ions and the laser beam intensity are uniform within the irradiation volume. If this is not true, further considerations must be made to appropriately normalize to the photon flux.[18-19] A fourth assumption made is that photon densities are low enough so that only a single photon is absorbed by a particular ion and two-photon effects do not occur. The validity of this

assumption must be evaluated on a case-by-case basis and the methods for validation are described in §2.9.4. A fifth assumption made is that all ions undergo fragmentation either by direct dissociation on a repulsive curve or by some type of unimolecular dissociation mechanism. If dissociation occurs *via* another type of mechanism, for instance by a series of subsequent rearrangement or fragmentation steps, then analysis using the above equations can only be performed with extreme caution since each product channel will not have a single rate constant for unimolecular dissociation, $k_i(E)$. An example of such a system is presented in Chapter 3.

A final consideration that must be made when interpreting action spectra is the term $Q_i(E,\tau)$. This term expresses the dependence of fragment ion formation on the dissociation kinetics. If dissociation occurs on a timescale that is much shorter than the time interval between irradiation and fragment ion mass analysis then the quantum yield obtained will represent the limit as $\tau \rightarrow \infty$ and details in the experimental setup should not greatly affect the photodissociation spectrum. This situation is assumed to be the case for several transition metal complexes that we have studied and are described in Chapters 4, 5, and 7. Alternatively, if dissociation occurs on a timescale that is longer than or of the same order of magnitude as the time interval between irradiation and fragment ion mass analysis, the experimental data will be highly dependent on the presence of a kinetic shift.[20] The degree of kinetic shift will be highly dependent upon the experimental setup used. This situation is observed for the mononucleotides and is discussed in more detail in Chapter 3.

2.9.2 Depletion spectra

Taking into account the three conditions for photodissociation stated in §2.1, the number of parent ions that dissociate following irradiation is given by

Equation 2.9

$$P_d(E,\tau) = P_0 \cdot \sigma(E) \cdot F \cdot Q_d(E,\tau)$$

where $P_d(E,\tau)$ is the number of parent ions that dissociate as a result of irradiation, P_0 is the number of parent ions in the irradiation volume, $\sigma(E)$ is the absorption cross section for the

parent ion molecule that is a function of the photon energy E, F is the photon flux within the irradiation volume, and $Q_d(E,\tau)$ is the quantum yield for photodissociation, which is given by

Equation 2.10

$$Q_d(E,\tau) = (1 - Q_r)\left(1 - e^{-\int_{\tau_0}^{\tau} k_T(E)dt}\right)$$

where $k_T(E)$ is the total unimolecular dissociation rate for parent ions fragmenting into all channels and integration is performed for the time interval between irradiation (τ_0) and fragment ion mass analysis (τ). The factor of $(1 - Q_r)$ is included to account for the possibility of radiative decay as a relaxation mechanism. Rearrangement of Equation 2.9 leads to the equation

Equation 2.11

$$\sigma(E) \cdot Q_d(E,\tau) = \Omega_d(E,\tau) = \frac{P_d(E,\tau)}{P_0 \cdot F} = \frac{\left(1 - \frac{P_u(E,\tau)}{P_0}\right)}{F}$$

where the product $\sigma(E)\cdot Q_d(E,\tau)$ is denoted as the photodissociation cross section, $\Omega_d(E,\tau)$, for depletion of the parent ion, and $P_u(E,\tau)$ is the number of *un*dissociated parent ions following irradiation where the relation $P_d + P_u = P_0$ has been used. The quantity P_u is used rather than P_d since it is the value that is actually measured during the experiment. Thus, by monitoring the number of *un*dissociated parent ions as a function of photon energy and normalizing to both the amount of parent ion and photon flux within the irradiation volume, it is possible to obtain a photodissociation depletion spectrum that will contain information pertaining to the gas-phase absorption cross section as well as the photodissociation quantum yield. Implicit in these equations are several important assumptions. These assumptions are the same as for photodissociation action and are discussed in detail in §2.9.1.

2.9.3 Branching ratios

It is not possible to obtain absolute photodissociation quantum yields since the quantum yield for nonradiative decay is not known and the timescale between irradiation and fragment ion mass analysis cannot be well characterized. However, it is possible to obtain relative branching ratios for each of the fragment channels by comparing their relative intensity at fixed photon energy. These values are calculated using peak areas from Gaussian fits of fragment ion

mass spectra, which are normalized to the area of parent ion mass spectra. It is important to consider that these values are still only approximate since the detection efficiency will vary as a function of ion mass. Since the same acceleration potential is used for all species, all parent ions have the same kinetic energy but different velocities due to their different mass-to-charge ratios and are thus expected to have different detection efficiencies. This problem is exacerbated by the fact that all product ions will have the same velocity as the parent ions did prior to dissociation. This will result in heavier fragment ions having higher kinetic energy and momentum than lighter ones. Since correcting for the combination of these two effects would be extremely difficult, only raw, uncorrected branching ratios are typically presented.

2.9.4 Fluence measurements

As mentioned in §2.9.1 and §2.9.2, interpretation of photodissociation action and depletion spectra are reliant upon the assumption that only single-photon absorption events take place. To validate this assumption, signals used to obtain photodissociation spectra (either fragment action or parent depletion) are measured as a function of photon flux. If they depend linearly on the photon flux then only single photon-events are assumed to take place. If the signals are shown to be non-linear with respect to photon flux, then multi-photon processes must occur. Systems for which multi-photon processes have been observed are described in Chapters 4 and 5.

2.10 Technical considerations

2.10.1 Correction for baseline offsets and background fragmentation

When obtaining photodissociation action spectra it is important to obtain an appropriate baseline and correct for the possibility that not all fragment ions measured are the result of irradiation. Both of these effects are accounted for using a baseline/background subtraction by operating the mass spectrometer at a repetition rate of 40 Hz and the laser at a repetition rate of 20 Hz (see §2.8 for detailed information on experiment timing). Mass spectra obtained with laser irradiation are used to obtain photofragment ion signals and those obtained without laser irradiation are used as reference spectra for baseline offset and background ion signal. Figure 2.21 depicts a pair of oscilloscope screenshots representing data where these factors are of considerable importance. The oscilloscope trace in Figure 2.21a shows a typical fragment ion

signal obtained during a mass spectrum cycle with the laser on. The trace in Figure 2.21b shows the same fragment ion signal but was obtained during a reference cycle of the mass spectrometer where the laser was not triggered. The first point to note is that both traces have an obvious baseline offset. In the case of Figure 2.21a, there is a clearly-visible peak but the baseline offset causes the average value of the data within the oscilloscope window to be negative. If a photodissociation spectrum were to be obtained without taking this into account, it would have a negative baseline, which is not physically meaningful. The baseline of the mass spectrum can also have a positive offset that will have a corresponding effect on the photodissociation spectrum. In either case, it is possible to obtain the value of the baseline prior to taking a photodissociation spectrum and subtracting this value from all subsequent measurements. However, this baseline offset typically varies with time and must be accounted for throughout the entire spectrum. For this reason, baseline subtraction is performed on the fly using data from the reference mass spectra recorded without firing the laser. In addition to correcting for baseline offset, subtraction of the reference mass spectra also accounts for the presence of fragment ions that do not result from photodissociation (see Figure 2.21b). These fragment ions are presumably formed by unimolecular dissociation of vibrationally "hot" ions formed in the ESI source and must be accounted for to ensure that photodissociation spectra have an appropriate zero background.

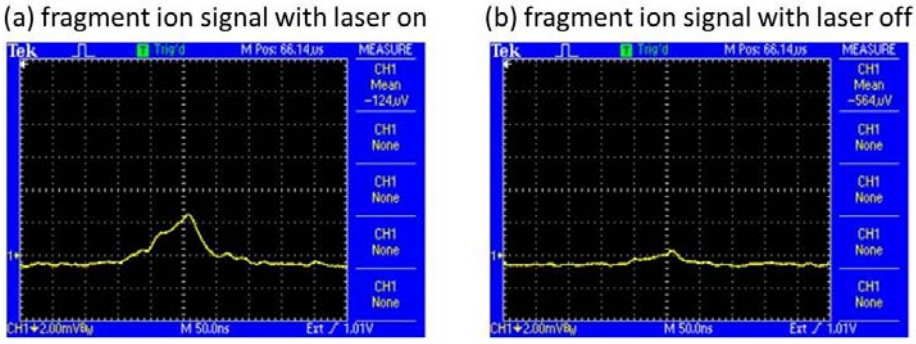

Figure 2.21. Representative oscilloscope traces for fragment ion signal with (a) and without (b) laser irradiation. Note that the non-zero offset of the baseline results in an overall negative CH1 Mean, despite the clear presence of ion signal.

2.10.2 Correction for oscilloscope scaling factor

While performing baseline/background corrections is critical for fragment action spectra,[2] it is of much less importance when obtaining depletion spectra since parent ion signals are typically above 0.1 V and can be as high as 1.5 V. Additionally, obtaining depletion spectra involves measuring the ratio of undepleted *vs.* total parent ions (P_u/P_0, see §2.9.2), making it more important to consider that the two measurement oscilloscopes may not have the same response for a given voltage. To account for this, an oscilloscope scaling factor is measured prior to obtaining all depletion spectra. The laser beam is blocked so that signals measured from both of the alternating 20 Hz cycles of the mass spectrometer represent the total parent ion signal, P_0. The ratio of these two signals is then used to scale all subsequent measurements when recording depletion spectra.

2.10.3 Normalizing to photon flux

The laser pulse energy is measured using a Coherent J8LP pyroelectric joulemeter. The output voltage of the pyroelectric joulemeter is not calibrated for energy but will be proportional to the pulse energy. Consequently, our spectra do not quantitatively represent photodissociation cross sections but will be proportional to them. The output voltage of the meter is proportional to the laser pulse energy over our entire wavelength range and is monitored using two measurement oscilloscopes (see §2.7). Because the laser is run at only half the repetition rate of the mass spectrometer, the laser signal will only be recorded on one of the two oscilloscopes. Similar to when measuring fragment signal (§2.10.1), the laser signal from the primary oscilloscope is corrected by subtracting the value measured on the reference oscilloscope to account for the presence of a baseline offset. As measured, the voltages are proportional to the pulse energy. Therefore, they are divided by the photon energy so that the resulting value is proportional to the photon flux through the irradiation volume.

2.10.4 Normalizing to parent ion

When obtaining photodissociation depletion spectra, normalization to parent ions is not necessary since the spectra already involve measuring the ratio of undepleted *vs.* total parent

[2] Photofragment ion signals can have peak heights as small as 0.5 mV. Such small values may be on the same order of magnitude or even smaller than the baseline offsets.

ions (see §2.9.2). However, it is necessary to normalize to the parent ion signal when measuring photodissociation action spectra to account for the fluctuation of parent ion signal as a function of time. This fluctuation is typically rather small[3] so it is not accounted for directly. Instead, we account for potential hysteresis by always recording spectra in pairs; first in one direction then in the opposite. Additionally, when concatenating multiple wavelength regions into a full spectrum, we include a scaling factor to each of the spectral ranges using a blind approach to avoid any conscious or unconscious biasing. In principle, parent ion scaling can be accomplished empirically. Possible future upgrades to the experiment to include empirical scaling are outlined below.

2.10.4.1 Heavier mass fragments

When photofragment ions have *m*/*z* values higher than that of the parent ion, [4] scaling to parent ion intensities can be performed by monitoring the output of the reflectron MCP detector on a third measurement oscilloscope. This third oscilloscope must be triggered to record the reference mass spectrum taken without laser irradiation so that the parent ion signal measured represents the total, undepleted number of parent ions. A third oscilloscope is necessary since parent ion signal will appear at much shorter flight times than fragment ions. In principle, scaling of the reflectron to optimize fragment ion transmission will result in poor transmission and detection efficiency for parent ions and the reference parent ion signal will not be optimal. However, if the measured signal is directly proportional to the number of parent ions present in the irradiation volume, normalization will be possible.

2.10.4.2 Lighter mass fragments

When photofragment ions have *m*/*z* values lower than that of the parent ion, scaling to the number of parent ions can be performed by monitoring the output of the linear MCP detector on a third measurement oscilloscope. A third oscilloscope is necessary since a separate detector would be used. This third oscilloscope must also be triggered to record the reference mass spectrum taken without laser irradiation. Measurement of parent ions on the linear detector is made possible by scaling the reflectron to optimize fragment ion trajectories. In this

[3] Parent ion fluctuation is typically between 0 and 5 % over the time required for obtaining a portion of a spectrum.

[4] This will only be the case if the parent ion is a multiply-charged ion. See §2.3 for more information.

case, the reflectron voltage must be scaled to lower voltages. Consequently, the higher *m*/*z* parent ions will penetrate through the entire reflectron and will be able to reach the linear detector. Because the kinetic energy of parent ions will decrease upon passage through the reflectron, their detection efficiency will be lowered. However, the measured signal will still be proportional to the total number of parent ions within the irradiation volume.

2.10.5 Averaging of spectra

In order to ensure the reproducibility of the data, photodissociation spectra are recorded over the course of several, different days and averaged together. Because optimization of the OPO and SHG/SFM stage is generally performed on a daily basis, the exact wavelengths used when obtaining spectra typically vary from day to day. As a result, a linear interpolation of individual data points is used to average multiple spectra.

2.10.6 Eliminating 60 Hz noise

Over the course of designing and building the experimental apparatus, 60 Hz noise from the electrical supply lines in the lab was found to have a substantial influence on the quality of data. The 60 Hz noise is especially problematic for our experiment since it is a multiple of the 20 Hz repetition rate of the experiment. In principle, this should not be a problem since the experiment should always run in phase with the AC power. However, there is a slight difference in frequency between the AC power and the digital delay generator. This difference manifests itself as a beat frequency that appears in the baseline of all photodissociation spectra, the magnitude and frequency of which changes dramatically from day to day. Typically, the spacing in the beat pattern is on the same order of what is expected of spectral features. Thus, it is critical to eliminate this source of noise. Initial solutions to this problem involved adjusting the experiment timing so that it was synchronized to the 60 Hz noise. However, this resulted in potential misfiring of the laser system. The solution currently employed involves running the experiment at a repetition rate of 19.8 Hz (50.5 ms period). While this does not directly eliminate the problem, it alters the beat frequency such that it is removed by averaging.

2.10.7 Detector saturation from UV-scattering

When the laser beam enters the interaction chamber, a small portion of light is scattered from the laser windows. Due to the close proximity of the laser interaction region and the

reflectron detector, some of the scattered light may reach the detector. This does not present a problem for photon energies below the work function of the MCPs. However, around wavelengths of 315 nm (~3.9 eV), the MCPs begin to detect the scattered light. As the photon energy increases, so does the sensitivity of the MCPs. Eventually, the effect is severe enough to substantially deplete the electrons present in the MCP, saturating the detector and reducing the detection efficiency of the MCP for periods of time that are far longer than the experimental timescale. In addition to adversely affecting the signal-to-noise level of the experiment, this reduction in detection efficiency varies as a function of the photon energy and is considerably difficult to characterize adequately.

To circumvent this problem, a combination of two approaches was used. The first utilizes a series of baffling tubes mounted to the interior of the laser interaction chamber to shield the detector from the scattered UV light. The baffles are made of aluminum tubing that has been bead-blasted and coated with colloidal graphite (Aerodag G) to eliminate any potentially reflective surfaces. While this approach greatly reduces the amount of scattered light reaching the detector, it does not completely eliminate saturation.

The second part of the combined approache involves switching on the detector after the laser pulse has been fired so that scattered light does not induce electrical gain when it strikes the MCP. Usually, this can easily be accomplished by reducing the detector voltage prior to triggering the laser and then switching it to the normal operating voltage immediately following the laser pulse to restore the detector gain. However, this is a non-trivial task when the MCPs are configured to detect negatively charged species. In order to detect anions, the front face of the MCP is held at ground potential and the back face and anode are held at positive high-voltages. A high-voltage capacitor is used to separate the anode voltage from the signal line while still allowing passage of the transient ion signals (see Figure 2.14). However, the rapid pulsing necessary to quickly turn on the detector could result in a transient high-voltage pulse that is transmitted through the capacitor, creating the risk of damaging any components in the signal line.

To circumvent this problem, the detector is switched on not by rapid pulsing the high-voltage supply to the back face and anode but rather by rapid switching of the front face between high potential and ground. This is accomplished using the simple circuit depicted in Figure 2.22, which provides an extension to the MCP voltage supply circuits already discussed in §2.5. This extension includes additional resistance between the front face of the MCP and ground. When operating voltages are applied to the detector, this added resistance will lower the voltage across the MCPs by a factor of ~2. This reduction will result in lower signal gain so that the detector is in an "off" state. In parallel with this added resistance is a high-voltage transistor that can be switched on and off using a TTL input pulse. When the transistor is turned on, the added resistance between the front face of the detector and ground is bypassed so that the full voltage is restored across the MCPs. This results in the detector being in an "on" state so that ion signal can be measured.

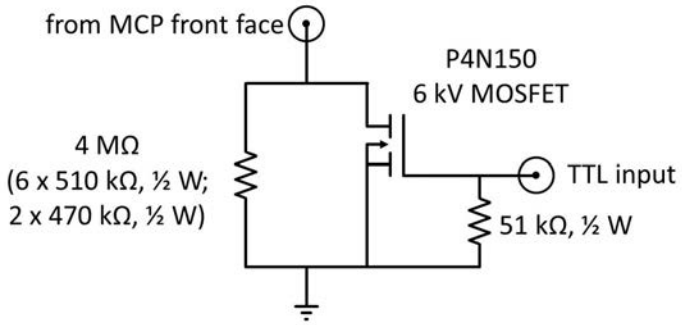

Figure 2.22. Switching circuit used for on and off the reflectron MCP detector.

While this approach solves the UV saturation problem, the detector does not turn on instantly. The amount of time required is highly dependent upon the total resistance of the voltage supply circuit and the capacitance used to couple the anode to the signal line. Through a series of system tests, an optimal on time of ~40 µs was determined to fully restore the gain of the MCPs.

2.11 References for Chapter 2

1. Yamashita, M. and Fenn, J.B., "Negative-Ion Production with the Electrospray Ion-Source." *Journal of Physical Chemistry*, 1984. **88**(20): p. 4671.

2. Yamashita, M. and Fenn, J.B., "Electrospray Ion-Source - Another Variation on the Free-Jet Theme." *Journal of Physical Chemistry*, 1984. **88**(20): p. 4451.

3. Fenn, J.B., Mann, M., Meng, C.K., Wong, S.F., and Whitehouse, C.M., "Electrospray Ionization for Mass-Spectrometry of Large Biomolecules." *Science*, 1989. **246**(4926): p. 64.

4. Loo, J.A., Udseth, H.R., and Smith, R.D., "Peptide and protein-analysis by electrospray ionization mass-spectrometry and capillary electrophoresis mass-spectrometry." *Analytical Biochemistry*, 1989. **179**(2): p. 404.

5. Blades, A.T., Ikonomou, M.G., and Kebarle, P., "Mechanism of Electrospray Mass-Spectrometry - Electrospray as an Electrolysis Cell." *Analytical Chemistry*, 1991. **63**(19): p. 2109.

6. Ikonomou, M.G., Blades, A.T., and Kebarle, P., "Electrospray Ion Spray - A Comparison of Mechanisms and Performance." *Analytical Chemistry*, 1991. **63**(18): p. 1989.

7. Kebarle, P. and Tang, L., "From Ions in Solution to Ions in the Gas-Phase - The Mechanism of Electrospray Mass-Spectrometry." *Analytical Chemistry*, 1993. **65**(22): p. A972.

8. Tang, L. and Kebarle, P., "Dependence of ion intensity in electrospray mass-spectrometry on the concentration of the analytes in the electrosprayed solution." *Analytical Chemistry*, 1993. **65**(24): p. 3654.

9. Gomez, A. and Tang, K.Q., "Charge and Fission of Droplets in Electrostatic Sprays." *Physics of Fluids*, 1994. **6**(1): p. 404.

10. Tang, K. and Gomez, A., "On the structure of an electrostatic spray of monodisperse droplets." *Physics of Fluids*, 1994. **6**(7): p. 2317.

11. Hoffmann, E. and Stroobant, V., *Mass Spectrometry: Principles and Applications*. Second ed. 2006, West Sussex: John Wiley & Sons, Ltd.

12. Gerlich, D., "Inhomogeneous RF-Fields - A Versatile Tool for the Study of Processes with Slow Ions." *Advances in Chemical Physics*, 1992. **82**: p. 1.

13. Jones, R.M., Gerlich, D., and Anderson, S.L., "Simple radio-frequency power source for ion guides and ion traps." *Review of Scientific Instruments*, 1997. **68**(9): p. 3357.

14. Luca, A., Schlemmer, S., Cermak, I., and Gerlich, D., "On the combination of a linear field free trap with a time-of-flight mass spectrometer." *Review of Scientific Instruments*, 2001. **72**(7): p. 2900.

15. Gerlich, D., "Molecular ions and nanoparticles in RF and AC traps." *Hyperfine Interactions*, 2003. **146**(1-4): p. 293.

16. Wiley, W.C. and McLaren, I.H., "Time-of-flight mass spectrometry with improved resolution." *Review of Scientific Instruments*, 1955. **26**(12): p. 1150.

17. Stoermer, C.W., Gilb, S., Friedrich, J., Schooss, D., and Kappes, M.M., "A high resolution dual mass gate for ion separation in laser desorption/ionization time of flight mass spectrometry." *Review of Scientific Instruments*, 1998. **69**(4): p. 1661.

18. Walther, C., Becker, S., Dietrich, G., Kluge, H.J., Lindinger, M., Lutzenkirchen, K., Schweikhard, L., and Ziegler, J., "Photo fragmentation of metal clusters stored in a Penning trap." *Zeitschrift Fur Physik D-Atoms Molecules and Clusters*, 1996. **38**(1): p. 51.

19. Friedrich, J., Gilb, S., Ehrler, O.T., Behrendt, A., and Kappes, M.M., "Electronic photodissociation spectroscopy of isolated IrX_6^{2-} (X=Cl,Br)." *Journal of Chemical Physics*, 2002. **117**(6): p. 2635.

20. Chupka, W.A., "Effect of Unimolecular Decay Kinetics on the Interpretation of Appearance Potentials." *Journal of Chemical Physics*, 1959. **30**(1): p. 191.

3 Mononucleotides

This chapter has been reproduced in part from the following previously-published articles:

a) Marcum, J.C., Halevi, A., and Weber, J.M., "Photodamage to isolated mononucleotides – photodissociation spectra and fragment channels." *Physical Chemistry Chemical Physics*, 2009. **11**: p. 1740. Reproduced by permission of the PCCP Owner Societies.

b) Marcum, J.C., Kaufman, S.H., and Weber, J.M., "UV-photodissociation of non-cyclic and cyclic mononucleotides." *International Journal of Mass Spectrometry*, 2011. doi:10.1016/j.ijms.2011.01.021

3.1 Background

The study of UV-induced photofragmentation of gas-phase nucleotides provides a basis for the description of their intrinsic photophysical and photochemical properties. While nucleotides in the absence of solvent can be expected to behave differently from physiological conditions, this comparison may aid in a better molecular-level understanding of possible processes involved in UV photodamage to DNA and the role of the solvent in condensed phase DNA photochemistry.[1] Additionally, gas-phase experiments provide insight into the fragmentation processes that occur following the activation of oligonucleotides in mass spectrometry studies.

Nucleotide photofragmentation should involve a sequence of events comprised of three general processes: absorption, energy redistribution, and dissociation. A complete description of each of these three processes is necessary to understand the nucleotide photofragmentation as a whole. Each of these three areas has individually received much attention, prompting studies of both condensed- and gas-phase systems ranging from individual nucleobases to oligonucleotides where secondary and tertiary structure may play important roles. In order to elucidate the complete process of nucleotide photofragmentation, it is natural to start with the mononucleotides (see Figure 3.1). These are the smallest repeating units of DNA and, as such, constitute simple systems that are small enough to study the complete photofragmentation process while still retaining many of the functional groups known to play important roles in fragmentation of much larger systems. Even within this greatly reduced picture of DNA, there are a considerable number of possible nucleotides, making a complete analysis daunting. This

work is thus restricted to the canonical tautomers of adenine, cytosine, guanine, and thymine. Additionally, it is possible to ionize and study gas-phase nucleotides in cationic form where the excess positive charge is formed by protonation of a nucleobase.[2] However, nucleotides in biological systems exist primarily in anionic form where the excess charge results from deprotonation of the acidic phosphate groups,[3] resulting in a large body of mass spectrometric studies that utilize oligonucleotides in their anionic form to obtain sequence information.[2] For these reasons, our work focuses on anionic, deprotonated nucleotides.

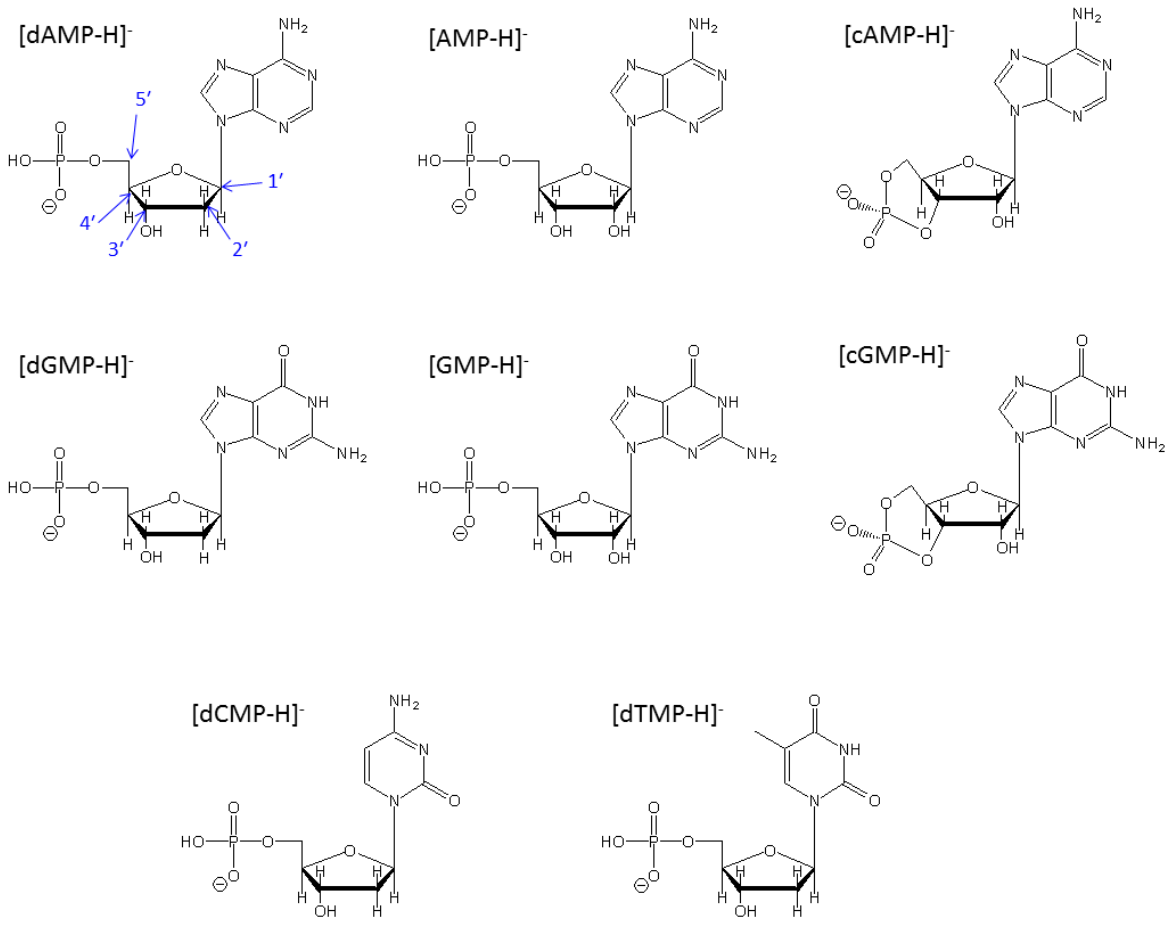

Figure 3.1. Structures of the eight deprotonated mononucleotides studied. The numbering scheme for the five sugar carbon atoms is provided for the structure of 2′-deoxyadenosine-5′-monophosphate.

3.1.1 Excited electronic states

The first step in the series of events that describe nucleotide photofragmentation is the absorption of light. The primary absorbing UV chromophores in nucleotides are the nucleobases.[4] There is a great deal of spectroscopic information pertaining to the individual

nucleobases and this body of work forms the basis of knowledge for all studies on higher-order DNA/RNA systems.[1, 5] In aqueous environments, all of the nucleobases show broad absorption features in the general range of 4-6 eV. Absorption is expected to continue further into the UV, but absorption features of the solvent, and possibly bands involving charge transfer from the nucleobases to the solvent, make analysis more difficult. Numerous theoretical studies (see [5] and references therein) attribute the features in the range of 4-6 eV mainly to $\pi \rightarrow \pi^*$ and $n \rightarrow \pi^*$ transitions. The dipole-forbidden $n \rightarrow \pi^*$ transitions have much weaker oscillator strength when compared to the $\pi \rightarrow \pi^*$ transitions[1] and, as a result, contributions due to $\pi \rightarrow \pi^*$ transitions are expected to dominate the spectra. There is currently slight disagreement among theoretical studies pertaining to the relative ordering of the involved $\pi\pi^*$ and $n\pi^*$ states,[5] but there is a fairly good consensus regarding the relative ordering of the origin bands for the lowest energy $\pi \rightarrow \pi^*$ transitions of the nucleobases. Experiments on jet-cooled nucleobases,[6-12] corroborate many of the findings of theory, including the relative ordering of the origin bands as C < G < T < A for the canonical tautomers of nucleobases.[12]

Gas-phase studies on nucleosides (which consist of a nucleobase attached to a ribose sugar) have been far less available. Some work has been performed by Nir et al. using REMPI as well as IR-UV and UV-UV hole burning on jet-cooled guanosine as well as several substituted guanosines, but only the non-canonical enol form of guanosine could be detected.[7, 13] The authors suggested that this behavior could possibly be due to the reduced excited state lifetime of the keto form, which would affect their ability to detect it. However, the fact that guanosine had origin bands very close to those of the analogous guanine tautomers suggests that substitution at the 9H position does not greatly affect the relevant electronic transitions.

Studies focused on larger oligonucleotides in aqueous environments have discovered that UV-excitations involve delocalized excimer/exciplex states rather than the $\pi\pi^*$ states observed in smaller systems.[14-16] This shift in the character of the excited states has been predominately attributed to π-stacking interactions between the nucleobases. Rather than being localized to a single nucleobase, these states are expected to be delocalized over a

considerable number of bases.[14-16] Consequently, these states may not play as critical of a role in situations where π-stacking is not as prevalent, such as unfolded DNA/RNA or in the gas-phase where base stacking may not be structurally relevant.[17-18]

3.1.2 Electronic relaxation and vibrational energy redistribution

Following the absorption of ultraviolet radiation, nucleobases have been shown to undergo internal conversion from the initially excited electronic state back into a vibrationally "hot" electronic ground state on a timescale of up to a few picoseconds.[5] Early condensed-phase studies by Pecourt et al. and Peon et al. determined the singlet excited state lifetimes of aqueous nucleosides to be between 290 and 760 fs, depending on the nucleobase present.[19-21] Further work compared the excited state lifetimes of nucleosides to nucleotides and individual nucleobases.[21-23] While the presence of sugar and/or phosphate subgroups was found to have an effect on the excited state lifetimes, the differences were not substantial and the underlying photophysical process of rapid internal conversion can be expected to take place for all systems. Later work on gas-phase nucleobases found a strong excitation wavelength dependence on the relaxation lifetimes of the isolated bases. Excitation at the S_1 origin band resulted in considerably longer decay lifetimes, presumably due to the lack of available vibrational energy to facilitate internal conversion.[24] Excitation into states with considerable vibrational energy led to lifetimes on the order of 1 ps, which were much closer to aqueous results.[25-26] The very similar electronic relaxation times of free and solvated nucleobases suggest that solvation of nucleobases does not dramatically change the relaxation mechanism, despite the presence of H-bonding interactions between the base and solvent.

The short excited-state lifetimes of nucleobases are thought to be made possible by conical intersections that enable efficient coupling of ground and excited electronic states.[19, 5, 16] It has been proposed that relaxation can proceed directly from the initially excited $\pi\pi^*$ states[27] as well as via $n\pi^*$[28] or $\pi\sigma^*$[29-31] states. The nuclear motion responsible for relaxation through $\pi\sigma^*$ states has been suggested to involve severe strain on nucleobase N-H bonds that could promote H-atom loss or transfer.[29-30] The charged nature of nucleotides makes them amenable to mass spectrometric techniques, allowing them to be isolated from the perturbing effects of solvent and counterions so that their intrinsic behavior can be

investigated. However, few groups have combined laser spectroscopic and mass spectrometry techniques in the past and no experiments on the electronic excited state lifetimes of gas-phase nucleotides have been performed to date.

As mentioned above, the working hypothesis used by most researchers in this area is that rapid electronic relaxation occurs, producing a vibrationally hot molecule in the electronic ground state. One important question is how the energy is redistributed from there. If electronic relaxation proceeds mostly *via* conical intersections involving the nucleobase, one can expect that redistribution starts with most of the excitation energy localized in the base, while the rest of the molecule has a vibrational population corresponding to its temperature before UV absorption. In comparison with other activation methods (e.g. by collisions or infrared multiphoton absorption), the way in which vibrational and conformational phase space is explored during and after activation can be expected to greatly influence the fate of the molecule all the way to fragmentation.

3.1.3 Thermal fragmentation nucleotides

The rapid electronic relaxation following UV-excitation results in highly vibrationally-excited nucleotides in the electronic ground state. In the condensed phase, the vibrational energy can be rapidly dissipated into the surrounding chemical environment. This introduces questions pertaining to how energy will be redistributed in the nucleotide, what timescales are important for the redistribution, and what would happen if the vibrational energy remains in the molecule instead of being dissipated by coupling to the solvent. Additionally, it is unclear whether or not there is a small probability of producing photofragments either by direct dissociation on a repulsive electronic state or by vibrational predissociation during the short time needed for solvent-mediated vibrational relaxation. Although such fragmentation reactions may be rare events, they would still incur biologically relevant damage and necessitate enzymatic repair. If direct dissociation is absent, fragmentation of the nucleotides following UV absorption will occur by thermal processes. This means that the physical mechanisms for fragmentation can be expected to be similar to those that are involved in other thermal activation methods such as collision-induced dissociation (CID), infrared multi-photon

dissociation (IRMPD), post-source decay (PSD) or blackbody infrared dissociation (BIRD).[3, 32-35]

One of the first studies on ultraviolet photodissociation (UVPD) of nucleotides was performed by Nielsen et al. on deprotonated and protonated adenosine-5′-monophosphate ($[AMP-H]^-$ and $[AMP+H]^+$ respectively).[36] In their study, the lifetime of the excited electronic excited states could not be monitored directly, but the survival lifetime of the parent ion was measured following irradiation at 4.66 eV by monitoring the production of neutral fragments. The authors determined that fragmentation of the parent ions following UV irradiation is dominated by processes occurring on a microsecond timescale. This observation is consistent with a unimolecular decay mechanism that is the result of rapid internal conversion from the initially excited electronic state into a vibrationally hot electronic ground state. However, a smaller (up to 20%) contribution of direct dissociation could not be excluded. More recent work by Aravind et al. revisited these kinetics with improved temporal resolution.[37] They determined that the production of neutrals takes place on two different timescales of 95 ns and 2.4 μs. These timescales also point to thermal fragmentation of the nucleotide since they are considerably longer than one would expect from direct electronic processes. While this work did provide benchmark data concerning the general nature of the UVPD process for nucleotides, only neutral products were monitored.[5] The experiment used did not afford selective identification of these or ionic fragments. This information is vital to the ability to develop a more complete understanding of the entire UVPD process, from cradle to grave.

Up until this point, the only pathway that has been discussed is that of unimolecular decay, where fragmentation presumably results in a number of neutral and charged molecular fragments. In addition to these mechanisms, UV-irradiation of nucleotides has also been shown to induce electron detachment.[38-43] The amount of electron detachment that is observed is typically dependent upon two major factors. The first factor is the charge state of the parent

[5] It should be noted that the study by Aravind et al. did explore the ionic fragments produced as a result of UVPD.[37] However, this work was performed shortly after some of our own results on the subject had already been published. While the product ions observed in their study did agree qualitatively with those formed in our initial study, several differences were apparent. Further work from our group addressed these differences and is discussed in detail below.

ion. In cases where the parent ion is highly negatively charged, electron detachment can be the dominant loss mechanism due to its ability to reduce Coulomb strain.[6][39, 41] The second factor is the identity of the nucleobases that are present. Gabelica et al. showed that nucleotides rich in guanine tend to have a higher detachment yield than nucleotides with little to no guanine.[41, 43] This behavior is consistent with the fact that guanine has the lowest electron detachment energy of the canonical nucleobases.[44, 40] In systems where the charge state is low and there are few guanines present, dissociation can be expected to proceed *via* unimolecular dissociation mechanisms that follow fast internal conversion. However, as either the charge state or the number of guanines is increased, electron detachment could become the dominant process. Gabelica et al. reported that electron detachment in nucleotides has a strong dependence on photon energy.[41, 43] The authors attributed this effect to electronic autodetachment, whereby vertical electronic excitation leads to resonant enhancement of electron detachment, necessitating a better understanding of the electronic states that are involved in UV-absorption of gas-phase nucleotides.

Studies of UV-photodissociation spectroscopy can contribute two very useful pieces of information pertaining to the processes discussed above. First, they can provide selective identification and branching ratios of the fragment ion species resulting from dissociation. This information can be used to determine details of the energy redistribution process and of the ensuing dissociation mechanisms. Photodissociation spectra can also be used to obtain spectroscopic properties of nucleotides as isolated species in the gas-phase that can be used to better understand the electronic autodetachment process, in which electronic absorption leads to resonant enhancement of electron detachment in highly-charged oligonucleotides. Additionally, this spectroscopic information can be compared to aqueous absorption spectra of the same species to determine how solvent affects the electronic properties of nucleotides.

[6] See Chapter 4 for a more detailed discussion on gas-phase multianions.

3.2 Methods

3.2.1 Photodissociation spectra

Details of the experimental methods used in this work are described in Chapter 2 of this thesis. Data were obtained for the four canonical deoxyribo-mononucleotides as well as the cyclic and non-cyclic versions of the ribonucleotides of adenine and guanine. Solutions for electrospray were made using various nucleotide sodium salts dissolved in an ~1:1 mixture of methanol and water. The specific solutions used are listed in Table 3.1.

Table 3.1. Details of the nucleotide solutions used for electrospray ionization.

Approximate Concentration [mM]	Salt	Manufacturer
1	2′-deoxyribo-adenosine-5′-monophosphate disodium salt	MP Biomedicals
1	2′-deoxyribo-cytosine-5′-monophosphate disodium salt	MP Biomedicals
1	2′-deoxyribo-guanosine-5′-monophosphate disodium salt	MP Biomedicals
1	2′-deoxyribo-thymidine-5′-monophosphate disodium salt	MP Biomedicals
5	adenosine-5′-monophosphate disodium salt	MP Biomedicals
5	guanosine-5′-monophosphate disodium salt hexahydrate	MP Biomedicals
5	adenosine-3′,5′-cyclic-monophosphate sodium salt	MP Biomedicals
5	guanosine-3′,5′-cyclic-monophosphate disodium salt	Sigma-Aldrich

As mentioned in Chapter 2, branching ratios for the various fragment channels were calculated using peak areas from Gaussian fits to the parent ion mass spectra. For this particular study, caution must be exercised when using these values since the detection efficiency will vary as a function of ion mass. Since the same acceleration potential is used for all species, all parent ions have the same kinetic energy but different velocities due to their different mass-to-charge ratios and are thus expected to have different detection efficiencies. This problem is

exacerbated by the fact that all product ions will have the same velocity as the parent ions did prior to dissociation. This will result in heavier fragment ions having higher kinetic energy and momentum than lighter ones. Since correcting for the combination of these two effects would be extremely difficult, only raw, uncorrected branching ratios are presented.

3.2.2 Aqueous absorption spectra

Aqueous absorption spectra were obtained for the four canonical deoxyribo-mononucleotides. Four solutions were made by dissolving the appropriate amounts of the same sodium salts mentioned in the previous section (§3.2.1) into deionized water so that each had a concentration of ~70 µM. Spectra were taken using a Varian Cary 500 Scan UV-Visible-NIR spectrometer (version 8.01) with a 10 mm path length, 0.25 nm step size, 2 nm bandwidth, and an integration time of 0.1 sec.

3.2.3 Computational

Gas-phase acidities for the four canonical tautomers of the nucleobases were calculated using density functional theory,[45] employing the B3LYP density functional[46-47] with aug-cc-pVTZ basis sets[48] for all atoms. Geometry optimizations were performed for the canonical tautomers of the four nucleobases as well as for deprotonated nucleobases in which the proton was removed from the nitrogen atom that would be involved in the CN glycosidic bond. Adiabatic electron binding energies were calculated by reoptimizing the geometries of the deprotonated bases after removal of one electron. All calculations were carried out using the TURBOMOLE V5.9.1 suite of programs.[49]

3.3 Results and discussion

3.3.1 Fragment channels

During the electrospray process, all eight of the mononucleotides studied become deprotonated resulting in monoanions that we abbreviate as $[M-H]^-$, where M = dAMP, dCMP, dGMP, dTMP, AMP, GMP, cAMP, and cGMP. In line with chemical intuition as well as with calculations by Ortiz and coworkers,[50] we assume that the excess negative charge is localized on the phosphate. This is not necessarily the case in highly-charged oligonucleotides, where the large Coulomb repulsion between the excess charges can, in principle, be relieved by localizing

negative charge to one of the bases.[39] Upon absorption of ultraviolet radiation, all eight species undergo dissociation into two general classes of fragment ions. Branching ratios for all fragment channels of all parent ions can be seen in Figure 3.2 and a summary of all fragment ion masses and assignments is presented in Table 3.2.

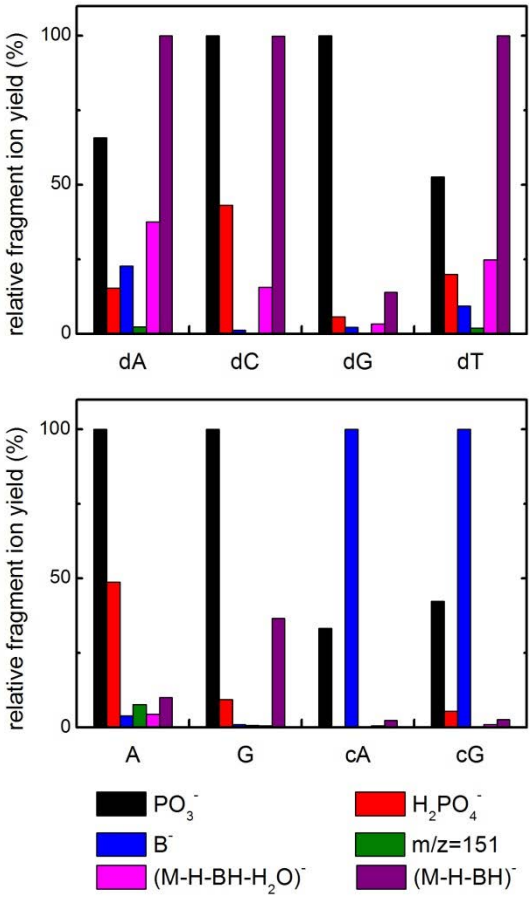

Figure 3.2. Branching ratios for the different fragment channels for 2′-deoxyribomononucleotides (top), ribomononucleotides (bottom left), and the cyclic-mononucleotides (bottom right). Branching ratios are grouped according to parent ions $[M-H]^-$. For all fragment channels involving base loss, B represents the relevant nucleobase. All values have been scaled so that the fragment ion with the highest recorded intensity has a relative fragment ion yield of 100%.

Table 3.2. Overview of all observed fragment masses and assignments. A tentative assignment of the fragment with m/z = 151 is discussed in the text.

	M =							
Parent $[M-H]^-$	dAMP		AMP		cAMP		dCMP	
Fragments	m/z	assignment	m/z	assignment	m/z	assignment	m/z	assignment
	79	PO_3^-	79	PO_3^-	79	PO_3^-	79	PO_3^-
	97	$H_2PO_4^-$	97	$H_2PO_4^-$	-	-	97	$H_2PO_4^-$
	134	A^-	134	A^-	134	A^-	-	-
	-	-	139	see text	-	-	-	-
	151	see text	151	see text	-	-	-	-
	177	$[M-H-BH-H_2O]^-$	193	$[M-H-BH-H_2O]^-$	175	$[M-H-BH-H_2O]^-$	177	$[M-H-BH-H_2O]^-$
	195	$[M-H-BH]^-$	211	$[M-H-BH]^-$	193	$[M-H-BH]^-$	195	$[M-H-BH]^-$
	M =							
Parent $[M-H]^-$	dGMP		GMP		cGMP		dTMP	
Fragments	m/z	assignment	m/z	assignment	m/z	assignment	m/z	assignment
	79	PO_3^-	79	PO_3^-	79	PO_3^-	79	PO_3^-
	97	$H_2PO_4^-$	97	$H_2PO_4^-$	97	$H_2PO_4^-$	97	$H_2PO_4^-$
	150	G^-	150	G^-	150	G^-	125	T^-
	-	-	-	-	-	-	-	-
	-	-	151	see text	-	-	151	see text
	177	$[M-H-BH-H_2O]^-$	193	$[M-H-BH-H_2O]^-$	175	$[M-H-BH-H_2O]^-$	177	$[M-H-BH-H_2O]^-$
	195	$[M-H-BH]^-$	211	$[M-H-BH]^-$	193	$[M-H-BH]^-$	195	$[M-H-BH]^-$

The first class of fragments is based on CN glycosidic bond cleavage (GBC), leading to formation of the deprotonated base, B^- (B = A, C, G, T), as well as an ion of the form $[M-H-BH]^-$ that corresponds to the loss of neutral, protonated base (BH) from the initial deprotonated mononucleotide. Also in this class of fragments is the species $[M-H-BH-H_2O]^-$, which is presumably formed *via* the loss of water from the fragment ion $[M-H-BH]^-$ (see below).[51] Another fragment channel in this class, which is not observed for all parent ions, has m/z = 151. This fragment has been observed before,[52] but it has not been identified. A fragment ion that presumably had m/z = 152 was recently observed by Aravind et al. following UVPD of $[AMP-H]^-$ and was assigned as $B^-\cdot(H_2O)$.[37] While this could be a possibility, the fact that we only observe m/z = 151 and the mass to charge ratio of the peak does not depend on the

identity of the attached nucleobase suggests that the fragment involves the sugar-phosphate group that remains after glycosidic bond cleavage and not the nucleobase itself.

The second class of fragments consists of the phosphate-based products PO_3^- and $H_2PO_4^-$, which are formed by cleaving phosphate-sugar bonds. A final fragment ion, which we only observe for the parent ion $[AMP-H]^-$, has m/z = 139. Interestingly, this fragment seems to appear in the fragment ion mass spectrum of Aravind et al., although they did not explicitly label it.[37] The low abundance of this peak, combined with the fact that it is not common to any other parent ion, suggests that it may not be of much significance. We do not believe that peak assignment is appropriate without further study but mention its observation for completeness. All observed fragment ions correspond to loss of genetic information: loss of the base in the case of CN glycosidic bond cleavage and strand-breaking in the case of the phosphate-based products.

3.3.2 Energy redistribution and thermal dissociation mechanisms

An interesting point to note is that most of the fragment ions that we observe are the result of a considerable amount of nuclear rearrangement. All fragment channels have previously been seen following the activation of gas-phase nucleotides and oligonucleotides using a number of "thermal" methods including CID, IRMPD, PSD, and BIRD. [3, 32-35] Many of these methods involve the thermal excitation of molecular vibrations, leading to an increase in total energy in the molecule, which can undergo a number of rearrangement reactions that lead to the observed products. This suggests that direct bond cleavage from an electronically excited state does not occur and rather the molecule fragments due to a large amount of vibrational energy. This is consistent with previous work that indicated that nucleobases and nucleotides may undergo fast internal conversion through conical intersections to reach a vibrationally excited ground electronic state.[36, 5] The electronic energy that is converted into vibrational energy in the molecule (up to 5.8 eV in our experiment) can then be used to induce the nuclear rearrangement necessary for unimolecular fragmentation. The only fragment channel that could possibly result from direct dissociation on a repulsive curve is the negatively-charged base anion, B^-. While this is generally viewed as an unlikely possibility, there are no

experimental data suited to completely exclude this process. In fact, our results suggest that such a mechanism may be of more importance than previously believed (see below).

There is currently a large and active community of researchers working to ascertain molecular-level details for nucleotide fragmentation mechanisms following thermal activation. The vast majority of experiments have focused on oligonucleotides and the few available studies on mononucleotides have used these larger systems as a starting point. This is surprising since studies on mononucleotides should provide considerably simpler problems of greatly reduced dimensionality. In a comprehensive review by Wu and McLuckey, the authors stress that no single mechanism is able to account for all oligonucleotide fragmentation phenomena, a fact that is particularly disconcerting since most proposed mechanisms have substantial theoretical and/or experimental support.[2] Despite this lack of agreement, several important points can be applied to UVPD of mononucleotides since fragmentation is expected to occur *via* thermal mechanisms.

In the case of GBC-based fragments, the nucleobase fragment can be formed either as a deprotonated anion (B^-) or as a protonated neutral species (BH). In order for the parent molecule to lose BH, proton transfer to the nucleobase must occur. An important question is whether proton transfer occurs either before or after base loss. In some studies, support was given that proton transfer precedes loss of the nucleobase, resulting in a zwitterionic intermediate.[34] Other studies favored a mechanism where proton transfer follows nucleobase loss, involving an encounter complex between B^- and the remainder of the parent molecule.[53]

One area in which there is considerable agreement deals with the threshold energies for different fragment channels. Nucleobase loss, resulting in formation of neutral BH, is typically considered to be one of the most energetically favored channels involving glycosidic bond cleavage.[2] One exception to this is the case of highly-charged oligonucleotides. In these systems, loss of B^- is preferred over loss of BH since it should partially reduce the Coulomb

strain that is caused by the excess negative charge.[7][54] In studies where the timescale for activation is far slower than for energy redistribution (such as the case for slow "heating" of the target involving multiple low-energy collisions[51] or absorption of multiple infrared photons[55, 35]), the fragment channel with the lowest activation barrier should either be the only active channel or at least be the dominant pathway (see Figure 3.3).[56] Since UVPD involves depositing all energy into the molecule in a single step on a timescale much faster than that necessary for thermal fragmentation, it is not surprising that we observe multiple fragment channels for each parent ion. The fact that we observe $[M\text{-}H\text{-}BH]^-$ as one of the dominant loss channels for the deoxyribo-mononucleotides is consistent with loss of neutral BH being one of the lowest-energy GBC-based fragment channels for oligonucleotides.[2]

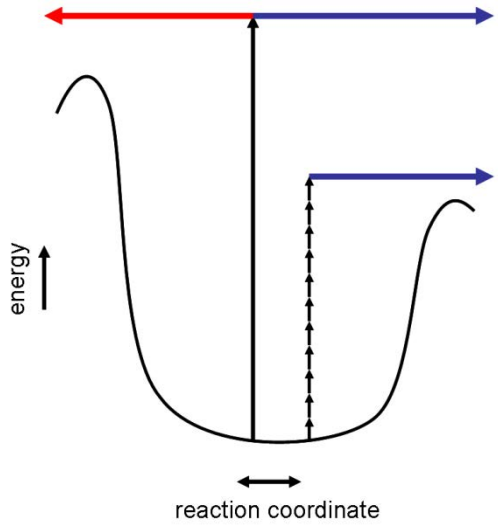

Figure 3.3. Schematic representation of "slow heating" and "fast heating" processes. The short, vertical arrows depict multiple, low-energy deposition events that occur over a long time when compared to fragmentation. The long, vertical arrow depicts a single, high-energy deposition event that occurs on a timescale that is fast when compared to fragmentation. The horizontal arrows represent fragmentation into the various accessible product channels.

Prior to our work, the only study that has attempted to uncover the mechanisms for thermal fragmentation of mononucleotides was performed by Ho and Kebarle,[57] who utilized CID under single-collision conditions to activate parent ions. By measuring fragmentation yields as a function of the center-of-mass collision energy, they were able to determine the threshold enthalpies for the individual fragment channels. Comparison of their experimental data with

[7] See Chapter 4 for a more detailed discussion on gas-phase multianions.

theoretical threshold enthalpies obtained using semi-empirical calculations and transition state theory led Ho and Kebarle to propose a set of fragmentation mechanisms. The formation of phosphate-based products from the 5′-monophosphates was proposed to occur by two separate mechanisms. In the first mechanism (Scheme 3.1), the phosphate group abstracts a proton from the 4′ carbon of the sugar in an E2-type elimination, resulting in the formation of $H_2PO_4^-$. In the second mechanism (Scheme 3.2), transfer of a proton from a phosphate OH group to the phosphoric acid ester oxygen, with concomitant PO bond cleavage, results in PO_3^- fragment ions. These mechanisms are fairly straightforward and are consistent with many of the mechanisms that have been proposed for nucleotide backbone cleavage.[2]

Scheme 3.1

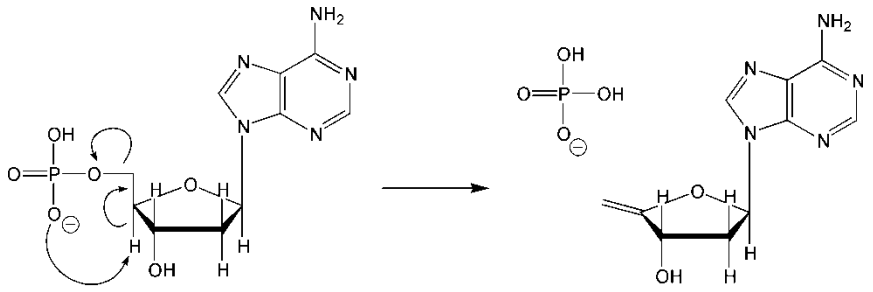

Scheme 3.2

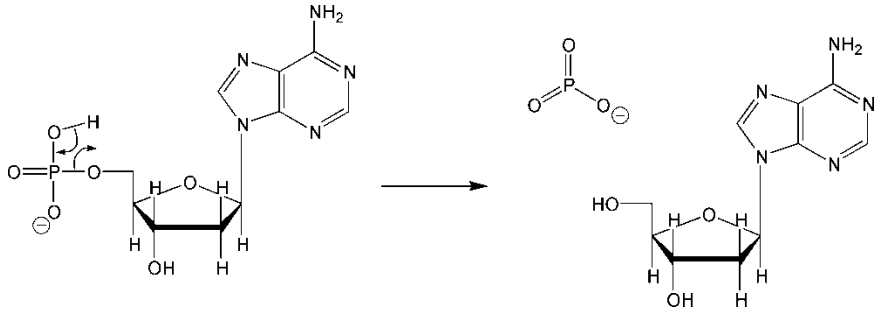

The situation is far less clear for mechanisms involving glycosidic bond cleavage. The mechanism proposed by Ho and Kebarle, based upon earlier work on dinucleotides by Rodgers et al.,[53] involved proton transfer from the 2′ carbon on the deoxyribose to the phosphate group (Scheme 3.3). This proton transfer is accompanied by loss of the nucleobase in an E2-type elimination process. The B^- ion that is formed remains attached to the remainder of the molecule in a weakly-bound encounter complex. This encounter complex can then dissociate, resulting in B^- fragment ions. Alternatively, a second proton transfer step may occur prior to

dissociation of the complex, resulting in neutral BH fragments and $[M\text{-}H\text{-}BH]^-$ fragment ions. If sufficient energy remains in the $[M\text{-}H\text{-}BH]^-$ anionic fragment, it can lose a water molecule, formed presumably[58] from the 3′-hydroxyl group and the 4′-CH group of the deoxyribose.

Scheme 3.3

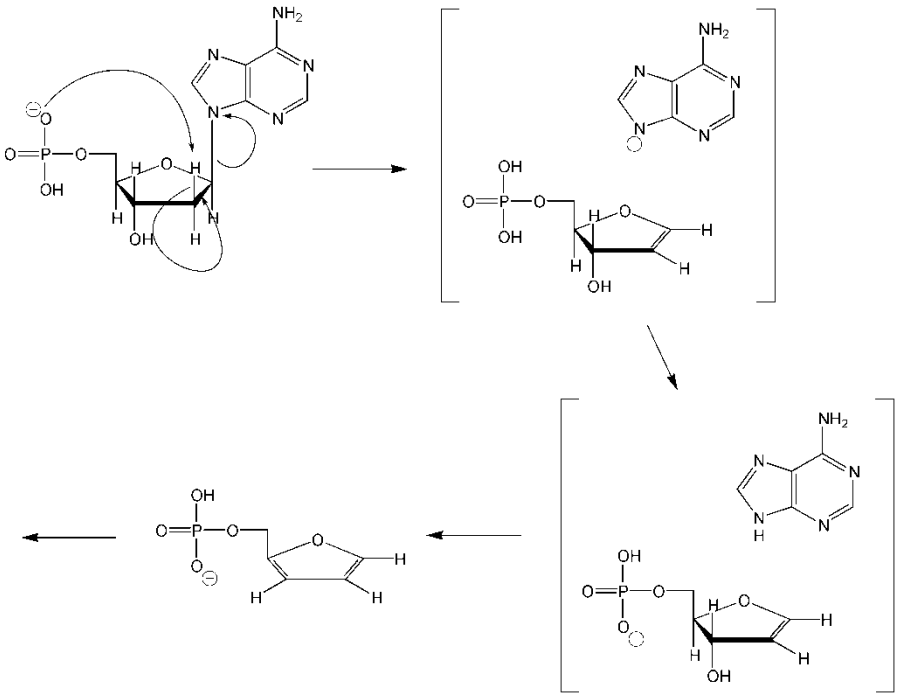

It is far less clear to interpret the identity of the fragment ion with m/z = 151. In principle, it could be formed as the result of losing CO_2 (m/z = 44) from $[M\text{-}H\text{-}BH]^-$. However, this would only hold for the deoxyribonucleotides for which the $[M\text{-}H\text{-}BH]^-$ ion has m/z = 195 and would not work for the ribonucleotides for which the $[M\text{-}H\text{-}BH]^-$ ion has m/z = 211. One possibility for the identity of this ion is the subsequent loss of C_2H_2 from the deoxyribonucleotides fragment $[dBMP\text{-}H\text{-}BH\text{-}H_2O]^-$ to give the ion $[dBMP\text{-}H\text{-}BH\text{-}H_2O\text{-}C_2H_2]^-$, which has m/z = 151. If a ribonucleotide is used as the parent ion instead, subsequent loss of C_2H_2O from the ribonucleotide fragment $[BMP\text{-}H\text{-}BH\text{-}H_2O]^-$ will give the ion $[BMP\text{-}H\text{-}BH\text{-}H_2O\text{-}C_2H_2O]^-$, which will also have m/z = 151. Due to the successive loss of nucleobase and water, the fragment ion $[M\text{-}H\text{-}BH\text{-}H_2O]^-$ should consist of a substituted furan ring. Furan has previously been shown to lose C_2H_2 as a result of thermal decomposition.[59] However, the presence of the charged phosphate group, as well as an extra hydroxyl group at the 2′ position in the case of the ribonucleotides, will most likely lead to a considerably different mechanism.

The mechanisms described above provide potentially attractive explanations for the observed fragment channels. However, closer inspection of the data raises several important questions. Perhaps the most surprising behavior is in the fragmentation of the cyclic mononucleotides. In both $[cAMP\text{-}H]^-$ and $[cGMP\text{-}H]^-$, the phosphate group is tethered to the sugar in two separate locations (see Figure 3.1), hindering formation of phosphate-based products as well as the conformational rearrangement that is necessary for the E2-mechanism that leads to glycosidic bond cleavage. Interestingly, formation of B^- was found to be the dominant fragmentation process (see Figure 3.2). If the previously proposed E2-type mechanism (Scheme 3.3) is still active, then the phosphate group can only abstract a proton at the 2□ carbon by first breaking one of the two phosphoric acid ester bonds. Most of the mechanisms that have been suggested to describe nucleotide backbone fragmentation involve proton transfer to the phosphate group.[2] Since there are very few acidic protons on the cyclic nucleobases, these mechanisms seem rather unlikely. However, branching ratio measurements reveal that PO_3^- is also an abundant fragment channel, accounting for approximately 25% of the total fragment ion signal that was measured for each parent ion (see Figure 3.2). Additionally, irradiation of $[cGMP\text{-}H]^-$ resulted in the formation of $H_2PO_4^-$ fragment ions, albeit with a small yield. In order for these fragments to be formed, at least two bonds between the phosphate and sugar groups must be broken and, in the case of $H_2PO_4^-$, proton transfer must occur. If the phosphate group can be liberated in a way that it can participate in an E2-type reaction, then the dominance of B^- loss over BH may simply be due to the lack of acidic protons available for transfer to the nucleobase.

While we cannot rule out E2-type mechanisms where the phosphate group acts as a nucleophile to induce glycosidic bond cleavage, it is necessary to consider other possible mechanisms where the phosphate group does not participate. One such mechanism is a 1,2-elimination of the nucleobase (see Scheme 3.4). This mechanism has been proposed previously[54] but discarded in favor of the phosphate-mediated elimination that was proposed by Rodgers et al.[53] One possible advantage to this reaction is that it does not involve the phosphate group and the necessary nuclear motion is localized on and near the nucleobase where energy deposition is presumed to occur for UVPD. This mechanism does have one major

disadvantage. The initial products formed during this mechanism are the neutral protonated base, BH, and the corresponding anion $[M\text{-}H\text{-}BH]^-$, not the deprotonated base, B^-. In principle, the resulting fragments can be formed in an encounter complex (as in the case of the phosphate-based elimination discussed above) that undergoes subsequent proton transfer from the nucleobase to somewhere on the sugar or phosphate groups, resulting in the formation of B^-. However, this proton transfer can be expected to be enthalpically unfavorable due to the relative gas-phase acidities of the phosphate group and nucleobase. Additionally, dissociation of the encounter complex to yield BH should be entropically favored over proton transfer, particularly at high energies.[57] While this mechanism can explain the small amount of $[M\text{-}H\text{-}BH]^-$ fragment ions that we observe following irradiation of the cyclic mononucleotides (see Figure 3.2) , it cannot explain the dominance of B^- fragments.

Scheme 3.4

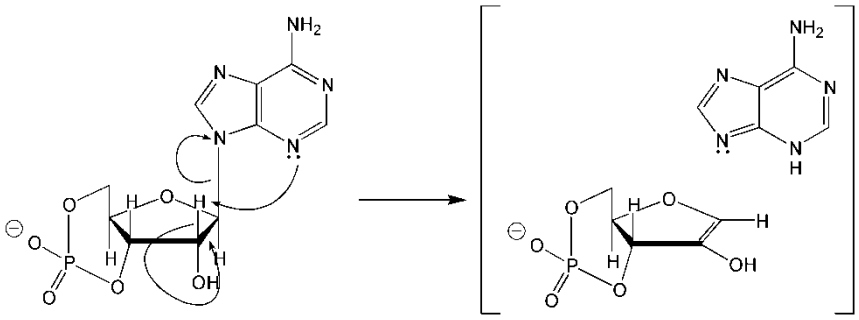

A second possible mechanism that involves glycosidic bond cleavage without the aid of the phosphate group is depicted in Scheme 3.5. This mechanism, which is similar to some that have been proposed before for both nucleotide anions[33] and cations,[3] involves a direct heterolytic bond cleavage of the CN glycosidic bond leading to B^- and a zwitterionic fragment that is resonance stabilized due to the sugar oxygen.[60] If this initial elimination step is followed by abstraction of the proton located at the 2 sugar position (analogous to an E1 mechanism), it would lead to the same products and problems associated with the 1,2-eliminiation mechanism. However, if dissociation of the encounter complex takes place before proton transfer can occur, B^- would be the resulting fragment ion. While proton transfer to the nucleobase should be the enthalpically favored process, dissociation of the encounter complex should be largely entropically favored.[57]

Scheme 3.5

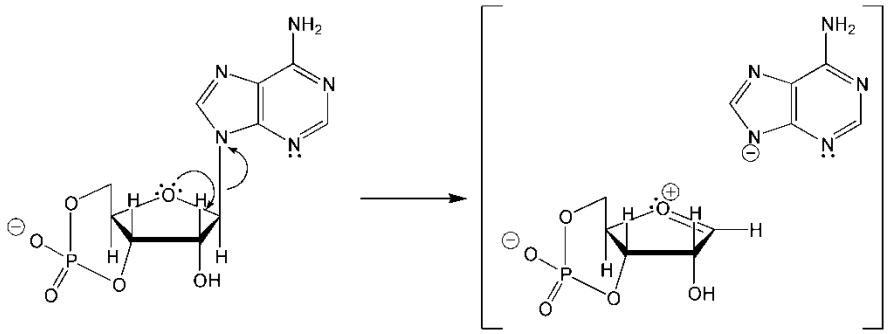

A final mechanism that must be considered is direct dissociation on a repulsive electronic curve, which could also be responsible for at least part of the observed B^- intensity. However, this mechanism should not be active in IRMPD of $[cAMP\text{-}H]^-$, where A^- has been observed as the only fragment channel and excitation should not involve electronic excitation.[55] Additionally, our results for all of the other, non-cyclic-, mononucleotides show that $[M\text{-}H\text{-}BH]^-$ (BH loss) is favored over B^- loss.

Another problem that must be taken into account is that the fragment ion branching ratios for all non-cyclic-mononucleotides following UVPD do not match those obtained in the CID experiment by Ho and Kebarle.[57] This is most apparent when comparing the relative yields for the B^- and $[M\text{-}H\text{-}BH]^-$ channels, which correspond to the loss of charged and neutral base fragments respectively. Additionally, the branching ratios that we observe for UVPD of $[cAMP\text{-}H]^-$ do not match those observed following IRMPD of $[cAMP\text{-}H]^-$ where loss of the negatively charged base, A^-, was the only product observed.[55] There are a number of possible explanations for these differences in branching ratios, but most of them cannot account for all observed behavior.

The first set of possible explanations involves consideration of the different activation mechanisms involved in the various experiments. As mentioned above, if the timescale for activation is slow compared to the timescale for nuclear rearrangement and fragmentation, branching ratios should be weighted toward product channels with the lowest energy thresholds. This explanation can be used to account for the differences between UVPD and IRMPD of $[cAMP\text{-}H]^-$. In slow heating mechanisms, each deposition event imparts only a small

amount of energy into the molecule that is far less than the lowest possible threshold to fragmentation. As a result, fragmentation can only occur following multiple energy deposition events. In this limiting case, activation of the molecule to internal energies that are high enough to cause fragmentation may take place on the microsecond to millisecond timescale. Because the activation process is slow and each deposition event imparts an amount of energy that is small compared to the threshold energy and to the spacing between different thresholds, only one fragment channel should be observed, corresponding to the channel with the lowest threshold energy (see Figure 3.3). Since IRMPD is a slow heating mechanism, it is not surprising that the only observed fragment channel for $[cAMP\text{-}H]^-$ is A^-[55] whereas UPVD (a rapid activation method) results in considerably more fragment ion species.

In principle, this effect of slow *vs.* fast heating could also lead to the differences in branching ratios between our UVPD experiments and CID experiments. However, the high-energy CID experiments by Ho and Kebarle involved single-collision statistics. This means that all activation energy was deposited during a single collision. This results in activation timescales that should be substantially shorter than those for fragmentation, similar to UVPD. Consequently, multiple fragment channels are active (see Figure 3.3). Unlike the limiting case of slow heating processes, where understanding the branching ratios is more trivial since only one product channel should be active, understanding branching ratios for rapid heating processes is far more complex. In principle, the branching ratios can be understood on the basis of some form of unimolecular rate theory, such as in the Rice-Ramsperger-Kassel-Marcus (RRKM) approach. However, these theories will only provide an accurate description if the internal energy of the molecule is uniformly distributed over all degrees of freedom. This will only be the case if the timescale for complete energy redistribution is much shorter than the timescale for fragmentation. If this is true, the branching ratios should be independent of the mechanism of activation. In other words, the molecule will have no memory of how energy was deposited and fragmentation will follow a nearly ergodic exploration of phase space prior to fragmentation. In the limiting case where energy redistribution takes place on a timescale that is slow compared to fragmentation, all branching ratios should reflect a nearly ergodic process

that is independent of the activation mechanism used. However, if fragmentation occurs on a faster timescale, not all of the energy from activation may be available for reaction.

If fragmentation occurs on a faster timescale than energy redistribution, the process will be markedly non-ergodic. Fragmentation branching ratios will thus be strongly dependent upon how energy is deposited into the molecule. An obvious example of non-ergodic fragmentation would be UV absorption followed by direct dissociation from a repulsive electronic state. In this case, dissociation takes place on timescales that are much shorter than those required for the energy to couple into other non-dissociative states. The amount of energy that is available should be largely dependent upon how the energy is deposited into the molecule. In principle, this behavior should persist for both UVPD and single-collision, high-energy CID. However, the molecular collision geometry in CID, and thus the site of energy deposition, cannot be controlled or monitored and only the ensemble average can be obtained. Since each collision should occur under different conditions, the amount of available energy for fragmentation should be different for every collision. This is not the case for UVPD where activation occurs from the same electronic transitions every time. Our results from UVPD of the non-cyclic ribonucleotides show an increased prevalence for loss of neutral BH, suggesting that there is less energy available for reaction than is for the ensemble average of high-energy CID. If as little as 0.5 eV (for example two quanta of either CH or OH stretch) is “stored” in parts of phase space that are unrelated to GBC-based reactions, there could be substantial effects on the branching ratios, tending toward more $[M\text{-}H\text{-}BH]^-$ than B^- based on the fact that loss of neutral BH has a lower threshold energy than loss of anionic B^-. Based on this discussion, we postulate that both single-collision CID and UVPD demonstrate at least some contribution due to non-ergodic relaxation pathways.

Another related factor is the total amount of energy deposited during activation in each of the two experiments. Activation by means of UVPD will result in well-defined amounts of energy deposited into the molecule, limited by the bandwidth of the laser (< 1 meV), which is negligible in comparison to the activation energies of 4-6 eV. This uncertainty is considerably larger for the CID experiments by Ho and Kebarle that specified activation energy by the center-

of-mass collision energy. Since most collisions will occur with an impact parameter greater than zero, the distribution of activation energies will have an average that is less than the specified center-of-mass collision energy. This means that comparison between the single-collision CID and UVPD results is not as straightforward since the two activation methods will not impart the same amount of energy. However, the data by Ho and Kebarle show that as the activation energy is increased, the fragment B^- increases in importance relative to $[M-H-BH]^-$ fragments. Since the CID energies are less than UVPD energies, $[M-H-BH]^-$ should be more favored for CID at a given energy than for UVPD, which is contrary to the observed results.

A final possible reason for the differences in branching ratios is the kinetic shift effect. Up until this point, it has been assumed that any ion that is excited to energies above the dissociation threshold for a given channel will fragment on the timescale of the experiment. However, this is not always the case. According to experiments by Nielsen et al.[36] and Aravind et al.,[37] the timescale for adenosine-5□-monophosphate fragmentation is on the order of nano- to microseconds. If the time between activation and fragment ion mass analysis is less than these dissociation timescales, then it is likely that not all activated ions undergo fragmentation by the time they are detected. Changing the amount of time between activation and fragment ion mass analysis will lead to a change in product branching ratios, which could explain the differences between the two experiments. However, the timescale between activation and detection in the two experiments are fairly comparable (between ~34 and ~47 μs for the Ho and Kebarle experiment[57] and between ~26 and ~29 μs for our experiment), suggesting that the kinetic shift for the two experiments should not be substantially different.

3.3.3 Photodissociation spectra

For each parent ion, photodissociation action spectra were recorded for as many fragment channels as possible to gauge any variability that might be present. Product channels for which spectra were not obtained typically had fragment ion yields that were far too low to take spectra. Each of the photodissociation spectra for $[M-H]^-$ parent ions consists of several broad features in the general range of ~4-6 eV. These include a broad peak or group of peaks below ~5.5 eV and, in some cases, an increase in the photodissociation cross sections at higher

energies that extend beyond our spectral range. Part of the spectral congestion observed is certainly due to the internal energy of parent ions that should be roughly at room temperature,[61] but if the relaxation of the electronically excited states proceeds on sub-picosecond timescales,[5, 62] lifetime broadening could also play a role.

The shapes of the fragment spectra are very similar for the fragments belonging to the same parent ion. Despite the general similarities, there are small but noticeable differences in the relative importance of the two absorption features. Specifically, the increase of the photodissociation cross section at high energies is not as prominent for the GBC-based fragments as it is for phosphate-based fragments. Additionally, some of the spectral features below ~5.5 eV show varying degrees of suppression, depending on the parent and fragment ion considered. These differences are explained in detail in §3.3.4 below.

In order to determine how the mononucleotide spectra are affected by solvation, Figure 3.4 compares the parent ion depletion spectra of the four canonical deoxyribo-mononucleotides to their respective aqueous absorption spectra. Peaks in the solution spectra exhibit solvatochromic shifts of up to 0.22 eV (see Table 3.3). There are some differences in the relative intensities of the absorption bands. These differences are most pronounced for $[dCMP-H]^-$. It is likely that multiple electronic absorption bands and their corresponding Franck-Condon progressions are hidden underneath the broad, congested feature. However, since the individual vibronic transitions are not resolved, solvatochromic shifts are best characterized by noting the shifts of the absorption peak and of the half-maximum values of both slopes individually (Table 3.3).

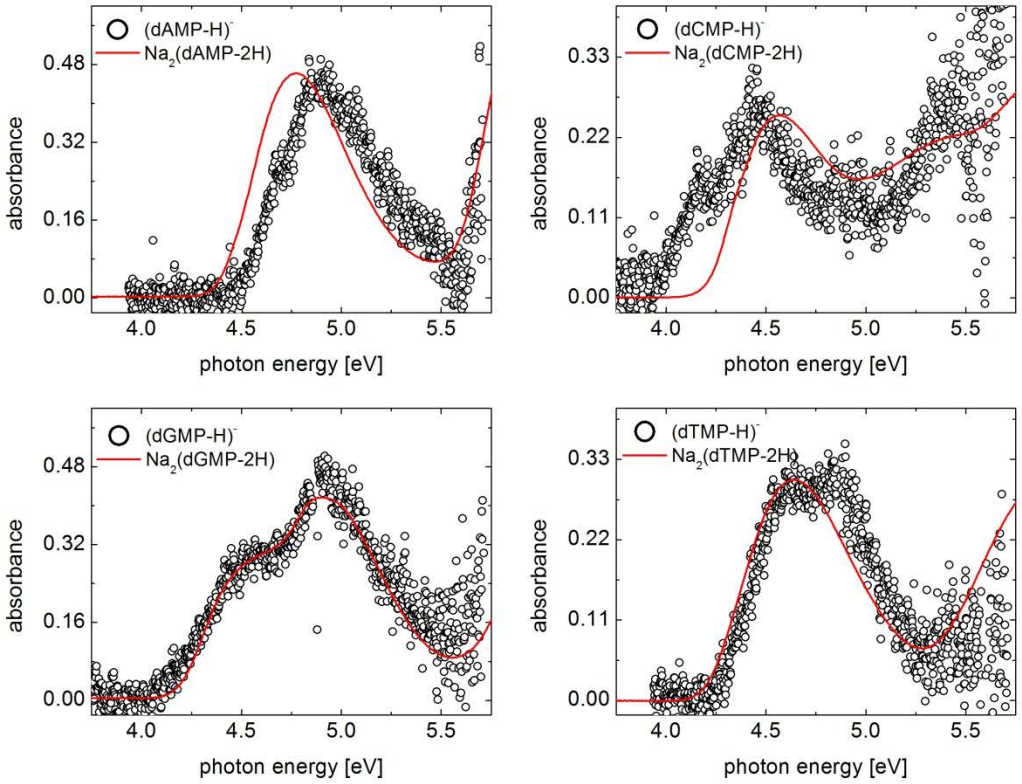

Figure 3.4. Comparison between parent ion depletion spectra (open circles) and aqueous solution absorption spectra (solid line) of the 2⍰-deoxyribomononucleotides. Depletion spectra are for the parent ions of the form $[dBMP-H]^-$, where the base is indicated in each panel. Aqueous absorption spectra are for ~70 µM solutions of the disodium salts of the nucleotides. Depletion data have been normalized to the peaks of the aqueous solution absorption spectra in each case for easier comparison.

Table 3.3. Solvatochromic shifts (E_{aq}-E_{gas}) between absorption features in aqueous solution (energy E_{aq}) and in the gas-phase (energy E_{gas}) for the peak absorptions and the points of half-maximum on the low-energy and high-energy sides of the main absorption bands, respectively. All shifts are given in eV.

Base	Peak	Low-Energy Half-Maximum	Low-Energy Half-Maximum
Adenine	-0.12	-0.1	-0.15
Cytosine	0.13	0.22	n/a[8]
Guanine	0[9]	0	0
Thymine	0/-0.21[10]	-0.05	-0.09

[8] The aqueous absorption spectrum does not drop below the half-maximum level on the high-energy slope of the main absorption.

[9] The more intense, high-energy feature was used for comparison.

[10] The first and second values are with respect to the first and second partially-resolved peak positions, respectively.

In order to study the effects of changes in the sugar-phosphate backbone on the electronic structure of mononucleotides, comparison can be made between the spectra of the deoxyribo-, ribo- and cyclic- mononucleotides. The overall spectral envelopes for the different adenine- and guanine-based nucleotides are independent of the details in the phosphate-sugar backbone (see Figure 3.5). This suggests that the UV absorption is localized predominately on the nucleobase with very little contribution from the rest of the molecules.

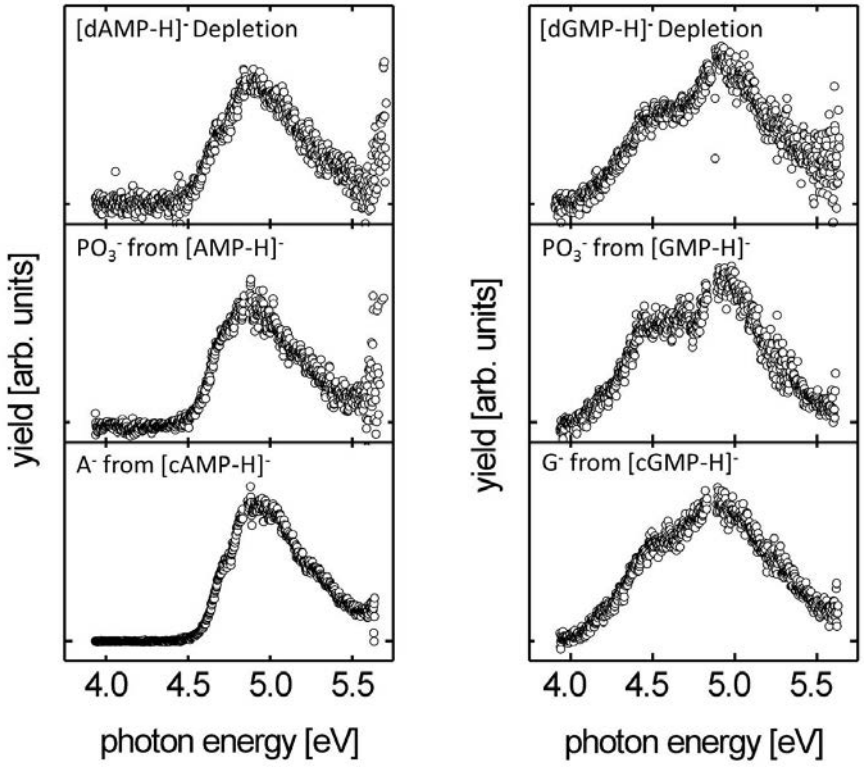

Figure 3.5. Comparison of the photodissociation spectra for the various chemical modifications. Left: Comparison of parent ion depletion of $[dAMP\text{-}H]^-$ with the most abundant fragment channels from $[AMP\text{-}H]^-$ and $[cAMP\text{-}H]^-$. Right: Comparison of parent ion depletion of $[dGMP\text{-}H]^-$ with the most abundant fragment channels from $[GMP\text{-}H]^-$ and $[cGMP\text{-}H]^-$.

3.3.3.1 [dAMP-H]-

Figure 3.6 shows the UV photodissociation spectrum of $[dAMP-H]^-$. The main absorption band is found between ~4.5 and 5.5 eV, peaking at 4.9 eV with a slight shoulder at 4.7 eV. Toward photon energies above ~5.5 eV, the photodissociation cross section increases steeply. The absorption spectrum of the aqueous solution spectrum is shifted toward lower photon energies when compared to the gas-phase results (see Figure 3.4), with the shifts being 0.1-0.15 eV towards lower energies in solution. Moreover, the absorption spectrum of the solution does not exhibit a discernable low-energy shoulder.

3.3.3.2 [dGMP-H]-

Figure 3.6 shows UV photodissociation spectra of $[dGMP-H]^-$. For $[dGMP-H]^-$, the high-energy increase of the fragmentation cross section probably sets in at higher energies than those afforded in our experiment. Consequently, only the low energy feature between ~4.0 and 5.6 eV is observed in the photodissociation spectra. This feature consists of at least two partially resolved electronic bands; one at 4.5 eV and the other at 4.9 eV. The relative intensity of the lower energy band in the fragment action spectra is strongly dependent on the fragment channel. The aqueous absorption spectrum is very similar to the gas-phase depletion spectrum (Figure 3.4), with the same roughly bimodal distribution and only small solvatochromic shifts toward higher energies (Table 3.3).

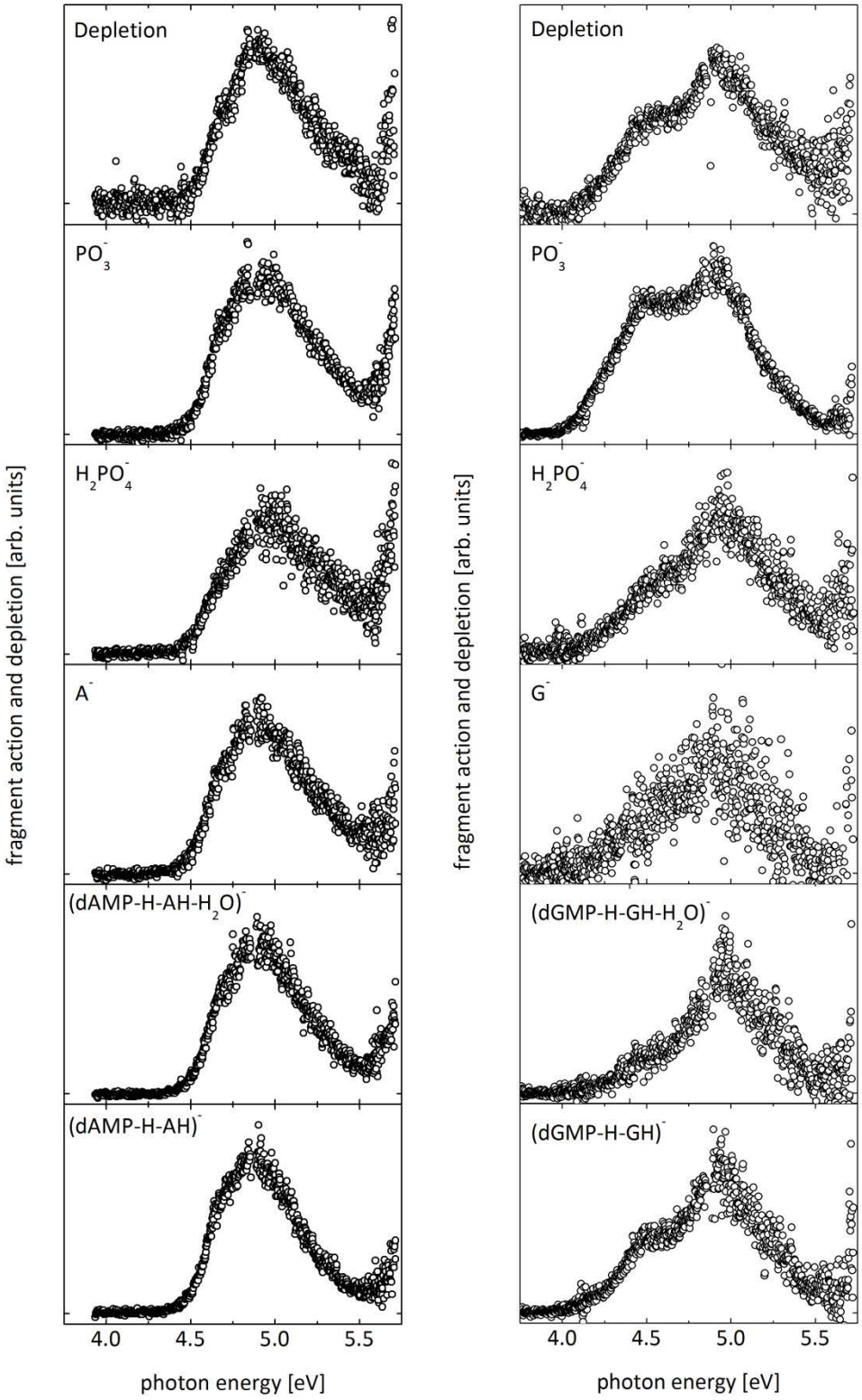

Figure 3.6. Photodissociation spectra for the $[dAMP\text{-}H]^-$ parent ion (left) and $[dGMP\text{-}H]^-$ parent ion (right). The recorded channels are indicated in each panel.

3.3.3.3 [dCMP-H]$^-$

Figure 3.7 shows UV photodissociation spectra of [dCMP-H]$^-$. The low-energy absorption band in the photodissociation spectra is found between ~3.9 and 5.0 eV. The increase of the photodissociation spectrum towards higher photon energies is much more intense relative to the lower-energy feature than for any of the other nucleotides under study. The low-energy band has a clear shoulder at ~4.15 eV, indicating that several electronic bands contribute to the envelope of the broad absorption feature. This shoulder is most pronounced for parent ion depletion and for the PO_3^- and [dCMP-H-CH]$^-$ fragment ions and has a lower relative intensity in the other fragment channels. Interestingly, the deprotonated base fragment ion C^- is not observed significantly above the noise level, in contrast to all of the other canonical deoxyribonucleotides. Comparison of the gas-phase photodissociation spectrum to the aqueous absorption spectrum (Figure 3.4) shows the most pronounced differences for [dCMP-H]$^-$. The low-energy shoulder observed in the gas-phase spectrum is completely missing from the solution spectrum. In contrast, there is a much higher absorption cross section around 5 eV in the solution spectrum than would be apparent from the corresponding region in the gas-phase spectrum. The aqueous absorption spectrum shifts by 0.13-0.22 eV toward higher energies.

3.3.3.4 [dTMP-H]$^-$

Figure 3.7 shows the photodissociation spectra for [dTMP-H]$^-$. Similar to the other nucleotides, these spectra show a feature between ~4.2 and 5.4 eV, which consists of at least two components, and an increase in the dissociation cross section at higher photon energies. As in the case of [dAMP-H]$^-$ parent ions, the lower energy component of the main absorption feature is only weakly dependent on the fragment channel. The aqueous absorption spectrum (Figure 3.4) is nearly identical to the gas-phase depletion spectrum with only very small solvatochromic shifts toward lower energies (Table 3.3).

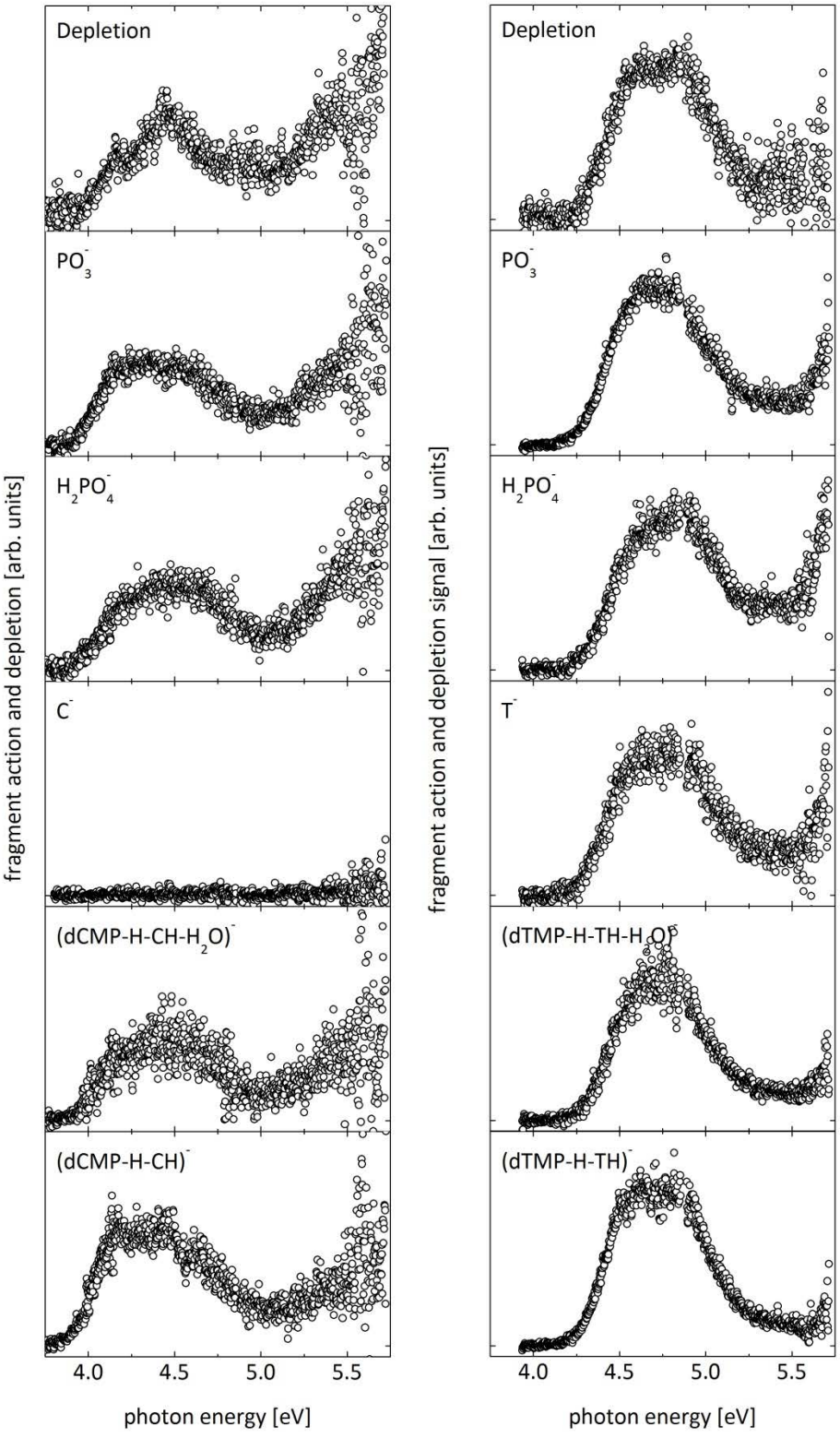

Figure 3.7. Photodissociation spectra for the $[dCMP-H]^-$ parent ion (left) and $[dTMP-H]^-$ parent ion (right). The recorded channels are indicated in each panel.

3.3.3.5 [AMP-H]$^-$

Figure 3.8 shows the photodissociation spectra for [AMP-H]$^-$. The spectra are qualitatively very similar to the spectra for its deoxyribo- analogue. The main absorption band is found between ~4.5 and 5.5 eV, peaking at 4.9 eV with a slight shoulder at 4.7 eV. Toward photon energies above ~5.5 eV, the photodissociation cross section increases steeply. The main difference between these spectra and those for [dAMP-H]$^-$ is the degree of spectral suppression of low energy features, most notably the low-energy shoulder in the A$^-$ fragment action spectrum.

3.3.3.6 [GMP-H]$^-$

Figure 3.8 shows the photodissociation spectra for [GMP-H]$^-$. As was the case for adenine-based nucleotides, [GMP-H]$^-$ is qualitatively very similar to the spectra of its deoxyribo-analogue. The spectra have a main feature between ~4.0 and 5.5 eV that consists of two overlapping peaks. The main difference between these spectra and those for [dGMP-H]$^-$ is the degree at which low-energy features are suppressed. In particular, the low-energy peak of the [GMP-H-BH]$^-$ channel shows, by far, the least suppression. Note that action spectra could not be obtained for the three channels G$^-$, [GMP-H-BH-H_2O]$^-$, and m/z = 151 due to low fragment ion intensities.

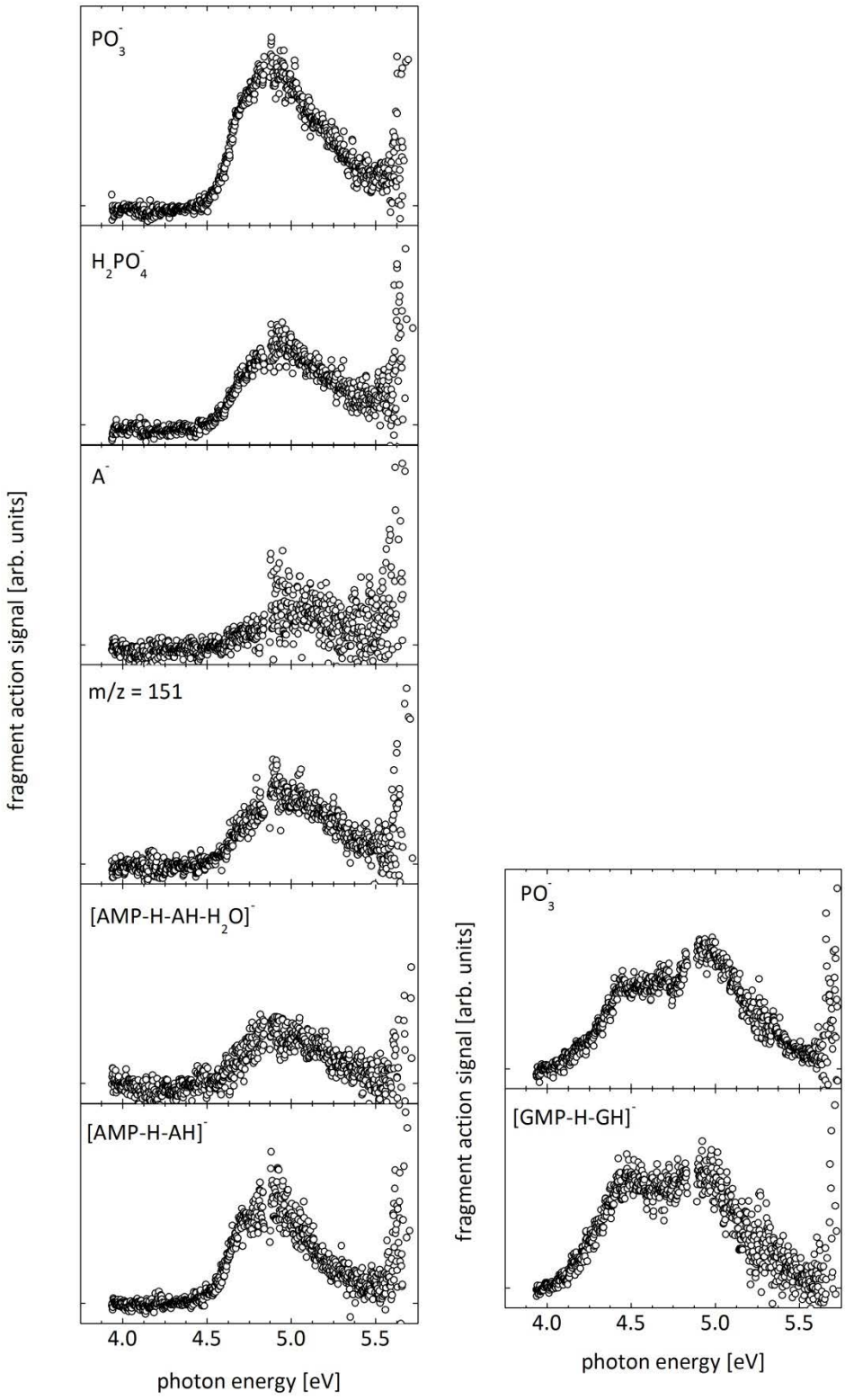

Figure 3.8. Photodissociation spectra for the $[AMP\text{-}H]^-$ parent ion (left) and $[GMP\text{-}H]^-$ (right). The recorded channels are indicated in each panel.

3.3.3.7 [cAMP-H]$^-$

Figure 3.9 shows the photodissociation spectra for [cAMP-H]$^-$. These spectra look qualitatively very similar to spectra for both [dAMP-H]$^-$ and [AMP-H]$^-$ parent ions, with a main, broad feature between ~4.5 and 5.5 eV. The main difference between these spectra and those for the other two adenine-based mononucleotides is the increased signal-to-noise level, allowing several features to be better resolved. This is especially apparent for the A$^-$ fragment ion channel where low- and high-energy shoulders at ~4.75 and 5.25 eV are particularly well-defined.

3.3.3.8 [cGMP-H]$^-$

Figure 3.9 shows the photodissociation spectra for [cGMP-H]$^-$, which are qualitatively very similar to the other two guanine-based mononucleotides. The spectra consist of a broad feature between ~4.0 and 5.5 eV that is clearly made up of two peaks. An interesting point to note is the substantial variability of the low-energy peak between each of the product ion channels.

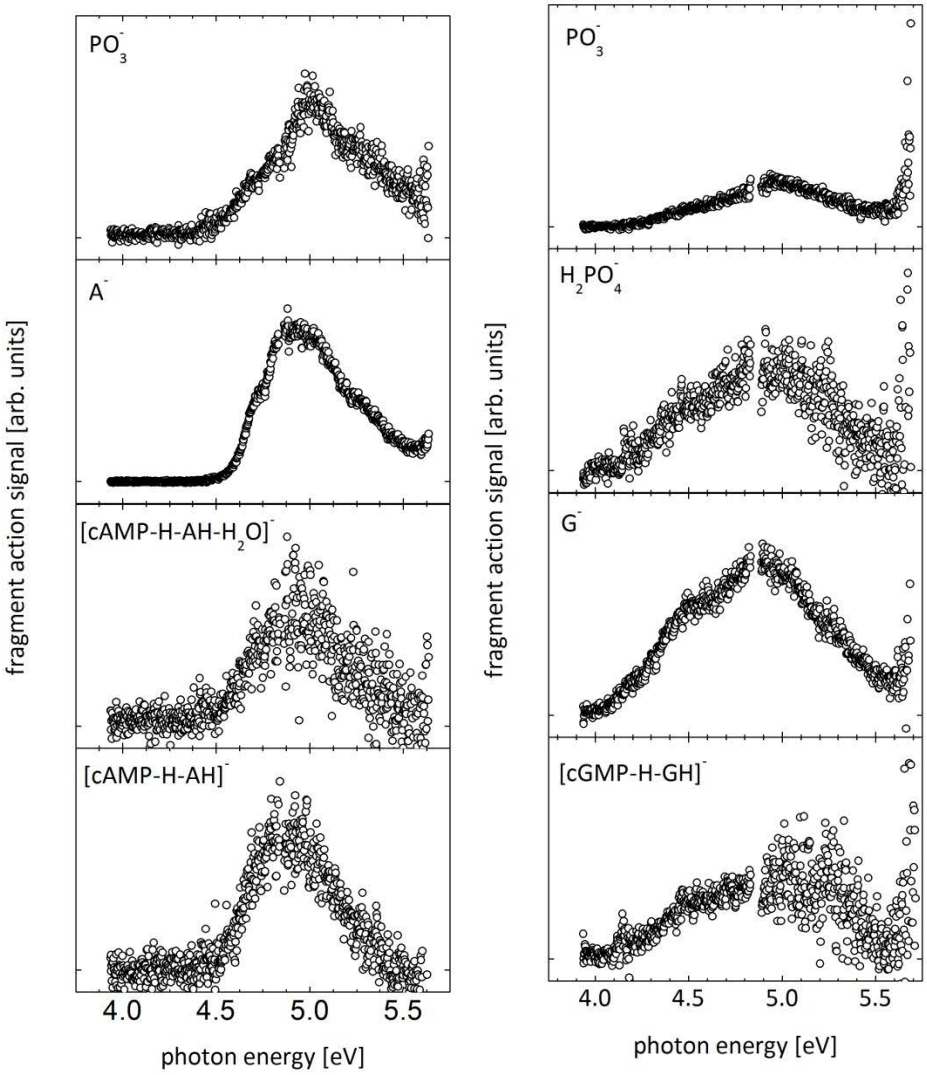

Figure 3.9. Photodissociation spectra for the $[cAMP\text{-}H]^-$ and $[cGMP\text{-}H]^-$ parent ions. The recorded channels are indicated in each panel.

3.3.4 Explanation of spectral suppression

As mentioned above, some of the spectral features below ~5.5 eV show varying degrees of suppression, depending on the parent and fragment ion considered. This behavior can be seen for nearly all parent ions but is most pronounced in the action spectra of $[dGMP\text{-}H]^-$ where the feature at ~4.5 eV is most suppressed in the $[dGMP\text{-}H\text{-}GH\text{-}H_2O]^-$ channel and least suppressed in the PO_3^- channel. The extent of suppression can be related to the different threshold and appearance energies for each fragment channel. Threshold energies correspond to the minimum amount of energy required for fragmentation to occur. Appearance energies correspond to the minimum amount of energy required to observe complete fragmentation on

the timescale of the experiment. This second value is related to the kinetic shift effect and is described in §2.9. Comparison of this suppression to results obtained in CID studies (Table 3.4)[57] reveals that the fragment channels with the least spectral suppression correspond to channels with the lowest fragmentation thresholds and appearance energies. The most pronounced example is for the $[dGMP-H]^-$ parent ion, where PO_3^- has the lowest appearance energy for all fragment channels (3.10 eV), well below the onset of the absorption spectrum at 4.0 eV. In contrast, the other fragment channels have appearance energies from 4.56-4.94 eV, resulting in significant attenuation of the low-energy part of the fragment action spectra. While the CID data do not include threshold or appearance energies for the $[dGMP-H-BH-H_2O]^-$ fragment channel, the trend can be qualitatively extended by assuming that water loss from the fragment $[dGMP-H-BH]^-$ involves a higher threshold energy than if no water loss had occurred. This is consistent with the $[dGMP-H]^-$ spectra since the low energy feature is more suppressed for the $[dGMP-H-BH-H_2O]^-$ channel than for the $[dGMP-H-BH]^-$ channel.

Table 3.4. Experimental threshold energies for various fragment channels for several of the mononucleotides as reported by Ho and Kebarle.[57] Quoted $\Delta H^{\ddagger}$ values represent actual thresholds whereas E_0 values "apparent thresholds," which represent the amount of energy required to ensure complete dissociation on the timescale of their experiment (34-47μs). All values are quoted in eV.

Parent Ion $[M-H]^-$	Fragment Ion							
	B^-		$[M-H-BH]^-$		PO_3^-		$H_2PO_4^-$	
M =	E_0	$\Delta H^{\ddagger}$	E_0	$\Delta H^{\ddagger}$	E_0	$\Delta H^{\ddagger}$	E_0	$\Delta H^{\ddagger}$
dAMP	4.04	1.59	3.53	1.50	3.70	1.50	4.26	2.02
dCMP	4.08	1.72	3.61	1.55	3.31	1.42	4.47	2.06
dGMP	4.94	1.59	4.56	1.59	3.10	1.29	4.94	2.06
dTMP	3.48	1.55	3.01	1.42	3.18	1.33	4.34	1.98
AMP	4.34	1.68	4.04	1.59	3.10	1.25	4.04	1.76

Another pronounced example of this behavior is for $[dCMP-H]^-$. For this parent ion, the low-energy shoulder near ~4.2 eV is most pronounced for the PO_3^- and $[dCMP-H-CH]^-$ fragment channels. These two channels have appearance energies of 3.31 and 3.61 eV, respectively, and are significantly below the onset of the low-energy absorption band. In contrast, the $H_2PO_4^-$ fragment channel does exhibit significant suppression of the ~4.2 eV shoulder. The threshold energy for this channel has been determined to be 4.47 eV,[57] which is near the peak of the

envelope of the low-energy absorption band. Interestingly, this explanation cannot explain the fact that the C^- fragment ion is not observed at all for $[dCMP-H]^-$ parent ions since it has a threshold energy (4.08 eV [57]) that is below that of other channels that are observed. Instead, this behavior can be explained by the relative gas-phase acidities for each of the nucleobases. Calculated gas-phase acidities by Kenttämaa [63-64] and from our own lab for deprotonation energies of the canonical tautomers of the nucleobases at the nitrogen atom involved in the CN glycosidic bond predict cytosine deprotonation to occur at ~0.4 eV higher than those of the other bases, which are all within 0.1 eV of each other (see Table 3.5). This implies that proton abstraction by C^- is much more favorable than by the other deprotonated bases. This increased propensity for proton abstraction should lead to the loss of neutral cytosine (CH) rather than C^-.

Table 3.5. Calculated deprotonation and adiabatic detachment energies for the four canonical nucleobases.

Base	Deprotonation Energy [eV]	Adiabatic Detachment Energy [eV]
Adenine	14.97	3.12
Cytosine	15.36	2.90
Guanine	14.96	2.84
Thymine	14.88	3.12

3.4 Conclusions

We have performed a series of experiments to probe the gas-phase ultraviolet photodissociation of mononucleotides. For these species, the photodissociation process involves a series of steps that begins with absorption of an ultraviolet photon to induce $\pi \rightarrow \pi^*$ transitions, is followed by fast internal conversion to a vibrationally hot electronic ground state, and ends with fragmentation that can occur *via* a number of thermal fragmentation mechanisms. Comparison between the gas-phase photodissociation spectra and aqueous absorption spectra reveal varying solvatochromic shifts to either higher or lower energies upon solvation. Chemical modifications to the nucleotides do not result in substantial changes to the gas-phase spectra, confirming that the nucleobases are the main chromophores and that the sugar-phosphate portion does not significantly contribute to absorption spectra. Suppression of low-energy spectral features in many of the action spectra is attributed to the appearance

energies of each fragment channel. Spectra that demonstrate the most suppression correspond to channels with higher appearance energies. Spectra that demonstrate little to no suppression correspond to fragmentation thresholds and appearance energies that are significantly below the onset of spectral features.

Fragmentation of nucleotides occurs *via* a complex series of reactions that involve substantial nuclear rearrangement. A number of potential fragmentation mechanisms have been considered but none can fully explain all of the observed data. This leads us to propose that multiple fragmentation mechanisms are active at the same time. Depending on the structural and chemical details of the species in question as well as the activation mechanism involved, the different fragmentation mechanisms could take on varying degrees of importance. For instance, the likelihood of an E2-type reaction for the cyclic-mononucleotides is greatly reduced due to the tethering of the phosphate group to the sugar moiety and the lack of acidic protons available for transfer. On the other hand, branching ratios for non-cyclic mononucleotides are shown to be different depending on the activation mechanism used. While the preferred GBC-based channel following CID is loss of anionic B^-, UVPD shows a preference for loss of neutral, protonated base, BH.

3.5 References for Chapter 3

1. Wang, S.Y., ed. "Photochemistry and Photobiology of Nucleic Acids." Vol. 1. 1976, Academic Press: New York, San Francisco, London.

2. Wu, J. and McLuckey, S.A., "Gas-phase fragmentation of oligonucleotide ions." *International Journal of Mass Spectrometry*, 2004. **237**(2-3): p. 197.

3. Phillips, D.R. and McCloskey, J.A., "A comprehensive study of the low-energy collision-induced dissociation of dinucleoside monophosphates." *International Journal of Mass Spectrometry and Ion Processes*, 1993. **128**(1-2): p. 61.

4. Eisinger, J. and Shulman, R.G., "Excited Electronic States of DNA." *Science*, 1968. **161**(3848): p. 1311.

5. Crespo-Hernandez, C.E., Cohen, B., Hare, P.M., and Kohler, B., "Ultrafast excited-state dynamics in nucleic acids." *Chemical Reviews*, 2004. **104**(4): p. 1977.

6. Fujii, M., Tamura, T., Mikami, N., and Ito, M., "Electronic spectra of uracil in a supersonic jet." *Chemical Physics Letters*, 1986. **126**(6): p. 583.

7. Nir, E., Imhof, P., Kleinermanns, K., and de Vries, M.S., "REMPI spectroscopy of laser desorbed guanosines." *Journal of the American Chemical Society*, 2000. **122**(33): p. 8091.

8. Nir, E., Janzen, C., Imhof, P., Kleinermanns, K., and de Vries, M.S., "Guanine tautomerism revealed by UV-UV and IR-UV hole burning spectroscopy." *Journal of Chemical Physics*, 2001. **115**(10): p. 4604.

9. Nir, E. and de Vries, M.S., "Fragmentation of laser-desorbed 9-substituted adenines." *International Journal of Mass Spectrometry*, 2002. **219**(1): p. 133.

10. Nir, E., Janzen, C., Imhof, P., Kleinermanns, K., and de Vries, M.S., "Pairing of the nucleobases guanine and cytosine in the gas phase studied by IR-UV double-resonance spectroscopy and ab initio calculations." *Physical Chemistry Chemical Physics*, 2002. **4**(5): p. 732.

11. Nir, E., Plutzer, C., Kleinermanns, K., and de Vries, M., "Properties of isolated DNA bases, base pairs and nucleosides examined by laser spectroscopy." *European Physical Journal D*, 2002. **20**(3): p. 317.

12. de Vries, M.S. and Hobza, P., "Gas-phase spectroscopy of biomolecular building blocks." *Annual Review of Physical Chemistry*, 2007. **58**: p. 585.

13. Nir, E., Hunig, I., Kleinermanns, K., and de Vries, M.S., "Conformers of guanosines and their vibrations in the electronic ground and excited states, as revealed by double-resonance spectroscopy and ab initio calculations." *Chemphyschem*, 2004. **5**(1): p. 131.

14. Crespo-Hernandez, C.E., Cohen, B., and Kohler, B., "Base stacking controls excited-state dynamics in A-T DNA." *Nature*, 2005. **436**(7054): p. 1141.

15. Takaya, T., Su, C., de La Harpe, K., Crespo-Hernandez, C.E., and Kohler, B., "UV excitation of single DNA and RNA strands produces high yields of exciplex states between two stacked bases." *Proceedings of the National Academy of Sciences of the United States of America*, 2008. **105**(30): p. 10285.

16. Middleton, C.T., de La Harpe, K., Su, C., Law, Y.K., Crespo-Hernandez, C.E., and Kohler, B., "DNA Excited-State Dynamics: From Single Bases to the Double Helix." *Annual Review of Physical Chemistry*, 2009. **60**: p. 217.

17. Gidden, J. and Bowers, M.T., "Gas-phase conformational and energetic properties of deprotonated dinucleotides." *European Physical Journal D*, 2002. **20**(3): p. 409.

18. Wyttenbach, T. and Bowers, M.T., "Intermolecular interactions in biomolecular systems examined by mass spectrometry." *Annual Review of Physical Chemistry*, 2007. **58**: p. 511.

19. Pecourt, J.M.L., Peon, J., and Kohler, B., "Ultrafast internal conversion of electronically excited RNA and DNA nucleosides in water." *Journal of the American Chemical Society*, 2000. **122**(38): p. 9348.

20. Pecourt, J.M.L., Peon, J., and Kohler, B., "DNA excited-state dynamics: Ultrafast internal conversion and vibrational cooling in a series of nucleosides." *Journal of the American Chemical Society*, 2001. **123**(42): p. 10370.

21. Peon, J. and Zewail, A.H., "DNA/RNA nucleotides and nucleosides: direct measurement of excited-state lifetimes by femtosecond fluorescence up-conversion." *Chemical Physics Letters*, 2001. **348**(3-4): p. 255.

22. Gustavsson, T., Sharonov, A., and Markovitsi, D., "Thymine, thymidine and thymidine 5 '-monophosphate studied by femtosecond fluorescence upconversion spectroscopy." *Chemical Physics Letters*, 2002. **351**(3-4): p. 195.

23. Gustavsson, T., Sharonov, A., Onidas, D., and Markovitsi, D., "Adenine, deoxyadenosine and deoxyadenosine 5 '-monophosphate studied by femtosecond fluorescence upconversion spectroscopy." *Chemical Physics Letters*, 2002. **356**(1-2): p. 49.

24. Piuzzi, F., Mons, M., Dimicoli, I., Tardivel, B., and Zhao, Q., "Ultraviolet spectroscopy and tautomerism of the DNA base guanine and its hydrate formed in a supersonic jet." *Chemical Physics*, 2001. **270**(1): p. 205.

25. Kang, H., Lee, K.T., Jung, B., Ko, Y.J., and Kim, S.K., "Intrinsic lifetimes of the excited state of DNA and RNA bases." *Journal of the American Chemical Society*, 2002. **124**(44): p. 12958.

26. Kang, H., Jung, B., and Kim, S.K., "Mechanism for ultrafast internal conversion of adenine." *Journal of Chemical Physics*, 2003. **118**(15): p. 6717.

27. Merchan, M. and Serrano-Andres, L., "Ultrafast internal conversion of excited cytosine via the lowest ππ* electronic singlet state." *Journal of the American Chemical Society*, 2003. **125**(27): p. 8108.

28. Ismail, N., Blancafort, L., Olivucci, M., Kohler, B., and Robb, M.A., "Ultrafast decay of electronically excited singlet cytosine via ππ* to nπ* state switch." *Journal of the American Chemical Society*, 2002. **124**(24): p. 6818.

29. Sobolewski, A.L. and Domcke, W., "On the mechanism of nonradiative decay of DNA bases: ab initio and TDDFT results for the excited states of 9H-adenine." *European Physical Journal D*, 2002. **20**(3): p. 369.

30. Sobolewski, A.L., Domcke, W., Dedonder-Lardeux, C., and Jouvet, C., "Excited-state hydrogen detachment and hydrogen transfer driven by repulsive $^1\pi\sigma^*$ states: A new

paradigm for nonradiative decay in aromatic biomolecules." *Physical Chemistry Chemical Physics*, 2002. **4**(7): p. 1093.

31. Satzger, H., Townsend, D., Zgierski, M.Z., Patchkovskii, S., Ullrich, S., and Stolow, A., "Primary processes underlying the photostability of isolated DNA bases: Adenine." *Proceedings of the National Academy of Sciences of the United States of America*, 2006. **103**(27): p. 10196.

32. McLuckey, S.A. and Goeringer, D.E., "Slow heating methods in tandem mass spectrometry." *Journal of Mass Spectrometry*, 1997. **32**(5): p. 461.

33. Klassen, J.S., Schnier, P.D., and Williams, E.R., "Blackbody infrared radiative dissociation of oligonucleotide anions." *Journal of the American Society for Mass Spectrometry*, 1998. **9**(11): p. 1117.

34. Wan, K.X. and Gross, M.L., "Fragmentation mechanisms of oligodeoxynucleotides: Effects of replacing phosphates with methylphosphonates and thymines with other bases in T-rich sequences." *Journal of the American Society for Mass Spectrometry*, 2001. **12**(5): p. 580.

35. Yang, J. and Hakansson, K., "Characterization of oligodeoxynucleotide fragmentation pathways in infrared multiphoton dissociation and electron detachment dissociation by Fourier transform ion cyclotron double resonance." *European Journal of Mass Spectrometry*, 2009. **15**(2): p. 293.

36. Nielsen, S.B., Andersen, J.U., Forster, J.S., Hvelplund, P., Liu, B., Pedersen, U.V., and Tomita, S., "Photodestruction of adenosine 5 '-monophosphate (AMP) nucleotide ions in vacuo: Statistical versus nonstatistical processes." *Physical Review Letters*, 2003. **91**(4).

37. Aravind, G., Antoine, R., Klaerke, B., Lemoine, J., Racaud, A., Rahbek, D.B., Rajput, J., Dugourd, P., and Andersen, L.H., "Sub-microsecond photodissociation pathways of gas phase adenosine 5 '-monophosphate nucleotide ions." *Physical Chemistry Chemical Physics*, 2010. **12**(14): p. 3486.

38. Guan, Z.Q., Kelleher, N.L., Oconnor, P.B., Aaserud, D.J., Little, D.P., and McLafferty, F.W., "193 nm photodissociation of larger multiply-charged biomolecules." *International Journal of Mass Spectrometry*, 1996. **157**: p. 357.

39. Weber, J.M., Ioffe, I.N., Berndt, K.M., Loffler, D., Friedrich, J., Ehrler, O.T., Danell, A.S., Parks, J.H., and Kappes, M.M., "Photoelectron spectroscopy of isolated multiply negatively charged oligonucleotides." *Journal of the American Chemical Society*, 2004. **126**(27): p. 8585.

40. Yang, X., Wang, X.B., Vorpagel, E.R., and Wang, L.S., "Direct experimental observation of the low ionization potentials of guanine in free oligonucleotides by using photoelectron

spectroscopy." *Proceedings of the National Academy of Sciences of the United States of America*, 2004. **101**(51): p. 17588.

41. Gabelica, V., Tabarin, T., Antoine, R., Rosu, F., Compagnon, I., Broyer, M., De Pauw, E., and Dugourd, P., "Electron photodetachment dissociation of DNA polyanions in a quadrupole ion trap mass spectrometer." *Analytical Chemistry*, 2006. **78**(18): p. 6564.

42. Gabelica, V., Rosu, F., De Pauw, E., Antoine, R., Tabarin, T., Broyer, M., and Dugourd, P., "Electron photodetachment dissociation of DNA anions with covalently or noncovalently bound chromophores." *Journal of the American Society for Mass Spectrometry*, 2007. **18**(11): p. 1990.

43. Gabelica, V., Rosu, F., Tabarin, T., Kinet, C., Antoine, R., Broyer, M., De Pauw, E., and Dugourd, P., "Base-dependent electron photodetachment from negatively charged DNA strands upon 260-nm laser irradiation." *Journal of the American Chemical Society*, 2007. **129**(15): p. 4706.

44. Hush, N.S. and Cheung, A.S., "Ionization potentials and donor properties of nucleic-acid bases and related compounds." *Chemical Physics Letters*, 1975. **34**(1): p. 11.

45. Parr, R.G. and Yang, W., *Density-Functional Theory of Atoms and Molecules*. 1989, New York: Oxford University Press.

46. Becke, A.D., "Denisty-functional exchange-energy approximation with correct asymptotic-behavior." *Physical Review A*, 1988. **38**(6): p. 3098.

47. Lee, C.T., Yang, W.T., and Parr, R.G., "Development of the Colle-Salvetti Correlation-Energy Formula into a Functional of the Electron-Density." *Physical Review B*, 1988. **37**(2): p. 785.

48. Dunning, T.H., "Gaussian-Basis Sets for Use in Correlated Molecular Calculations. 1. The Atoms Boron Through Neon and Hydrogen." *Journal of Chemical Physics*, 1989. **90**(2): p. 1007.

49. Ahlrichs, R., Bar, M., Haser, M., Horn, H., and Kolmel, C., "Electronic-structure calculations on workstation computers - The program system TURBOMOLE." *Chemical Physics Letters*, 1989. **162**(3): p. 165.

50. Zakjevskii, V.V., King, S.J., Dolgounitcheva, O., Zakrzewski, V.G., and Ortiz, J.V., "Base and phosphate electron detachment energies of deoxyribonucleotide anions." *Journal of the American Chemical Society*, 2006. **128**(41): p. 13350.

51. Habibigoudarzi, S. and McLuckey, S.A., "Ion-trap collisional activation of the deprotonated deoxymononucleoside and deoxydinucleoside monophosphates." *Journal of the American Society for Mass Spectrometry*, 1995. **6**(2): p. 102.

52. Cerny, R.L., Gross, M.L., and Grotjahn, L., "Fast-atom-bombardment combined with tandem mass-spectrometry for the study of dinucleotides." *Analytical Biochemistry*, 1986. **156**(2): p. 424.

53. Rodgers, M.T., Campbell, S., Marzluff, E.M., and Beauchamp, J.L., "Low-energy collision-induced dissociation of deprotonated dinucleotides - Determination of the energetically favored dissociation pathways and the relative acidities of the nucleic-acid bases." *International Journal of Mass Spectrometry and Ion Processes*, 1994. **137**: p. 121.

54. McLuckey, S.A. and Habibigoudarzi, S., "Decompositinos of multiply-charged oligonucleotide anions." *Journal of the American Chemical Society*, 1993. **115**(25): p. 12085.

55. Chiavarino, B., Crestoni, M.E., Fornarini, S., Lanucara, F., Lemaire, J., Maitre, P., and Scuderib, D., "Infrared spectroscopy of isolated nucleotides 1. The cyclic 3 ',5 '-adenosine monophosphate anion." *International Journal of Mass Spectrometry*, 2008. **270**(3): p. 111.

56. Wysocki, V.H., Resing, K.A., Zhang, Q.F., and Cheng, G.L., "Mass spectrometry of peptides and proteins." *Methods*, 2005. **35**(3): p. 211.

57. Ho, Y.H. and Kebarle, P., "Studies of the dissociation mechanisms of deprotonated mononucleotides by energy resolved collision-induced dissociation." *International Journal of Mass Spectrometry*, 1997. **165**: p. 433.

58. Wu, J. and McLuckey, S.A., "Ion/ion reactions of multiply charged nucleic acid anions: electron transfer, proton transfer, and ion attachment." *International Journal of Mass Spectrometry*, 2003. **228**(2-3): p. 577.

59. Vasiliou, A., Nimlos, M.R., Daily, J.W., and Ellison, G.B., "Thermal Decomposition of Furan Generates Propargyl Radicals." *Journal of Physical Chemistry A*, 2009. **113**(30): p. 8540.

60. Jones, M., Jr., *Organic Chemistry*. 2 ed. 2000, New York, NY: W.W. Norton & Company, Inc.

61. Boyarkin, O.V., Mercier, S.R., Kamariotis, A., and Rizzo, T.R., "Electronic spectroscopy of cold, protonated tryptophan and tyrosine." *Journal of the American Chemical Society*, 2006. **128**(9): p. 2816.

62. Nielsen, S.B. and Solling, T.I., "Are conical intersections responsible for the ultrafast processes of adenine, protonated adenine, and the corresponding nucleosides?" *Chemphyschem*, 2005. **6**(7): p. 1276.

63. Huang, Y.Q. and Kenttamaa, H., "Theoretical estimations of the 298 K gas-phase acidities of the pyrimidine-based nucleobases uracil, thymine, and cytosine." *Journal of Physical Chemistry A*, 2003. **107**(24): p. 4893.

64. Huang, Y.Q. and Kenttamaa, H., "Theoretical estimations of the 298 K gas-phase acidities of the purine-based nucleobases adenine and guanine." *Journal of Physical Chemistry A*, 2004. **108**(20): p. 4485.

4 Transition Metal Complexes I: $IrBr_6^{2-}$

This chapter has been reprinted with permission from Marcum, J.C. and Weber, J.M., "Electronic photodissociation spectra and decay pathways of gas-phase $IrBr_6^{2-}$." *Journal of Chemical Physics*, 2009. **131**: 194309.

4.1 Background

The chemistry of simple transition metal compounds has long been a focus of inorganic chemistry. In addition to investigations of their descriptive chemistry, [1-2] such species have also served as test systems for theoretical constructs such as molecular orbital theory.[3] Most knowledge of transition metal complexes comes from condensed phase experiments, where the presence of solvent and/or counter ions serves to stabilize these compounds as well as to modify their chemical and spectroscopic properties. Often, these compounds can carry more than one excess negative charge and charge-stabilizing interactions with solvent and/or counterions become even more important. In order to study the intrinsic properties of such species and gauge the influence of the solvent, it is necessary to perform experiments in the gas phase, where perturbations from counterions or solvent molecules are absent.

In multiply-charged anions, excess charge leads to a large intramolecular Coulomb repulsion. This effect manifests itself in the form of repulsive Coulomb Barriers (RCBs) (see Figure 4.1), which have a dramatic influence on the thermodynamic and electronic stability of these molecules.[4-12] These barriers result from the interaction of an excess electron with an already negatively charged molecule. In one general picture, RCBs can be thought of as feature on an adiabatic electronic surface that is constructed from diabatic curves with different electron configurations.[4] For instance, in dianions, one diabatic curve corresponds to a monoanion and a free electron and demonstrates long-range Coulomb repulsion, forming the outer part of a RCB. The second diabatic curve arises from the interaction of the excess electron with the nuclei in the anion resulting in short-range attraction that shapes the inner part of the potential. Depending on the specific details of the interactions involved, it is possible for the molecule to be either stable or metastable. If the inner part of the potential is lower in energy than the outer part, the molecule will be stable. If the inner part is higher in energy than the outer part, the molecule will be metastable. It is also possible for multianions to dissociate into

two or more ionic fragments that also experience long-range Coulomb repulsion and short-range attraction. We can define an "outer" barrier height as the energy difference between the top of the RCB and the separated charges at infinite distance. An analogous "inner" barrier height is then defined as the energy difference between the top of the RCB and the short-range minimum in the potential energy surface. Since the height and shape of a RCB depends on the charge distributions before and after charge separation, every process that leads to a different product state will have its own corresponding RCB. The electrostatic strain in multianions can be released through electron loss or ionic fragmentation. Whereas electron detachment from multianions may occur by tunneling through or excitation over the RCB, ionic fragment can usually only proceed upon excitation over the barrier, since the much heavier masses of ionic fragments can be expected to preclude tunneling.

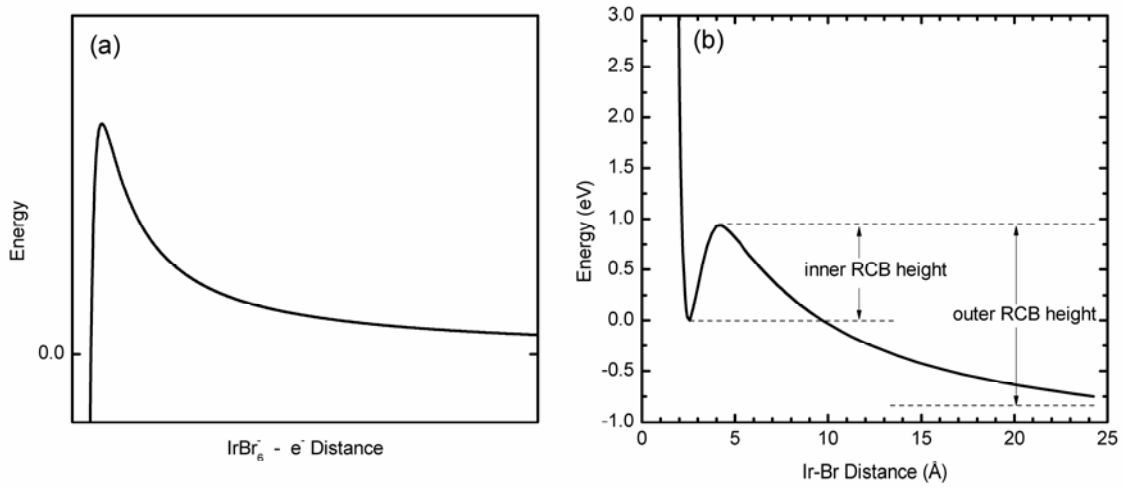

Figure 4.1. Schematic potential energy curve for (a) electron detachment from $IrBr_6^{2-}$ and (b) dissociation of $IrBr_6^{2-}$ into $IrBr_5^-$ and Br^- fragments highlighting the inner and out RCB heights. The ionic fragmentation channel was calculated using density functional theory (see §4.2.3 for details). The figures are scaled so that the zero energy level in (a) corresponds to infinite separation of the electron and monoanion and in (b) corresponds to the equilibrium structure of the $IrBr_6^{2-}$ dianion.

The last decade has seen rapid growth in the understanding of gas-phase multianions. Pioneering work by Wang and co-workers[13-14] utilized photoelectron spectroscopy to investigate the electronic properties of dianions and have led to the observation of electronic RCBs in a wide variety of species. Several multianionic species that are known to be stable in the condensed phase have been identified to only be metastable in the gas phase, some of which with lifetimes ranging up to many seconds.[14-16, 8, 11, 17] Others, such as SO_4^{2-}, have

not been observed in the gas phase at all.[18-20] The thermodynamic stability of these species in the condensed phase can then only be attributed to stabilizing interactions with counterions and/or solvent molecules. One dianion that has received a considerable amount of attention is hexabromoiridate (IV), $IrBr_6^{2-}$. Wang et al. studied $IrBr_6^{2-}$ using photoelectron spectroscopy.[14] They estimated the adiabatic detachment energy to be 0.96(6) eV and found a vertical detachment energy of 1.09(5) eV and an electronic outer RCB height of ≤ 2 eV for the lowest energy state of the resulting monoanion, $IrBr_6^-$.

Kappes and co-workers investigated the photodissociation spectrum of $IrBr_6^{2-}$ in the visible spectral region.[21] They found that the photodepletion spectrum of $IrBr_6^{2-}$ closely resembles the visible aqueous absorption spectrum and exhibits small solvatochromic shifts. Moreover, they observed Br^- and $IrBr_n^-$ (n = 3-5) as fragment channels and concluded that $IrBr_5^-$ is formed by absorption of a single photon, while $IrBr_4^-$ and $IrBr_3^-$ are generated by absorption of at least two photons in the visible region. They attributed the formation of $IrBr_5^-$ to delayed fragmentation of a hot $IrBr_6^{2-}$ ground state ion formed by a fast radiationless transition from the initially excited electronic state. In a follow-up to this work, the Kappes group studied the time-resolved dynamics of $IrBr_6^{2-}$ after electronic excitation.[22] They found that, after irradiation with 1.6 eV light, $IrBr_6^{2-}$ undergoes successive nonadiabatic relaxation from the initial excited state by way of an intermediate state back into the electronic ground state with time constants of 2.1(3) and 21(2) ps. Following this electronic relaxation, the vibrationally "hot" $IrBr_6^{2-}$ ion undergoes delayed fragmentation to form $IrBr_5^-$ and Br^- ions with a time constant of 79 ± 21 ps. Kinetic modeling of these data using a three-step process yielded an inner RCB height of approximately 0.95 eV. Consideration of the kinetic energy release of the fragment ions led to a lower limit of the outer RCB height of ≤ 1.6 eV.

Dessent and co-workers used collision induced dissociation (CID) to probe the relative ordering of the inner RCB heights for electron detachment and ionic fragmentation.[23] Their results determined that the inner RCB height for ionic fragmentation is lower than that of electron detachment, in agreement with the earlier experiments by the Wang and Kappes groups. These studies also found that fragmentation of $IrBr_6^{2-}$ predominately results in the

formation of Br^- and $IrBr_5^-$, although further loss of a Br atom to produce $IrBr_4^-$ is also possible. Further experiments using high-energy CID determined that electron detachment to form $IrBr_6^-$ is also a prominent process.[24] Experiments investigating the effect of K^+ on $IrBr_6^{2-}$ found the major fragmentation products to be $IrBr_5^-$ and KBr, revealing that the nature of the favored fragment channel does not change upon counter ion perturbation.[25] As expected, the counter ion was also found to stabilize the anion as evidenced by a higher collision energy necessary for fragmentation.

In order to further develop this area, we studied the photofragment action results for $IrBr_6^{2-}$ between 1.08 and 5.6 eV photon energy, considerably beyond the energy range studied in earlier work by the Kappes group.[21] We focus on the action spectra for the different channels, which turn out to be highly energy specific.

4.2 Methods

4.2.1 Photodissociation spectra

The experimental methods used in this work are described in detail in Chapter 2 of this thesis. Ions were produced from electrospray ionization using an ~10 mM solution of K_2IrBr_6 (Sigma-Aldrich) in an ~1:1 mixture of methanol and water. Due to the fragile nature of $IrBr_6^{2-}$, the difference between the capillary and skimmer voltages was kept to a minimum. Typical voltages were on the order of -80 V for the capillary and -15 V for the skimmer. This strategy helps to minimize the energy of collisions between the formed ions and background gas, leading to less fragmentation prior to reaching thermal equilibrium in the hexapole ion trap. For monitoring of Br^- fragment ions, the acceleration stage is kept at -4000 V and the reflectron is scaled down to the appropriate voltage. Because $IrBr_6^{2-}$ is a dianion, it will have a *lower* mass-to-charge ratio than the fragments $IrBr_6^-$, $IrBr_5^-$, and $IrBr_4^-$. Consequently, monitoring these fragments should require the reflectron voltage to be scaled up. However, this is not possible since our reflectron has an upper voltage limit of - 4500 V. Instead, the acceleration voltage is scaled down from the nominal -4000 V to -2250 V for recording of $IrBr_6^-$, $IrBr_5^-$, and $IrBr_4^-$ fragment ion action spectra.

The relative detection efficiencies for the various fragment ions are unknown in this procedure and are expected to vary substantially. In particular, the Br^- ion will have especially small detection efficiency, since it will have a rather low kinetic energy upon formation (~900 eV when parent ions are prepared with ~3750 eV of kinetic energy). This prevents us from obtaining absolute branching ratios in our experiment.

4.2.2 Aqueous absorption spectra

UV-Visible spectra of ~0.5 mM K_2IrBr_6 (Sigma-Aldrich) in water were acquired using a Varian Cary 500 Scan UV-Visible-NIR spectrometer (version 8.01) with a 10 mm path length, 0.25 nm step size, 2 nm bandwidth, and an integration time of 0.1 sec.

4.2.3 Computational

A potential energy curve for the dissociation of $IrBr_6^{2-}$ into $IrBr_5^-$ and Br^- fragments (see Figure 4.1) was calculated using the TURBOMOLE V5.9 suite of programs.[26] All calculations were performed using density functional theory[27] with the B3LYP functional[28-29] and a def2-TZVPP basis set.[30] Scalar relativistic effects were taken into account using the def2-ecp effective core potential (multielectron fit to Wood-Boring orbital energies).[31] The initial starting geometry was constructed to be of O_h symmetry but all geometry optimizations were performed without symmetry restrictions (C_1). Each point along the potential energy surface was calculated by fixing the length of one of the Ir-Br bonds at various values and allowing all other atoms to relax.

4.3 Results

Following irradiation of $IrBr_6^{2-}$, four photoproducts were observed: $IrBr_6^-$, $IrBr_5^-$, $IrBr_4^-$, and Br^-. Figure 4.2 depicts all gas-phase action spectra for $IrBr_6^{2-}$ as well as an aqueous absorption spectrum of K_2IrBr_6. Each of the photodissociation spectra (Figure 4.2b-e) can be roughly divided into three main regions of interest. The first region is labeled as VIS and includes photon energies below ~3.0 eV. The second region is labeled as UV1 and includes photon energies between ~3.0 and 5.1 eV. The final region is labeled as UV2 and includes photon energies above ~5.1 eV. These regions are based on the spectral features that are observed as well as previous spectral assignments made by Friedrich et al.[21] and Schatz,[32] which are reviewed in detail in the discussion section below. In the following paragraphs, a general

overview is given of the features in each fragment action spectrum but interpretation is deferred until §4.4.

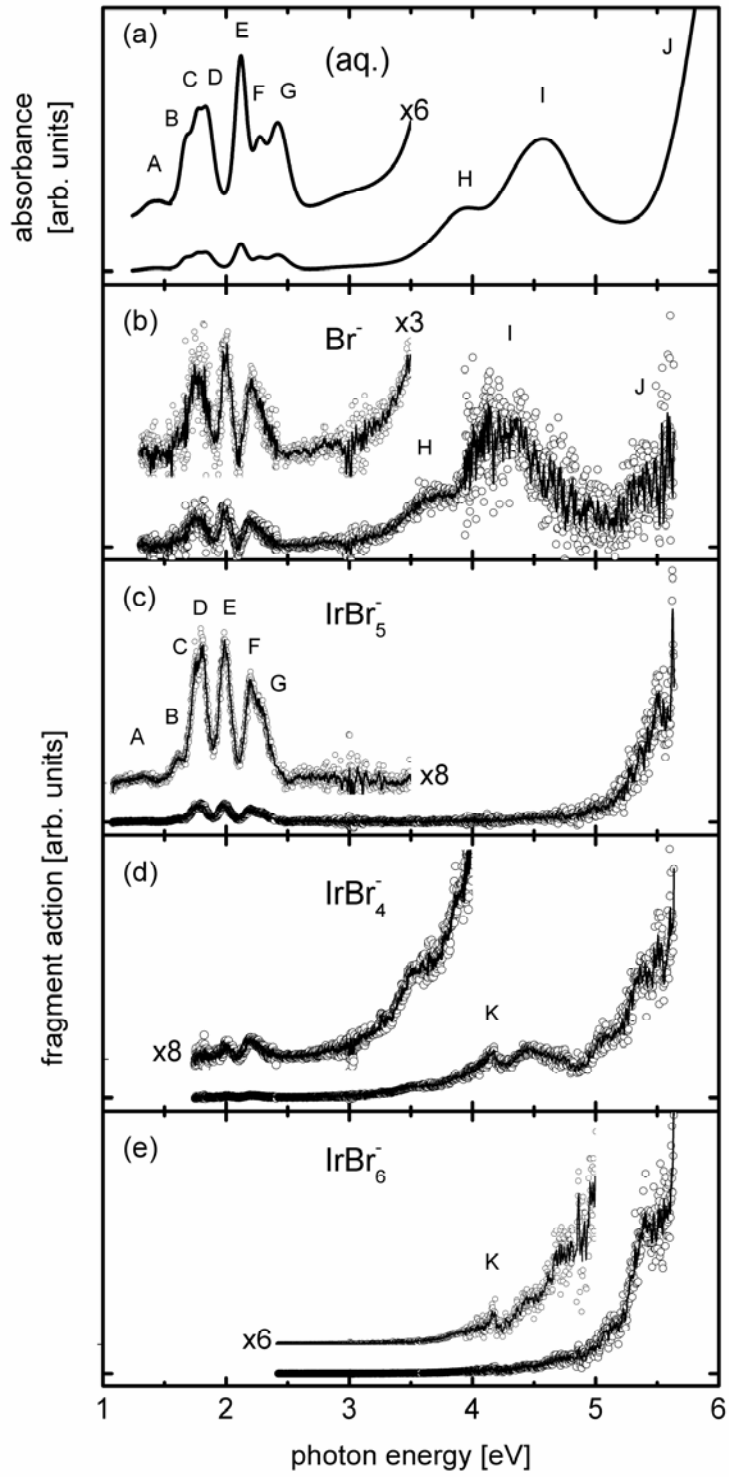

Figure 4.2. Electronic spectra for $IrBr_6^{2-}$. (a) Absorption of an ~0.5 mM aqueous solution of K_2IrBr_6, (b) Br^- action, (c) $IrBr_5^-$ action, (d) $IrBr_4^-$ action, and (e) $IrBr_6^-$ action.

4.3.1 $IrBr_5^-$ action

The photofragment action spectrum obtained by monitoring the formation of $IrBr_5^-$ as a function of photon energy is shown in Figure 4.2c. This VIS region of the spectrum contains a group of features similar to those that are found in the Br^- fragment channel (see §4.3.2 below). Gaussian fits of this peak group yields peaks at 1.33(1), 1.63(1), 1.73(1), 1.81(1), 1.99(1), 2.19(1), and 2.26(1) eV. With the exception of the peak labeled "B" at 1.63 eV, these peak positions are in agreement, within error, with the values obtained in the previous study by Friedrich et al.[21] using photodepletion measurements. The difference in the position of peak B can be attributed to the differences in photon densities between the two experiments as two-photon effects are presumed to be important near and below 1.6 eV. [21] We identify all of the features noted by Friedrich et al. but our extended spectral range allows us to observe one additional peak at 1.33(1) eV. The UV1 region of the spectrum shows a distinct lack of spectral features, except for a slow onset of fragmentation at ~4.25 eV. However, this feature might be more accurately associated with the tail of the main feature in the UV2 region. The feature in UV2 is comprised of a large increase in signal that continues past the spectral range in our experiment. We observe a number of shoulders, but the low signal to noise level in this region prevents us from pointing out any definite features.

4.3.2 Br^- action

The photofragment action spectrum involving formation of Br^- is shown in Figure 4.2b. The overall shape in the VIS region is very similar to that of the $IrBr_5^-$ channel. Also in this region is a gentle rise in signal occurring between ~2.5 and 3.25 eV. This feature is most likely the low-energy tail of peaks located in the UV1 region. The UV1 region contains a broad group of peaks centered near 4.1 eV. Gaussian fits of this group place two peaks at 3.54(10) and 4.24(20) eV. Following these two peaks in the UV2 region is an increase in signal that persists until the end of our spectral range. We note that the intensity of this feature is approximately the same as that of the 4.24 eV peak in the UV1 region.

4.3.3 $IrBr_4^-$ action

The photofragment action spectrum for formation of $IrBr_4^-$ is shown in Figure 4.2d. One important characteristic to note is the suppression of features in the VIS region of the

spectrum. The first feature that we observe is a peak near 2 eV that has a sharp cutoff on the low-energy side. A second feature between ~2.1 and 2.4 eV includes a peak at 2.2 eV with a high-energy shoulder. Following these features is a gentle increase in signal between ~2.5 and 3.25 eV, although this feature is most likely the low-energy tail of UV1 features. However, the detailed substructure of this group of peaks is considerably different than for Br^-. We assume that the 3.54 and 4.24 eV peaks from the Br^- channel are also present in the $IrBr_4^-$ channel, but there are additional features present in the $IrBr_4^-$ channel that are clearly not present in the Br^- channel. These features consist of a shoulder at ~3.85 eV, a sharp peak at 4.16(1) eV and a peak at ~4.45 eV that has a high-energy shoulder near 4.7 eV. The UV2 region of the spectrum contains an increase in signal that continues until the end of our spectral range and includes a number of additional features. There is a shoulder that occurs near 5.1 eV and a very steep rise in signal from ~5.2-5.4 eV followed by a less-steep increase toward higher energies. The dissociation cross section of the UV2 feature is significantly higher than the features present in the UV1 region of the spectrum.

4.3.4 $IrBr_6^-$ action

In the $IrBr_6^-$ action spectrum (Figure 4.2e), there is no detectable ion signal at the energies of the main absorptions of the $IrBr_6^{2-}$ parent ion in the VIS region. We observe product ions beginning at photon energies of ~2.6 eV. The $IrBr_6^-$ yield then increases quasi-exponentially until the high-energy limit of our spectral range. This spectrum also contains a number of features at higher photon energies in regions UV1 and UV2. Most notably, there is a prominent sharp peak at 4.16(1) eV as well as a sharp rise in $IrBr_6^-$ signal between ~5.2 and 5.4 eV that is immediately followed by a less-steep increase in signal. Other smaller features include small bumps at ~4.4 and ~4.7 eV as well as a shoulder near 5.1 eV.

4.4 Discussion

4.4.1 Peak assignments and comparison to aqueous solution spectrum

In order to make spectral assignments, we compare the gas-phase data to the spectrum of an aqueous solution of K_2IrBr_6 (Figure 4.2a). At first glance, the gas-phase spectrum that most resembles the aqueous spectrum is the Br^- action spectrum. This fragment channel possesses all of the spectroscopic features of the aqueous spectrum with approximately the same shape

and relative intensities. The $IrBr_5^-$ channel shows marked differences in comparison to the aqueous spectrum, most notably the complete lack of features in the UV1 region, but it is useful for the spectral assignments in the VIS region. Like the Br^- action spectrum, it has a very similar appearance to the VIS region of the aqueous spectrum. The VIS features have been labeled A-G on each of the two spectra in Figure 4.2a and Figure 4.2c. The UV1 and UV2 features observed in the Br^- action channel have been labeled H-J in Figure 4.2a and b. We note that it is very likely that several unresolved features are hidden underneath the broad spectral envelope of the UV features. It is not as straightforward to compare the $IrBr_4^-$ action spectrum to the aqueous spectrum due to the lack of features below ~2 eV and added complexity in the UV1 and UV2 regions. Likewise, the $IrBr_6^-$ action spectrum contains features that are rather different than those found in the aqueous spectrum.

To date, the only assignments made on the gas-phase photodissociation spectrum of $IrBr_6^{2-}$ were made by Friedrich et al. [21] in the range of 1.55-2.9 eV that were based on earlier work by Schatz and co-workers[33, 32] on magnetic circular dichroism of $IrBr_6^{2-}$ in various solvents and crystals. All electronic transitions are attributed to ligand-to-metal charge transfer (LMCT) bands, where electron density shifts from molecular orbitals mainly associated with the ligands to molecular orbitals that are mainly associated with the metal *d*-orbitals. Some *d-d* band transitions are also expected to be present in this region but they are dipole-forbidden and are thus expected to be much weaker than the LMCT bands.[32]

There are two general approaches to describing the excited electronic states of dianions. One approach (mentioned in §4.1) utilizes excited states obtained from adiabatic curves that arise from the avoided crossing of attractive and repulsive diabatic curves.[4] The other approach utilizes excited states obtained from classical ligand-field and molecular orbital description of the dianion that do not explicitly consider the destabilization due to Coulomb repulsion.[3] Because our data agree rather well with the molecular orbital description, we have chosen to use this approach for the majority of our spectral assignments. In §4.4.2, where possible fragmentation mechanisms are discussed, we point out a spectral feature that is better explained using the second approach of considering the adiabatic curves that arise from

avoided crossings. In this section, specific assignments are made using a qualitative molecular orbital description[32, 3] of $IrBr_6^{2-}$ in an octahedral geometry with contributions due to spin-orbit coupling, but neglecting π-backbonding interactions from ligand *p*-orbitals. A schematic energy level diagram for the molecular orbitals involved is shown in Figure 4.3. In the ground electronic state of $IrBr_6^{2-}$, all "ligand" orbitals are completely filled and the "metal" t_{2g} orbitals contain a total of 5 electrons. In the presence of spin-orbit coupling, the "metal" t_{2g} orbitals will split into two states where 4 electrons are located in the lower-energy u_g orbital and a single, unpaired electron is located in the higher-energy e_g orbital. In a LMCT transition, an electron is excited from one of the filled ligand orbitals into the metal e_g orbital ($t_{2g}(d)$ in the absence of spin-orbit coupling). This transition fills the electron hole in the metal orbital leaving a hole in one of the ligand orbitals. This one-electron picture allows for a straightforward interpretation of the states involved in the electronic transitions of $IrBr_6^{2-}$ since the symmetry of a state is simply the symmetry of the orbital in which the electron hole is located. A schematic representation of the electronic states is shown in Figure 4.4.

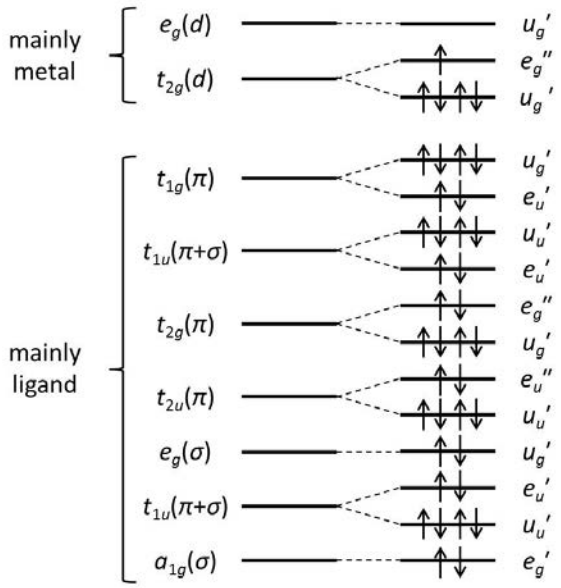

Figure 4.3. Schematic molecular orbital diagram for the ground state of $IrBr_6^{2-}$ as described by Schatz.[32] The orbitals are shown both without (left) and with spin-orbit coupling (right, in Griffith double group notation). The lower-lying orbitals are mostly associated with the ligands, while the higher-lying orbitals are mainly metal *d*-orbitals. The highest-energy occupied orbital, e_g [$t_{2g}(d)$] , is only half-filled.

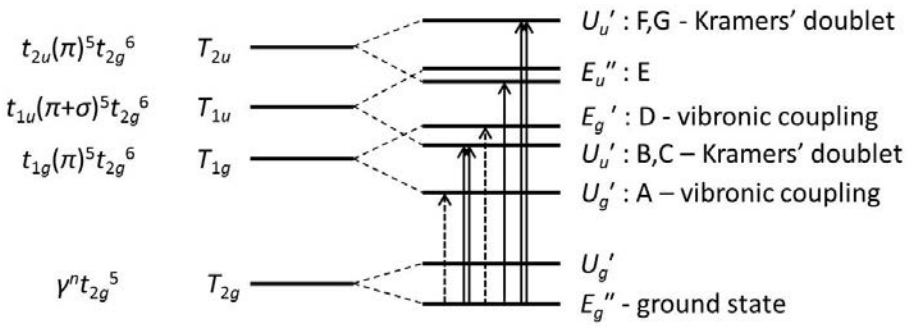

Figure 4.4. Schematic energy level diagram of all states involved in the VIS region transitions according to Schatz[32] (not to scale). Electron configurations of the ground and excited states are shown on the left. The term of each state is labeled excluding (left) and including spin-orbit coupling (right, in Griffith double group notation). Capital letters on the right correspond to the features observed in the gas-phase photodissociation spectrum (see Table 4.1). The lines represent transitions in the visible region. Dashed lines correspond to nominally dipole-forbidden transitions, which are probably allowed due to vibronic coupling.[33, 32] Double arrows correspond to transitions ending in split final states.

Of the spectroscopic features in the VIS region, peaks B-G have all previously been assigned by Friedrich et al.[21] Peak A has not been previously observed in the gas-phase, but a corresponding condensed-phase absorption band can be seen in Figure 4.2a. Using the energy level diagrams in Figure 4.3 and Figure 4.4, we assign this peak to the transition $U_g(^2T_{1g}) \leftarrow E_g(^2T_{2g})$, which is the only remaining possible LMCT transition in this energy range. This transition is dipole forbidden but should be vibronically allowed.[33, 32] The features present in the UV1 and UV2 regions have not been previously observed or assigned in the gas-phase. Schatz made rough assignments of the peaks in the 3.1-5.0 eV range of condensed-phase $IrBr_6^{2-}$ spectra.[32] Using the same energy level diagrams as described above, Schatz attributed these peaks to LMCT bands that arise from an electron being excited from one of the ligand orbitals to the u_g orbital ($e_g(d)$ in the absence of spin-orbit coupling). We assign the features H and I in our gas-phase spectra to transitions of this type. According to this model, excitation in the UV yields three unpaired electrons; one in the metal $e_g(d)$ orbital, one in the metal $t_{2g}(d)$ orbital, and one in the ligand orbital from where the excited electron originated. This results in a rather complicated situation and a detailed analysis of the unresolved bands in UV1 and UV2 regions is beyond the scope of this paper. The feature labeled as J in the UV2 region of our spectra has not yet been observed and we refrain from making an assignment. Our experiment is complicated by the fact that parent ions are at room temperature prior to

irradiation, which we expect causes the rather strong spectral congestion. Based on low-temperature data by Schatz[33, 32] we expect that future experiments with cold ions could yield vibronically-resolved spectra.

A summary of all peak positions, widths, and spectral assignments is presented in Table 4.1 along with peak positions of the corresponding features in the aqueous solution spectrum. As can be seen from these data, all peaks undergo a shift to higher energies upon solvation. As described by Friedrich et al.[21] for peaks in the VIS region, this shift can be attributed to differential solvation of the ground and excited states of the ion. The shifting of electron density from the ligands to the metal should result in an excited state that is not as favorably solvated as the ground state. This will lead to a shift in the corresponding electronic transitions to higher energies upon solvation. Since the UV1 and UV2 transitions are also due to LMCT, the excited states that are formed should also be shifted to higher energies upon solvation, in agreement with the experimental observations. The shifts measured for the VIS region vary between 0.02 and 0.16 eV and the peaks H and I in the UV1 region have shifts of 0.34 and 0.32 eV, respectively.

Table 4.1. Spectroscopic features and assignments for photodissociation spectra of $IrBr_6^{2-}$. Energies and widths for peaks A-I and K are from Gaussian fits to the data. Since feature J is predominately outside of our spectral range, the listed values only represent the low-energy onset of the feature.

Label	Energy [eV]	Width [eV]	Peak Assignment	Solution Features [eV]
A	1.33(1)	0.1	$U_g'(^2T_{1g})\leftarrow E_g''(^2T_{2g})$	1.44
B	1.63(1)	0.1	$U_u'(^2T_{1u})\leftarrow E_g''(^2T_{2g})$	1.67
C	1.73(1)	0.06	$U_u'(^2T_{1u})\leftarrow E_g''(^2T_{2g})$	1.75
D	1.81(1)	0.09	$E_g'(^2T_{1g})\leftarrow E_g''(^2T_{2g})$	1.83
E	1.99(1)	0.09	$E_u''(^2T_{2u})\leftarrow E_g''(^2T_{2g})$	2.12
F	2.19(1)	0.06	$E_u'(^2T_{1u})\leftarrow E_g''(^2T_{2g})$ or $U_u'(^2T_{2u})\leftarrow E_g''(^2T_{2g})$	2.26
G	2.26(1)	0.17	$U_u'(^2T_{2u})\leftarrow E_g''(^2T_{2g})$	2.42
H	3.54(10)	0.3	metal $e_g(d)\leftarrow$ ligand	3.85
I	4.24(20)	0.64	metal $e_g(d)\leftarrow$ ligand	4.58
J	> 5.1	n/a	n/a	> 5.1
K	4.16(1)	~0.05	n/a	n/a

4.4.2 Fragmentation mechanisms

It was shown in the previous sections that there is a large amount of variability between the spectra recorded from different fragment channels. This behavior can be explained by considering the fragmentation mechanisms that lead to each product ion. In principle, there are two different classes of reaction pathways that we will call direct and indirect. Even though we do not have explicit evidence from our experimental data that could distinguish between either of these two classes of pathways, it is appropriate to discuss the possible mechanisms for the observed fragment channels. In the case of a direct mechanism, photoexcitation would lead to an excited electronic state that is above the dissociation limit of that state and is either represented by a repulsive curve or is directly and efficiently coupled to a repulsive curve. In this case, a molecule in the excited state will undergo fast dissociation into products along the dissociation coordinate without much coupling to the other vibrational degrees of freedom. Depending on the specific excited state involved, different fragment channels and photoproducts may be accessed. In the case of an indirect mechanism, photoexcitation leads to an excited electronic state that undergoes radiationless decay into a vibrationally "hot" ground state where it can thermally dissociate.

All of the fragment ions that we observe are singly charged, which implies that two charged particles are generated in all of the processes leading up to the observed products. The Br^- channel can be quite complicated if all possible mechanisms are considered. The Br^- ion can be produced in combination with $IrBr_5^-$ or $IrBr_4^-$ (in the latter case together with a neutral Br atom). Despite the number of mechanisms that potentially involve Br^- formation, the action spectrum is fairly straightforward to interpret. As noted in the previous section on peak assignments, the Br^- action spectrum is remarkably similar to the aqueous spectrum of K_2IrBr_6 and all peaks are attributed to LMCT bands. The similarities between the two spectra suggest that every electronic excitation can lead to the production of Br^- photofragments. Measurements on the laser polarization-dependent kinetic energy release of Br^- from $IrBr_6^{2-}$ at 2.33 eV by Friedrich et al.[21] and time-resolved experiments by Rensing et al.[22] suggest a delayed fragmentation mechanism. However, this interpretation does not necessarily hold at higher energies. Within the VIS range, all of the electronic transitions shift electron density

from molecular orbitals of predominately ligand character to a $t_{2g}(d)$ molecular orbital located primarily on the Ir metal center. In context of ligand and crystal field theories,[1-3] the $t_{2g}(d)$ orbital is typically regarded as a nonbonding orbital (neglecting π-backbonding) where most of the electron density is located in areas that bisect the Ir-Br bonds. On the other hand, transitions in the UV1 and possibly UV2 ranges shift electron density into an $e_g(d)$ molecular orbital located primarily on the Ir metal center. This orbital is typically regarded as antibonding[1-3] and has its electron density located along the Ir-Br bond axes, therefore creating an excited state that could be considered "more repulsive" than transitions to the $t_{2g}(d)$ orbital. This could result in a direct dissociation mechanism for transitions in the UV1 and UV2 regions.

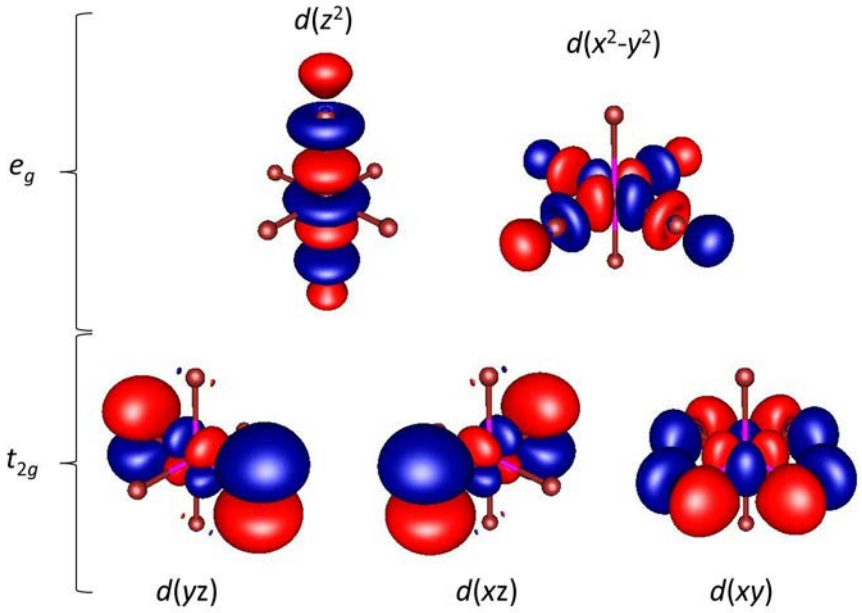

Figure 4.5. Contour plots of the metal-based molecular orbitals of $IrBr_6^{2-}$.

In contrast to the channels where electronic excitation leads to bond-breaking, the $IrBr_6^-$ channel arises from a considerably different mechanism. Here, the $IrBr_6^-$ monoanion results from electron detachment of the parent $IrBr_6^{2-}$ dianion. Monitoring $IrBr_6^-$ as a function of the photon energy will therefore result in a spectrum that contains similar information to a photodetachment spectrum. However, this is not exactly the same since monitoring the formation of $IrBr_6^-$ does not include any dissociative electron detachment that may occur. The

observed overall increase in signal as a function of photon energy can be attributed to threshold effects. For photon energies that are lower than the inner barrier height of the RCB for ground state $IrBr_6^{2-}$ but above the second adiabatic electron affinity, photodetachment may occur through electron tunneling. As the photon energy is increased, the electron should experience a lower and narrower barrier that should result in higher tunneling probabilities and thus an increase in the photodetachment cross section. In principle, once the photon energy is higher than the inner height of the RCB, the photodetachment yield should rapidly approach a constant value in accordance with Wigner's threshold law for two products experiencing Coulomb repulsion.[34] However, the various excited states of the product monoanion $IrBr_6^-$ must also be considered. As photon energy is increased, more of these product states are energetically accessible, each of which should contribute additional yield to the overall detachment cross section. This effect has been observed before in the dianion $PtBr_4^{2-}$.[35] The first appearance of $IrBr_6^-$ that we observe is at ~2.6 eV. Wang et al. estimated an upper limit of ~3 eV for the inner RCB height. Observation of $IrBr_6^-$ at 2.6 eV is consistent with this upper limit especially when taking into account electron tunneling. The features observed in the UV1 and UV2 regions of the spectrum can be attributed to several possible factors. One likely cause is the increase in the total detachment cross section that should occur as new detachment channels open with increasing photon energy. Depending on the location of these new thresholds with respect to their corresponding RCBs, the detachment yield could potentially experience sudden increases. The peak at 4.16 eV is not as easily understood using this explanation. In principle, the molecule could be excited into a state that favors ionic fragmentation, leading to the observed reduction in the photodetachment cross section on the high-energy side of the peak. However, this mechanism would imply an enhancement in the fragmentation channels at photon energies between 4.16 and 4.3 eV where this dip occurs. The peak observed in the Br^- channel is too broad to confirm this explanation. Moreover, there would have to be an increase in yield in this energy range in other fragment spectra as well. This is obviously not the case as there is little to no signal in this region of the $IrBr_5^-$ channel and the $IrBr_4^-$ channel shows the same feature as the $IrBr_6^-$ channel at this energy. Instead, we attributed the 4.16 eV peak to a resonant enhancement in the detachment cross section. It is

important to note that this enhancement is likely to go beyond the resonant excitations seen in condensed-phase absorption spectra of $IrBr_6^{2-}$ or the Br^- action spectrum that are explained using a molecular orbital theory-based approach. A possible candidate for the origin of this feature would be a resonance effect that is entirely due to RCB effects, where the adiabatic states involved arise from the avoided crossing of attractive and repulsive diabatic curves. An electron that is excited to an adiabatic state that is above the dissociation limit and contains a RCB can be in part described by a continuum wave function. In this description, the lifetime of the excited electron can be sufficiently lengthened due to effects that are similar to shape resonances observed in electron scattering. In a semiclassical picture, an increased lifetime will result in more "attempts" at tunneling and, consequently, a higher detachment yield. This could very likely lead to the sharp peak at 4.16 eV. The width of this peak could be indicative of a resonance lifetime of ~40 fs.

Before analyzing the $IrBr_4^-$ spectrum, it is useful to consider the different mechanisms that could potentially be involved in ionic fragmentation. A brief summary of these main reactions, without intermediate steps, is listed in Scheme 4.1.

Scheme 4.1

$$IrBr_6^{2-} + h\nu \rightarrow IrBr_4^- + Br_2^- \quad \textbf{(Scheme 4.1a)}$$

$$IrBr_6^{2-} + h\nu \rightarrow IrBr_4^- + Br_2 + e^- \quad \textbf{(Scheme 4.1b)}$$

$$IrBr_6^{2-} + h\nu \rightarrow IrBr_4^- + 2\ Br + e^- \quad \textbf{(Scheme 4.1c)}$$

$$IrBr_6^{2-} + h\nu \rightarrow IrBr_4^- + Br^- + Br \quad \textbf{(Scheme 4.1d)}$$

Since we do not observe any Br_2^- fragment ions, we rule out Scheme 4.1a as a possible mechanism. When considering the other three channels, it is important to note that they may proceed *via* several intermediate steps depending on whether or not fragmentation proceeds *via* a direct or indirect mechanism. As mentioned above, two experiments from the Kappes group were interpreted in terms of delayed fragmentation in the VIS region.[21-22] Fluence measurements taken in their experiment showed that $IrBr_4^-$ formation was due to a two-photon process at 1.78 eV. Interestingly, we do not observe any $IrBr_4^-$ at this energy in our experiment. A comparison between the approximate photon densities of our experiment to those required

for $IrBr_4^-$ formation (as determined by Friedrich et al.) suggests that we should not see any two-photon effects at 1.78 eV and that $IrBr_4^-$ formation may only be significant in the energy range between ~2.0 and 3.0 eV and possibly between ~3.15 and 4.0 eV where our photon densities are sufficiently high. This would explain the onset of $IrBr_4^-$ at 2.0 eV. However, our own fluence measurements at 3.65, 4.13, and 4.46 eV indicate that $IrBr_4^-$ is produced *via* a one-photon process at these photon energies in our experiment.

The shape of the UV1 and UV2 regions in the $IrBr_4^-$ action spectrum reveals some interesting information on how $IrBr_4^-$ is formed above ~3 eV. As mentioned in §4.3.3, the structure of the $IrBr_4^-$ action spectrum in the UV regions has an overall shape that is similar to the Br^- spectrum but also has some additional features. Upon careful inspection, these features are all found to correspond to features in the $IrBr_6^-$ action spectrum. This suggests that at least part of the $IrBr_4^-$ action spectrum is closely related to the electron detachment channel. Taking into account the possible reactions listed in Scheme 4.1, we tentatively assign feature K, which is observed in the UV1 region of the $IrBr_4^-$ channel but is not observed in the Br^- channel, to dissociative electron detachment. Upon UV irradiation, an electron can be detached from $IrBr_6^{2-}$ leaving behind an excited $IrBr_6^-$ monoanion according to the process

Scheme 4.2

$$IrBr_6^{2-} + h\nu \rightarrow [IrBr_6^-]^* + e^-.$$

Any $IrBr_6^-$ ions that are sufficiently excited to undergo dissociation into $IrBr_4^-$ on the timescale of our experiment (~35 μs) will be registered in the $IrBr_4^-$ channel. The involvement of electron detachment in fragmentation mechanisms has been invoked before for dianions in a study by Bojesen et al.[36] to describe the surprisingly low kinetic energy release associated with fragmentation of $Pt(CN)_4^{2-}$ following high-energy CID, where electronic excitation is possible, Bojesen et al. suggested that a detached electron could carry away most of the remaining energy.

While dissociative detachment can explain some specific features in the $IrBr_4^-$ channel, it does not account for every feature. In addition to the features that are attributed to dissociative detachment, there is still a broad envelope of peaks in the UV1 region that resemble the Br^- channel as well as the aqueous absorption spectrum. We explain these

features the same way we account for the Br^- channel. Upon irradiation in the UV, $IrBr_6^{2-}$ may fragment *via* bond-breaking mechanism according to Scheme 4.1d into $IrBr_4^-$, Br^-, and neutral Br.

The product $IrBr_5^-$ can also be formed *via* multiple mechanisms, which are outlined in Scheme 4.3.

Scheme 4.3

$$IrBr_6^{2-} + h\nu \rightarrow IrBr_5^- + Br^- \quad \textbf{(Scheme 4.3a)}$$

$$IrBr_6^{2-} + h\nu \rightarrow IrBr_5^- + Br + e^- \quad \textbf{(Scheme 4.3b)}$$

In analogy to the $IrBr_4^-$ channel, these mechanisms can be broken into one that proceeds by bond cleavage into two ionic fragments (Scheme 4.3a) and another that proceeds by dissociative detachment (Scheme 4.3b). The signal in the VIS region of the spectrum alone does not contain information about the mechanism involved, but it is not in conflict with the delayed fragmentation mechanism invoked by Friedrich et al.[21] that results in formation of $IrBr_5^-$ and Br^- products. Additionally, the lack of signal below 2.6 eV in the $IrBr_6^-$ channel suggests that electron detachment, and consequently dissociative detachment, is not important in the VIS region.

The most interesting aspect of the $IrBr_5^-$ action spectrum is the distinct lack of signal in the UV1 region and the return of signal in the UV2 region. It is possible that once the parent $IrBr_6^{2-}$ ion is excited to sufficiently high energies, an indirect process could produce "hot" $IrBr_5^-$ as an intermediate in unimolecular dissociation. This could then decay leading to exclusive formation of $IrBr_4^-$ ions and explain the lack of $IrBr_5^-$ formation in the UV1 region. However, if this mechanism were true, it would not explain the return of the $IrBr_5^-$ signal in the UV2 region, which will also have sufficient energy to exclusively form $IrBr_4^-$ *via* this indirect process. If the only processes that are considered are due to unimolecular decay, the disappearance of $IrBr_5^-$ in the UV1 region and its eventual return in the UV2 region could be explained by multiple fragmentation mechanisms. As the photon energy is increased, more mechanisms may become energetically possible allowing for kinetic competition between $IrBr_5^-$ and $IrBr_4^-$ ions. In principle, the return of $IrBr_5^-$ in the UV2 region could be attributed to dissociative electron detachment. However, the rise in signal in the UV2 region does not contain many of the

features common to the $IrBr_6^-$ and $IrBr_4^-$ fragment channels that are attributed to electron detachment. Most notably, the return of the $IrBr_5^-$ fragment signal does not occur until ~4.25 eV, whereas electron detachment is known to occur at photon energies as low as 2.6 eV and one of the most prominent features that we attribute to electron detachment appears only at 4.16 eV. This suggests that dissociative detachment is not an important mechanism for the formation of $IrBr_5^-$ product ions. It is reasonable to assume that the coupling of the excited states to the various fragment channels is different for the VIS and UV1 excitations, considering the different nature of the transitions in the two regions. As mentioned above, the transitions are attributed to LMCT bands where the electron density is shifted into a metal $t_{2g}(d)$ orbital in the case of a VIS transition and into a metal $e_g(d)$ orbital in the case of a UV1 transition, each of which have different bonding character.

4.5 Conclusions

We have observed the complete set of LMCT transitions in the VIS region and a number of additional LMCT transitions in the UV1 region that are compatible with previous assignments based on the orbital scheme invoked by Schatz for condensed-phase $IrBr_6^{2-}$. The photodissociation action spectrum of the Br^- fragment channel is very similar to the spectrum of an aqueous solution of $IrBr_6^{2-}$, revealing solvatochromic shifts of up to 0.16 eV in the visible and ~0.33 eV in the UV. The behavior of the dissociation and electron detachment channels paints a very complex picture of the possible decay mechanisms, where a combination of direct dissociation, unimolecular decay, and dissociative detachment are all expected to play possible roles.

4.6 References for Chapter 4

1. Miessler, G.L. and Tarr, D.A., *Inorganic Chemistry*. 2 ed. 1998, Upper Saddle River, New Jersey: Prentice-Hall.

2. Cotton, F.A., Wilkinson, G., Murillo, C.A., and Bochmann, M., *Advanced Inorganic Chemistry*. 6 ed. 1999: John Wiley & Sons.

3. Jean, Y., *Molecular Orbitals of Transition Metal Complexes*. 2005, New York: Oxford University Press Inc.

4. Scheller, M.K., Compton, R.N., and Cederbaum, L.S., "Gas-phase multiply-charged anions." *Science*, 1995. **270**(5239): p. 1160.

5. Wang, L.S., Ding, C.F., Wang, X.B., Nicholas, J.B., and Nicholas, B., "Probing the potential barriers and intramolecular electrostatic interactions in free doubly charged anions." *Physical Review Letters*, 1998. **81**(13): p. 2667.

6. Wang, X.B., Ding, C.F., and Wang, L.S., "Photodetachment spectroscopy of a doubly charged anion: Direct observation of the repulsive Coulomb barrier." *Physical Review Letters*, 1998. **81**(16): p. 3351.

7. Friedrich, J., Weis, P., Kaller, J., Whetten, R.L., and Kappes, M.M., "Alkali halide cluster dianions: metastability and threshold sizes." *European Physical Journal D*, 1999. **9**(1-4): p. 269.

8. Weis, P., Hampe, O., Gilb, S., and Kappes, M.M., "Metastability of isolated platinum and palladium tetrahalide dianions and the role of electron tunneling." *Chemical Physics Letters*, 2000. **321**(5-6): p. 426.

9. Dreuw, A. and Cederbaum, L.S., "Nature of the repulsive Coulomb barrier in multiply charged negative ions (vol A63, art. no. 012501, 2000)." *Physical Review A*, 2001. **63**(4).

10. Dreuw, A. and Cederbaum, L.S., "Multiply charged anions in the gas phase." *Chemical Reviews*, 2002. **102**(1): p. 181.

11. Arnold, K., Balaban, T.S., Blom, M.N., Ehrler, O.T., Gilb, S., Hampe, O., van Lier, J.E., Weber, J.M., and Kappes, M.M., "Electron autodetachment from isolated nickel and copper phthalocyanine-tetrasulfonate tetraanions: Isomer specific rates." *Journal of Physical Chemistry A*, 2003. **107**(6): p. 794.

12. Simons, J., "Molecular anions." *Journal of Physical Chemistry A*, 2008. **112**(29): p. 6401.

13. Wang, L.S., Ding, C.F., Wang, X.B., and Barlow, S.E., "Photodetachment photoelectron spectroscopy of multiply charged anions using electrospray ionization." *Review of Scientific Instruments*, 1999. **70**(4): p. 1957.

14. Wang, X.B. and Wang, L.S., "Photodetachment of free hexahalogenometallate doubly charged anions in the gas phase: ML_6^{2-}, (M=Re, Os, Ir, Pt; L=Cl and Br)." *Journal of Chemical Physics*, 1999. **111**(10): p. 4497.

15. Wang, X.B. and Wang, L.S., "Experimental search for the smallest stable multiply charged anions in the gas phase." *Physical Review Letters*, 1999. **83**(17): p. 3402.

16. Wang, X.B. and Wang, L.S., "Observation of negative electron-binding energy in a molecule." *Nature*, 1999. **400**(6741): p. 245.

17. Weber, J.M., Ioffe, I.N., Berndt, K.M., Loffler, D., Friedrich, J., Ehrler, O.T., Danell, A.S., Parks, J.H., and Kappes, M.M., "Photoelectron spectroscopy of isolated multiply negatively charged oligonucleotides." *Journal of the American Chemical Society*, 2004. **126**(27): p. 8585.

18. Blades, A.T. and Kebarle, P., "Study of the stability and hydration of doubly-charged ions in the gas-phase - SO_4^{2-}, $S_2O_6^{2-}$, $S_2O_8^{2-}$ and some related species." *Journal of the American Chemical Society*, 1994. **116**(23): p. 10761.

19. Wang, X.B., Nicholas, J.B., and Wang, L.S., "Electronic instability of isolated SO_4^{2-} and its solvation stabilization." *Journal of Chemical Physics*, 2000. **113**(24): p. 10837.

20. Zhou, J., Santambrogio, G., Brummer, M., Moore, D.T., Meijer, G., Neumark, D.M., and Asmis, K.R., "Infrared spectroscopy of hydrated sulfate dianions." *Journal of Chemical Physics*, 2006. **125**(11).

21. Friedrich, J., Gilb, S., Ehrler, O.T., Behrendt, A., and Kappes, M.M., "Electronic photodissociation spectroscopy of isolated IrX_6^{2-} (X=Cl,Br)." *Journal of Chemical Physics*, 2002. **117**(6): p. 2635.

22. Rensing, C., Ehrler, O.T., Yang, J.P., Unterreiner, A.N., and Kappes, M.M., "Photodissociation dynamics of $IrBr_6^{2-}$ dianions by time-resolved photoelectron spectroscopy." *Journal of Chemical Physics*, 2009. **130**(23).

23. Boxford, W.E., Pearce, J.K., and Dessent, C.E.H., "Ionic fragmentation versus electron detachment in isolated transition metal complex dianions." *Chemical Physics Letters*, 2004. **399**(4-6): p. 465.

24. Boxford, W.E., El Ghazaly, M.O.A., Dessent, C.E.H., and Nielsen, S.B., "High-energy collision induced dissociation of iridium hexa-halide dianions: Observation of triple electron detachment and other decay pathways." *International Journal of Mass Spectrometry*, 2005. **244**(1): p. 60.

25. Burke, R.M., Boxford, W.E., Panja, S., Nielsen, S.B., and Dessent, C.E.H., "On the propensity for electron transfer in high-energy collisions of iridium complex anions with cesium atoms." *Chemical Physics Letters*, 2007. **442**(4-6): p. 201.

26. Ahlrichs, R., Bar, M., Haser, M., Horn, H., and Kolmel, C., "Electronic-structure calculations on workstation computers - The program system TURBOMOLE." *Chemical Physics Letters*, 1989. **162**(3): p. 165.

27. Parr, R.G. and Yang, W., *Density-Functional Theory of Atoms and Molecules*. 1989, New York: Oxford University Press.

28. Becke, A.D., "Denisty-functional exchange-energy approximation with correct asymptotic-behavior." *Physical Review A*, 1988. **38**(6): p. 3098.

29. Lee, C.T., Yang, W.T., and Parr, R.G., "Development of the Colle-Salvetti Correlation-Energy Formula into a Functional of the Electron-Density." *Physical Review B*, 1988. **37**(2): p. 785.

30. Weigend, F., Haser, M., Patzelt, H., and Ahlrichs, R., "RI-MP2: optimized auxiliary basis sets and demonstration of efficiency." *Chemical Physics Letters*, 1998. **294**(1-3): p. 143.

31. Andrae, D., Haussermann, U., Dolg, M., Stoll, H., and Preuss, H., "Energy-adjusted ab-initio pseudopotentials for the 2nd and 3rd row transition-elements." *Theoretica Chimica Acta*, 1990. **77**(2): p. 123.

32. Schatz, P.N., "MCD Spectra of Charge-Transfeer Transitions: Octahedral Ir^{4+}," in *Electronic States of Inorganic Compounds*, P. Day, Editor. 1975, D. Reidel Publishing Company: Dordrecht, Boston. p. 223.

33. Dickinson, J.R., Piepho, S.B., Spencer, J.A., and Schatz, P.N., "High-Resolution Magnetic Circular-Dichroism and Absorption-Spectra of $Cs_2ZrBr_6:Ir^{4+}$." *Journal of Chemical Physics*, 1972. **56**(6): p. 2668.

34. Wigner, E.P., "On he behavior of cross sections near thresholds." *Physical Review*, 1948. **73**(9): p. 1002.

35. Loffler, D., Weber, J.M., and Kappes, M.M., "Photodetachment spectroscopy of $PtBr_4^{2-}$: Probing the Coulomb barrier of a doubly charged anion." *Journal of Chemical Physics*, 2005. **123**(22).

36. Bojesen, G., Hvelplund, P., Jorgensen, T.J.D., and Nielsen, S.B., "Probing the lowest coordination number of dianionic platinum-cyanide complexes in the gas phase: Dynamics of the charge dissociation process." *Journal of Chemical Physics*, 2000. **113**(16): p. 6608.

5 Transition Metal Complexes II: $IrBr_n^-$

5.1 Background

The last several decades have seen a resurgence of physical and chemical experiments on transition metal complexes, in part due to the advent of experimental techniques that allow for the study of such complexes in the gas-phase.[1-10] Studies of transition metal complexes in the gas-phase are advantageous since they can provide detailed information on *intrinsic* molecular properties by isolating species of interest from the perturbing effects of solvent or counterions. While many studies have been performed on fully-coordinated transition metal complexes, [1-6, 11, 7-10] much less information is available on smaller, under-coordinated species. Despite this lack of attention, it would be advantageous to develop an understanding of these species since they are likely to play important roles in transition metal chemistry. For instance, many transition metal complexes readily participate in ligand exchange in solution. In cases where exchange occurs *via* a dissociative mechanism, under-coordinated species will exist as transient, reactive intermediates.[12-13] Additionally, such under-coordinated, reactive species may be formed following photodissociation as a consequence of the light sensitivity of many transition metal complexes. Obtaining relevant thermodynamic and spectroscopic data on these species *in situ* is non-trivial due to their transient nature. Furthermore, under-coordinated complexes are likely to be present as part of a complicated mixture, where overlapping spectral signatures from a large number of related species can make analysis difficult. Gas-phase studies can be used to circumvent these problems by probing the complexes as individual, isolated species.

In addition to their potential importance in solution-phase processes, under-coordinated species are also of interest for more fundamental processes in the gas-phase. In particular, many experiments have been performed to prove the nature of the repulsive Coulomb barriers (RCBs) that exist in multiply-charged anionic compounds. [14, 1-5, 15-16, 6, 17, 11, 7-9, 18, 10] The specific details of a RCB are dependent upon a number of factors that include the asymptotic behavior of multiply-charged anions as dissociation occurs. Upon dissociation, each electronic state of the products will correspond to a unique RCB on the potential energy

surface.[14, 1, 19-20, 16] For cases where fragments correspond to simple species (such as neutral or charged halogen atoms), detailed spectroscopic information describing electronic states is widely available.[21-22] However, information on the electronic excited states of fragment species that contain the transition metal is much less available. Many of these species will correspond to under-coordinated transition-metal complexes. Therefore, determining their thermodynamic and spectroscopic properties would be desirable.

In this paper, we describe the fragmentation and electronic photodissociation spectroscopy of two under-coordinated bromoiridates, $IrBr_5^-$ and $IrBr_4^-$. Both species are well-known fragments of the prototypical gas-phase multiply-charged anion $IrBr_6^{2-}$.[6, 17, 7, 9-10] These species have been observed following collision-induced-dissociation[17, 7, 9] as well as photodissociation.[6, 23, 10] The ion $IrBr_5^-$ corresponds to the lowest-energy decay pathway of $IrBr_6^{2-}$, where it is formed *via* ionic fragmentation and is most likely accompanied by Br^- fragment ions. [6, Marcum, 2009 #133, 17, 7, 9-10] The ion $IrBr_4^-$ can be formed from decay of $IrBr_6^{2-}$ *via* a number of possible mechanisms that may include thermal dissociation, direct dissociation on a repulsive curve, and dissociative electron detachment.[6, 17, 7, 9, 23, 10] In particular, it has been observed as a decay product of $IrBr_6^{2-}$ following a two-photon process.[6, 23, 10] However, it was not clear whether $IrBr_4^-$ is formed as a primary photoproduct following absorption of two photons by $IrBr_6^{2-}$ or as a secondary photoproduct whereby the first photon promotes dissociation of $IrBr_6^{2-}$ into the primary photoproduct, $IrBr_5^-$, which dissociates upon absorption of the second photon. [6, 10] For the latter process to occur, $IrBr_5^-$ would have to demonstrate absorption at some of the same wavelengths as $IrBr_6^{2-}$ and have a low-enough dissociation threshold to facilitate breaking of an Ir-Br bond.

5.2 Methods

5.2.1 Photodissociation spectra

Details of the experimental methods used in this work are described in Chapter 2 of this thesis. Ions of interest were produced using electrospray ionization of an ~4 mM aqueous solution of K_2IrBr_6 (Sigma-Aldrich). The $IrBr_5^-$ and $IrBr_4^-$ ions that were studied in this experiment are presumably formed by fragmentation of $IrBr_6^{2-}$ in the initial stages of our ESI source, prior to

reaching the room-temperature hexapole ion trap where ions are assumed to reach thermal equilibrium. In general, production of these two ions is optimized by using a larger voltage difference between the capillary and skimmer. This should facilitate the higher-energy collisions necessary for fragmentation of $IrBr_6^{2-}$ into the $IrBr_5^-$ and $IrBr_4^-$ ions.

5.2.2 Computational

In order to determine theoretical thresholds for fragmentation channels, geometry optimizations were performed on parent and fragment ions using the TURBOMOLE V6.2 suite of programs.[24] We employed density functional theory (DFT)[25] with the B3LYP functional[26-27] and a def2-TZVPP basis set[28] for all atoms. The def2-ecp effective core potential (multi-electron fit to Wood-Boring orbital energies)[29] was used to account for scalar relativistic effects. All geometry optimizations were performed without symmetry constraints starting from several initial structures that are typical of transition metal complexes for coordinate numbers of the species studied in this experiment. For example, optimizations for four-coordinate species were started from square-planar, tetrahedron, and butterfly geometries and five-coordinate species were started from square-pyramid and trigonal-bipyramid geometries. Additionally, optimizations were performed for a variety of unrestricted, open-shell multiplicities. Vibrational frequencies were calculated using analytical second derivatives.[30-31] The obtained frequencies were used to correct the calculated gas-phase thresholds for zero-point energy. For comparison to apparent experimental thresholds, the vibrational energy content of the ions was taken into account using the equation

Equation 5.1

$$U_{vib} = \sum_i \frac{h\nu_i}{(e^{h\nu_i/kT} - 1)}$$

where ν_i represents the frequencies of the individual vibrational modes, h is Planck's constant, k is Boltzmann's constant, and T is the temperature of the ions. Because ions are accumulated in a room-temperature hexapole ion trap, we assume the ion temperature to be 300 K.

5.3 Results and discussion

5.3.1 Photodissociation spectra and fragment channels for $IrBr_4^-$

Following irradiation of $IrBr_4^-$, the two fragment ions observed were Br^- and $IrBr_3^-$, the latter corresponding to the loss of a neutral bromine atom. Due to the extremely low kinetic energy of Br^- ions following dissociation, they have correspondingly low detection efficiencies. This prevented us from using this fragment channel to obtain a photodissociation spectrum or to quantify the branching ratios. Additionally, all product channels are accompanied by neutral fragments. However, the current experiment does not allow for identification of these species.

A photodissociation spectrum of $IrBr_4^-$, obtained by monitoring the $IrBr_3^-$ ions as a function of wavelength, is shown in Figure 5.1. The spectrum consists of three main features: a peak centered near 2.7 eV, a second peak centered near 3.5 eV, and a broad feature centered near 4.5 eV that has apparent high- and low-energy shoulders around 4.1 and 5.3 eV, respectively. Before interpreting the spectral features, it is necessary to consider the thresholds for each fragment channel since photodissociation can only occur if enough energy is deposited into the molecule during absorption. Calculated threshold energies for $IrBr_4^-$ were obtained using density functional theory and are summarized in Table 5.1. The two lowest-energy fragment channels correspond to loss of either a neutral bromine atom or a Br^- ion and both have thresholds of approximately 2.7 eV. When compared to the $IrBr_4^-$ photodissociation action spectrum, the threshold for $IrBr_3^-$ is found to correspond roughly to the first spectral feature. In principle, $IrBr_3^-$ should not be formed at photon energies less than the appropriate dissociation threshold. However, parent ions are assumed to reach thermal equilibrium in the room temperature hexapole ion trap and they should have vibrational energies corresponding to a temperature of approximately 300 K prior to irradiation. Based on calculated harmonic frequencies, this temperature corresponds to an average vibrational energy of approximately 0.16 eV. If an additional 1.5 *kT* of rotational energy is included, there will be a total internal energy of approximately 0.2 eV. Taking this internal energy into account suggests that we should begin to see $IrBr_3^-$ fragment ions at approximately 2.5 eV, which is in good agreement with the onset of the features in our spectrum. This also suggests that any spectral features

present below ~2.5 eV should not be observed since absorption of a photon does not provide enough energy for fragmentation.

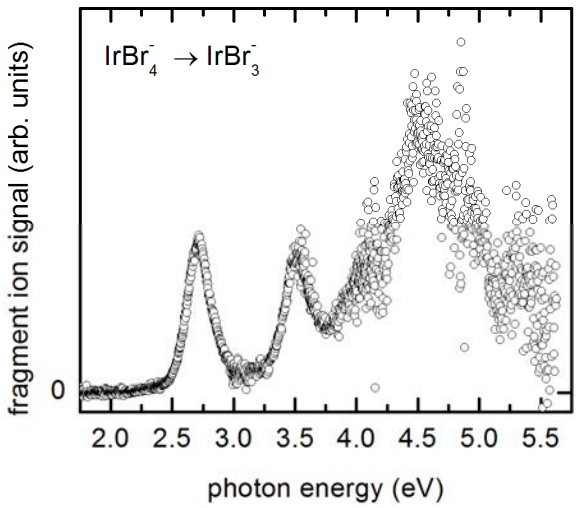

Figure 5.1. Photodissociation action spectrum of $IrBr_4^-$ obtained by monitoring $IrBr_3^-$ fragments as a function of photon energy.

Table 5.1. Calculated threshold energies for various fragment channels resulting from photodissociation of $IrBr_4^-$. The channel corresponding to experimentally observed fragments is in bold.

$IrBr_4^-$ Photodissociation	
Fragment Channel	Energy [eV]
$IrBr_3^0 + Br^0 + e^-$	5.97
$IrBr_2^- + 2\ Br^0$	5.16
$IrBr_2^0 + Br^- + Br^0$	4.76
$IrBr_4^0 + e^-$	4.11
$IrBr_3^0 + Br^-$	2.71
$IrBr_3^- + Br^0$	**2.70**

Other product channels that have calculated thresholds within the energy range of the current experiment correspond to electron detachment from $IrBr_4^-$ at 4.1 eV and loss of two neutral bromine atoms to form $IrBr_2^-$ at 5.15 eV. Since our experiment does not have the ability to detect electrons or to selectively identify neutral fragments, we are unable to experimentally

verify the presence of the detachment channel. It is possible that the decrease in $IrBr_3^-$ fragment ion signal toward the higher-energy end of our spectral range (which is in the vicinity of the $IrBr_2^-$ threshold energy) could be due to there being enough energy present to ensure a limited survival probability of $IrBr_3^-$ over the timescale of our experiment (see below). Alternatively, it is possible that this decrease in ion signal occurs entirely due to a decrease in the absorption cross section. The lack of $IrBr_2^-$ fragment ions in the experiment suggests the latter explanation. However, more experiments with higher photon energies would need to be performed to verify this behavior.

In order to interpret $IrBr_4^-$ spectral features, it is necessary to understand the electronic structure of the complex. However, a complete description is a tremendous undertaking due to a number of complex factors that include spin-orbit coupling, relativistic effects, and the possibility of an open-shell configuration. As an alternative, much insight can be gained by use of a simple, qualitative molecular orbital approach. The ground state structure of the complex predicted by DFT calculations lies between a square-plane and a tetrahedron and has a triplet configuration (see Figure 5.2). This structure and configuration is approximately 220 meV lower in energy than a square-planar triplet and approximately 460 meV lower in energy than a square-planar singlet. This result can be understood using a molecular orbital picture that consists of four-coordinate $Ir^{(III)}$ in a d^6 electron configuration with contributions from ligand *p*-orbital donors. Structures consisting of a tetrahedron (T_d symmetry) and square-plane (D_{4h} symmetry) constitute high-symmetry limits to the possible geometries of $IrBr_4^-$ with well-known molecular orbital diagrams.[32, 13, 33] These geometries, along with their corresponding molecular orbital diagrams, are shown in Figure 5.2. In order for $IrBr_4^-$ to have a tetrahedral geometry, four electrons will need to be distributed in the upper t_2 state. This configuration should induce Jahn-Teller distortion to lower symmetry. The most direct way of lowering the symmetry is for the four bromide ligands to move toward being square planar so that the molecule has D_{2d} symmetry. At the opposite extreme, all four ligands and the iridium atom lie in the same plane so that $IrBr_4^-$ adopts a square-planar geometry. In this geometry, the energy gap between the *d*(*xy*) and doubly-degenerate *d*(*xz*) and *d*(*yz*) orbitals should be small enough to allow the possibility of both high- and low-spin configurations. If the complex adopts a low-spin

singlet configuration, then a square planar geometry will be the most stable configuration and distortion should not occur. However, if it adopts a high-spin configuration, Jahn-Teller distortion to lower symmetries is expected. In this case, the bromide ligands should move out of the plane toward a tetrahedron, resulting in the complex having D_{2d} symmetry. This distortion will lead to a change in the molecular orbital energies so that the configuration has two paired electrons in the *d*(*xy*) orbital and two unpaired electrons distributed among the two doubly-degenerate *d*(*xz*) and *d*(*yz*) orbitals. The DFT results are in good agreement with the molecular orbital picture developed from both extremes. In either case, this lowering of the molecular symmetry to D_{2d} has significant consequences for the interpretation of spectral features. Because the DFT-predicted structure lies closer to a square-planar structure than a tetrahedron (see Figure 5.2), it is easier to approach the spectroscopy from this limit.

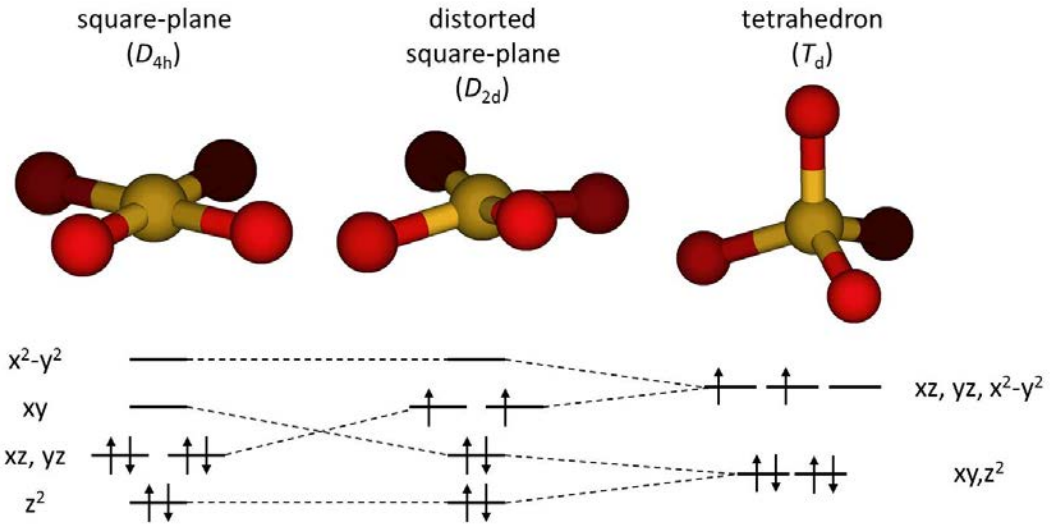

Figure 5.2. Several potential geometries of the $IrBr_4^-$ complex with their corresponding schematic molecular orbital energy diagrams. Note that the relative energies in each molecular orbital diagram are not to scale. The middle structure, corresponding to a distorted square plane with D_{2h} symmetry, is calculated to be the lowest-energy geometry when it has a triplet electron configuration.

In the square-planar, high-symmetry (D_{4h}) limit, ligand-to-metal charge-transfer (LMCT) bands would be expected to dominate the electronic spectrum of $IrBr_4^-$. Transitions would promote electron density from predominately ligand-based molecular orbitals to metal-based *d*-orbitals. Lower-energy transitions would involve promoting electron density into the doubly-degenerate *d*(*xz*) and *d*(*yz*) metal orbitals (e_g in the D_{4h} point group) and higher-energy

transitions to the $d(x^2\text{-}y^2)$ orbital (b_{1g} in the D_{4h} point group). In principle, *d-d* transitions should be in the same approximate energy range as the LMCT bands but are electric-dipole forbidden and should be of considerably weaker intensity. However, the situation changes considerably when the geometry distorts to the lower-symmetry D_{2d} point group. When this occurs, the number of irreducible representations is greatly decreased, allowing metal *d*-orbitals to mix with various ligand orbitals that would not transform together in the D_{4h} point group. Consequently, the allowed transitions cannot be described as of "purely" LMCT character but will also include character due to *d-d* transitions. Additionally, this mixing will result in a splitting of the ligand orbitals involved in the transitions, increasing the number of bands to be expected in the spectrum. It is likely that most of the observed features correspond to transitions that involve promoting electron density from mixed ligand-metal orbitals into either of the metal-based $d(x^2\text{-}y^2)$ or doubly-degenerate $d(xz)$ and $d(yz)$ orbitals.

5.3.2 Photodissociation spectra and fragment channels for $IrBr_5^-$

Following irradiation of $IrBr_5^-$, the two fragment ions observed are $IrBr_4^-$ and $IrBr_3^-$, corresponding to the loss of one and two neutral bromine atoms respectively. A search was conducted for Br^- fragment ions but none were found. As noted above, the low kinetic energy of Br^- upon formation will result in correspondingly low detection efficiencies. Taking this into consideration, Br^- may be an active fragmentation channel, but the present experiment does not allow for a definite conclusion.

Photodissociation spectra for $IrBr_5^-$ obtained by monitoring $IrBr_4^-$ and $IrBr_3^-$ fragment ions are shown in Figure 5.3. The spectrum obtained by monitoring the $IrBr_4^-$ fragment channel consists of four main peaks centered near 1.75, 2.05, 3.2, and 4.15 eV as well as a broad region of constant intensity between 2.25 and 2.8 eV. Following the peak at 4.15 eV, the ion signal decreases to zero and does not return at higher photon energies accessible in our experiment. The spectrum obtained by monitoring the $IrBr_3^-$ fragment channel is entirely different. This spectrum consists of one main feature; an onset and rise of fragment ion signal beginning near 4.0 eV that has several shoulders. Additionally, there are several very minor features that can be seen between 2.1 and 3.5 eV.

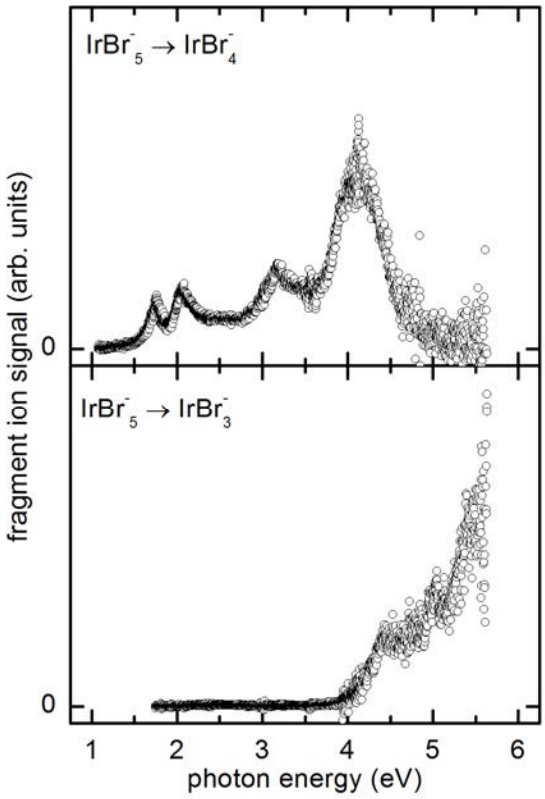

Figure 5.3. Photodissociation action spectrum of $IrBr_5^-$ obtained by monitoring $IrBr_4^-$ (top) and $IrBr_3^-$ (bottom) fragment ions as a function of photon energy.

In order to understand why these two action spectra are so different, we calculated the threshold energies for each fragment channel. These values are summarized in Table 5.2. The threshold energy for the $IrBr_4^-$ fragment channel, corresponding to the loss of a single, neutral bromine atom, is calculated to be 1.46 eV and below the onset of spectral features in the corresponding action spectrum. Assuming that fragment ions have a temperature of ~300 K, they should have a vibrational energy of approximately 0.22 eV and, with 1.5 *kT* of rotational energy, an internal energy of approximately 0.26 eV. This means that fragment ions should not be energetically accessible below ~1.2 eV. The second energetically accessible fragment channel corresponds to the loss of a single Br^- ion and has a calculated threshold at 2.3 eV. However, we did not observe this fragment channel in our experiment.

Table 5.2. Calculated threshold energies for various fragment channels resulting from photodissociation of $IrBr_5^-$. Channels corresponding to experimentally observed fragments are in bold.

$IrBr_5^-$ Photodissociation	
Fragment Channel	Energy [eV]
$IrBr_4^0 + Br^0 + e^-$	5.57
$IrBr_5^0 + e^-$	4.52
$IrBr_3^0 + Br^- + Br^0$	4.17
$IrBr_3^- + 2\ Br^0$	**4.16**
$IrBr_4^0 + Br^-$	2.31
$IrBr_4^- + Br^0$	**1.46**

The calculated threshold energy for the $IrBr_3^-$ channel, which corresponds to the loss of two neutral bromine atoms, is at 4.16 eV. This threshold value can be used to explain the drastic difference between the two action spectra obtained. In the vicinity of this threshold, the $IrBr_4^-$ channel dies out while the $IrBr_3^-$ channel grows in. At energies below the threshold, $IrBr_4^-$ should be the only energetically accessible fragment channel. Once this threshold is reached, loss of a second bromine atom becomes energetically possible, leading to the formation of $IrBr_3^-$. The fact that this switch in the active fragmentation occurs at energies slightly below the calculated threshold can be attributed to the roughly 0.26 eV of internal energy that the parent $IrBr_5^-$ ions should have prior to irradiation (assuming a parent ion temperature of 300 K). The decrease and ultimate disappearance of $IrBr_4^-$ fragment ion signal above this threshold can be explained by it having a reduced survival probability on the timescale of our experiment. If only a single bromine atom is lost at energies above this threshold, the produced $IrBr_4^-$ fragments should have a sufficient amount of energy remaining for further loss of a second bromine atom. Previous work by Rensing et al. on the fully coordinated species $IrBr_6^{2-}$ determined that certain electronic excitations will lead to dissociation on a timescale of ~79 ps.[10] If dissociation of $IrBr_5^-$ (including loss of a second bromine atom) proceeds by means of a similar mechanism, fragmentation can be expected to occur on a much faster timescale than the ~20 μs between irradiation and product ion mass analysis in our experiment. We have observed similar energy dependence in the UV photodissociation of $AuCl_4^-$ in recent work (see Chapter 6).

Consideration of the threshold for $IrBr_3^-$ formation also raises the question as to what the minor features are that appear between 3.1 and 3.5 eV in the $IrBr_3^-$ action spectrum since there is only enough energy for the loss of a single bromine atom at these energies. These features can be explained on the basis of two-photon effects. If two photons are absorbed by the $IrBr_5^-$ fragment prior to dissociation, there will be enough energy available for loss of two bromine atoms. Alternatively, it is possible that absorption of the first photon leads to dissociation of $IrBr_5^-$ into $IrBr_4^-$, which can then absorb a second photon and dissociate to form $IrBr_3^-$ product ions. Both possibilities are likely since both $IrBr_5^-$ and $IrBr_4^-$ have absorption features in this region of the spectrum (see above). Similar behavior has previously been observed for the related system $IrBr_6^{2-}$, where loss of multiple ligands was interpreted as a two-photon process.[6] Regardless of the actual mechanism, features due to the absorption of two photons should be much less intense than features arising from single photon processes. The low fragment ion intensity supports this explanation, but prevented fluence measurements.

As stated above when discussing $IrBr_4^-$, obtaining a detailed understanding of the electronic structure of hexabromoiridate complexes is non-trivial and beyond the scope of this study. However, several important insights can be made by considering a qualitative molecular orbital picture for $IrBr_5^-$. The lowest-energy structure for $IrBr_5^-$ is shown in Figure 5.4 and consists of a distorted square-based pyramid of double multiplicity. The distortions observed are most easily understood by considering the d^6 configuration of the complex. For simplicity, only σ-bonds are included at first and π-bonds are accounted for as a final consideration. Using this approach, the initial geometry that is considered has the iridium atom slightly above the plane made up of the four equatorial bromide ligands with the final, axial ligand above the iridium. This geometry, along with its metal-based molecular orbital diagram, is shown in Figure 5.4. The lowest of the *d*-block orbitals consists of a $d(xy)$ orbital, followed by a doubly-degenerate level made up of the $d(xz)$ and $d(yz)$ orbitals, the $d(z^2)$ and eventually the $d(x^2\text{-}y^2)$ orbitals at higher energies. Because of the d^5 configuration, the doubly-degenerate level will be the highest-occupied molecular orbital (HOMO) but will lead to fractional occupation numbers. This will cause the molecule to distort by increasing the bond angles between the axial Ir-Br bond and one of the two pairs of opposing equatorial Ir-Br ligand bonds so that the $d(xz)$ and

d(*yz*) orbitals split (see Figure 5.4). The good agreement between the calculated geometry and this qualitative molecular orbital picture as well as between the experimental and calculated threshold energies suggests that DFT is a reasonable method for these systems. However, two additional factors complicate the system considerably, making a detailed spectral analysis intractable.

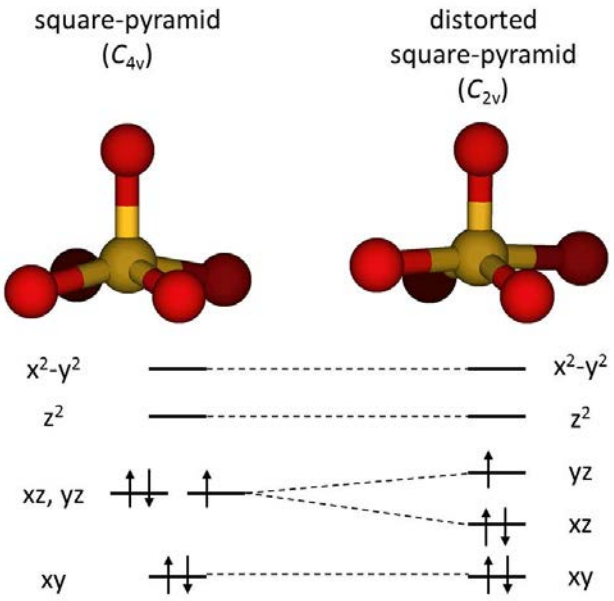

Figure 5.4. Two potential geometries of the $IrBr_5^-$ complex with their corresponding schematic molecular orbital energy diagrams. Note that the relative energies in each molecular orbital diagram are not to scale. The structure on the right, corresponding to a distorted square-pyramid with C_{2v} symmetry, is calculated to be the lowest energy geometry and has a doublet configuration.

Up until this point, ligand *p*-orbitals have not been considered. In principle, they should not provide a significant problem for analysis since they will simply cause a slight reordering of all metal-based molecular orbitals. However, the expected distortion of $IrBr_5^-$ will result in the molecule having C_{2v} symmetry, leading to a substantial degree of mixing between many of the molecular orbitals that would belong to different irreducible representations in a higher-symmetry point group. As in the case of $IrBr_4^-$, this will preclude assignments of transitions to purely LMCT or metal *d*-*d* character. However, the two remaining *d*-block orbitals, $d(z^2)$ and $d(x^2\text{-}y^2)$, are not expected to exhibit as much π-mixing with ligand p-orbitals as the *d*(xy), *d*(xz) and *d*(yz) orbitals. This means that the observed spectral features should still involve transitions to promote electron density into these orbitals (in addition to the singly-occupied HOMO),

similar to the transitions observed for the octahedral complex $IrBr_6^{2-}$.[6, 23] The main distinction would be the complexity of the low-lying orbitals involved in the $IrBr_5^-$ transitions.

5.3.3 Photo-induced dissociation mechanism

An important question to ask at this point concerns the mechanism by which bromoiridate dissociation occurs. At low energies, there is only enough energy available for $IrBr_5^-$ fragmentation to occur *via* loss of a single ligand. As soon as the loss of a second ligand becomes energetically accessible, this new channel turns on at the expense of the channel where only a single ligand is lost. The fact that this switching of the two channels occurs in the vicinity of the calculated fragmentation threshold suggests a thermal dissociation mechanism. This complementarity was not observed for the $IrBr_4^-$ ion. However, this is most likely due to the fact that the relevant threshold for loss of two ligands is calculated to be extremely close to the high-energy limit of our spectral range. Furthermore, no spectral features occur below the calculated threshold energy for loss of a single ligand. This, combined with the fact that $IrBr_4^-$ is expected to behave similarly whether it is a parent ion or an intermediate ion formed during dissociation of $IrBr_5^-$, implies that $IrBr_4^-$ also fragments *via* a thermal mechanism.

We have observed similar dissociation behavior for four-coordinate $Au^{(III)}$ complexes (see Chapter 6). Additionally, this mechanism is consistent with the one developed by Rensing et al. for the closely-related complex, $IrBr_6^{2-}$.[6] According to their mechanism, electronic excitation at 1.6 eV was followed by ultrafast, nonadiabatic relaxation into a vibrationally "hot" ground electronic state in which thermal, delayed emission of Br^- could occur. While the dissociation mechanism for $IrBr_5^-$ and $IrBr_4^-$ does agree with the mechanism for $IrBr_6^{2-}$ at 1.6 eV, it does not seem to agree with proposed mechanism for $IrBr_6^{2-}$ at higher photon energies. For photon energies in the range of ~3-5 eV, we previously proposed a direct dissociation mechanism for $IrBr_6^{2-}$, whereby fragmentation is likely to occur on a repulsive electronic curve (see Chapter 4).[23] The explanation for why two very different mechanisms are necessary to describe $IrBr_6^{2-}$ fragmentation in these two energy ranges had to do with the nature of the electronic transitions active in the two ranges. Low-energy features below ~3 eV in the $IrBr_6^{2-}$ spectrum have been assigned to LMCT bands where electron density is promoted from orbitals of predominately ligand character to the metal-based $t_{2g}(d)$ orbital that is typically regarded as a

non-bonding orbital where electron density is located primarily between the Ir-Br bond axes. On the other hand, high-energy features between ~3-5 eV were assigned to LMCT bands where electron density is promoted from ligand-based orbitals to the metal-based $e_g(d)$ orbital that is typically regarded as a strongly antibonding orbital where electron density is located along the Ir-Br bond axes. This electronic excited states prepared in this second set of transitions could then be interpreted as being more repulsive than those prepared in the first set. Since both $IrBr_5^-$ and $IrBr_4^-$ should to have both types of transitions within our spectral range (see above), they could be expected to fragment by direct, non-thermal mechanisms for a number of electronic transitions. However, it is important to note that $IrBr_6^{2-}$ is a dianion whereas $IrBr_5^-$ and $IrBr_4^-$ are not. The large amount strain present in $IrBr_6^{2-}$ due to intramolecular Coulomb repulsion should be substantially relieved by loss of a charged fragment ion. This high degree of strain should not be present in $IrBr_5^-$ and $IrBr_4^-$. Consequently, electronic excited states prepared by promoting electron density to the antibonding $e_g(d)$ orbital should not be as repulsive as in the case of $IrBr_6^{2-}$.

5.4 Conclusions

We have identified prominent fragment channels and obtained photodissociation spectra for the under-coordinated bromoiridate complexes $IrBr_5^-$ and $IrBr_4^-$. The fragment action spectra for the $IrBr_5^-$ parent ion are found to be highly energy dependent. Complementarity in the two fragment channels, combined with DFT-calculated threshold energies, implies a thermal fragmentation mechanism. Similar mechanisms are expected for the $IrBr_4^-$ parent ion since the onset of spectral features coincides with the calculated threshold for the lowest-energy fragment channel.

Features observed in the $IrBr_5^-$ and $IrBr_4^-$ photodissociation spectra are expected to be highly complicated due to factors such as spin-orbit coupling and relativistic effects. In addition, the open-shell configurations predicted for both species cause geometric distortions that decrease their molecular symmetry to low-order point groups. This will lead to significant mixing of ligand- and metal-based molecular orbitals, making assignment of spectral features non-trivial. However, the observed transitions are expected to promote electron density to the

metal-based $d(z^2)$ and $d(x^2\text{-}y^2)$ orbitals for $IrBr_5^-$ and to the metal-based $d(x^2\text{-}y^2)$ or doubly-degenerate $d(xz)$ and $d(yz)$ orbitals for $IrBr_4^-$.

5.5 References for Chapter 5

1. Wang, L.S., Ding, C.F., Wang, X.B., Nicholas, J.B., and Nicholas, B., "Probing the potential barriers and intramolecular electrostatic interactions in free doubly charged anions." *Physical Review Letters*, 1998. **81**(13): p. 2667.

2. Wang, X.B., Ding, C.F., and Wang, L.S., "Photodetachment spectroscopy of a doubly charged anion: Direct observation of the repulsive Coulomb barrier." *Physical Review Letters*, 1998. **81**(16): p. 3351.

3. Wang, L.S., Ding, C.F., Wang, X.B., and Barlow, S.E., "Photodetachment photoelectron spectroscopy of multiply charged anions using electrospray ionization." *Review of Scientific Instruments*, 1999. **70**(4): p. 1957.

4. Wang, X.B. and Wang, L.S., "Experimental search for the smallest stable multiply charged anions in the gas phase." *Physical Review Letters*, 1999. **83**(17): p. 3402.

5. Bojesen, G., Hvelplund, P., Jorgensen, T.J.D., and Nielsen, S.B., "Probing the lowest coordination number of dianionic platinum-cyanide complexes in the gas phase: Dynamics of the charge dissociation process." *Journal of Chemical Physics*, 2000. **113**(16): p. 6608.

6. Friedrich, J., Gilb, S., Ehrler, O.T., Behrendt, A., and Kappes, M.M., "Electronic photodissociation spectroscopy of isolated IrX_6^{2-} (X=Cl,Br)." *Journal of Chemical Physics*, 2002. **117**(6): p. 2635.

7. Boxford, W.E., El Ghazaly, M.O.A., Dessent, C.E.H., and Nielsen, S.B., "High-energy collision induced dissociation of iridium hexa-halide dianions: Observation of triple electron detachment and other decay pathways." *International Journal of Mass Spectrometry*, 2005. **244**(1): p. 60.

8. Loffler, D., Weber, J.M., and Kappes, M.M., "Photodetachment spectroscopy of $PtBr_4^{2-}$: Probing the Coulomb barrier of a doubly charged anion." *Journal of Chemical Physics*, 2005. **123**(22).

9. Burke, R.M., Boxford, W.E., Panja, S., Nielsen, S.B., and Dessent, C.E.H., "On the propensity for electron transfer in high-energy collisions of iridium complex anions with cesium atoms." *Chemical Physics Letters*, 2007. **442**(4-6): p. 201.

10. Rensing, C., Ehrler, O.T., Yang, J.P., Unterreiner, A.N., and Kappes, M.M., "Photodissociation dynamics of $IrBr_6^{2-}$ dianions by time-resolved photoelectron spectroscopy." *Journal of Chemical Physics*, 2009. **130**(23).

11. Boxford, W.E. and Dessent, C.E.H., "On the stability of $IrCl_6^{3-}$ and other triply charged anions: Solvent stabilization versus ionic fragmentation and electron detachment for the $IrCl_6^{3-}\cdot(H_2O)_n$ n=0-10 microsolvated clusters." *Journal of Physical Chemistry A*, 2005. **109**(26): p. 5836.

12. Langford, C.H. and Gray, H.B., *Ligand Substitution Processes*. 1966, New York, NY: W. A. Benjamin, Inc.

13. Miessler, G.L. and Tarr, D.A., *Inorganic Chemistry*. 2 ed. 1998, Upper Saddle River, New Jersey: Prentice-Hall.

14. Scheller, M.K., Compton, R.N., and Cederbaum, L.S., "Gas-phase multiply-charged anions." *Science*, 1995. **270**(5239): p. 1160.

15. Dreuw, A. and Cederbaum, L.S., "Nature of the repulsive Coulomb barrier in multiply charged negative ions (vol A63, art. no. 012501, 2000)." *Physical Review A*, 2001. **63**(4).

16. Dreuw, A. and Cederbaum, L.S., "Multiply charged anions in the gas phase." *Chemical Reviews*, 2002. **102**(1): p. 181.

17. Boxford, W.E., Pearce, J.K., and Dessent, C.E.H., "Ionic fragmentation versus electron detachment in isolated transition metal complex dianions." *Chemical Physics Letters*, 2004. **399**(4-6): p. 465.

18. Simons, J., "Molecular anions." *Journal of Physical Chemistry A*, 2008. **112**(29): p. 6401.

19. Wang, X.B. and Wang, L.S., "Photodetachment of free hexahalogenometallate doubly charged anions in the gas phase: ML_6^{2-}, (M=Re, Os, Ir, Pt; L=Cl and Br)." *Journal of Chemical Physics*, 1999. **111**(10): p. 4497.

20. Wang, X.B., Nicholas, J.B., and Wang, L.S., "Intramolecular Coulomb repulsion and anisotropies of the repulsive Coulomb barrier in multiply charged anions." *Journal of Chemical Physics*, 2000. **113**(2): p. 653.

21. Herzberg, G., *Atomic Spectra and Atomic Structure*. 2nd ed. 1944, New York, NY: Dover.

22. Haynes, W.M., ed. "CRC Handbook of Chemistry and Physics." 91 ed. 2010, CRC Press/Taylor and Francis: Boca Raton, FL.

23. Marcum, J.C. and Weber, J.M., "Electronic photodissociation spectra and decay pathways of gas-phase $IrBr_6^{2-}$." *Journal of Chemical Physics*, 2009. **131**(19).

24. Ahlrichs, R., Bar, M., Haser, M., Horn, H., and Kolmel, C., "Electronic-structure calculations on workstation computers - The program system TURBOMOLE." *Chemical Physics Letters*, 1989. **162**(3): p. 165.

25. Parr, R.G. and Yang, W., *Density-Functional Theory of Atoms and Molecules*. 1989, New York: Oxford University Press.

26. Becke, A.D., "Denisty-functional exchange-energy approximation with correct asymptotic-behavior." *Physical Review A*, 1988. **38**(6): p. 3098.

27. Lee, C.T., Yang, W.T., and Parr, R.G., "Development of the Colle-Salvetti Correlation-Energy Formula into a Functional of the Electron-Density." *Physical Review B*, 1988. **37**(2): p. 785.

28. Weigend, F., Haser, M., Patzelt, H., and Ahlrichs, R., "RI-MP2: optimized auxiliary basis sets and demonstration of efficiency." *Chemical Physics Letters*, 1998. **294**(1-3): p. 143.

29. Andrae, D., Haussermann, U., Dolg, M., Stoll, H., and Preuss, H., "Energy-adjusted ab-initio pseudopotentials for the 2nd and 3rd row transition-elements." *Theoretica Chimica Acta*, 1990. **77**(2): p. 123.

30. Deglmann, P. and Furche, F., "Efficient characterization of stationary points on potential energy surfaces." *Journal of Chemical Physics*, 2002. **117**(21): p. 9535.

31. Deglmann, P., Furche, F., and Ahlrichs, R., "An efficient implementation of second analytical derivatives for density functional methods." *Chemical Physics Letters*, 2002. **362**(5-6): p. 511.

32. Basch, H. and Gray, H.B., "Molecular Orbital Theory for Square-Planar Metal Halide Complexes." *Inorganic Chemistry*, 1967. **6**(2): p. 365.

33. Jean, Y., *Molecular Orbitals of Transition Metal Complexes*. 2005, New York: Oxford University Press Inc.

6 Transition Metal Complexes III: $AuCl_n(OH)_m^-$

This chapter has been reproduced in part with permission from Marcum, J.C., Kaufman, S.H., and Weber, J.M., "Gas-Phase Experiments on Au(III) Photochemistry." *Journal of Physical Chemistry A*, 2011. dx.doi.org/10.1021/jp200797v. Copyright 2011 American Chemical Society.

6.1 Background

Studies of transition metal salts in solution are often complicated due to the large number of relevant species simultaneously present under a given set of conditions as well as by overlapping spectral signatures that make confirmation of individual components difficult. In order to better understand and control the details of speciation, it is advantageous to study the relevant complexes as isolated species in the gas-phase. This approach can provide spectroscopic and thermodynamic information about individual species without interference from other components in solution including counterions or even the solvent itself.

One transition metal complex that has received much attention due to its importance in the transport and deposition of gold in geochemical processes [1-8], as well as its widespread use in various chemical and photochemical reactions, is the anion tetrachloroaurate(III), $AuCl_4^-$. Most notably, $AuCl_4^-$ has been used in the synthesis of gold nanoparticles.[9-14] While many common synthetic approaches use wet chemistry to reduce $Au^{(III)}$ for nanoparticle formation, photoreduction is also used in a number of syntheses.[15] In particular, several recent studies have attempted to exploit photochemical approaches to nanoparticle synthesis and have focused on determining mechanistic information pertaining to $AuCl_4^-$ photochemistry.[16-19] These studies have led to the development of a general framework for the mechanisms but they disagree with each other on a number of important questions, in particular those pertaining to the reduction of gold. In early work by Kurihara et al., a mechanism was developed in which irradiation of $Au^{(III)}Cl_4^-$ resulted in simultaneous dissociation and gold reduction, forming $Au^{(II)}Cl_3^-$ and neutral Cl as products.[16] Further reduction of gold would then occur by a combination of disproportionation step that converts $Au^{(II)}Cl_3^-$ into $Au^{(III)}Cl_4^-$ and $Au^{(I)}Cl_2^-$ as well as a subsequent photodissociation and reduction step that converts $Au^{(I)}Cl_2^-$ to neutral gold atoms. Implicit in this mechanism is the formation of a caged complex immediately

following dissociation of $AuCl_4^-$. More recent work by Eustis et al. made several modifications to this mechanism that involved a stronger emphasis on the disproportionation reactions as well as a solvent-mediated photoreduction step in which glycol acts as a reducing agent.[17-18] Work by Harada et al. developed similar mechanisms but suggested that the reduction of $Au^{(I)}Cl_2^-$ to neutral gold atoms may take place *via* a sequence of radical reactions that are facilitated by the solvent.[19] While these studies established benchmarks for $AuCl_4^-$ photochemistry, none con unambiguously pinpoint the role of solvent or the detailed molecular-level mechanism of gold reduction.

One factor that complicates the chemistry and photochemistry of $Au^{(III)}$ is its speciation. In aqueous solution, the gold in tetrachloroaurate may undergo one of several changes in complexation through ligand exchange between Cl^- and available OH^- to form species of the form $AuCl_n(OH)_{4-n}^-$.[1-8] As expected, the extent of ligand exchange that occurs will depend upon the relative activities of Cl^- and OH^- in solution and will thus be highly affected by the solution pH and chloride ion concentration. For a given chloride ion activity, solutions with low pH values will tend to favor $AuCl_4^-$ as the dominant species while those with high pH values will tend to favor $Au(OH)_4^-$. Solutions of intermediate pH should consist of several mixed chloro-hydroxy species. Increasing the chloride ion activity will result in suppressing ligand exchange so that higher pH values are necessary to form gold-hydroxy species.[6] The details of the solution involved will dictate the nature of gold speciation and could lead to important consequences for synthetic methods as well as for the geochemical transport and deposition of gold.

Because these solutions have the potential for such high complexity, condensed-phase studies of gold photochemistry and speciation can be notably difficult. To address this issue, we studied $AuCl_4^-$ and its hydrolysis products as isolated species in the gas-phase using electrospray ionization mass spectrometry and ultraviolet photodissociation spectroscopy. We make spectral assignments for $AuCl_4^-$ and $AuCl_2(OH)_2^-$ based on a molecular orbital approach for square planar d^8 complexes to help elucidate the possible nature of the reduction process. Comparison of experimental data with calculated fragment thresholds allows us to understand how dissociation and reduction processes occur in the absence of solvent. By additional

comparison with computational results that utilize a conductor-like screening model to include solvent effects, we are able to gain greater insight into the role solvent plays in photodissociation and reduction.

6.2 Methods

6.2.1 Photodissociation spectra

The experimental methods used in this work are described in detail in Chapter 2 of this thesis. Due to the possibility of ligand exchange, aqueous solutions containing only $KAuCl_4$ are acidic. Mixed ligand species were produced by varying the pH of an aqueous solution containing tetrachloroaurate. For solutions with higher pH, a solution was made by dissolving 1-3 mg of potassium tetrachloroaurate(III) hydrate ($KAuCl_4 \cdot xH_2O$, Alfa Aesar) in 1 mL of ~15 mM aqueous solution of NaOH (Fisher Scientific, reagent grade). The pH of the solution was monitored using pH-indicator strips (colorpHast; pH 0-14 and pH 2.0-9.0) and adjusted by adding small (~10 µL) aliquots of ~1 M aqueous sodium hydroxide solution.

Due to the high reduction potential of gold in the various complexes, using an aqueous solution of the $Au^{III)}$ complexes for electrospray is non-trivial. The ions of interest are anions so electrospray ionization is performed in negative ion mode with needle voltages typically at or around -2000 V. These high negative voltages cause gold to be reduced and lead to the formation of gold colloids and/or particles that can be as large as 100 µm in diameter. Consequently, the electrospray needle rapidly becomes clogged, which limits and eventually stops the flow of solution through the needle and preventing the electrospray process from occurring. In principle, this situation could be circumvented by using an alternate solvent that would not facilitate reduction as easily. This approach was used for investigations of the tetrachloroaurate(III) ion, $AuCl_4^-$, by performing electrospray from an ~5 mM solution of $KAuCl_4 \cdot xH_2O$ dissolved in acetonitrile (Sigma, reagent grade). However, this approach is not practical for the study of the mixed chloro-hydroxy species since water is necessary for hydrolysis to take place. To be able to form the species of interest while hindering the clogging process, we performed electrospray ionization from aliquots containing 75 µL of the pH-

adjusted aqueous solutions (see above) with 75 µL of acetonitrile (Sigma, reagent grade). All aliquots were used within one hour of being prepared.

6.2.2 Aqueous absorption spectra

An aqueous absorption spectrum of $AuCl_4^-$ was obtained for an ~16 µM solution of $KAuCl_4 \cdot xH_2O$ (Alfa Aesar) dissolved in ~0.05 M aqueous HCl solution. The pH of the solution was kept below 2 to ensure that no hydrolysis occurred. The spectrum was taken using a Varian Cary 500 Scan UV-Visible-NIR spectrometer (version 8.01) with a 10 mm path length, 1 nm step size, 2 nm bandwidth, and an integration time of 0.1 sec.

6.2.3 Computational

In order to determine theoretical thresholds for fragmentation channels, geometry optimizations were performed on the parent as well as all fragment ions using the TURBOMOLE V5.9.1 and V6.2 suites of programs.[20] We employed density functional theory (DFT)[21] with the B3LYP[22-23] and PBE0[24] functionals and a def2-TZVPP basis set[25] for all atoms. Computational results obtained using the PBE0 functional are provided in Appendix A. Scalar relativistic effects were taken into account for gold using the def2-ecp effective core potential (multielectron fit to Wood-Boring orbital energies).[26] Vibrational frequencies were calculated using analytical second derivatives.[27-28] The obtained frequencies were used to correct the calculated gas-phase thresholds for zero-point energy. For comparison with apparent experimental thresholds, the vibrational energy content of the ions needs to be taken into account. The average vibrational energy of parent ions was determined using the equation

Equation 6.1

$$U_{vib} = \sum_i \frac{h\nu_i}{(e^{h\nu_i/kT} - 1)}$$

where ν_i represents the frequencies of the individual vibrational modes, *h* is Planck's constant, *k* is Boltzmann's constant, and *T* is the temperature of the ions. Because ions are accumulated in a room-temperature hexapole ion trap, we assume the ion temperature to be 300 K. The orbital character of the transitions was determined using time-dependent density functional theory (TDDFT)[29-30] utilizing the B3LYP functional. (Results obtained using the PBE0 functional are provided in Appendix A)

In order to determine the effect of solvation on threshold energies, the conductor-like screening model (COSMO) was used,[31] employing a dielectric constant of 80.1 (corresponding to water at 20°C) and a molecular-shaped cavity constructed using radii of 3.05 Å for chlorine, 2.82 Å for oxygen, 2.39 Å for hydrogen, and 2.96 Å for gold. These values were obtained by adding a solvation radius of 1.3 Å to the atomic radius for each element.[32] The COSMO results are presented without zero-point corrections.

6.3 Results and discussion

6.3.1 Mass spectra

Figure 6.1 depicts a mass spectrum of $AuCl_4^-$ obtained following electrospray ionization (ESI) of potassium tetrachloroaurate hydrate dissolved in acetonitrile as well as the relevant sections of mass spectra obtained using electrospray of an ~5 mM potassium tetrachloroaurate solution with a pH between 6 and 7 (see §6.2.1 for more details on the solution used). These spectra clearly show the presence of mixed chloro-hydroxy species in the pH-adjusted aqueous solution resulting from ligand exchange between chloride and hydroxide ions. The absence of $Au(OH)_4^-$ in these spectra is likely due to the pH of the solution used. This is corroborated by the comparatively low abundance of $AuCl(OH)_3^-$, which should also require a high solution pH to be present in significant amounts.[2, 6, 8] No explicit search for $Au(OH)_4^-$ was conducted.

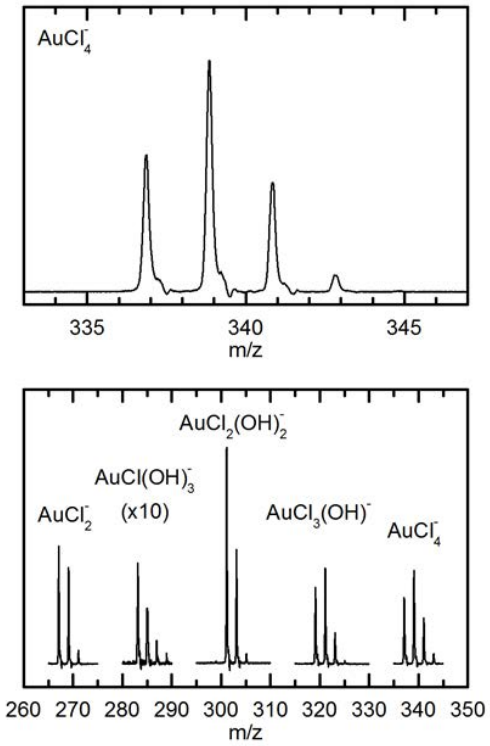

Figure 6.1. Top: Mass spectrum of $KAuCl_4$ dissolved in acetonitrile depicting the signal for the tetrachloroaurate ion. Bottom: Sections of mass spectra for a 1:1 mixture of acetonitrile and a pH adjusted (6-7) aqueous solution of $KAuCl_4$. Mixed chloro-hydroxy species result from the hydrolysis of the tetrachloroaurate ion.

The presence of $AuCl_2^-$ in the mass spectra can be explained by several possibilities. First, it is possible that it is present in solution as a stable species. This idea has been explored on many occasions by a number of researchers and is quite controversial.[1-7] Alternatively, $AuCl_2^-$ could be produced in solution as a transient photoproduct following exposure of the mixture to light.[16-19] Since we typically exercise caution to ensure that the solutions for electrospray are protected from light exposure, we do not believe this to be responsible for the presence of $AuCl_2^-$ in our mass spectra. Additionally, $AuCl_2^-$ could be formed during the electrospray process itself as the ionic strength of the shrinking droplets reaches extreme values. A final possibility is that $AuCl_2^-$ is formed as a fragment ion within the initial stages of our mass spectrometer. It is expected that the ions do not reach thermal equilibrium until they are held within the hexapole ion trap so it is possible for fragmentation to occur prior to trapping. Because of the last two possibilities, we cannot infer the presence of $AuCl_2^-$ in solution from its presence in ESI mass spectra.

While several of the chloro-hydroxy species were observed in this experiment, the difficulties associated with preparing electrospray solutions for these ions (see §6.2.1) result in ion signals that are not stable over long periods of time. The mixed chloro-hydroxy complex that proved to be the most stable in our instrument was the disubstituted species $AuCl_2(OH)_2^-$. It was possible to maintain a stable signal of this ion for times approaching one hour, sufficient to obtain photodissociation spectra. All other mixed species were not stable for long enough periods of time to acquire spectra or determine photoproducts.

6.3.2 Photodissociation spectra and fragment channels for $AuCl_4^-$

The only fragment ions observed following irradiation of $AuCl_4^-$ were $AuCl_3^-$ and $AuCl_2^-$. These channels correspond to the loss of one and two neutral Cl atoms, respectively. An exhaustive search for Cl^- fragment ions was conducted but none were found. However, due to the low kinetic energy of Cl^- photoproducts and their correspondingly low detection efficiency, we cannot rule out that they are generated as a minor fragment channel. All observed product ions should be accompanied by corresponding neutral fragments. However, the current experimental setup does not allow for selective identification of these species.

A photodissociation depletion spectrum of $AuCl_4^-$ is shown in Figure 6.2 along with an absorption spectrum of $KAuCl_4$ in aqueous HCl solution for comparison. At first glance, the gas-phase depletion spectrum appears to be remarkably similar to the aqueous absorption spectrum, suggesting that the nature of the electronic transitions does not change significantly upon solvation. Both spectra include a high-energy peak between 5 and 6 eV and a smaller, low-energy peak between 3.5 and 4.5 eV. Upon closer inspection, it is clear that the peak between 3.5 and 4.5 eV also includes a leading, low-energy component that is present at energies as low as 3.0 eV. While there are obvious similarities between the depletion and aqueous absorption spectra, several differences can be seen. Both of the main features show slight solvatochromic shifts. The low-energy peak, which has a maximum at ~3.85 eV in the gas-phase spectrum, is shifted by ~0.1 eV toward higher energies upon solvation. The high-energy peak shifts from ~5.40 eV in the gas-phase spectrum to ~5.49 eV in the aqueous absorption spectrum. Additionally, the high-energy peak shows a low-energy shoulder located between 5.1 and 5.2 eV, whereas this feature is not apparent in the aqueous absorption spectrum.

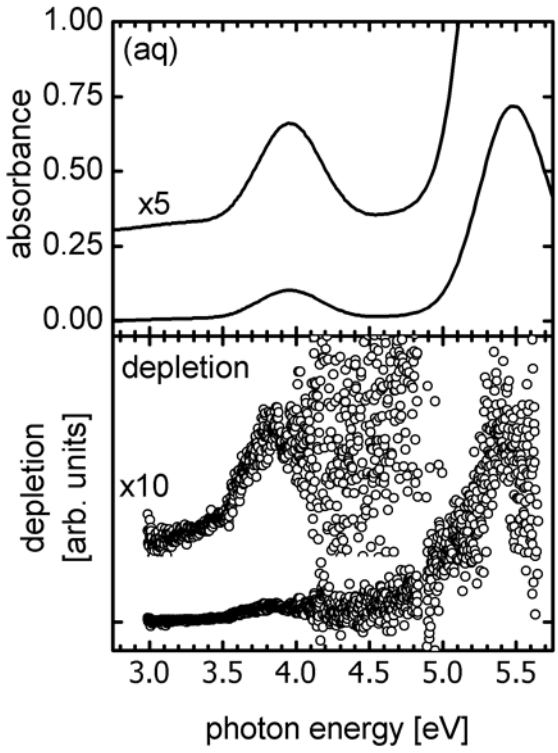

Figure 6.2. Electronic spectra of $AuCl_4^-$. Magnified versions of spectra are included as insets to highlight spectral details. Top: absorption spectrum of $KAuCl_4$ taken in aqueous HCl solution to suppress hydrolysis. Bottom: Photodissociation spectrum of gas-phase $AuCl_4^-$ obtained by monitoring the loss of parent ion. The rapid change in the signal-to-noise level that occurs in the depletion spectrum near 4.1 eV is attributed to a switch in the configuration of the laser system to a region where we have less photon flux.

It is instructive to consider the nature of the electronic transitions observed in the photodissociation spectra to better understand the fragmentation processes and connect our results to previous theoretical approaches used to interpret spectral features. Rough spectral assignments can be made by comparison to condensed-phase data and by using an approach based upon molecular orbital theory of a square-planar transition metal complex with a d^8 electron configuration and contributions from π-backbonding.[33-35] In this description, the highest-energy medal *d*-orbitals are expected to be ordered in terms of their energies as $(z^2) < (xz),(yz) < (xy) < (x^2\text{-}y^2)$ (see Figure 6.3). Our calculations predict a slightly different ordering (see Appendix A), but the differences do not affect the interpretation of the observed spectral features. Of these orbitals, the $d(x^2\text{-}y^2)$ is the lowest unoccupied molecular orbital (LUMO) and all other orbitals are doubly occupied (Figure 6.3), leading to a singlet ground state configuration. Mixed with these orbitals are a number of occupied, non-bonding, ligand-based

orbitals as well as orbitals that arise from the interaction of chloride 3*p* orbitals with the gold 5*d* and 6*p* orbitals. While these ligand-based orbitals are expected to lie primarily below the metal *d*-orbitals, some of them may have higher energies, depending on the species in question.[34-35] In gold, the metal *d*-orbitals do not all lie above the occupied ligand-based orbitals, presumably due to its increased ability to accept electrons (in comparison to other noble metals such as Pt and Pd), which could stabilize the metal-based orbitals.[33] Absorptions due to *d*-*d* transitions are electric dipole-forbidden and should be considerably weaker than transitions due to ligand-to-metal charge transfer (LMCT). Consequently, the LMCT bands (which have energies similar to some of the *d*-*d* transitions) are expected to dominate the spectrum. The dominant transitions in condensed-phase $AuCl_4^-$ spectra have been assigned as LMCT bands between ligand-based p_π and p_σ orbitals to the LUMO that occur at 3.93 and 5.49 eV respectively.[36-38] The low-energy shoulder of the 3.93 eV peak was suggested to be due to a *d*-*d* transition (originally described as a crystal field band) of significantly lower intensity than the LMCT bands. Our own analysis of these transitions using TDDFT predicts similar transitions (Figure 6.3). The dominant LMCT bands predicted by TDDFT involve a shift in electron density from ligand-base molecular orbitals with e_u symmetry (doubly degenerate) to the LUMO of the complex that is an antibonding orbital of b_{1g} symmetry that consists of the gold $5d(x^2\text{-}y^2)$ orbital and chlorine 3*p* orbitals. Both of these transitions are of the type $^1E_u \leftarrow {}^1A_{1g}$ in the D_{4h} point group. While TDDFT adequately predicts the orbital character of the LMCT transitions and their contributions to the overall shape of the spectrum, the calculated transition energies do not accurately match the experimental data and were strongly dependent upon the density functional that was used (see Appendix A). We assign the high-energy peak between 5 and 6 eV to the $^1E_u \leftarrow {}^1A_{1g}$ transition and the low-energy peak between 3.5 and 4.5 eV to the transition $^1E_u' \leftarrow {}^1A_{1g}$. While we cannot make any definitive assignments for the low-energy shoulders of each peak, it is very likely that they could be due to lower intensity *d*-*d* transitions or splitting from spin-orbit coupling.

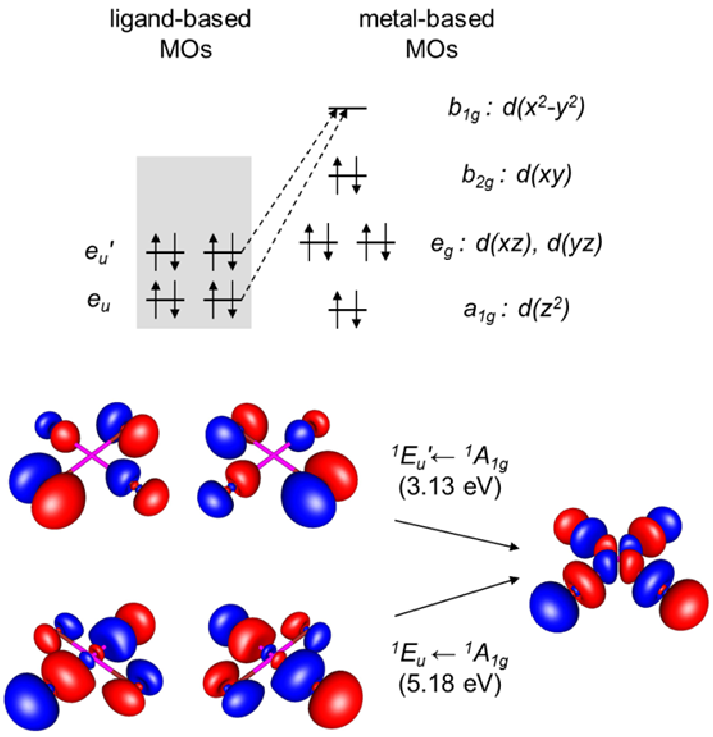

Figure 6.3. Top: Schematic molecular orbital energy levels for $AuCl_4^-$ as a square planar d^8 metal complex with π-backbonding (not to scale, see Appendix A). The gray shaded area represents the approximate energy region where a number of ligand-based MOs are located. The ligand-based levels that are schematically depicted are for the e_u orbitals involved in the charge-transfer transitions observed in our spectra (dashed arrows). Bottom: Contour plots of the molecular orbitals involved in the observed transitions along with transition energies calculated using TDDFT with the B3LYP functional and a def2-TZVPP basis set.

Photodissociation action spectra for both observed fragment channels, as well as the photodissociation depletion spectrum for comparison, are shown in Figure 6.4. Fragment ion intensities have been scaled to reflect the relative branching ratios measured at 3.75 eV (~35% $AuCl_2^-$; ~65% $AuCl_3^-$). The action spectra reveal that the fragmentation branching ratios are highly energy-dependent. The $AuCl_2^-$ channel contains many of the features present in the depletion spectrum. There is a peak between 3.5 and 4.5 eV as well as a much larger peak at ~5.4 eV that includes a low-energy shoulder between 5.1 and 5.2 eV. The only notable difference is that the low-energy peak in the $AuCl_2^-$ action spectrum has its maximum at a slightly higher energy than the corresponding peak in the depletion spectrum. The $AuCl_3^-$ channel shows drastically different behavior. It has an onset near 3.0 eV and reaches a peak at ~3.83 eV. The signal then rapidly drops off and is completely gone by ~4.2 eV and does not return within the spectral range of the experiment. This contrasting behavior implies that the

two fragment action spectra are complementary to one another. The $AuCl_3^-$ channel has an earlier onset, is the dominant channel at lower energies and is eventually overcome as the $AuCl_2^-$ channel becomes the dominant (and only active) channel at higher energies. This observation helps to explain the apparent differences between the $AuCl_2^-$ fragment action and the depletion spectra. The switch from $Au^{(II)}Cl_3^-$ to $Au^{(I)}Cl_2^-$ as the dominant fragment species occurs within the spectral region of the peak around 3.8 eV. The presence of this feature in the depletion spectrum is due to formation of *both* product ions, the lower-energy part corresponding to formation of $Au^{(II)}Cl_3^-$ and the higher-energy part to $Au^{(I)}Cl_2^-$ formation. As a consequence, this low-energy feature has slightly different peak energies in all three spectra.

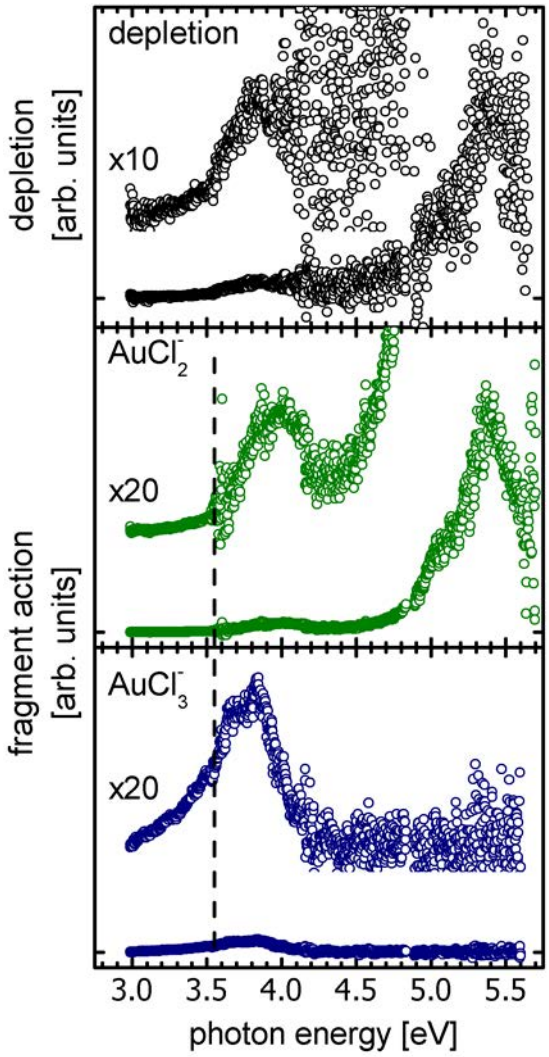

Figure 6.4. Gas-phase electronic spectra of $AuCl_4^-$. Magnified versions of spectra are included as insets to highlight spectral features. Fragment action spectra have been scaled to reflect their relative branching ratios. A dashed line has been included that corresponds to the threshold energy for the $AuCl_2^-$ channel (3.54 eV) calculated using the B3LYP functional. Top: Depletion spectrum of $AuCl_4^-$. Middle: Photodissociation action spectrum obtained by monitoring the fragment ion $AuCl_2^-$. Bottom: Photodissociation action spectrum obtained by monitoring the fragment ion $AuCl_3^-$.

To help understand the energy dependence of fragmentation, we calculated threshold energies for each fragment channel using density functional theory. The results from these calculations are depicted graphically in Figure 6.5 (a table of all calculated threshold energies for $AuCl_4^-$, including results obtained using the PBE0 functional, are provided in Appendix A). As expected, the lowest threshold energy corresponds to the loss of a single, neutral chlorine atom since it involves breaking only one chemical bond. Additionally, the fact that the channel corresponding to loss of a single Cl atom is lower than the loss of a single Cl^- ion can be

attributed to $AuCl_3$ having a higher electron affinity than Cl. Since the $AuCl_3^-$ + Cl fragmentation threshold energy (2.34 eV) is significantly below any spectral features of the parent ion, fragmentation into $AuCl_3^-$ should be energetically possible following absorption at any wavelength in the current experiment. This is not the case for the $AuCl_2^-$ channel since it is formed *via* the loss of two neutral chlorine atoms and has a higher threshold of 3.54 eV. Formation of $AuCl_2^-$ fragments should not be observed until the corresponding threshold is reached. As can be seen in Figure 6.4, the onset of $AuCl_2^-$ occurs at energies slightly lower than the calculated threshold. This early onset can be explained by considering that the ions should be roughly at room temperature following the electrospray process and will possess a substantial amount of internal energy. Based on the calculated harmonic frequencies of $AuCl_4^-$, parent ions should have an average vibrational energy of approximately 0.14 eV at 300 K. By also considering an average rotational energy of 1.5 *kT*, the total internal energy of parent ions will be approximately 0.18 eV. This excess energy makes dissociation energetically accessible, even when photon energy is slightly below a particular fragmentation threshold.

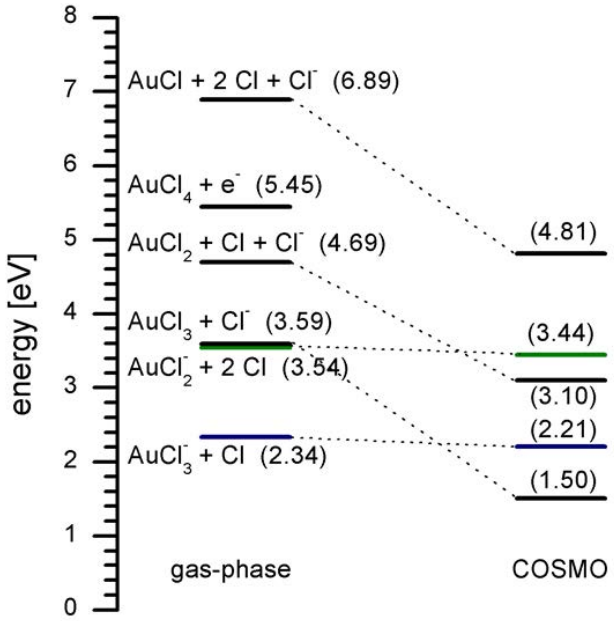

Figure 6.5. Threshold energies for various fragment channels calculated using DFT with the B3LYP functional and a def2-TZVPP basis set. Energies for the gas-phase (left) and using COSMO to account for solvent effects (right). Threshold energies for the fragment channels observed in the present experiment are depicted in color to match the photofragment action spectra for the respective channels in Figure 6.4. Additional computational results obtained using the PBE0 functional can be found in Appendix A.

The disappearance of the $AuCl_3^-$ channel as the $AuCl_2^-$ channel turns on in the threshold region for $AuCl_2^-$ is very different from the behavior of the transition metal complex $IrBr_6^{2-}$, where some electronic transitions couple to specific fragmentation channels (see Chapter 4).[39] The fragment-specific coupling in $IrBr_6^{2-}$ was suggested to be due to the very different nature of the excitations, where different groups of transitions involved shifting electron density from ligand-based molecular orbitals into one of several different metal-based orbitals, each with very different bonding character. In the present study, both of the dominant LMCT transitions shift electron density from ligand-based orbitals into the same metal-based orbital (see Figure 6.3) so the different transitions are not expected to demonstrate coupling to specific fragment channels.

As mentioned above, at photon energies below the threshold for $AuCl_2^-$ formation only $AuCl_3^-$ should be observed since it is the only fragment ion that is energetically accessible. Above this threshold it is possible to lose either one or two chlorine atoms. However, in the event that a single chlorine atom is lost at energies above the threshold for $AuCl_2^-$ formation, there should still be a sufficient amount of energy remaining in the $AuCl_3^-$ fragment ion for the loss of a second chlorine atom. As long as the timescales for loss of the second chlorine atom is short compared to the timescale between irradiation and fragment ion mass analysis, the survival probability of $AuCl_3^-$ above this threshold should be comparatively small, and $AuCl_2^-$ should be the preferred fragment channel. Experiments on the anion $IrBr_6^{2-}$ showed that certain electronic excited states were found to decay back into a vibrationally hot ground electronic state in ~20 ps followed by thermal dissociation into the fragments $IrBr_5^-$ and Br^- in ~80 ps.[40] If fragmentation of $AuCl_4^-$ occurs *via* a similar mechanism, the dissociation timescale will be sufficiently shorter than the ~20 μs between irradiation and fragment ion mass analysis in our experiment. Additionally, these relative timescales are different enough that any effects due to a kinetic shift should be insignificant. The experimental results are consistent with a fragmentation mechanism that involves thermal dissociation of a vibrationally hot molecule. However, we cannot infer from our data whether the dissociation takes place on the electronic ground state surface or on a low-lying excited state. Similarly, it is not possible to determine whether one of the ligands dissociates from a repulsive electronic excited state.

While fragmentation *via* loss of neutral chlorine atoms seems to be the dominant mode of fragmentation, there is still a question of the role played by other fragment channels. As mentioned above, Cl^- ions could not be found, despite the fact that two fragment channels leading to Cl^- should be energetically accessible in our experiment (see Figure 6.5). One might expect that the $AuCl_3^-$ and $AuCl_2^-$ channels may become inactive or decrease in importance as these other fragmentation thresholds are reached. This does not seem to be the case since we do not observe changes in the fragment action in the vicinity of these thresholds. One possible reason for the absence of Cl^- fragments is that the electronic states involved exclusively couple to channels where the excess electron remains on the gold complex. Another explanation is the preferential loss of neutral Cl atoms due to kinetic effects where loss of Cl^- ions occurs far too slowly to be a competitive fragment channel.

6.3.3 Photodissociation spectra and fragment channels for $AuCl_2(OH)_2^-$

In order to understand the spectroscopy and thermodynamics of the disubstituted chloro-hydroxy compound, it is necessary to consider the different possible isomers. As described above, $Au^{(III)}$ has a d^8 electron configuration and, in the presence of four ligands, adopts a square-planar geometry.[41-42] This results in the possibility of both *cis*- and *trans*- isomers for the $AuCl_2(OH)_2^-$ complex. Additionally, rotation of the OH groups about the Au-O bonds will result in several conformers for each of the two isomers where the O-H bonds point in different directions. Structures for all isomers are depicted in Figure 6.6 and their relative energies calculated using density functional theory with the B3LYP functional are collected in Table 6.1 (all calculated energies, including those determined using the PBE0 functional, can be found in supplementary information). Isomers are named according to their *cis*- or *trans*- configuration as well as the relative orientation of the hydroxyl groups. Conformers for which the hydroxyl groups point in opposite directions (one clockwise and one counter-clockwise) are referred to as *–hetero* whereas conformers with the hydroxyl groups pointing in the same direction are referred to as *–homo*. The relative ordering energies can be explained by considering the intramolecular hydrogen bonding and dipole-dipole interactions of the hydroxyl groups. Isomers that permit a homodromic arrangement of the hydroxyl groups are stabilized by cooperative effects and are lower in energy. This behavior is reminiscent of that observed in

cluster studies in which water has a propensity to form cyclic structures. The isomer for which these interactions are optimized is the *cis-homo* isomer where two hydroxyl groups can interact directly. This isomer is thus lowest in energy. In contrast, the highest-energy isomer, *trans-hetero*, benefits least from H-bonding or dipole-dipole interactions.

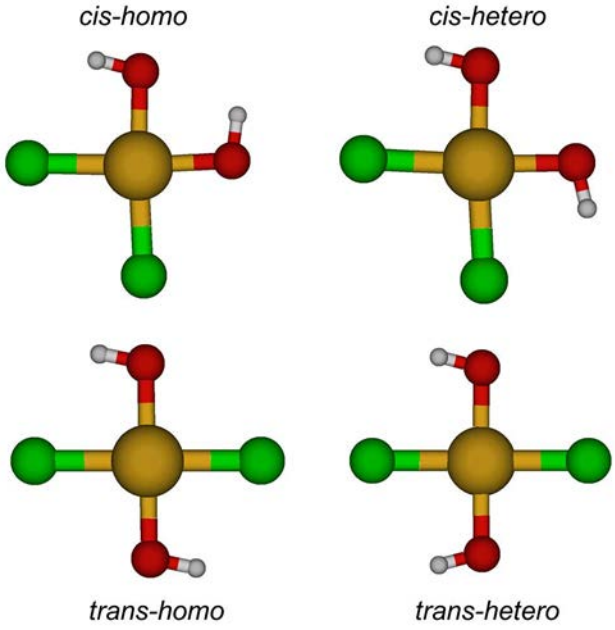

Figure 6.6. Isomers of $AuCl_2(OH)_2^-$. Convention for naming can be found in the text.

Table 6.1. Table of relative energies calculated using the B3LYP density functional and corresponding Boltzmann populations for isomers of the $AuCl_2(OH)_2^-$ ion (results obtained using the PBE0 functional can be found in Appendix A).

	B3LYP			
	Relative Energy [meV]		Boltzmann Population	
Isomer	Gas-Phase	COSMO	Gas-Phase	COSMO
cis-homo	0	7	1.00	0.76
cis-hetero	5	0	0.84	1.00
trans-homo	34	15	0.27	0.57
trans-hetero	70	18	0.07	0.50

Based on the calculated energies, it is possible to obtain Boltzmann factors to determine the approximate relative populations of each isomer in our experiment (Table 6.1). However, these values assume that thermal equilibrium between the four isomers is established in the

gas-phase. This is probably not the case since *cis-trans* isomerization involves ligand migration and is unlikely to occur in the gas-phase. Since our experiment utilizes electrospray ionization to promote ions into the gas-phase, the distribution of isomers should be reminiscent of the thermal equilibrium that is established in aqueous solution. In order to account for solvent effects, we determined the relative energies of each isomer using COSMO calculations. This model only takes into account the dielectric polarizablity of the solvent and does not include structural effects such as hydrogen bonding. Consideration of these continuum solvent effects results in a slight reordering of the relative energies as well as a smaller energy range between each of the isomers, presumably because the cooperative effects play a less important role when compared to interactions with the solvent. Using these calculated energies leads to relative populations that are much more comparable to one another than those obtained using the calculated gas-phase energies (Table 6.1). Furthermore, inclusion of solvent structural effects such as hydrogen bonding is expected to deemphasize the intramolecular interactions even further, resulting in a much tighter relative energy gap and, consequently, very similar relative populations in solution. Thus the four isomers are expected to have similar relative populations in the gas-phase as well.

The two fragment ions observed following UV-irradiation of $AuCl_2(OH)_2^-$ were $AuCl_2^-$ and $AuClOH^-$. Both of these channels correspond to loss of two neutral ligands, a single chlorine and a hydroxyl in the case of $AuClOH^-$ and two neutral hydroxyls in the case of $AuCl_2^-$. No Cl^- or OH^- ions were detected. As noted above, the low kinetic energy of these low-mass fragment ions is expected to result in low detection efficiencies and we thus cannot rule out that they are generated as minor photoproducts. An interesting point to note (which is explained below) is that no fragment channels corresponding to the loss of a single ligand are observed.

Photodissociation spectra obtained by monitoring each fragment channel are shown in Figure 6.7. Both gas-phase spectra contain two main features: a low-energy peak centered near 4.5 eV and a higher-energy peak centered around 5.4 eV that has a pronounced low-energy shoulder near 5.1 eV. A rigorous interpretation of these features is difficult since there are likely to be four isomers present in our experiment, most of which belong to different

symmetry point groups. However, a zeroth-order approach can be used in which the identity and directionality of the ligands is ignored and the molecule is treated as D_{4h} so that a comparison can be made to data for $AuCl_4^-$ (see §6.3.2). Using this analogy, the absorptions observed for $AuCl_2(OH)_2^-$ should be due to LMCT bands where electron density is shifted from orbitals that are associated predominately with the ligands to the LUMO of the complex that consists of an antibonding σ^* orbital made up of ligand p orbitals and the metal $d(x^2\text{-}y^2)$ orbital (see §6.3.2).

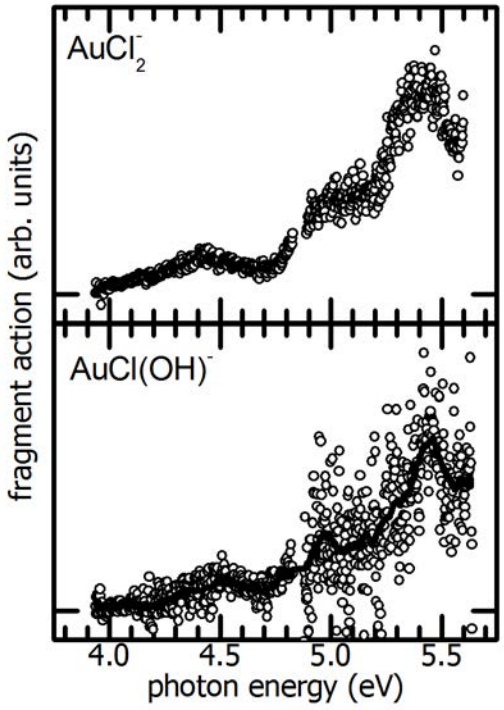

Figure 6.7. Top: Photodissociation action spectrum of $AuCl_2(OH)_2^-$ obtained by monitoring the fragment ion $AuCl_2^-$ (loss of two OH ligands). Bottom: Photodissociation action spectrum of $AuCl_2(OH)_2^-$ obtained by monitoring the fragment ion $AuClOH^-$ (loss of one Cl and one OH ligand). The full, black line is a sliding average over 0.1 eV to guide the eye.

Inclusion of the hydroxide ligands perturbs this zeroth-order picture in two distinct ways. The first effect of ligand exchange involves the relative energies of all molecular orbitals involved. In the language of ligand-field theory, hydroxide is a stronger-field ligand than chloride and will lead to a greater orbital splitting. This increased splitting will lead to higher energy transitions when compared to species with fewer hydroxide ligands such as $AuCl_3(OH)^-$ and $AuCl_4^-$. This effect is clearly observed when comparing the positions of the low-energy

peaks in the $AuCl_2(OH)_2^-$ and $AuCl_4^-$ spectra. The low-energy feature is shifted from near 3.85 eV in the $AuCl_4^-$ spectra to around 4.5 eV in the $AuCl_2(OH)_2^-$ spectra. Interestingly, the high-energy features do not seem to shift depending on the number of hydroxide ligands, although they appear to be more separated in the $AuCl_2(OH)_2^-$ spectra. While this shift cannot be directly monitored in the condensed-phase due to the overlapping features of the many species present, a recent study by Usher et al. predicted a similar shift to higher energies for the disubstituted species in a pH-controlled aqueous solution.[8]

The second effect of exchanging hydroxide ligands for chloride involves breaking the molecular symmetry from the highly symmetric D_{4h} point group to groups of lower symmetry (C_{2h}, C_{2v}, or C_s depending on the isomer considered). This will remove the degeneracy of the two doubly-degenerate groups of ligand MOs involved in the predominant transitions, most likely leading to splitting of spectral features. Due to the broad nature of the spectral features and inherent presence of multiple isomers in the present experiment, no splitting can be explicitly identified. In addition to the expected splitting of spectral features, the lower symmetry of the disubstituted complexes should cause the "non-bonding" orbitals of predominately ligand character to exhibit substantial mixing with meal *d*-orbitals. This will lead to transitions that involve multiple orbitals (including metal *d*-orbitals) and cannot be defined as of "purely" LMCT character.

As mentioned above, all fragment channels observed following UV-irradiation of $AuCl_2(OH)_2^-$ correspond to the loss of two ligands. This behavior can be understood in terms of a thermal dissociation mechanism comparable to that of $AuCl_4^-$ (see §6.3.2). A list of calculated threshold energies for the fragmentation of $AuCl_2(OH)_2^-$ is presented in Table 6.2. For simplicity, all threshold energies are relative to the lowest energy isomer, *cis-homo*. The calculated values suggest that the amount of energy required for both the $AuCl_2^-$ and $AuClOH^-$ channels lies below the onset of the $AuCl_2(OH)_2^-$ spectral features. Because all absorption events will lead to internal energies above these thresholds, any fragment ions created by the loss of a single ligand are expected to have very low survival probabilities over the timescale of our

experiment. Thus the only fragment ions that should be observed involve the loss of at least two ligands.

Table 6.2. Threshold energies for various fragment channels of $AuCl_2(OH)_2^-$ calculated using DFT with the B3LYP functional and a def2-TZVPP basis set. All values are measured with respect to the lowest energy isomer (*cis-homo*) of gas-phase $AuCl_2(OH)_2^-$. Channels listed in bold correspond to fragments observed in the present experiment.

Fragment Channel	Energy [eV]	
	B3LYP	
	Gas-phase	COSMO
$AuCl^0 + OH^- + OH^0 + Cl^0$	8.34	5.64
$Au(OH)^0 + Cl^- + Cl^0 + OH^0$	6.82	5.06
$AuCl(OH)^0 + OH^- + Cl^0$	6.30	4.04
$AuCl^0 + Cl^- + 2\ OH^0$	6.20	4.34
$AuCl_2^0 + OH^- + OH^0$	6.15	3.93
$AuCl_2(OH)^0 + OH^-$	5.18	2.48
$Au(OH)_2^- + 2\ Cl^0$	4.77	4.37
$AuCl_2(OH)_2^0 + e^-$	4.64	6.38
$Au(OH)_2^0 + Cl^- + Cl^0$	4.37	2.93
$AuCl(OH)^0 + Cl^- + OH^0$	4.16	2.74
$AuCl(OH)^- + Cl^0 + OH^0$	**3.81**	**3.66**
$AuCl(OH)_2^0 + Cl^-$	3.28	1.39
$AuCl(OH)_2^- + Cl^0$	2.98	2.81
$AuCl_2^- + 2\ OH^0$	**2.85**	**2.98**
$AuCl_2(OH)^- + OH^0$	2.23	2.23

Another interesting effect observed is the lack of an apparent energy dependence in the fragment branching ratios of $AuCl_2(OH)_2^-$. Whereas the two product channels of $AuCl_4^-$ were found to be complimentary (one channel turned on as the other turned off) the same spectral features are observed in both action spectra of $AuCl_2(OH)_2^-$, implying that the branching ratios remain fixed within the energy range of the experiment. This behavior can be explained by the relative fragmentation thresholds for each channel. The $AuCl_2^-$ fragment ion has the lowest threshold energy and the highest relative yield, suggesting that it is the thermodynamically favored product. In fact, the threshold for this channel is even lower than that for $AuCl(OH)_2^-$.

Even loss of two hydroxyls should be favored over the loss of a single chlorine atom. This poses the question as to why $AuClOH^-$ is observed at all. However, it is important to consider the kinetics of the process as well. The lower threshold for loss of two hydroxyls will result in $AuCl_2^-$ being the kinetically favored product but $AuClOH^-$ should still be observed, albeit with a smaller branching ratio determined by the relative rates for each dissociation channel. This also explains the fact that $Au(OH)_2^-$ could not be observed. Because the loss of hydroxyl groups is highly favored over the loss of chlorines, the branching ratio for $Au(OH)_2^-$ should be significantly lower than that for the two observed channels, even when the photon energy is above the appropriate threshold.

6.3.4 Implications for condensed-phase photochemistry

The observations discussed above present several consequences for the photochemistry of gold complexes in aqueous solution. In the gas-phase, loss of neutral chlorine atoms results in the reduction of the gold atom during fragmentation. For the complex $Au^{(III)}Cl_4^-$, reduction of $Au^{(III)}$ to $Au^{(II)}$ occurs if one Cl atom is lost and reduction to $Au^{(I)}$ occurs if two atoms are lost. The excitation wavelength determines whether one or two chlorine atoms are lost and, consequently, the degree of gold reduction that occurs. Lower photon energies favor reduction to $Au^{(II)}$ whereas higher energies lead to $Au^{(I)}$. The gas-phase results differ from models developed for photochemical nanoparticle generation by Kurihara et al.[16] and Eustis et al.,[17-18] who suggest that $Au^{(II)}Cl_3^-$ is the only primary photoproduct following the photoreduction of $Au^{(III)}Cl_4^-$. The ion $Au^{(I)}Cl_2^-$, which is clearly a primary photoproduct in the gas-phase, only appears in their proposed condensed-phase mechanisms in a subsequent step involving the disproportionation of $Au^{(II)}Cl_3^-$. However, we note that in the condensed-phase the loss of a second Cl atom in a thermal process could be suppressed by energy dissipation into the solvent depending on the relative timescales for each process. Exchange of chloride ligands with hydroxide as a result of increasing the pH will lead to higher-energy spectral features. In principle, this could make photoreduction more difficult. However, ligand exchange also shifts the fragmentation thresholds to much lower energies, making loss of the two ligands and increased gold reduction more energetically accessible.

In addition to the energy dependence of the dissociation process, the fact that fragmentation does happen in the gas-phase makes it clear that solvent is not actually necessary for photoreduction. This is in contrast to previous experiments that highlighted the obviously strong role of solvent composition during photoreduction.[17] The present experiment calls into question what its specific role actually is. It is likely that the presence of water may actually hinder the dissociation process, for example through caging and recombination. The potential importance of caging was previously addressed by Kurihara et al. and was a part of the basis for developing their proposed reaction schemes.[16] If caging is important, decreasing the mole fraction of water (while increasing the mole fraction of another solvent) could lead to an increase in the rate of photoreduction by decreasing caging effects.

In order to better understand what the effects of solvation might be on the energetics of photodissociation, COSMO calculations were performed. We again stress that this model only takes the solvent into account in terms of a continuum model and neglects the molecular structure of the solvent. It therefore cannot account for some important effects such as hydrogen bonding or the ability for solvent to participate as a chemical reactant. With these caveats in mind, it is still valuable to study the effects of the surrounding dielectric on the relevant energetics. The results of the COSMO calculations performed for $AuCl_4^-$ are presented in Figure 6.5 and for $AuCl_2(OH)_2^-$ are presented in Table 6.2. For the parent ion $AuCl_4^-$, solvation has the effect of lowering the energy of all fragment channels. These effects are most dramatic when dissociation produces Cl^- ions. Solvation of $AuCl_2(OH)_2^-$ has a similar effect but thresholds for channels resulting only from the loss of hydroxyl radicals either demonstrate no change or go up in energy. This leads to a drastic reordering of the relative fragmentation thresholds so that loss of Cl^- becomes the energetically-preferred channel, raising the question of how photoreduction occurs since the loss of a single chloride would not result in the reduction of gold.

6.4 Conclusions

Electrospray ionization mass spectra for $AuCl_4^-$ and a number of its pH-dependent hydrolysis products reveal that $AuCl_n(OH)_{4-n}^-$ complexes are present in aqueous solutions of tetrachloroaurate(III) and are involved in the aqueous speciation of gold. Ultraviolet-

photodissociation spectra for $AuCl_4^-$ and its hydrolysis product $AuCl_2(OH)_2^-$ have been measured in the gas-phase. Comparison of the $AuCl_4^-$ depletion spectrum to the absorption spectrum of aqueous $KAuCl_4$ solution reveals similar features, suggesting that the nature of the electronic transitions does not change much upon solvation. Exchanging chloride ligands for hydroxide results in an observed blue-shift of the spectra, in agreement with ligand-field theory and the spectrochemical series. No direct comparison between the gas-phase $AuCl_2(OH)_2^-$ spectra and its condensed phase counterpart can be made due to the large number of species present in solution with overlapping spectral features. However, the gas-phase spectrum is in very good qualitative agreement with previous predictions on its aqueous absorption spectrum.[2, 8]

Analysis of fragment action spectra for $AuCl_4^-$ reveals that the photodissociation process is strongly energy dependent. We exclusively observe the loss of one or two chlorine atoms, depending on the photon energy, resulting in photoreduction of the central gold atom from $Au^{(III)}$ to $Au^{(II)}$ and $Au^{(I)}$, respectively. This behavior is consistent with thermal dissociation of a vibrationally hot molecule following electronic excitation. Fragment action spectra for $AuCl_2(OH)_2^-$ behave similarly but we observe only the loss of two ligands since all photon energies used in the experiment are above the necessary threshold. In this case, the branching ratios for each fragment ion qualitatively reflect the threshold energies for their respective dissociation channels. These results have implications regarding the photochemistry of $Au^{(III)}$ complexes in solution. Our gas-phase results show that the photoreduction of gold in these species can occur *without* the participation of solvent. The role of solvent, which has been proposed in some earlier work to aid the initial reduction reaction, is therefore called into question. In fact, observing photoreduction in the absence of solvent may imply that solvation may hinder the reduction (which is concomitant with dissociation). Possible examples of how solvent could hinder the reduction include caging, changing the energetics to favor production of Cl^-, enabling intersystem crossing, or facilitating the dissipation of energy. In any case, condensed-phase experiments aimed at studying the details of wavelength-dependent photoreduction of gold would certainly prove useful. Additionally, gas-phase cluster experiments involving sequential solvation of the gold complexes with water could be fruitful for further insight to the connection between the gas- and condensed-phases.

6.5 References for Chapter 6

1. Pan, P. and Wood, S.A., "Gold-chloride complexes in very acidic aqueous solutions and at temperatures25-300°C - A laser raman-spectroscopic study." *Geochimica Et Cosmochimica Acta*, 1991. **55**(8): p. 2365.

2. Peck, J.A., Tait, C.D., Swanson, B.I., and Brown, G.E., "Speciation of Aqueous Gold(III) Chlorides from Ultraviolet Visible Absorption and Raman Resonance Raman Spectroscopies." *Geochimica Et Cosmochimica Acta*, 1991. **55**(3): p. 671.

3. Farges, F., Sharps, J.A., and Brown, G.E., "Local environment around gold(III) in aqueous chloride solutions - An EXAFS spectroscopy study." *Geochimica Et Cosmochimica Acta*, 1993. **57**(6): p. 1243.

4. Tossell, J.A., "The speciation of gold in aqueous solution: A theoretical study." *Geochimica Et Cosmochimica Acta*, 1996. **60**(1): p. 17.

5. Gammons, C.H., Yu, Y.M., and WiliamsJones, A.E., "The disproportionation of gold(I) chloride complexes at 25 to 200°C." *Geochimica Et Cosmochimica Acta*, 1997. **61**(10): p. 1971.

6. Murphy, P.J. and LaGrange, M.S., "Raman spectroscopy of gold chloro-hydroxy speciation in fluids at ambient temperature and pressure: A re-evaluation of the effects of pH and chloride concentration." *Geochimica Et Cosmochimica Acta*, 1998. **62**(21-22): p. 3515.

7. Murphy, P.J., Stevens, G., and LaGrange, M.S., "The effects of temperature and pressure on gold-chloride speciation in hydrothermal fluids: A Raman spectroscopic study." *Geochimica Et Cosmochimica Acta*, 2000. **64**(3): p. 479.

8. Usher, A., McPhail, D.C., and Brugger, J., "A spectrophotometric study of aqueous Au(III) halide-hydroxide complexes at 25-80°C." *Geochimica Et Cosmochimica Acta*, 2009. **73**(11): p. 3359.

9. Turkevich, J., Stevenson, P.C., and Hillier, J., "A study of the nucleation and growth processes in the synthesis of colloidal gold." *Discussions of the Faraday Society*, 1951(11): p. 55.

10. Turkevich, J., Stevenson, P.C., and Hillier, J., "The formation of colloidal gold." *Journal of Physical Chemistry*, 1953. **57**(7): p. 670.

11. Esumi, K., Suzuki, A., Aihara, N., Usui, K., and Torigoe, K., "Preparation of gold colloids with UV irradiation using dendrimers as stabilizer." *Langmuir*, 1998. **14**(12): p. 3157.

12. Roucoux, A., Schulz, J., and Patin, H., "Reduced transition metal colloids: A novel family of reusable catalysts?" *Chemical Reviews*, 2002. **102**(10): p. 3757.

13. Eustis, S. and El-Sayed, M.A., "Why gold nanoparticles are more precious than pretty gold: Noble metal surface plasmon resonance and its enhancement of the radiative and nonradiative properties of nanocrystals of different shapes." *Chemical Society Reviews*, 2006. **35**(3): p. 209.

14. Kimling, J., Maier, M., Okenve, B., Kotaidis, V., Ballot, H., and Plech, A., "Turkevich method for gold nanoparticle synthesis revisited." *Journal of Physical Chemistry B*, 2006. **110**(32): p. 15700.

15. Sakamoto, M., Fujistuka, M., and Majima, T., "Light as a construction tool of metal nanoparticles: Synthesis and mechanism." *Journal of Photochemistry and Photobiology C-Photochemistry Reviews*, 2009. **10**(1): p. 33.

16. Kurihara, K., Kizling, J., Stenius, P., and Fendler, J.H., "Laser and Pulse Radiolytically Induced Colloidal Gold Formation in Water and in Water-in-Oil Microemulsions." *Journal of the American Chemical Society*, 1983. **105**(9): p. 2574.

17. Eustis, S., Hsu, H.Y., and El-Sayed, M.A., "Gold nanoparticle formation from photochemical reduction of Au^{3+} by continuous excitation in colloidal solutions. A proposed molecular mechanism." *Journal of Physical Chemistry B*, 2005. **109**(11): p. 4811.

18. Eustis, S. and El-Sayed, M.A., "Molecular mechanism of the photochemical generation of gold nanoparticles in ethylene glycol: Support for the disproportionation mechanism." *Journal of Physical Chemistry B*, 2006. **110**(29): p. 14014.

19. Harada, M. and Einaga, H., "In situ XAFS studies of au particle formation by photoreduction in polymer solutions." *Langmuir*, 2007. **23**(12): p. 6536.

20. Ahlrichs, R., Bar, M., Haser, M., Horn, H., and Kolmel, C., "Electronic-structure calculations on workstation computers - The program system TURBOMOLE." *Chemical Physics Letters*, 1989. **162**(3): p. 165.

21. Parr, R.G. and Yang, W., *Density-Functional Theory of Atoms and Molecules*. 1989, New York: Oxford University Press.

22. Becke, A.D., "Denisty-functional exchange-energy approximation with correct asymptotic-behavior." *Physical Review A*, 1988. **38**(6): p. 3098.

23. Lee, C.T., Yang, W.T., and Parr, R.G., "Development of the Colle-Salvetti Correlation-Energy Formula into a Functional of the Electron-Density." *Physical Review B*, 1988. **37**(2): p. 785.

24. Perdew, J.P., Burke, K., and Ernzerhof, M., "Generalized gradient approximation made simple." *Physical Review Letters*, 1996. **77**(18): p. 3865.

25. Weigend, F., Haser, M., Patzelt, H., and Ahlrichs, R., "RI-MP2: optimized auxiliary basis sets and demonstration of efficiency." *Chemical Physics Letters*, 1998. **294**(1-3): p. 143.

26. Andrae, D., Haussermann, U., Dolg, M., Stoll, H., and Preuss, H., "Energy-adjusted ab-initio pseudopotentials for the 2nd and 3rd row transition-elements." *Theoretica Chimica Acta*, 1990. **77**(2): p. 123.

27. Deglmann, P. and Furche, F., "Efficient characterization of stationary points on potential energy surfaces." *Journal of Chemical Physics*, 2002. **117**(21): p. 9535.

28. Deglmann, P., Furche, F., and Ahlrichs, R., "An efficient implementation of second analytical derivatives for density functional methods." *Chemical Physics Letters*, 2002. **362**(5-6): p. 511.

29. Bauernschmitt, R. and Ahlrichs, R., "Treatment of electronic excitations within the adiabatic approximation of time dependent density functional theory." *Chemical Physics Letters*, 1996. **256**(4-5): p. 454.

30. Bauernschmitt, R., Haser, M., Treutler, O., and Ahlrichs, R., "Calculation of excitation energies within time-dependent density functional theory using auxiliary basis set expansions." *Chemical Physics Letters*, 1997. **264**(6): p. 573.

31. Klamt, A. and Schuurmann, G., "COSMO - A new approach to dielectric screening in solvents with explicit expressions for the screening energy and its gradient." *Journal of the Chemical Society-Perkin Transactions 2*, 1993(5): p. 799.

32. Haynes, W.M., ed. "CRC Handbook of Chemistry and Physics." 91 ed. 2010, CRC Press/Taylor and Francis: Boca Raton, FL.

33. Gray, H.B. and Ballhausen, C.J., "A Molecular Orbital Theory for Square Planar Metal Complexes." *Journal of the American Chemical Society*, 1963. **85**(3): p. 260.

34. Basch, H. and Gray, H.B., "Molecular Orbital Theory for Square-Planar Metal Halide Complexes." *Inorganic Chemistry*, 1967. **6**(2): p. 365.

35. Messmer, R.P., Interran.Lv, and Johnson, K.H., "Electronic structure of square-planar transition-metal complexes. 1. $PtCl_4^{2-}$ and $PdCl_4^{2-}$ ions." *Journal of the American Chemical Society*, 1974. **96**(12): p. 3847.

36. Chakravorty, A., "UV Spectrum of $KAuCl_4$." *Naturwissenschaften*, 1961. **48**(9): p. 375.

37. Chakravorty, A., "Comments on Colour of Alkyl-Gold(III) Complexes." *Naturwissenschaften*, 1961. **48**(20): p. 643.

38. Gangopadhyaya, A. and Chakravorty, A., "Charge Transfer Spectra of Some Gold(III) Complexes." *Journal of Chemical Physics*, 1961. **35**(6): p. 2206.

39. Marcum, J.C. and Weber, J.M., "Electronic photodissociation spectra and decay pathways of gas-phase $IrBr_6^{2-}$." *Journal of Chemical Physics*, 2009. **131**(19).

40. Rensing, C., Ehrler, O.T., Yang, J.P., Unterreiner, A.N., and Kappes, M.M., "Photodissociation dynamics of $IrBr_6^{2-}$ dianions by time-resolved photoelectron spectroscopy." *Journal of Chemical Physics*, 2009. **130**(23).

41. Miessler, G.L. and Tarr, D.A., *Inorganic Chemistry*. 2 ed. 1998, Upper Saddle River, New Jersey: Prentice-Hall.

42. Jean, Y., *Molecular Orbitals of Transition Metal Complexes*. 2005, New York: Oxford University Press Inc.

1

7 A Tangent On Small Molecule Clusters: $CH_3NO_2^-\cdot(H_2O)_n$

This chapter has been reproduced in part with permission from Marcum, J.C. and Weber, J.M., "Microhydration of Nitromethane Anions from Both a Solute and Solvent Perspective." *Journal of Physical Chemistry A*, 2010. **114**: p. 8933. Copyright 2010 American Chemical Society.

7.1 Background

Over the last few decades, there has been much interest in the microhydration of negative ions.[1-13] In particular, cluster studies focusing on the structural and electronic properties have proven particularly fruitful. These studies have been used to elucidate details of water network formation and the way anions are embedded in such networks by probing the clusters as they are built one water molecule at a time. In particular, infrared photodissociation spectroscopy has often been applied to these problems with great success.[7, 11] Currently, hydration of atomic and diatomic anions is reasonably well understood.[7] Larger systems, such as triatomic anions or triatomic domains of larger molecules, are expected to demonstrate more complexity than these smaller systems, but preliminary studies on the structure of their monohydrates have yielded some basic insight.[14] However, with the exception of very few examples,[15-17] higher levels of hydration have not been explored for these larger domains. This leaves open many opportunities for investigation of the hydration of larger anions.

One of the unanswered questions is whether or not these larger ions have a reasonably general set of rules for binding motifs and hydration shell structure, similar to those for hydration of monoatomic anions.[7] So far, there are not sufficient studies to establish an answer. In some cases, even monohydrates of larger domains are not straightforward.[16-17] In general, a water molecule can form one or two hydrogen bonds to an anions. In triatomic domains of anions, the monohydrate binding motif seems to depend largely on the distance between the charge centers.[14] For relatively large solute ions such as CS_2^-, the first water ligand typically acts as a "double donor" with both of its OH groups involved in a H-bond to the ion. For simplicity, this double ionic H-bonded water is abbreviated DIHB. For small ions such as NO_2^-, the HOH bond angle in the water would incur far too much strain to maintain a robust DIHB. Instead, the water molecule forms a single H-bond to the ion, leaving the second OH

group essentially free. This second geometry is referred to as a single ionic H-bond (SIHB) and is the general hydration motif for smaller species such as the halides. However, this simple rule does not necessarily hold for larger anions. Two recent studies from our group have demonstrated that a water molecule binds to $C_6F_6^-$ as a double donor,[16] but only with a single H-bond to SF_6^-,[17] even though the F-F distances in both molecules have the right magnitude for a double donor configuration.

Similarly, there is not enough data currently available to predict the onset of water network formation around a large solute anion. For small ions such as the halides, the hydration level needed for water network formation can be correlated with the proton affinity and size of the anion.[7, 14, 18] For instance, F^- is very compact and disrupts water network formation, while the hydrated heavier halides clearly display water networks already at the dehydrate level.[19, 7, 20] The situation is less clear for larger molecules. The $C_6F_6^-$ dehydrate anion promotes water-water H-bonds,[16] whereas water networks are not formed around SF_6^- when less than three water ligands are present.[17]

Investigations of hydrated anions using photoelectron spectroscopy often yield insight from the solute perspective, showing how the anion properties change with the size of the hydration shell.[21, 2, 5, 22-23] In contrast, most infrared studies on anion hydration have focused on the solvent rather than the solute, since the vibrational patterns of the water molecules show the most prominent effects. However, as the excess electron penetrates the nuclear framework of a molecular anion, its distribution can greatly influence its chemical properties, as demonstrated, for example, by SF_6^-.[17] In cases where molecular vibrations of the anion are experimentally accessible, following the evolution of the solute structure as the hydration shell grows should prove interesting.

In order to address some of these questions, we have obtained infrared spectroscopy data on the sequential microhydration of the nitromethane anion, $CH_3NO_2^-$. Structural information is obtained for the hydration motifs of up to four water molecules using the spectral pattern of water OH stretching bands in concert with density functional theory. Additionally, CH stretching

bands of the nitromethane “host” anion are used to shed light on the effect of hydration from a solute perspective.

7.2 Methods

7.2.1 Ar-predissociation spectroscopy

The method and apparatus for obtaining infrared spectroscopic information of cluster anions has previously been described in detail elsewhere [24, 16] and are qualitatively similar to those described for electronic photodissociation spectroscopy in Chapter 2. Therefore, only a brief description will be provided here. A supersonic expansion of argon is generated by a pulsed Even-Lavie valve (stagnation pressure 14 bar). Nitromethane and water are entrained at ambient pressure into the supersonic flow by independently controlled, pulsed valves (General Valve, Series 9). Electrons are injected at 800 eV kinetic energy into the high density region of the expansion, creating a plasma in which slow secondary electrons can form anions by electron attachment. Among other species, ions of the composition $CH_3NO_2^-\cdot(H_2O)_n\cdot Ar$ are generated.

The ion beam is injected into a Wiley-McLaren time-of-flight mass spectrometer (TOF-MS), where ions of interest are mass selected by a pulsed mass gate in the first space focus. Here, ions are irradiated with the output from a pulsed optical parametric converter (Laser-Vision), delivering pulses in the mid-infrared (~2100 – 3800 cm^{-1}, ~2 cm^{-1} bandwidth) with a duration of approximately 7 ns and pulse energies of several millijoules. If the irradiated $CH_3NO_2^-\cdot(H_2O)_n\cdot Ar$ species absorbs a photon, Ar atoms are evaporated and fragment ions are formed according to the following reaction:

Scheme 7.1

$$CH_3NO_2^-\cdot(H_2O)_n\cdot Ar + h\nu \rightarrow CH_3NO_2^-\cdot(H_2O)_n + Ar$$

The $CH_3NO_2^-\cdot(H_2O)_n$ fragment ions are then separated from any remaining undissociated parent ions using a reflectron and the photofragment ion intensity is monitored as a function of the infrared photon energy. The experiment is repeated on different days for each ion species to ensure reproducibility and several scans are averaged for each spectrum to increase the

signal-to-noise ratio. The energy scale is calibrated to the previous experimental data of Robertson et al. on the $CH_3NO_2^-\cdot H_2O$ complex.[14]

7.2.2 Computational

In order to obtain structural information from infrared spectra, it is necessary to compare the experimental data to simulated infrared spectra from calculated isomer structures. We used density functional theory (DFT)[25] employing the B3LYP functional[26-27] and an aug-cc-pVTZ basis set[28] for all atoms as implemented in the TURBOMOLE V5.9.1 suite of programs.[29] Different starting points were chosen based on chemical intuition. All calculations converged into a small number of minimum energy structures. Vibrational frequencies were calculated using analytical second derivatives.[30-31] These frequencies were used to correct all energies for zero-point energy and to simulate infrared spectra for all stationary points found on the potential energy surface. The calculations are based on the harmonic approximation, but effects due to anharmonicity have been accounted for by scaling the frequency values to reproduce the OH stretching frequencies of other known hydrated ions. Specifically, we calculated the structures and OH stretching frequencies of hydrated Cl-, Br-, CS2-, and OCS- and compared them to the corresponding experimental values.[32, 14] Using this approach, we obtained a scaling factor of 0.957. While this procedure is not a true anharmonic calculation, it has been applied with good success by many other groups to obtain the right patterns in hydrated anion clusters.[7] Due to the complexity of the isomers, especially for the trihydrate and tetrahydrate, no explicit search was conducted for transition states, although some were found during the search for stationary states. Despite an extensive isomer search, we stress that we cannot claim to have exhausted all possibilities in the search of very low-lying isomers, especially for the tri- and tetrahydrate.

It is important to note that all relative energies reported here are below 50 meV, which is within the uncertainty bracket for B3LYP. Moreover, the relative energies do not take into account entropic effects. Based on the idea that the Ar-solvated clusters are formed as an evaporative ensemble,[33] the Ar binding energy determines the final temperature equivalent of the cluster, which can be estimated to be around 50-100 K.[34-36] Entropic effects are therefore expected to be low but on the order of the energy differences between isomers. As a

consequence, we do not infer an actual ordering of the isomers from our calculations but rather view the calculated structures merely as rough guidelines for structural motifs.

7.3 Results and discussion

The spectra in Figure 7.1 show the Ar predissociation spectra of $CH_3NO_2^-\cdot(H_2O)_n\cdot Ar$, where n = 1-4. The spectral range shown here can be divided into two main regions. The lower frequency part, below ~3050 cm^{-1}, contains the CH stretching modes as dominant infrared chromophores, which encode the influence of hydration on the structure of the solute. In the higher frequency region, mainly OH stretching bands are observed, which carry information on the structure of the hydration shell. The two spectral regions will each be discussed separately below.

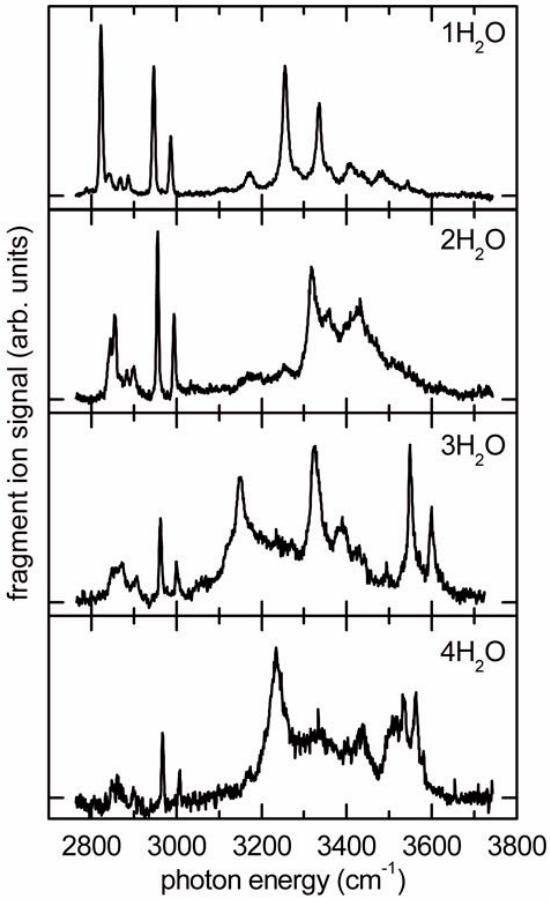

Figure 7.1. Overview of the entire recorded spectral range for $CH_3NO_2^-\cdot(H_2O)_n\cdot Ar$, where n = 1-4.

7.3.1 OH stretching bands

The oxygen atoms in the nitro group constitute the primary binding sites for water molecules. The distance between the O atoms is between the clear-cut cases for DIHB and SIHB configurations for triatomic anions and triatomic domains of larger species, similar to the case of acetate.[14] As a consequence, the OH stretching vibrations of the monohydrate display an extended progression of peaks. The calculated energy structure of the complex implies that the water molecule is in a DIHB configuration (see Figure 7.2).

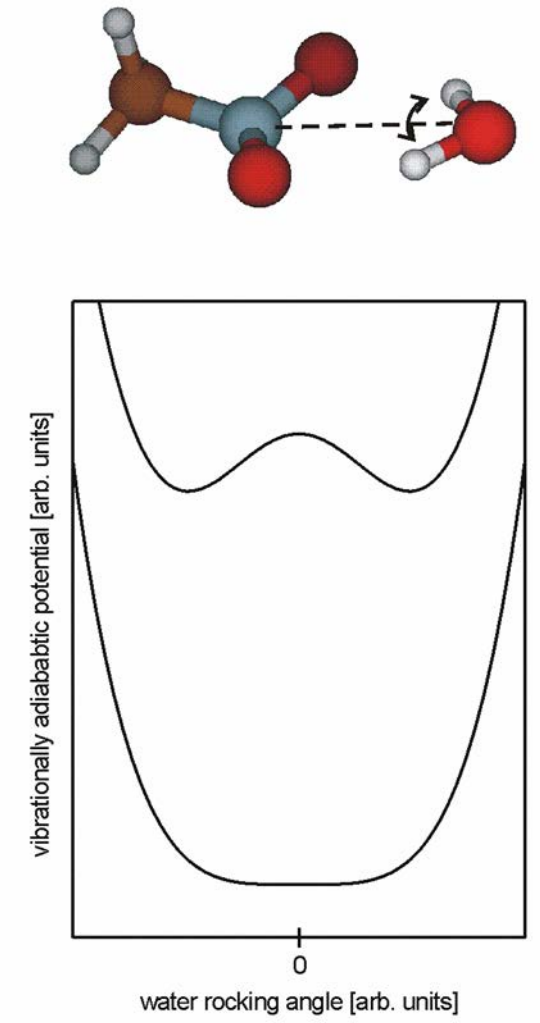

Figure 7.2. Structure (top) and schematic potential energy surface (bottom) of $CH_3NO_2^- \cdot (H_2O)$. The lower curve shows the potential energy surface of the vibrational ground state as a function of the water rocking angle. The upper curve shows the vibrational adiabatic curve for one quantum in the symmetric OH stretching vibration.

At first glance, the shape of the spectrum is surprising, since one would only expect to observe the signatures of the symmetric and antisymmetric OH stretching modes and possibly the overtone of the water bending mode that forms a Fermi resonance with the symmetric stretching mode and can be observed in the spectra of nearly all hydrated anions.[37, 7, 18, 17] The progression of peaks in the monohydrate spectrum has been observed and interpreted previously by the Johnson and Jordan groups,[38, 14] and our spectra are in excellent agreement with their work. The unexpected spectral details can be explained using a vibrationally adiabatic potential energy surface along the (slow) water rocking coordinate, which contains the time-averaged energy contributions of the (fast) OH stretching vibrations. The vibrational ground state has a flat minimum, corresponding to the DIHB geometry of the water molecule. However, the first excited state has a drastically different shape, favoring a SIHB motif to one of the O atoms in the nitro group, with the DIHB structure as a saddle point (see Figure 7.2). As a result, excitation of an OH stretching vibration launches OH rocking vibrations in the excited state. It is important to note that calculations based on the harmonic approximation will utterly fail to describe the observed OH stretching spectrum in such a complicated case.[38, 14]

In larger clusters, the water ligands' propensity to form networked structures often changes the hydration motif considerably. The trihydrate spectrum, while seeming rather complicated at first glance, is in fact easier to interpret, since it shows several characteristic bands that can be easily assigned. From comparison with other hydrated anions,[39] the peaks between 3100 and 3470 cm^{-1} can be attributed to OH oscillators that are H-bonded to the ion, while those between 3500 and 3650 cm^{-1} are usually associated with H-bonds between water ligands. The calculations show three low-lying structures within 5 meV (see Figure 7.3).

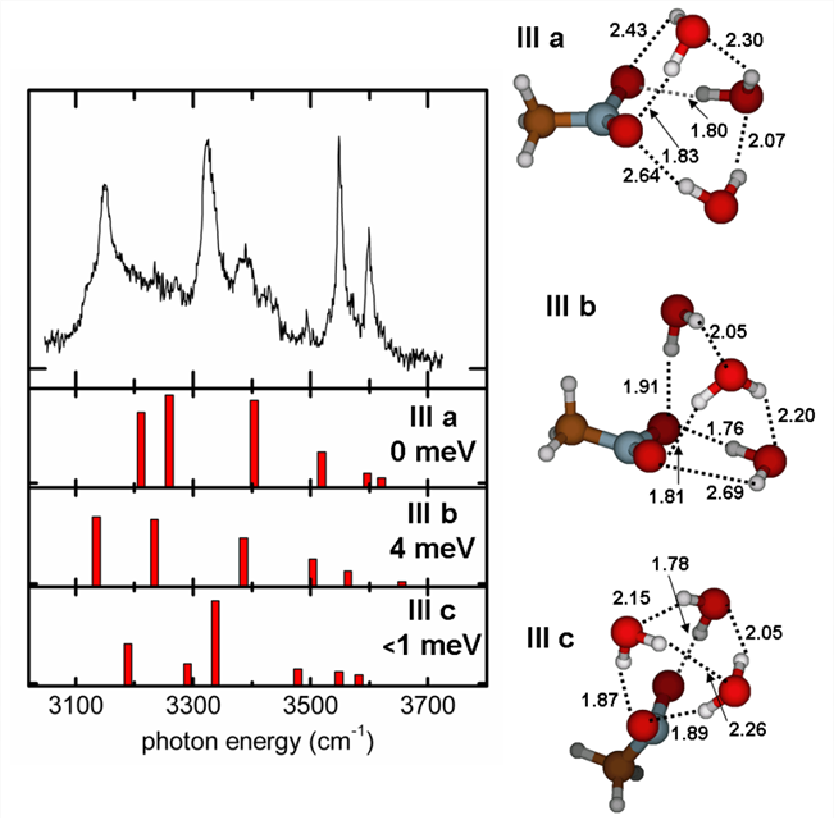

Figure 7.3. Experimental and calculated spectra of the OH stretching region of the trihydrate with selected calculated structures. Zero-point corrected energies are given for each calculated isomer. The ordinate shows the photodissociation action for the experimental spectrum and the IR absorption cross section for the simulated spectra, each in arbitrary units. H-bonding distances are given in Å.

In Isomer III-a, one water ligand bonds to the nitro group in an asymmetric DIHB motif. The other two water ligands forms a single H-bond to the nitro group and a water-water H-bond. These other two water ligands are located *anti* to the "unique" CH group closest to the nitro group. Another isomer (III-b) exists that is equivalent in the connectivity of the water ligands, but the two SIHB water molecules are *syn* to the "unique" CH bond. Isomers III-a and III-b can be interpreted as being based on the monohydrate structure, where the DIHB water molecule from the monohydrate affords a third oxygen atom as a binding site for subsequent water ligands. We note that these two isomers were first found by Motegi et al.[40] and are recovered in our DFT calculations as well.[11]

[11] We became aware of the high-level calculations by Motegi et al. prior to the publication of their work,[40. Motegi, H., Takayanagi, T., Tsuneda, T., Yagi, K., Nakanishi, R., and Nagata, T., "Theoretical Study on the Excess Electron Binding Mechanism in the $CH_3NO_2(H_2O)_n^-$ (n=1-6) Anion Clusters." *Journal of Physical Chemistry A*,

In the third low-lying isomer, the three water ligands form a homodromic ring, where each water molecule forms one strong H-bond to one of the O atoms of the nitro group and one H-bond to another water molecule in a double donor, single acceptor configuration. This structure is qualitatively different from the monohydrate-based isomers but is reminiscent of the binding motif seen in halide hydration.[39, 7] The main difference is that the anionic binding sites are not populated the same way, since one of the O atoms accepts two H-bonds, while the other accepts only one. As a result, the three water molecules do not have equivalent interactions with the ion, in contrast to halide hydrate. The common element of all low-lying isomers is the absence of dangling OH bonds. This is consistent with the absence of a free OH band that is typically observed near 3700 cm^{-1}.[7] All isomers mentioned above are viewed as isoenergetic and compatible with the experimental data. All of these isomers are potentially populated in the ion beam even if Isomer III-c has the overall best fit to the experimental IR spectrum. We note that much of the intensity observed between 3200 and 3300 cm^{-1} can be attributed to the bending overtone transitions of the water ligands.

The tetrahydrate spectrum (Figure 7.4) is in several ways reminiscent of the trihydrate spectrum. The absence of a free OH band and the presence of an intense group of absorptions between 3475 and 3600 cm^{-1} suggests a water network where all OH groups are involved in H-bonding. Additionally, there is an intense signature of H-bonding to the ion between 3200 and 3300 cm^{-1}. The lowest lying calculated isomer (IV-a) is similar to the trihydrate isomers III-a and III-b discussed above, where one water molecule is in a DIHB structure with the nitro group. The remaining three water molecules now form a homodromic ring where each molecule has one H-bond to a neighboring water molecule and one H-bond to a ring that is formed by the two oxygen atoms of the nitro group and the oxygen atom of the DIHB water molecule. The simulated spectrum of this isomer, first found by Motegi et al.,[40] fits the experimental spectrum rather well, and we expect it to be the dominant species in the beam.

2010. **114**(34): p. 8939.] which was eventually published as a companion paper to our own paper that this chapter has been partially reproduced from.

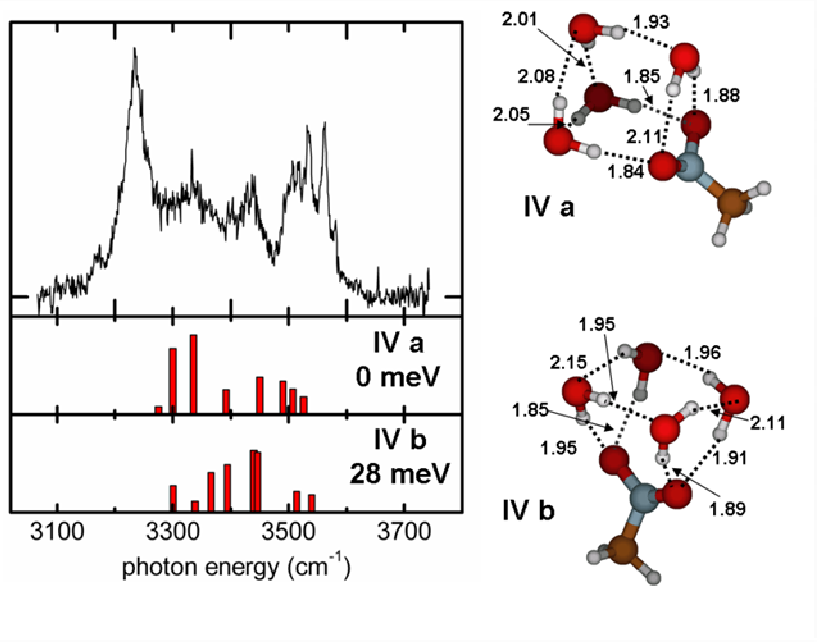

Figure 7.4. Experimental and calculated spectra of the OH stretching region of the tetrahydrate with selected calculated structures. Zero-point corrected energies are given for each calculated isomer. The ordinate shows the photodissociation action for the experimental spectrum and the IR absorption cross section for the simulated spectra, each in arbitrary units. H-bonding distances are given in Å.

The emergence of cyclic water sub-clusters in the tri- and tetrahydrate clusters can be understood in terms of the cooperative effects that have been described by Xantheas.[41] These cooperative effects are mainly the result of three-body terms that stabilize homodromic H-bonding networks. Interestingly, the homodromic four-membered ring structure (Isomer IV-b) is somewhat higher in energy. However, even partially cyclic isomers profit from cooperative effects, and we assume that the more spatially relaxed H-bonding network structure makes Isomer IV-a more energetically favorable. The calculated spectrum of Isomer IV-b is roughly consistent with the experimental spectrum but less so than Isomer IV-a.

While the limiting cases of the monohydrate complex and relatively large hydrated clusters can be well understood as discussed above, the dihydrate presents a very difficult case. The dihydrate spectrum shows a very broad envelope (see Figure 7.5), which could be explained by the population of several isomers. This is consistent with the fact that we found 5 nonequivalent isomers within 40 meV (and 3 within 10 meV) of the lowest energy configuration and several more at higher energies. For brevity, we will only discuss the lowest energy structures and sort them into groups that have the same general structural motif but have

small differences in details. In two of the lowest energy structures (II-a and II-b in Figure 7.5), both water molecules form one H-bond to one of the O atoms in the nitro group. One of the ligands has its remaining OH group nearly free, but aligns to the other O atom of the ion and is nearly coplanar with the ONO plane. The interaction with the charge on the nitro group leads to a red shift of approximately 50 cm^{-1} for the antisymmetric OH stretching vibration from the value typical of a free OH band. The second ligand interacts with the first, forming a weak H-bond that is probably very fragile due to the rather large H···O distance (~225 pm) and an unfavorable OHO angle (142°). Isomer II-b has the water molecule that is out of the ONO plane *syn* to the unique CH group and is calculated to be ~8 meV higher in energy. However, within the accuracy of the calculations, the two isomers are isoenergetic. The equivalence of the two isomers with respect to the nitro group is best seen if viewed along the ONO plane (see Figure 7.5). The next isomer family (II-c and II-d) has one water ligand in a DIHB configuration to the nitro group, while the second ligand forms only one H-bond to the nitro group and does not interact with the other water molecule. Isomer II-c was calculated to lie ~2 meV above Isomer II-a but ~6 meV below Isomer II-b. Isomer II-d is calculated to be ~13 meV higher in energy than Isomer II-c. Because both isomer groups are extremely close in energy (all four isomers are within ~15 meV) they can all be considered isoenergetic with each other within the confidence interval of the calculations. Another isomer (II-e), at ~35 meV above the lowest energy isomer, has both water molecules in DIHB structures, arranged symmetrically around the ONO plane. We found other structural motifs at higher energies. All the isomers discussed are calculated to be minimum energy structures, but their lowest energy frequencies are all below 30 cm^{-1}. In addition, several very low-lying transition states were found to be within 2 meV of the lowest energy isomer. These observations to form a picture that is consistent with a very flat potential energy surface, which may very well lead to broad absorption bands due to the lack of structural rigidity. Moreover, Isomers II-c, II-d, and II-e involve a water molecule whose binding motif is very similar to that of the monohydrate. This can lead to the same structure in the vibrationally excited state as for the monohydrate, rendering calculations based on the harmonic approximation useless. While there is some similarity between the calculated and experimental spectra for the three higher lying OH bands, the lowest energy band is not well

described for the two lower energy conformer families. In addition, it is entirely possible that more than one isomer is populated in the ion beam. In view of all these ambiguities, we refrain from assigning any specific structures to the dihydrate cluster.

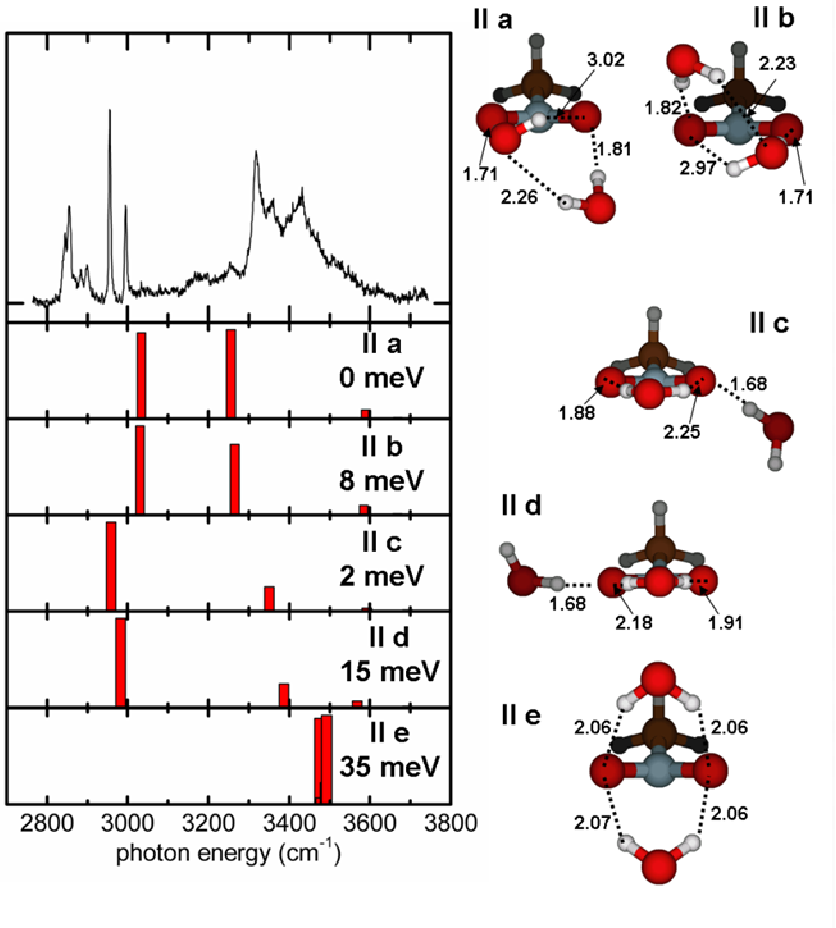

Figure 7.5. Experimental spectrum and selected calculated structures of the dihydrate with calculated OH stretching frequencies. Zero-point corrected energies are given for each calculated isomer. The ordinate shows the photodissociation action for the experimental spectrum and the IR absorption cross section for the simulated spectra, each in arbitrary units. H-bonding distances are given in Å.

7.3.2 CH stretching bands

While the OH stretching bands of the water ligands encode how the solvent is influenced by the presence of the ion, the CH stretching bands of the methyl group reflect some of the effects that the hydration environment has on the solution ion (Figure 7.6). The spectrum of the bare nitromethane anion shows three intense bands in the CH stretching region.[35-36] Upon hydration, these bands shift to higher frequencies. Moreover, the lowest lying band broadens

considerably, loses peak intensity relative to the other two, still-sharp bands, and moves into a group of weaker bands that gain intensity.

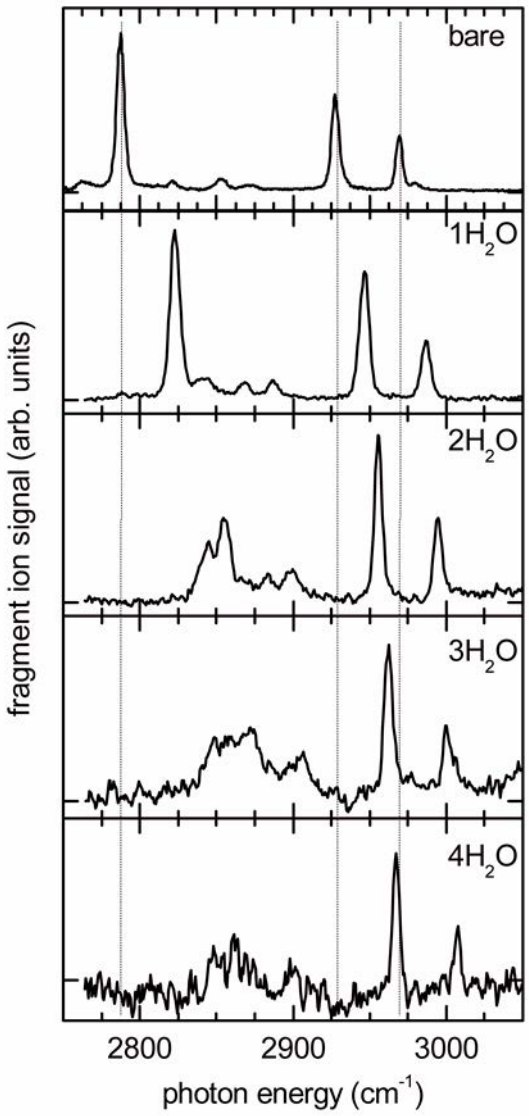

Figure 7.6. Experimental spectra of the CH stretching region for bare and hydrate nitromethane. The bare spectrum was obtained from the parent $CH_3NO_2^- \cdot Ar_4$. All hydrated spectra were obtained from the parent $CH_3NO_2^- \cdot (H_2O)_n \cdot Ar$.

To explain the changes of the CH stretching bands with hydration, we first note that the CH stretching bands of bare nitromethane are shifted strongly to lower frequencies upon electron attachment.[35-36] In particular, the totally symmetric methyl stretch shifts from 2974 cm^{-1} in the neutral molecule[42] to 2776 cm^{-1} in the anion.[35-36] The angle of the CN bond axis with the ONO plane changes drastically,[43] leading to an increased interaction of the (now

negatively charged) nitro group with the methyl group (see Figure 7.7). As a result, the totally symmetric methyl stretching mode evolves into a mode that is carried mainly by the motion of the CH group *syn* with the nitro group.[35-36] The CH_3 group also accommodates some of the excess electron density, as can be seen from the shape of the highest occupied molecular orbital (Figure 7.7).[43] This is one of the main reasons of the observed red shifts in the molecular vibrational modes. The two other CH stretching modes can be mainly characterized by a symmetric and an antisymmetric mode of the methylene group *anti* to the nitro group.[35-36] The fundamental of the totally symmetric methyl stretching mode interacts in strong Fermi resonances with several overtones and combination bands of HCH bending modes.[36] In contrast, the symmetric and antisymmetric methylene stretching modes interact much more weakly with the HCH bending modes.[36]

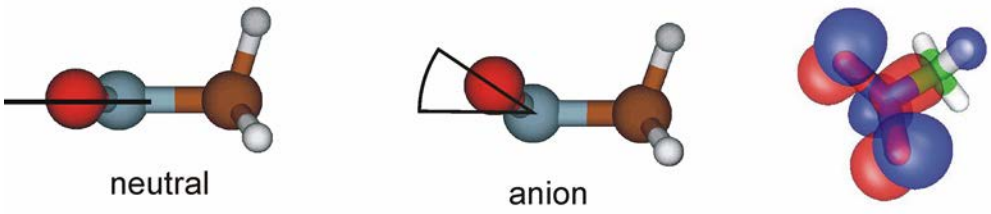

Figure 7.7. Structures of neutral nitromethane (left) of nitromethane anion (center) and the highest occupied molecular orbital of the anion (right).

In the language of physical organic chemistry, the strong red shift of the CH stretching modes can be qualitatively understood as a negative hyperconjugation effect. In hyperconjugation, electrons in a filled σ bond (usually CH or CC bonds) delocalize into an adjacent *p* or π orbital (nominally empty or partially filled), stabilizing the system. In the present case, electrons from the *p* orbital of the nitrogen atom delocalize into the σ^* orbital of the adjacent CH group, leading to a weakening the CH bonds in the methyl group and a concomitant shift of CH stretching bands toward lower frequencies with respect to their positions in neutral nitromethane.

Upon hydration, the water ligands polarize the excess electron. This can have dramatic effects, as recently observed in hydrated SF_6^- ions.[17] In the present case, hydration reduces

the amount of negative charge and, consequently, the effect of the excess electron on the methyl group. In fact, our calculations imply that the excess charge "spills out" into the water network and is shared nearly equally between the nitromethane molecule and the water cluster in the tetrahydrate (see Table 7.1). As a result, the CH stretching modes of the anion shift to the blue upon hydration. These shifts decrease with increasing hydration from ~15 cm^{-1} to ~6 cm^{-1} per water ligand for the symmetric and antisymmetric methylene stretching modes, respectively. In the case of the totally symmetric methyl stretching mode, a blue shift of ~33 cm^{-1} per water molecule for the first two water ligands leads to an even stronger Fermi interaction with the overtones and combination bands of HCH bending modes. As a result, the totally symmetric methyl stretching mode "smears out" in a broad background of HCH overtones and combination bands for the tri- and tetrahydrate. These effects demonstrate quite clearly how the water ligands polarize the electron away from the methyl group and thereby reduce the negative hyperconjugation effects in the CH stretching vibrations. The CH stretching bands in this case can serve as a sensitive probe of ligand effects on the solute.

Table 7.1. Löwdin charges on the methyl group and on the nitromethane molecule as a function of hydration for all lowest energy isomers.

Number of Water Molecules	Charge on CH_3 Group	Charge on Nitromethane
0	-0.207	-1
1	-0.127	-0.773
2	-0.107	-0.642
3	-0.077	-0.545
4	-0.063	-0.526

7.4 Conclusions

Nitromethane anions are hydrated at the nitro group, which carries most of the negative charge. The monohydrate has a DIHB configuration whose spectrum is complicated by vibrational adiabatic effects. In the dihydrate cluster, the water molecules compete for optimal interaction with the nitro group, forming a very fluxional geometry somewhat between a pure double donor configuration to the O atoms and robust water-water interaction. For the larger clusters, the water molecules form networks, partially employing ring structures. The excess charge penetrates into the methyl group of the nitromethane anion, resulting in a strong red shift of the CH stretching vibrational modes compared to the neutral molecule. Hydration

polarizes the negative charge toward the water ligands and reverses this effect to a small extent.

Finally, we note that the dissociation of $CH_3NO_2^-$ into CH_2NO and ON^- in the presence of water does not seem to be active in our clusters. While the resulting OH^- vibrational structure may be hidden underneath the OH bands of the water ligands, there should be a clear and intense signature in the CH stretching region, specifically to the blue of the symmetric and antisymmetric methylene stretching bands of $CH_3NO_2^-$. This would lead to a much more complicated spectrum in this particular frequency region than observed in our experiment. This suggests that dissociation into CH_2NO and OH^- requires a higher degree of solvation to occur.

7.5 References for Chapter 7

1. Castleman, A.W. and Bowen, K.H., "Clusters: Structure, energetics, and dynamics of intermediate states of matter." *Journal of Physical Chemistry*, 1996. **100**(31): p. 12911.

2. Schiedt, J. and Weinkauf, R., "Photodetachment photoelectron spectroscopy of mass selected anions: Anthracene and the anthracene-H_2O cluster." *Chemical Physics Letters*, 1997. **266**(1-2): p. 201.

3. Schiedt, J., Weinkauf, R., Neumark, D.M., and Schlag, E.W., "Anion spectroscopy of uracil, thymine and the amino-oxo and amino-hydroxy tautomers of cytosine and their water clusters." *Chemical Physics*, 1998. **239**(1-3): p. 511.

4. Lyapustina, S.A., Xu, S.K., Nilles, J.M., and Bowen, K.H., "Solvent-induced stabilization of the naphthalene anion by water molecules: A negative cluster ion photoelectron spectroscopic study." *Journal of Chemical Physics*, 2000. **112**(15): p. 6643.

5. Schiedt, J., Knott, W.J., Le Barbu, K., Schlag, E.W., and Weinkauf, R., "Microsolvation of similar-sized aromatic molecules: Photoelectron spectroscopy of bithiophene-, azulene-, and naphthalene-water anion clusters." *Journal of Chemical Physics*, 2000. **113**(21): p. 9470.

6. Pivonka, N.L., Kaposta, C., von Helden, G., Meijer, G., Woste, L., Neumark, D.M., and Asmis, K.R., "Gas phase infrared spectroscopy of cluster anions as a function of size: The effect of solvation on hydrogen-bonding in $Br^-\cdot(HBr)(1,2,3)$ clusters." *Journal of Chemical Physics*, 2002. **117**(14): p. 6493.

7. Robertson, W.H. and Johnson, M.A., "Molecular aspects of halide ion hydration: The cluster approach." *Annual Review of Physical Chemistry*, 2003. **54**: p. 173.

8. Xu, S.J., Nilles, M., and Bowen, K.H., "Zwitterion formation in hydrated amino acid, dipole bound anions: How many water molecules are required?" *Journal of Chemical Physics*, 2003. **119**(20): p. 10696.

9. Muntean, F., Taylor, M.S., McCoy, A.B., and Lineberger, W.C., "Femtosecond study of Cu(H_2O) dynamics." *Journal of Chemical Physics*, 2004. **121**(12): p. 5676.

10. Taylor, M.S., Muntean, F., Lineberger, W.C., and McCoy, A.B., "A theoretical and computational study of the anion, neutral, and cation Cu(H_2O) complexes." *Journal of Chemical Physics*, 2004. **121**(12): p. 5688.

11. Garrett, B.C., Dixon, D.A., Camaioni, D.M., Chipman, D.M., Johnson, M.A., Jonah, C.D., Kimmel, G.A., Miller, J.H., Rescigno, T.N., Rossky, P.J., Xantheas, S.S., Colson, S.D., Laufer, A.H., Ray, D., Barbara, P.F., Bartels, D.M., Becker, K.H., Bowen, H., Bradforth, S.E., Carmichael, I., Coe, J.V., Corrales, L.R., Cowin, J.P., Dupuis, M., Eisenthal, K.B., Franz, J.A., Gutowski, M.S., Jordan, K.D., Kay, B.D., LaVerne, J.A., Lymar, S.V., Madey, T.E., McCurdy, C.W., Meisel, D., Mukamel, S., Nilsson, A.R., Orlando, T.M., Petrik, N.G., Pimblott, S.M., Rustad, J.R., Schenter, G.K., Singer, S.J., Tokmakoff, A., Wang, L.S., Wittig, C., and Zwier, T.S., "Role of water in electron-initiated processes and radical chemistry: Issues and scientific advances." *Chemical Reviews*, 2005. **105**(1): p. 355.

12. Neumark, D.M., "Probing the transition state with negative ion photodetachment: experiment and theory." *Physical Chemistry Chemical Physics*, 2005. **7**(3): p. 433.

13. Verlet, J.R.R., Kammrath, A., Griffin, G.B., and Neumark, D.M., "Electron solvation in water clusters following charge transfer from iodide." *Journal of Chemical Physics*, 2005. **123**(23).

14. Robertson, W.H., Price, E.A., Weber, J.M., Shin, J.W., Weddle, G.H., and Johnson, M.A., "Infrared signatures of a water molecule attached to triatomic domains of molecular anions: Evolution of the H-bonding configuration with domain length." *Journal of Physical Chemistry A*, 2003. **107**(34): p. 6527.

15. Kawamata, H., Maeyama, T., and Mikami, N., "First observation of ionic π-hydrogen bonds; vibrational spectroscopy of dihydrated naphthalene anion ($Nph^-(H_2O)_2$)." *Chemical Physics Letters*, 2003. **370**(3-4): p. 535.

16. Schneider, H., Vogelhuber, K.M., and Weber, J.M., "Infrared spectroscopy of anionic hydrated fluorobenzenes." *Journal of Chemical Physics*, 2007. **127**(11).

17. Schneider, H. and Weber, J.M., "Infrared spectra of $SF_6^-\cdot(H_2O)_n$ (n=1-3): Incipient reaction and delayed onset of water network formation." *Journal of Chemical Physics*, 2007. **127**(24).

18. Schneider, H., Boese, A.D., and Weber, J.M., "Unusual hydrogen bonding behavior in binary complexes of coinage metal anions with water." *Journal of Chemical Physics*, 2005. **123**(8).

19. Ayotte, P., Nielsen, S.B., Weddle, G.H., Johnson, M.A., and Xantheas, S.S., "Spectroscopic observation of ion-induced water dimer dissociation in the $X\cdot(H_2O)_2$ (X = F, Cl, Br, I) clusters." *Journal of Physical Chemistry A*, 1999. **103**(50): p. 10665.

20. Roscioli, J.R., Diken, E.G., Johnson, M.A., Horvath, S., and McCoy, A.B., "Prying apart a water molecule with anionic H-bonding: A comparative spectroscopic study of the $X^-\cdot H_2O$ (X = OH, O, F, Cl, and Br) binary complexes in the 600-3800 cm^{-1} region." *Journal of Physical Chemistry A*, 2006. **110**(15): p. 4943.

21. Coe, J.V., Lee, G.H., Eaton, J.G., Arnold, S.T., Sarkas, H.W., Bowen, K.H., Ludewigt, C., Haberland, H., and Worsnop, D.R., "Photoelectron-spectroscopy of hydrated electron cluster anions, $(H_2O)_N$ =2-69." *Journal of Chemical Physics*, 1990. **92**(6): p. 3980.

22. Hendricks, J.H., de Clercq, H.L., Freidhoff, C.B., Arnold, S.T., Eaton, J.G., Fancher, C., Lyapustina, S.A., Snodgrass, J.T., and Bowen, K.H., "Anion solvation at the microscopic level: Photoelectron spectroscopy of the solvated anion clusters, $NO^-(Y)_n$, where Y=Ar, Kr, Xe, N_2O, H_2S, NH_3, H_2O, and $C_2H_4(OH)_2$." *Journal of Chemical Physics*, 2002. **116**(18): p. 7926.

23. Coe, J.V., Williams, S.M., and Bowen, K.H., "Photoelectron spectra of hydrated electron clusters vs. cluster size: connecting to bulk." *International Reviews in Physical Chemistry*, 2008. **27**(1): p. 27.

24. Weber, J.M. and Schneider, H., "Infrared spectra of $X^-\cdot CO_2\cdot$Ar cluster anions (X = Cl,Br,I)." *Journal of Chemical Physics*, 2004. **120**(21): p. 10056.

25. Parr, R.G. and Yang, W., *Density-Functional Theory of Atoms and Molecules*. 1989, New York: Oxford University Press.

26. Becke, A.D., "Denisty-functional exchange-energy approximation with correct asymptotic-behavior." *Physical Review A*, 1988. **38**(6): p. 3098.

27. Lee, C.T., Yang, W.T., and Parr, R.G., "Development of the Colle-Salvetti Correlation-Energy Formula into a Functional of the Electron-Density." *Physical Review B*, 1988. **37**(2): p. 785.

28. Dunning, T.H., "Gaussian-Basis Sets for Use in Correlated Molecular Calculations. 1. The Atoms Boron Through Neon and Hydrogen." *Journal of Chemical Physics*, 1989. **90**(2): p. 1007.

29. Ahlrichs, R., Bar, M., Haser, M., Horn, H., and Kolmel, C., "Electronic-structure calculations on workstation computers - The program system TURBOMOLE." *Chemical Physics Letters*, 1989. **162**(3): p. 165.

30. Deglmann, P. and Furche, F., "Efficient characterization of stationary points on potential energy surfaces." *Journal of Chemical Physics*, 2002. **117**(21): p. 9535.

31. Deglmann, P., Furche, F., and Ahlrichs, R., "An efficient implementation of second analytical derivatives for density functional methods." *Chemical Physics Letters*, 2002. **362**(5-6): p. 511.

32. Ayotte, P., Weddle, G.H., Kim, J., and Johnson, M.A., "Vibrational spectroscopy of the ionic hydrogen bond: Fermi resonances and ion-molecule stretching frequencies in the binary $X \cdot H_2O$ (X = Cl, Br, I) complexes via argon predissociation spectroscopy." *Journal of the American Chemical Society*, 1998. **120**(47): p. 12361.

33. Klots, C.E., "Evaporative Cooling." *Journal of Chemical Physics*, 1985. **83**(11): p. 5854.

34. Arnold, S.T., Arnold, J.G., Patel-Misra, D., Sarkas, H.W., and Bowen, K.H., in *Ion and Cluster Ion Spectroscopy and Structure*, J.P. Maier, Editor. 1994, Elsevier: New York.

35. Weber, J.M., Robertson, W.H., and Johnson, M.A., "Argon predissociation and electron autodetachment spectroscopy of size-selected $CH_3NO_2^- \cdot Ar_n$ clusters." *Journal of Chemical Physics*, 2001. **115**(23): p. 10718.

36. Schneider, H., Vogelhuber, K.M., Schinle, F., Stanton, J.F., and Weber, J.M., "Vibrational spectroscopy of nitroalkane chains using electron autodetachment and Ar predissociation." *Journal of Physical Chemistry A*, 2008. **112**(33): p. 7498.

37. Weber, J.M., Kelley, J.A., Nielsen, S.B., Ayotte, P., and Johnson, M.A., "Isolating the spectroscopic signature of a hydration shell with the use of clusters: Superoxide tetrahydrate." *Science*, 2000. **287**(5462): p. 2461.

38. Myshakin, E.M., Jordan, K.D., Sibert, E.L., and Johnson, M.A., "Large anharmonic effects in the infrared spectra of the symmetrical $CH_3NO_2^- \cdot (H_2O)$ and $CH_3CO_2^- \cdot (H_2O)$ complexes." *Journal of Chemical Physics*, 2003. **119**(19): p. 10138.

39. Ayotte, P., Weddle, G.H., and Johnson, M.A., "An infrared study of the competition between hydrogen-bond networking and ionic solvation: Halide-dependent distortions of the water trimer in the $X \cdot (H_2O)_3$, (X = Cl, Br, I) systems." *Journal of Chemical Physics*, 1999. **110**(15): p. 7129.

40. Motegi, H., Takayanagi, T., Tsuneda, T., Yagi, K., Nakanishi, R., and Nagata, T., "Theoretical Study on the Excess Electron Binding Mechanism in the $CH_3NO_2(H_2O)_n^-$ (n=1-6) Anion Clusters." *Journal of Physical Chemistry A*, 2010. **114**(34): p. 8939.

41. Xantheas, S.S., "Cooperativity and hydrogen bonding network in water clusters." *Chemical Physics*, 2000. **258**(2-3): p. 225.

42. Gorse, D., Cavagnat, D., Pesquer, M., and Lapouge, C., "Theoretical and Spectroscopic Study of Asymmetric Methyl Rotor Dynamics in Gaseous Partially Deuterated Nitromethanes." *Journal of Physical Chemistry*, 1993. **97**(17): p. 4262.

43. Adams, C.L., Schneider, H., Ervin, K.M., and Weber, J.M., "Low-Energy Photoelectron Imaging Spectroscopy of Nitromethane Anions: Electron Affinity, Vibrational Features, Anisotropies, and the Dipole-Bound State." *Journal of Chemical Physics*, 2009. **130**(7).

8 Bibliography

Abdoul-Carime, H., Huels, M. A., Illenberger, E. and Sanche, L. (2001). "Sensitizing DNA to secondary electron damage: Resonant formation of oxidative radicals from 5-halouracils." *Journal of the American Chemical Society* **123**(22): 5354-5355.

Abdoul-Carime, H. and Sanche, L. (2002). "Fragmentation of short single DNA strands by 1-30 eV electrons: dependence on base identity and sequence." *International Journal of Radiation Biology* **78**(2): 89-99.

Abo-Riziq, A., Grace, L., Nir, E., Kabelac, M., Hobza, P. and de Vries, M. S. (2005). "Photochemical selectivity in guanine-cytosine base-pair structures." *Proceedings of the National Academy of Sciences of the United States of America* **102**(1): 20-23.

Adams, C. L., Schneider, H., Ervin, K. M. and Weber, J. M. (2009). "Low-Energy Photoelectron Imaging Spectroscopy of Nitromethane Anions: Electron Affinity, Vibrational Features, Anisotropies, and the Dipole-Bound State." *Journal of Chemical Physics* **130**(7).

Ahlrichs, R., Bar, M., Haser, M., Horn, H. and Kolmel, C. (1989). "Electronic-structure calculations on workstation computers - The program system TURBOMOLE." *Chemical Physics Letters* **162**(3): 165-169.

Andrae, D., Haussermann, U., Dolg, M., Stoll, H. and Preuss, H. (1990). "Energy-adjusted ab-initio pseudopotentials for the 2nd and 3rd row transition-elements." *Theoretica Chimica Acta* **77**(2): 123-141.

Anusiewicz, W., Berdys, J., Sobczyk, M., Skurski, P. and Simons, J. (2004). "Effects of base π-stacking on damage to DNA by low-energy electrons." *Journal of Physical Chemistry A* **108**(51): 11381-11387.

Aravind, G., Antoine, R., Klaerke, B., Lemoine, J., Racaud, A., Rahbek, D. B., Rajput, J., Dugourd, P. and Andersen, L. H. (2010). "Sub-microsecond photodissociation pathways of gas phase adenosine 5 '-monophosphate nucleotide ions." *Physical Chemistry Chemical Physics* **12**(14): 3486-3490.

Arnold, K., Balaban, T. S., Blom, M. N., Ehrler, O. T., Gilb, S., Hampe, O., van Lier, J. E., Weber, J. M. and Kappes, M. M. (2003). "Electron autodetachment from isolated nickel and copper phthalocyanine-tetrasulfonate tetraanions: Isomer specific rates." *Journal of Physical Chemistry A* **107**(6): 794-803.

Arnold, S. T., Arnold, J. G., Patel-Misra, D., Sarkas, H. W. and Bowen, K. H. (1994). *Ion and Cluster Ion Spectroscopy and Structure*. J. P. Maier. New York, Elsevier.

Ayotte, P., Nielsen, S. B., Weddle, G. H., Johnson, M. A. and Xantheas, S. S. (1999). "Spectroscopic observation of ion-induced water dimer dissociation in the $X\cdot(H_2O)_2$ (X = F, Cl, Br, I) clusters." *Journal of Physical Chemistry A* **103**(50): 10665-10669.

Ayotte, P., Weddle, G. H. and Johnson, M. A. (1999). "An infrared study of the competition between hydrogen-bond networking and ionic solvation: Halide-dependent distortions of the water trimer in the $X\cdot(H_2O)_3$, (X = Cl, Br, I) systems." *Journal of Chemical Physics* **110**(15): 7129-7132.

Ayotte, P., Weddle, G. H., Kim, J. and Johnson, M. A. (1998). "Vibrational spectroscopy of the ionic hydrogen bond: Fermi resonances and ion-molecule stretching frequencies in the binary $X\cdot H_2O$ (X = Cl, Br, I) complexes via argon predissociation spectroscopy." *Journal of the American Chemical Society* **120**(47): 12361-12362.

Barrios, R., Skurski, P. and Simons, J. (2002). "Mechanism for damage to DNA by low-energy electrons." *Journal of Physical Chemistry B* **106**(33): 7991-7994.

Basch, H. and Gray, H. B. (1967). "Molecular Orbital Theory for Square-Planar Metal Halide Complexes." *Inorganic Chemistry* **6**(2): 365-&.

Bauernschmitt, R. and Ahlrichs, R. (1996). "Treatment of electronic excitations within the adiabatic approximation of time dependent density functional theory." *Chemical Physics Letters* **256**(4-5): 454-464.

Bauernschmitt, R., Haser, M., Treutler, O. and Ahlrichs, R. (1997). "Calculation of excitation energies within time-dependent density functional theory using auxiliary basis set expansions." *Chemical Physics Letters* **264**(6): 573-578.

Becke, A. D. (1988). "Denisty-functional exchange-energy approximation with correct asymptotic-behavior." *Physical Review A* **38**(6): 3098-3100.

Becke, A. D. (1993). "Density-functional thermochemistry. 3. The role of exact exchange." *Journal of Chemical Physics* **98**(7): 5648-5652.

Berdys, J., Anusiewicz, I., Skurski, P. and Simons, J. (2004). "Damage to model DNA fragments from very low-energy (< 1 eV) electrons." *Journal of the American Chemical Society* **126**(20): 6441-6447.

Berdys, J., Anusiewicz, I., Skurski, P. and Simons, J. (2004). "Theoretical study of damage to DNA by 0.2-1.5 eV electrons attached to cytosine." *Journal of Physical Chemistry A* **108**(15): 2999-3005.

Blades, A. T., Ikonomou, M. G. and Kebarle, P. (1991). "Mechanism of Electrospray Mass-Spectrometry - Electrospray as an Electrolysis Cell." *Analytical Chemistry* **63**(19): 2109-2114.

Blades, A. T. and Kebarle, P. (1994). "Study of the stability and hydration of doubly-charged ions in the gas-phase - SO_4^{2-}, $S_2O_6^{2-}$, $S_2O_8^{2-}$ and some related species." *Journal of the American Chemical Society* **116**(23): 10761-10766.

Bojesen, G., Hvelplund, P., Jorgensen, T. J. D. and Nielsen, S. B. (2000). "Probing the lowest coordination number of dianionic platinum-cyanide complexes in the gas phase: Dynamics of the charge dissociation process." *Journal of Chemical Physics* **113**(16): 6608-6612.

Boudaiffa, B., Cloutier, P., Hunting, D., Huels, M. A. and Sanche, L. (2000). "Resonant formation of DNA strand breaks by low-energy (3 to 20 eV) electrons." *Science* **287**(5458): 1658-1660.

Boxford, W. E. and Dessent, C. E. H. (2005). "On the stability of $IrCl_6^{3-}$ and other triply charged anions: Solvent stabilization versus ionic fragmentation and electron detachment for the $IrCl_6^{3-}\cdot(H_2O)_n$ n=0-10 microsolvated clusters." *Journal of Physical Chemistry A* **109**(26): 5836-5845.

Boxford, W. E., El Ghazaly, M. O. A., Dessent, C. E. H. and Nielsen, S. B. (2005). "High-energy collision induced dissociation of iridium hexa-halide dianions: Observation of triple electron detachment and other decay pathways." *International Journal of Mass Spectrometry* **244**(1): 60-64.

Boxford, W. E., Pearce, J. K. and Dessent, C. E. H. (2004). "Ionic fragmentation versus electron detachment in isolated transition metal complex dianions." *Chemical Physics Letters* **399**(4-6): 465-470.

Boyarkin, O. V., Mercier, S. R., Kamariotis, A. and Rizzo, T. R. (2006). "Electronic spectroscopy of cold, protonated tryptophan and tyrosine." *Journal of the American Chemical Society* **128**(9): 2816-2817.

Bragg, A. E., Verlet, J. R. R., Kammrath, A., Cheshnovsky, O. and Neumark, D. M. (2005). "Electronic relaxation dynamics of water cluster anions." *Journal of the American Chemical Society* **127**(43): 15283-15295.

Burke, R. M., Boxford, W. E., Panja, S., Nielsen, S. B. and Dessent, C. E. H. (2007). "On the propensity for electron transfer in high-energy collisions of iridium complex anions with cesium atoms." *Chemical Physics Letters* **442**(4-6): 201-205.

Cadet, J., Sage, E. and Douki, T. (2005). "Ultraviolet radiation-mediated damage to cellular DNA." *Mutation Research-Fundamental and Molecular Mechanisms of Mutagenesis* **571**(1-2): 3-17.

Castleman, A. W. and Bowen, K. H. (1996). "Clusters: Structure, energetics, and dynamics of intermediate states of matter." *Journal of Physical Chemistry* **100**(31): 12911-12944.

Cerny, R. L., Gross, M. L. and Grotjahn, L. (1986). "Fast-atom-bombardment combined with tandem mass-spectrometry for the study of dinucleotides." *Analytical Biochemistry* **156**(2): 424-435.

Chakravorty, A. (1961). "Comments on Colour of Alkyl-Gold(III) Complexes." *Naturwissenschaften* **48**(20): 643-&.

Chakravorty, A. (1961). "UV Spectrum of $KAuCl_4$." *Naturwissenschaften* **48**(9): 375-&.

Chiavarino, B., Crestoni, M. E., Fornarini, S., Lanucara, F., Lemaire, J., Maitre, P. and Scuderib, D. (2008). "Infrared spectroscopy of isolated nucleotides 1. The cyclic 3 ',5 '-adenosine monophosphate anion." *International Journal of Mass Spectrometry* **270**(3): 111-117.

Chupka, W. A. (1959). "Effect of Unimolecular Decay Kinetics on the Interpretation of Appearance Potentials." *Journal of Chemical Physics* **30**(1): 191-211.

Coe, J. V., Lee, G. H., Eaton, J. G., Arnold, S. T., Sarkas, H. W., Bowen, K. H., Ludewigt, C., Haberland, H. and Worsnop, D. R. (1990). "Photoelectron-spectroscopy of hydrated electron cluster anions, $(H_2O)_N$ =2-69." *Journal of Chemical Physics* **92**(6): 3980-3982.

Coe, J. V., Williams, S. M. and Bowen, K. H. (2008). "Photoelectron spectra of hydrated electron clusters vs. cluster size: connecting to bulk." *International Reviews in Physical Chemistry* **27**(1): 27-51.

Cotton, F. A., Wilkinson, G., Murillo, C. A. and Bochmann, M. (1999). *Advanced Inorganic Chemistry*, John Wiley & Sons.

Crespo-Hernandez, C. E., Cohen, B., Hare, P. M. and Kohler, B. (2004). "Ultrafast excited-state dynamics in nucleic acids." *Chemical Reviews* **104**(4): 1977-2019.

Crespo-Hernandez, C. E., Cohen, B. and Kohler, B. (2005). "Base stacking controls excited-state dynamics in A-T DNA." *Nature* **436**(7054): 1141-1144.

Danell, A. S. and Parks, J. H. (2003). "Fraying and electron autodetachment dynamics of trapped gas phase oligonucleotides." *Journal of the American Society for Mass Spectrometry* **14**(12): 1330-1339.

de Vries, M. S. and Hobza, P. (2007). "Gas-phase spectroscopy of biomolecular building blocks." *Annual Review of Physical Chemistry* **58**: 585-612.

Deglmann, P. and Furche, F. (2002). "Efficient characterization of stationary points on potential energy surfaces." *Journal of Chemical Physics* **117**(21): 9535-9538.

Deglmann, P., Furche, F. and Ahlrichs, R. (2002). "An efficient implementation of second analytical derivatives for density functional methods." *Chemical Physics Letters* **362**(5-6): 511-518.

Denifl, S., Ptasinska, S., Probst, M., Hrusak, J., Scheier, P. and Mark, T. D. (2004). "Electron attachment to the gas-phase DNA bases cytosine and thymine." *Journal of Physical Chemistry A* **108**(31): 6562-6569.

Depuy, C. H. and Bierbaum, V. M. (1981). "Gas-phase reactions of organic-anions as studied by the flowing afterglow technique." *Accounts of Chemical Research* **14**(5): 146-153.

Depuy, C. H., Grabowski, J. J. and Bierbaum, V. M. (1982). "Chemical-reactions of anions in the gas-phase." *Science* **218**(4576): 955-960.

Dickinson, J. R., Piepho, S. B., Spencer, J. A. and Schatz, P. N. (1972). "High-Resolution Magnetic Circular-Dichroism and Absorption-Spectra of Cs_2ZrBr_6:Ir^{4+}." *Journal of Chemical Physics* **56**(6): 2668-&.

Dreuw, A. and Cederbaum, L. S. (2001). "Nature of the repulsive Coulomb barrier in multiply charged negative ions (vol A63, art. no. 012501, 2000)." *Physical Review A* **63**(4).

Dreuw, A. and Cederbaum, L. S. (2002). "Multiply charged anions in the gas phase." *Chemical Reviews* **102**(1): 181-200.

Dunning, T. H. (1989). "Gaussian-Basis Sets for Use in Correlated Molecular Calculations. 1. The Atoms Boron Through Neon and Hydrogen." *Journal of Chemical Physics* **90**(2): 1007-1023.

Eisinger, J. and Shulman, R. G. (1968). "Excited Electronic States of DNA." *Science* **161**(3848): 1311-&.

Esumi, K., Suzuki, A., Aihara, N., Usui, K. and Torigoe, K. (1998). "Preparation of gold colloids with UV irradiation using dendrimers as stabilizer." *Langmuir* **14**(12): 3157-3159.

Eustis, S. and El-Sayed, M. A. (2006). "Molecular mechanism of the photochemical generation of gold nanoparticles in ethylene glycol: Support for the disproportionation mechanism." *Journal of Physical Chemistry B* **110**(29): 14014-14019.

Eustis, S. and El-Sayed, M. A. (2006). "Why gold nanoparticles are more precious than pretty gold: Noble metal surface plasmon resonance and its enhancement of the radiative and nonradiative properties of nanocrystals of different shapes." *Chemical Society Reviews* **35**(3): 209-217.

Eustis, S., Hsu, H. Y. and El-Sayed, M. A. (2005). "Gold nanoparticle formation from photochemical reduction of Au^{3+} by continuous excitation in colloidal solutions. A proposed molecular mechanism." *Journal of Physical Chemistry B* **109**(11): 4811-4815.

Evangelista, F. A., Paul, A. and Schaefer, H. F. (2004). "Radicals derived from adenine: Prediction of large electron affinities with a considerable spread." *Journal of Physical Chemistry A* **108**(16): 3565-3571.

Farges, F., Sharps, J. A. and Brown, G. E. (1993). "Local environment around gold(III) in aqueous chloride solutions - An EXAFS spectroscopy study." *Geochimica Et Cosmochimica Acta* **57**(6): 1243-1252.

Fenn, J. B., Mann, M., Meng, C. K., Wong, S. F. and Whitehouse, C. M. (1989). "Electrospray Ionization for Mass-Spectrometry of Large Biomolecules." *Science* **246**(4926): 64-71.

Friedrich, J., Gilb, S., Ehrler, O. T., Behrendt, A. and Kappes, M. M. (2002). "Electronic photodissociation spectroscopy of isolated IrX_6^{2-} (X=Cl,Br)." *Journal of Chemical Physics* **117**(6): 2635-2644.

Friedrich, J., Weis, P., Kaller, J., Whetten, R. L. and Kappes, M. M. (1999). "Alkali halide cluster dianions: metastability and threshold sizes." *European Physical Journal D* **9**(1-4): 269-272.

Fujii, M., Tamura, T., Mikami, N. and Ito, M. (1986). "Electronic spectra of uracil in a supersonic jet." *Chemical Physics Letters* **126**(6): 583-587.

Gabelica, V., Rosu, F., De Pauw, E., Antoine, R., Tabarin, T., Broyer, M. and Dugourd, P. (2007). "Electron photodetachment dissociation of DNA anions with covalently or noncovalently bound chromophores." *Journal of the American Society for Mass Spectrometry* **18**(11): 1990-2000.

Gabelica, V., Rosu, F., Tabarin, T., Kinet, C., Antoine, R., Broyer, M., De Pauw, E. and Dugourd, P. (2007). "Base-dependent electron photodetachment from negatively charged DNA strands upon 260-nm laser irradiation." *Journal of the American Chemical Society* **129**(15): 4706-4713.

Gabelica, V., Tabarin, T., Antoine, R., Rosu, F., Compagnon, I., Broyer, M., De Pauw, E. and Dugourd, P. (2006). "Electron photodetachment dissociation of DNA polyanions in a quadrupole ion trap mass spectrometer." *Analytical Chemistry* **78**(18): 6564-6572.

Gammons, C. H., Yu, Y. M. and WiliamsJones, A. E. (1997). "The disproportionation of gold(I) chloride complexes at 25 to 200°C." *Geochimica Et Cosmochimica Acta* **61**(10): 1971-1983.

Gangopadhyaya, A. and Chakravorty, A. (1961). "Charge Transfer Spectra of Some Gold(III) Complexes." *Journal of Chemical Physics* **35**(6): 2206-&.

Garrett, B. C., Dixon, D. A., Camaioni, D. M., Chipman, D. M., Johnson, M. A., Jonah, C. D., Kimmel, G. A., Miller, J. H., Rescigno, T. N., Rossky, P. J., Xantheas, S. S., Colson, S. D., Laufer, A. H., Ray, D., Barbara, P. F., Bartels, D. M., Becker, K. H., Bowen, H., Bradforth, S. E., Carmichael, I., Coe, J. V., Corrales, L. R., Cowin, J. P., Dupuis, M., Eisenthal, K. B., Franz, J. A., Gutowski, M. S., Jordan, K. D., Kay, B. D., LaVerne, J. A., Lymar, S. V., Madey, T. E., McCurdy, C. W., Meisel, D., Mukamel, S., Nilsson, A. R., Orlando, T. M., Petrik, N. G., Pimblott, S. M., Rustad, J. R., Schenter, G. K., Singer, S. J., Tokmakoff, A., Wang, L. S.,

Wittig, C. and Zwier, T. S. (2005). "Role of water in electron-initiated processes and radical chemistry: Issues and scientific advances." *Chemical Reviews* **105**(1): 355-389.

Gerlich, D. (1992). "Inhomogeneous RF-Fields - A Versatile Tool for the Study of Processes with Slow Ions." *Advances in Chemical Physics* **82**: 1-176.

Gerlich, D. (2003). "Molecular ions and nanoparticles in RF and AC traps." *Hyperfine Interactions* **146**(1-4): 293-306.

Gidden, J. and Bowers, M. T. (2002). "Gas-phase conformational and energetic properties of deprotonated dinucleotides." *European Physical Journal D* **20**(3): 409-419.

Gomez, A. and Tang, K. Q. (1994). "Charge and Fission of Droplets in Electrostatic Sprays." *Physics of Fluids* **6**(1): 404-414.

Gorse, D., Cavagnat, D., Pesquer, M. and Lapouge, C. (1993). "Theoretical and Spectroscopic Study of Asymmetric Methyl Rotor Dynamics in Gaseous Partially Deuterated Nitromethanes." *Journal of Physical Chemistry* **97**(17): 4262-4269.

Gray, H. B. and Ballhausen, C. J. (1963). "A Molecular Orbital Theory for Square Planar Metal Complexes." *Journal of the American Chemical Society* **85**(3): 260-&.

Grayson, M. A., Ed. (2002). *Measuring Mass: From Positive Rays to Proteins*. Philadelphia, PA, Chemical Heritage Foundation.

Guan, Z. Q., Kelleher, N. L., Oconnor, P. B., Aaserud, D. J., Little, D. P. and McLafferty, F. W. (1996). "193 nm photodissociation of larger multiply-charged biomolecules." *International Journal of Mass Spectrometry* **157**: 357-364.

Gustavsson, T., Sharonov, A. and Markovitsi, D. (2002). "Thymine, thymidine and thymidine 5 '-monophosphate studied by femtosecond fluorescence upconversion spectroscopy." *Chemical Physics Letters* **351**(3-4): 195-200.

Gustavsson, T., Sharonov, A., Onidas, D. and Markovitsi, D. (2002). "Adenine, deoxyadenosine and deoxyadenosine 5 '-monophosphate studied by femtosecond fluorescence upconversion spectroscopy." *Chemical Physics Letters* **356**(1-2): 49-54.

Habibigoudarzi, S. and McLuckey, S. A. (1995). "Ion-trap collisional activation of the deprotonated deoxymononucleoside and deoxydinucleoside monophosphates." *Journal of the American Society for Mass Spectrometry* **6**(2): 102-113.

Harada, M. and Einaga, H. (2007). "In situ XAFS studies of au particle formation by photoreduction in polymer solutions." *Langmuir* **23**(12): 6536-6543.

Haynes, W. M., Ed. (2010). *CRC Handbook of Chemistry and Physics*. Boca Raton, FL, CRC Press/Taylor and Francis.

Hendricks, J. H., de Clercq, H. L., Freidhoff, C. B., Arnold, S. T., Eaton, J. G., Fancher, C., Lyapustina, S. A., Snodgrass, J. T. and Bowen, K. H. (2002). "Anion solvation at the microscopic level: Photoelectron spectroscopy of the solvated anion clusters, $NO^-(Y)_n$, where Y=Ar, Kr, Xe, N_2O, H_2S, NH_3, H_2O, and $C_2H_4(OH)_2$." *Journal of Chemical Physics* **116**(18): 7926-7938.

Herzberg, G. (1944). *Atomic Spectra and Atomic Structure*. New York, NY, Dover.

Ho, Y. H. and Kebarle, P. (1997). "Studies of the dissociation mechanisms of deprotonated mononucleotides by energy resolved collision-induced dissociation." *International Journal of Mass Spectrometry* **165**: 433-455.

Hoffmann, E. and Stroobant, V. (2006). *Mass Spectrometry: Principles and Applications*. West Sussex, John Wiley & Sons, Ltd.

Huang, Y. Q. and Kenttamaa, H. (2003). "Theoretical estimations of the 298 K gas-phase acidities of the pyrimidine-based nucleobases uracil, thymine, and cytosine." *Journal of Physical Chemistry A* **107**(24): 4893-4897.

Huang, Y. Q. and Kenttamaa, H. (2004). "Theoretical estimations of the 298 K gas-phase acidities of the purine-based nucleobases adenine and guanine." *Journal of Physical Chemistry A* **108**(20): 4485-4490.

Hush, N. S. and Cheung, A. S. (1975). "Ionization potentials and donor properties of nucleic-acid bases and related compounds." *Chemical Physics Letters* **34**(1): 11-13.

Ikonomou, M. G., Blades, A. T. and Kebarle, P. (1991). "Electrospray Ion Spray - A Comparison of Mechanisms and Performance." *Analytical Chemistry* **63**(18): 1989-1998.

Ismail, N., Blancafort, L., Olivucci, M., Kohler, B. and Robb, M. A. (2002). "Ultrafast decay of electronically excited singlet cytosine via ππ* to nπ* state switch." *Journal of the American Chemical Society* **124**(24): 6818-6819.

Jean, Y. (2005). *Molecular Orbitals of Transition Metal Complexes*. New York, Oxford University Press Inc.

Jones, M., Jr. (2000). *Organic Chemistry*. New York, NY, W.W. Norton & Company, Inc.

Jones, R. M., Gerlich, D. and Anderson, S. L. (1997). "Simple radio-frequency power source for ion guides and ion traps." *Review of Scientific Instruments* **68**(9): 3357-3362.

Kang, H., Jung, B. and Kim, S. K. (2003). "Mechanism for ultrafast internal conversion of adenine." *Journal of Chemical Physics* **118**(15): 6717-6719.

Kang, H., Lee, K. T., Jung, B., Ko, Y. J. and Kim, S. K. (2002). "Intrinsic lifetimes of the excited state of DNA and RNA bases." *Journal of the American Chemical Society* **124**(44): 12958-12959.

Kawamata, H., Maeyama, T. and Mikami, N. (2003). "First observation of ionic π-hydrogen bonds; vibrational spectroscopy of dihydrated naphthalene anion ($Nph^-(H_2O)_2$)." *Chemical Physics Letters* **370**(3-4): 535-541.

Kebarle, P. and Tang, L. (1993). "From Ions in Solution to Ions in the Gas-Phase - The Mechanism of Electrospray Mass-Spectrometry." *Analytical Chemistry* **65**(22): A972-A986.

Kimling, J., Maier, M., Okenve, B., Kotaidis, V., Ballot, H. and Plech, A. (2006). "Turkevich method for gold nanoparticle synthesis revisited." *Journal of Physical Chemistry B* **110**(32): 15700-15707.

Klamt, A. and Schuurmann, G. (1993). "COSMO - A new approach to dielectric screening in solvents with explicit expressions for the screening energy and its gradient." *Journal of the Chemical Society-Perkin Transactions 2*(5): 799-805.

Klassen, J. S., Schnier, P. D. and Williams, E. R. (1998). "Blackbody infrared radiative dissociation of oligonucleotide anions." *Journal of the American Society for Mass Spectrometry* **9**(11): 1117-1124.

Klots, C. E. (1985). "Evaporative Cooling." *Journal of Chemical Physics* **83**(11): 5854-5860.

Kurihara, K., Kizling, J., Stenius, P. and Fendler, J. H. (1983). "Laser and Pulse Radiolytically Induced Colloidal Gold Formation in Water and in Water-in-Oil Microemulsions." *Journal of the American Chemical Society* **105**(9): 2574-2579.

Laidler, K. J., Meiser, J. H. and Sanctuary, B. C. (2003). *Physical Chemistry*. Boston, MA, Houghton Mifflin Company.

Langford, C. H. and Gray, H. B. (1966). *Ligand Substitution Processes*. New York, NY, W. A. Benjamin, Inc.

Lee, C. T., Yang, W. T. and Parr, R. G. (1988). "Development of the Colle-Salvetti Correlation-Energy Formula into a Functional of the Electron-Density." *Physical Review B* **37**(2): 785-789.

Liu, B., Haag, N., Johansson, H., Schmidt, H. T., Cederquist, H., Nielsen, S. B., Zettergren, H., Hvelplund, P., Manil, B. and Huber, B. A. (2008). "Electron capture induced dissociation of nucleotide anions in water nanodroplets." *Journal of Chemical Physics* **128**(7).

Liu, B., Nielsen, S. B., Hvelplund, P., Zettergren, H., Cederquist, H., Manil, B. and Huber, B. A. (2006). "Collision-induced dissociation of hydrated adenosine monophosphate

nucleotide ions: Protection of the ion in water nanoclusters." *Physical Review Letters* **97**(13).

Liu, B., Tomita, S., Rangama, J., Hvelplund, P. and Nielsen, S. B. (2003). "Electron attachment to "naked" and microsolvated nucleotide anions: Detection of long-lived dianions." *Chemphyschem* **4**(12): 1341-1344.

Loffler, D., Weber, J. M. and Kappes, M. M. (2005). "Photodetachment spectroscopy of $PtBr_4^{2-}$: Probing the Coulomb barrier of a doubly charged anion." *Journal of Chemical Physics* **123**(22).

Loo, J. A., Udseth, H. R. and Smith, R. D. (1989). "Peptide and protein-analysis by electrospray ionization mass-spectrometry and capillary electrophoresis mass-spectrometry." *Analytical Biochemistry* **179**(2): 404-412.

Luca, A., Schlemmer, S., Cermak, I. and Gerlich, D. (2001). "On the combination of a linear field free trap with a time-of-flight mass spectrometer." *Review of Scientific Instruments* **72**(7): 2900-2908.

Luo, Q., Li, J., Li, Q. S., Kim, S., Wheeler, S. E., Xie, Y. M. and Schaefer, H. F. (2005). "Electron affinities of the radicals derived from cytosine." *Physical Chemistry Chemical Physics* **7**(5): 861-865.

Lyapustina, S. A., Xu, S. K., Nilles, J. M. and Bowen, K. H. (2000). "Solvent-induced stabilization of the naphthalene anion by water molecules: A negative cluster ion photoelectron spectroscopic study." *Journal of Chemical Physics* **112**(15): 6643-6648.

Marcum, J. C., Halevi, A. and Weber, J. M. (2009). "Photodamage to isolated mononucleotides-photodissociation spectra and fragment channels." *Physical Chemistry Chemical Physics* **11**(11): 1740-1751.

Marcum, J. C. and Weber, J. M. (2009). "Electronic photodissociation spectra and decay pathways of gas-phase $IrBr_6^{2-}$." *Journal of Chemical Physics* **131**(19).

Marcum, J. C. and Weber, J. M. (2010). "Microhydration of Nitromethane Anions from Both a Solute and Solvent Perspective." *Journal of Physical Chemistry A* **114**(34): 8933-8938.

Martin, F., Burrow, P. D., Cai, Z. L., Cloutier, P., Hunting, D. and Sanche, L. (2004). "DNA strand breaks induced by 0-4 eV electrons: The role of shape resonances." *Physical Review Letters* **93**(6).

McLuckey, S. A. and Goeringer, D. E. (1997). "Slow heating methods in tandem mass spectrometry." *Journal of Mass Spectrometry* **32**(5): 461-474.

McLuckey, S. A. and Habibigoudarzi, S. (1993). "Decompositinos of multiply-charged oligonucleotide anions." *Journal of the American Chemical Society* **115**(25): 12085-12095.

McQuarrie, D. A. and Simon, J. D. (1997). *Physical Chemistry: A Molecular Approach*. Sausalito, CA, University Science Books.

Merchan, M. and Serrano-Andres, L. (2003). "Ultrafast internal conversion of excited cytosine via the lowest ππ* electronic singlet state." *Journal of the American Chemical Society* **125**(27): 8108-8109.

Messmer, R. P., Interran.Lv and Johnson, K. H. (1974). "Electronic structure of square-planar transition-metal complexes. 1. $PtCl_4^{2-}$ and $PdCl_4^{2-}$ ions." *Journal of the American Chemical Society* **96**(12): 3847-3854.

Middleton, C. T., de La Harpe, K., Su, C., Law, Y. K., Crespo-Hernandez, C. E. and Kohler, B. (2009). "DNA Excited-State Dynamics: From Single Bases to the Double Helix." *Annual Review of Physical Chemistry* **60**: 217-239.

Miessler, G. L. and Tarr, D. A. (1998). *Inorganic Chemistry*. Upper Saddle River, New Jersey, Prentice-Hall.

Motegi, H., Takayanagi, T., Tsuneda, T., Yagi, K., Nakanishi, R. and Nagata, T. (2010). "Theoretical Study on the Excess Electron Binding Mechanism in the $CH_3NO_2(H_2O)_n^-$ (n=1-6) Anion Clusters." *Journal of Physical Chemistry A* **114**(34): 8939-8947.

Mouret, S., Baudouin, C., Charveron, M., Favier, A., Cadet, J. and Douki, T. (2006). "Cyclobutane pyrimidine dimers are predominant DNA lesions in whole human skin exposed to UVA radiation." *Proceedings of the National Academy of Sciences of the United States of America* **103**(37): 13765-13770.

Muntean, F., Taylor, M. S., McCoy, A. B. and Lineberger, W. C. (2004). "Femtosecond study of $Cu(H_2O)$ dynamics." *Journal of Chemical Physics* **121**(12): 5676-5687.

Murphy, P. J. and LaGrange, M. S. (1998). "Raman spectroscopy of gold chloro-hydroxy speciation in fluids at ambient temperature and pressure: A re-evaluation of the effects of pH and chloride concentration." *Geochimica Et Cosmochimica Acta* **62**(21-22): 3515-3526.

Murphy, P. J., Stevens, G. and LaGrange, M. S. (2000). "The effects of temperature and pressure on gold-chloride speciation in hydrothermal fluids: A Raman spectroscopic study." *Geochimica Et Cosmochimica Acta* **64**(3): 479-494.

Myshakin, E. M., Jordan, K. D., Sibert, E. L. and Johnson, M. A. (2003). "Large anharmonic effects in the infrared spectra of the symmetrical $CH_3NO_2^-\cdot(H_2O)$ and $CH_3CO_2^-\cdot(H_2O)$ complexes." *Journal of Chemical Physics* **119**(19): 10138-10145.

Neumark, D. M. (2005). "Probing the transition state with negative ion photodetachment: experiment and theory." *Physical Chemistry Chemical Physics* **7**(3): 433-442.

Nielsen, S. B., Andersen, J. U., Forster, J. S., Hvelplund, P., Liu, B., Pedersen, U. V. and Tomita, S. (2003). "Photodestruction of adenosine 5 '-monophosphate (AMP) nucleotide ions in vacuo: Statistical versus nonstatistical processes." *Physical Review Letters* **91**(4).

Nielsen, S. B. and Solling, T. I. (2005). "Are conical intersections responsible for the ultrafast processes of adenine, protonated adenine, and the corresponding nucleosides?" *Chemphyschem* **6**(7): 1276-1281.

Nir, E. and de Vries, M. S. (2002). "Fragmentation of laser-desorbed 9-substituted adenines." *International Journal of Mass Spectrometry* **219**(1): 133-138.

Nir, E., Hunig, I., Kleinermanns, K. and de Vries, M. S. (2004). "Conformers of guanosines and their vibrations in the electronic ground and excited states, as revealed by double-resonance spectroscopy and ab initio calculations." *Chemphyschem* **5**(1): 131-137.

Nir, E., Imhof, P., Kleinermanns, K. and de Vries, M. S. (2000). "REMPI spectroscopy of laser desorbed guanosines." *Journal of the American Chemical Society* **122**(33): 8091-8092.

Nir, E., Janzen, C., Imhof, P., Kleinermanns, K. and de Vries, M. S. (2001). "Guanine tautomerism revealed by UV-UV and IR-UV hole burning spectroscopy." *Journal of Chemical Physics* **115**(10): 4604-4611.

Nir, E., Janzen, C., Imhof, P., Kleinermanns, K. and de Vries, M. S. (2002). "Pairing of the nucleobases guanine and cytosine in the gas phase studied by IR-UV double-resonance spectroscopy and ab initio calculations." *Physical Chemistry Chemical Physics* **4**(5): 732-739.

Nir, E., Plutzer, C., Kleinermanns, K. and de Vries, M. (2002). "Properties of isolated DNA bases, base pairs and nucleosides examined by laser spectroscopy." *European Physical Journal D* **20**(3): 317-329.

Pan, P. and Wood, S. A. (1991). "Gold-chloride complexes in very acidic aqueous solutions and at temperatures25-300°C - A laser raman-spectroscopic study." *Geochimica Et Cosmochimica Acta* **55**(8): 2365-2371.

Parr, R. G. and Yang, W. (1989). *Density-Functional Theory of Atoms and Molecules*. New York, Oxford University Press.

Parsons, B. F., Sheehan, S. M., Yen, T. A., Neumark, D. M., Wehres, N. and Weinkauf, R. (2007). "Anion photoelectron imaging of deprotonated thymine and cytosine." *Physical Chemistry Chemical Physics* **9**(25): 3291-3297.

Peck, J. A., Tait, C. D., Swanson, B. I. and Brown, G. E. (1991). "Speciation of Aqueous Gold(III) Chlorides from Ultraviolet Visible Absorption and Raman Resonance Raman Spectroscopies." *Geochimica Et Cosmochimica Acta* **55**(3): 671-676.

Pecourt, J. M. L., Peon, J. and Kohler, B. (2000). "Ultrafast internal conversion of electronically excited RNA and DNA nucleosides in water." *Journal of the American Chemical Society* **122**(38): 9348-9349.

Pecourt, J. M. L., Peon, J. and Kohler, B. (2001). "DNA excited-state dynamics: Ultrafast internal conversion and vibrational cooling in a series of nucleosides." *Journal of the American Chemical Society* **123**(42): 10370-10378.

Peon, J. and Zewail, A. H. (2001). "DNA/RNA nucleotides and nucleosides: direct measurement of excited-state lifetimes by femtosecond fluorescence up-conversion." *Chemical Physics Letters* **348**(3-4): 255-262.

Perdew, J. P., Burke, K. and Ernzerhof, M. (1996). "Generalized gradient approximation made simple." *Physical Review Letters* **77**(18): 3865-3868.

Perun, S., Sobolewski, A. L. and Domcke, W. (2005). "Ab initio studies on the radiationless decay mechanisms of the lowest excited singlet states of 9H-adenine." *Journal of the American Chemical Society* **127**(17): 6257-6265.

Phillips, D. R. and McCloskey, J. A. (1993). "A comprehensive study of the low-energy collision-induced dissociation of dinucleoside monophosphates." *International Journal of Mass Spectrometry and Ion Processes* **128**(1-2): 61-82.

Pilling, M. J. and Seakins, P. W. (2005). *Reaction Kinetics*. New York, NY, Oxford University Press.

Piuzzi, F., Mons, M., Dimicoli, I., Tardivel, B. and Zhao, Q. (2001). "Ultraviolet spectroscopy and tautomerism of the DNA base guanine and its hydrate formed in a supersonic jet." *Chemical Physics* **270**(1): 205-214.

Pivonka, N. L., Kaposta, C., von Helden, G., Meijer, G., Woste, L., Neumark, D. M. and Asmis, K. R. (2002). "Gas phase infrared spectroscopy of cluster anions as a function of size: The effect of solvation on hydrogen-bonding in $Br^{-}\cdot(HBr)(1,2,3)$ clusters." *Journal of Chemical Physics* **117**(14): 6493-6499.

Profeta, L. T. M., Larkin, J. D. and Schaefer, H. F. (2003). "The thymine radicals and their respective anions: molecular structures and electron affinities." *Molecular Physics* **101**(22): 3277-3284.

Ptasinska, S., Denifl, S., Mroz, B., Probst, M., Grill, V., Illenberger, E., Scheier, P. and Mark, T. D. (2005). "Bond selective dissociative electron attachment to thymine." *Journal of Chemical Physics* **123**(12).

Raff, L. M. (2001). *Principles of Physical Chemistry*. Upper Saddle River, NJ, Prentice-Hall.

Rensing, C., Ehrler, O. T., Yang, J. P., Unterreiner, A. N. and Kappes, M. M. (2009). "Photodissociation dynamics of $IrBr_6^{2-}$ dianions by time-resolved photoelectron spectroscopy." *Journal of Chemical Physics* **130**(23).

Robertson, W. H. and Johnson, M. A. (2003). "Molecular aspects of halide ion hydration: The cluster approach." *Annual Review of Physical Chemistry* **54**: 173-213.

Robertson, W. H., Price, E. A., Weber, J. M., Shin, J. W., Weddle, G. H. and Johnson, M. A. (2003). "Infrared signatures of a water molecule attached to triatomic domains of molecular anions: Evolution of the H-bonding configuration with domain length." *Journal of Physical Chemistry A* **107**(34): 6527-6532.

Rodgers, M. T., Campbell, S., Marzluff, E. M. and Beauchamp, J. L. (1994). "Low-energy collision-induced dissociation of deprotonated dinucleotides - Determination of the energetically favored dissociation pathways and the relative acidities of the nucleic-acid bases." *International Journal of Mass Spectrometry and Ion Processes* **137**: 121-149.

Roscioli, J. R., Diken, E. G., Johnson, M. A., Horvath, S. and McCoy, A. B. (2006). "Prying apart a water molecule with anionic H-bonding: A comparative spectroscopic study of the $X^-\cdot H_2O$ (X = OH, O, F, Cl, and Br) binary complexes in the 600-3800 cm^{-1} region." *Journal of Physical Chemistry A* **110**(15): 4943-4952.

Roucoux, A., Schulz, J. and Patin, H. (2002). "Reduced transition metal colloids: A novel family of reusable catalysts?" *Chemical Reviews* **102**(10): 3757-3778.

Sakamoto, M., Fujistuka, M. and Majima, T. (2009). "Light as a construction tool of metal nanoparticles: Synthesis and mechanism." *Journal of Photochemistry and Photobiology C-Photochemistry Reviews* **10**(1): 33-56.

Satzger, H., Townsend, D., Zgierski, M. Z., Patchkovskii, S., Ullrich, S. and Stolow, A. (2006). "Primary processes underlying the photostability of isolated DNA bases: Adenine." *Proceedings of the National Academy of Sciences of the United States of America* **103**(27): 10196-10201.

Schatz, P. N. (1975). MCD Spectra of Charge-Transfeer Transitions: Octahedral Ir^{4+}. *Electronic States of Inorganic Compounds*. P. Day. Dordrecht, Boston, D. Reidel Publishing Company**:** 223-240.

Scheller, M. K., Compton, R. N. and Cederbaum, L. S. (1995). "Gas-phase multiply-charged anions." *Science* **270**(5239): 1160-1166.

Schiedt, J., Knott, W. J., Le Barbu, K., Schlag, E. W. and Weinkauf, R. (2000). "Microsolvation of similar-sized aromatic molecules: Photoelectron spectroscopy of bithiophene-, azulene-, and naphthalene-water anion clusters." *Journal of Chemical Physics* **113**(21): 9470-9478.

Schiedt, J. and Weinkauf, R. (1997). "Photodetachment photoelectron spectroscopy of mass selected anions: Anthracene and the anthracene-H_2O cluster." *Chemical Physics Letters* **266**(1-2): 201-205.

Schiedt, J., Weinkauf, R., Neumark, D. M. and Schlag, E. W. (1998). "Anion spectroscopy of uracil, thymine and the amino-oxo and amino-hydroxy tautomers of cytosine and their water clusters." *Chemical Physics* **239**(1-3): 511-524.

Schneider, H., Boese, A. D. and Weber, J. M. (2005). "Unusual hydrogen bonding behavior in binary complexes of coinage metal anions with water." *Journal of Chemical Physics* **123**(8).

Schneider, H., Vogelhuber, K. M., Schinle, F., Stanton, J. F. and Weber, J. M. (2008). "Vibrational spectroscopy of nitroalkane chains using electron autodetachment and Ar predissociation." *Journal of Physical Chemistry A* **112**(33): 7498-7506.

Schneider, H., Vogelhuber, K. M. and Weber, J. M. (2007). "Infrared spectroscopy of anionic hydrated fluorobenzenes." *Journal of Chemical Physics* **127**(11).

Schneider, H. and Weber, J. M. (2007). "Infrared spectra of $SF_6^-\cdot(H_2O)_n$ (n=1-3): Incipient reaction and delayed onset of water network formation." *Journal of Chemical Physics* **127**(24).

Sharonov, A., Gustavsson, T., Carre, V., Renault, E. and Markovitsi, D. (2003). "Cytosine excited state dynamics studied by femtosecond fluorescence upconversion and transient absorption spectroscopy." *Chemical Physics Letters* **380**(1-2): 173-180.

Simons, J. (2008). "Molecular anions." *Journal of Physical Chemistry A* **112**(29): 6401-6511.

Sobolewski, A. L. and Domcke, W. (2002). "On the mechanism of nonradiative decay of DNA bases: ab initio and TDDFT results for the excited states of 9H-adenine." *European Physical Journal D* **20**(3): 369-374.

Sobolewski, A. L., Domcke, W., Dedonder-Lardeux, C. and Jouvet, C. (2002). "Excited-state hydrogen detachment and hydrogen transfer driven by repulsive $^1\pi\sigma^*$ states: A new paradigm for nonradiative decay in aromatic biomolecules." *Physical Chemistry Chemical Physics* **4**(7): 1093-1100.

Sobolewski, A. L., Domcke, W. and Hattig, C. (2005). "Tautomeric selectivity of the excited-state lifetime of guanine/cytosine base pairs: The role of electron-driven proton-transfer processes." *Proceedings of the National Academy of Sciences of the United States of America* **102**(50): 17903-17906.

Stoermer, C. W., Gilb, S., Friedrich, J., Schooss, D. and Kappes, M. M. (1998). "A high resolution dual mass gate for ion separation in laser desorption/ionization time of flight mass spectrometry." *Review of Scientific Instruments* **69**(4): 1661-1664.

Stokes, S. T., Grubisic, A., Li, X., Ko, Y. J. and Bowen, K. H. (2008). "Photoelectron spectroscopy of the parent anions of the nucleotides, adenosine-5 '-monophosphate and 2 ' deoxyadenosine-5 '-monophosphate." *Journal of Chemical Physics* **128**(4).

Takaya, T., Su, C., de La Harpe, K., Crespo-Hernandez, C. E. and Kohler, B. (2008). "UV excitation of single DNA and RNA strands produces high yields of exciplex states between two stacked bases." *Proceedings of the National Academy of Sciences of the United States of America* **105**(30): 10285-10290.

Tang, K. and Gomez, A. (1994). "On the structure of an electrostatic spray of monodisperse droplets." *Physics of Fluids* **6**(7): 2317-2332.

Tang, L. and Kebarle, P. (1993). "Dependence of ion intensity in electrospray mass-spectrometry on the concentration of the analytes in the electrosprayed solution." *Analytical Chemistry* **65**(24): 3654-3668.

Taylor, M. S., Muntean, F., Lineberger, W. C. and McCoy, A. B. (2004). "A theoretical and computational study of the anion, neutral, and cation Cu(H_2O) complexes." *Journal of Chemical Physics* **121**(12): 5688-5699.

Tossell, J. A. (1996). "The speciation of gold in aqueous solution: A theoretical study." *Geochimica Et Cosmochimica Acta* **60**(1): 17-29.

Turkevich, J., Stevenson, P. C. and Hillier, J. (1951). "A study of the nucleation and growth processes in the synthesis of colloidal gold." *Discussions of the Faraday Society*(11): 55.

Turkevich, J., Stevenson, P. C. and Hillier, J. (1953). "The formation of colloidal gold." *Journal of Physical Chemistry* **57**(7): 670-673.

Usher, A., McPhail, D. C. and Brugger, J. (2009). "A spectrophotometric study of aqueous Au(III) halide-hydroxide complexes at 25-80°C." *Geochimica Et Cosmochimica Acta* **73**(11): 3359-3380.

Vasiliou, A., Nimlos, M. R., Daily, J. W. and Ellison, G. B. (2009). "Thermal Decomposition of Furan Generates Propargyl Radicals." *Journal of Physical Chemistry A* **113**(30): 8540-8547.

Vazquez, M. V., Martinez, A., Dolgounitcheva, O. and Ortiz, J. V. (2006). "Deprotonated cytosine anions: A theoretical prediction of photoelectron spectra." *Journal of Physical Chemistry A* **110**(38): 11174-11177.

Verlet, J. R. R., Bragg, A. E., Kammrath, A., Cheshnovsky, O. and Neumark, D. M. (2005). "Comment on "Characterization of excess electrons in water-cluster anions by quantum simulations"." *Science* **310**(5755): 1769-1769.

Verlet, J. R. R., Kammrath, A., Griffin, G. B. and Neumark, D. M. (2005). "Electron solvation in water clusters following charge transfer from iodide." *Journal of Chemical Physics* **123**(23).

Walther, C., Becker, S., Dietrich, G., Kluge, H. J., Lindinger, M., Lutzenkirchen, K., Schweikhard, L. and Ziegler, J. (1996). "Photo fragmentation of metal clusters stored in a Penning trap." *Zeitschrift Fur Physik D-Atoms Molecules and Clusters* **38**(1): 51-58.

Wan, K. X. and Gross, M. L. (2001). "Fragmentation mechanisms of oligodeoxynucleotides: Effects of replacing phosphates with methylphosphonates and thymines with other bases in T-rich sequences." *Journal of the American Society for Mass Spectrometry* **12**(5): 580-589.

Wang, L. S., Ding, C. F., Wang, X. B. and Barlow, S. E. (1999). "Photodetachment photoelectron spectroscopy of multiply charged anions using electrospray ionization." *Review of Scientific Instruments* **70**(4): 1957-1966.

Wang, L. S., Ding, C. F., Wang, X. B., Nicholas, J. B. and Nicholas, B. (1998). "Probing the potential barriers and intramolecular electrostatic interactions in free doubly charged anions." *Physical Review Letters* **81**(13): 2667-2670.

Wang, S. Y., Ed. (1976). *Photochemistry and Photobiology of Nucleic Acids*. New York, San Francisco, London, Academic Press.

Wang, X. B., Ding, C. F. and Wang, L. S. (1998). "Photodetachment spectroscopy of a doubly charged anion: Direct observation of the repulsive Coulomb barrier." *Physical Review Letters* **81**(16): 3351-3354.

Wang, X. B., Nicholas, J. B. and Wang, L. S. (2000). "Electronic instability of isolated SO_4^{2-} and its solvation stabilization." *Journal of Chemical Physics* **113**(24): 10837-10840.

Wang, X. B., Nicholas, J. B. and Wang, L. S. (2000). "Intramolecular Coulomb repulsion and anisotropies of the repulsive Coulomb barrier in multiply charged anions." *Journal of Chemical Physics* **113**(2): 653-661.

Wang, X. B. and Wang, L. S. (1999). "Experimental search for the smallest stable multiply charged anions in the gas phase." *Physical Review Letters* **83**(17): 3402-3405.

Wang, X. B. and Wang, L. S. (1999). "Observation of negative electron-binding energy in a molecule." *Nature* **400**(6741): 245-248.

Wang, X. B. and Wang, L. S. (1999). "Photodetachment of free hexahalogenometallate doubly charged anions in the gas phase: ML_6^{2-}, (M=Re, Os, Ir, Pt; L=Cl and Br)." *Journal of Chemical Physics* **111**(10): 4497-4509.

Weber, J. M., Ioffe, I. N., Berndt, K. M., Loffler, D., Friedrich, J., Ehrler, O. T., Danell, A. S., Parks, J. H. and Kappes, M. M. (2004). "Photoelectron spectroscopy of isolated multiply negatively charged oligonucleotides." *Journal of the American Chemical Society* **126**(27): 8585-8589.

Weber, J. M., Kelley, J. A., Nielsen, S. B., Ayotte, P. and Johnson, M. A. (2000). "Isolating the spectroscopic signature of a hydration shell with the use of clusters: Superoxide tetrahydrate." *Science* **287**(5462): 2461-2463.

Weber, J. M., Robertson, W. H. and Johnson, M. A. (2001). "Argon predissociation and electron autodetachment spectroscopy of size-selected $CH_3NO_2^-\cdot Ar_n$ clusters." *Journal of Chemical Physics* **115**(23): 10718-10723.

Weber, J. M. and Schneider, H. (2004). "Infrared spectra of $X^-\cdot CO_2\cdot Ar$ cluster anions (X = Cl,Br,I)." *Journal of Chemical Physics* **120**(21): 10056-10061.

Weigend, F., Haser, M., Patzelt, H. and Ahlrichs, R. (1998). "RI-MP2: optimized auxiliary basis sets and demonstration of efficiency." *Chemical Physics Letters* **294**(1-3): 143-152.

Weis, P., Hampe, O., Gilb, S. and Kappes, M. M. (2000). "Metastability of isolated platinum and palladium tetrahalide dianions and the role of electron tunneling." *Chemical Physics Letters* **321**(5-6): 426-432.

Wigner, E. P. (1948). "On he behavior of cross sections near thresholds." *Physical Review* **73**(9): 1002-1009.

Wiley, W. C. and McLaren, I. H. (1955). "Time-of-flight mass spectrometry with improved resolution." *Review of Scientific Instruments* **26**(12): 1150-1157.

Wu, J. and McLuckey, S. A. (2003). "Ion/ion reactions of multiply charged nucleic acid anions: electron transfer, proton transfer, and ion attachment." *International Journal of Mass Spectrometry* **228**(2-3): 577-597.

Wu, J. and McLuckey, S. A. (2004). "Gas-phase fragmentation of oligonucleotide ions." *International Journal of Mass Spectrometry* **237**(2-3): 197-241.

Wysocki, V. H., Resing, K. A., Zhang, Q. F. and Cheng, G. L. (2005). "Mass spectrometry of peptides and proteins." *Methods* **35**(3): 211-222.

Wyttenbach, T. and Bowers, M. T. (2007). "Intermolecular interactions in biomolecular systems examined by mass spectrometry." *Annual Review of Physical Chemistry* **58**: 511-533.

Xantheas, S. S. (2000). "Cooperativity and hydrogen bonding network in water clusters." *Chemical Physics* **258**(2-3): 225-231.

Xu, S. J., Nilles, M. and Bowen, K. H. (2003). "Zwitterion formation in hydrated amino acid, dipole bound anions: How many water molecules are required?" *Journal of Chemical Physics* **119**(20): 10696-10701.

Yamashita, M. and Fenn, J. B. (1984). "Electrospray Ion-Source - Another Variation on the Free-Jet Theme." *Journal of Physical Chemistry* **88**(20): 4451-4459.

Yamashita, M. and Fenn, J. B. (1984). "Negative-Ion Production with the Electrospray Ion-Source." *Journal of Physical Chemistry* **88**(20): 4671-4675.

Yang, J. and Hakansson, K. (2009). "Characterization of oligodeoxynucleotide fragmentation pathways in infrared multiphoton dissociation and electron detachment dissociation by Fourier transform ion cyclotron double resonance." *European Journal of Mass Spectrometry* **15**(2): 293-304.

Yang, X., Wang, X. B., Vorpagel, E. R. and Wang, L. S. (2004). "Direct experimental observation of the low ionization potentials of guanine in free oligonucleotides by using photoelectron spectroscopy." *Proceedings of the National Academy of Sciences of the United States of America* **101**(51): 17588-17592.

Zakjevskii, V. V., King, S. J., Dolgounitcheva, O., Zakrzewski, V. G. and Ortiz, J. V. (2006). "Base and phosphate electron detachment energies of deoxyribonucleotide anions." *Journal of the American Chemical Society* **128**(41): 13350-13351.

Zhou, J., Santambrogio, G., Brummer, M., Moore, D. T., Meijer, G., Neumark, D. M. and Asmis, K. R. (2006). "Infrared spectroscopy of hydrated sulfate dianions." *Journal of Chemical Physics* **125**(11).

9 Appendix – Supplementary information for Chapter 6

Table 9.1. Table of all calculated threshold energies for $AuCl_4^-$ parent ions using both the B3LYP and PBE0 density functionals with a def2-TZVPP basis set. Gas-phase values include zero-point corrections but COSMO values do not. Channels listed in bold correspond to experimentally observed fragments.

Fragment Channel	Energy (eV)			
	B3LYP		PBE0	
	Gas-phase	COSMO	Gas-phase	COSMO
$Au^0 + 4\ Cl^0 + e^-$	12.76	14.68	13.50	15.45
$Au^- + 4\ Cl^0$	10.76	10.49	11.62	11.34
$AuCl^0 + 3\ Cl^0 + e^-$	10.11	11.39	10.67	11.94
$Au^0 + Cl^- + 3\ Cl^0$	9.54	8.10	10.23	8.81
$AuCl^- + 3\ Cl^0$	8.07	7.90	8.68	8.53
$AuCl_2^0 + 2\ Cl^0 + e^-$	7.91	9.68	8.34	10.14
$AuCl^0 + Cl^- + 2\ Cl^0$	6.89	4.81	7.40	5.30
$AuCl_3^0 + Cl^0 + e^-$	6.81	8.09	7.05	8.33
$AuCl_4^0 + e^-$	5.45	7.14	5.53	7.23
$AuCl_2^0 + Cl^- + Cl^0$	4.69	3.10	5.08	3.50
$AuCl_3^0 + Cl^-$	3.59	1.51	3.79	1.68
$AuCl_2^- + 2\ Cl^0$	**3.54**	**3.44**	**3.90**	**3.79**
$AuCl_3^- + Cl^0$	**2.34**	**2.21**	**2.58**	**2.43**

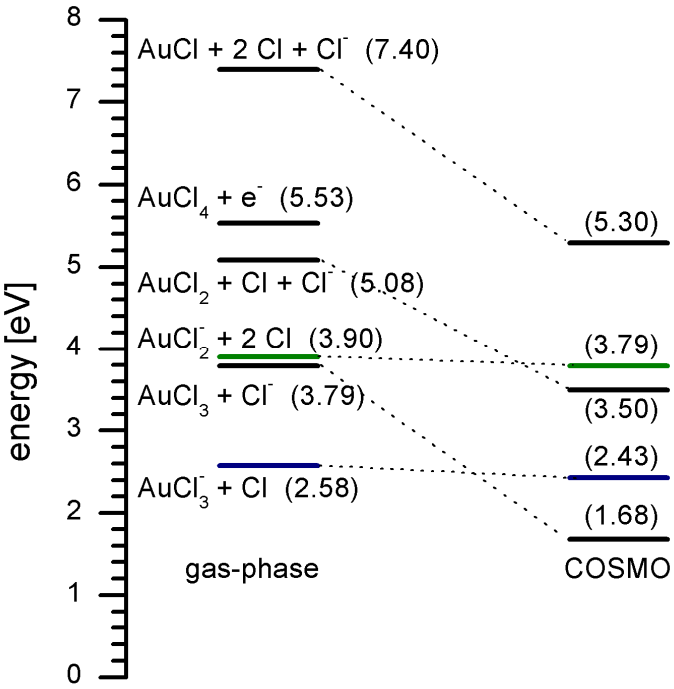

Figure 9.1. Threshold energies for various fragment channels of $AuCl_4^-$ calculated using DFT with the PBE0 functional and a def2-TZVPP basis set. Energies for the gas-phase (left) and using COSMO to account for solvent effects (right). Threshold energies for the fragment channels observed in the present experiment are depicted in color to match the photofragment action spectra for the respective fragment channels in Figure 6.4.

Table 9.2. Table of all calculated threshold energies for $AuCl_2(OH)_2^-$ parent ions using both the B3LYP and PBE0 density functionals with a def2-TZVPP basis set. Gas-phase values include zero-point energy corrections but COSMO values do not. Channels listed in bold correspond to experimentally observed fragments.

Fragment Channel	Energy [eV]			
	B3LYP		PBE0	
	Gas-phase	COSMO	Gas-phase	COSMO
$Au^0 + 2\ Cl^0 + 2\ OH^0 + e^-$	12.07	14.21	12.59	14.78
$Au^0 + OH^- + OH^0 + 2\ Cl^0$	10.99	8.93	11.60	9.56
$Au^- + 2\ Cl^0 + 2\ OH^0$	10.07	10.02	10.72	10.67
$Au(OH)^0 + OH^0 + 2\ Cl^0 + e^-$	10.04	11.64	10.53	12.14
$AuCl^0 + 2\ OH^0 + Cl^0 + e^-$	9.42	10.93	9.76	11.27
$Au(OH)^0 + OH^- + 2\ Cl^0$	8.96	6.36	9.53	6.92
$Au^0 + Cl^- + Cl^0 + 2\ OH^0$	8.85	7.63	9.33	8.14
$Au(OH)^- + OH^0 + 2\ Cl^0$	8.49	8.35	9.03	8.91
$AuCl^0 + OH^- + OH^0 + Cl^0$	8.34	5.64	8.77	6.05
$Au(OH)_2^0 + 2\ Cl^0 + e^-$	7.59	9.52	8.01	9.98
$AuCl(OH)^0 + Cl^0 + OH^0 + e^-$	7.38	9.32	7.69	9.66
$AuCl^- + 2\ OH^0 + Cl^0$	7.38	7.43	7.77	7.86
$AuCl_2^0 + 2\ OH^0 + e^-$	7.22	9.22	7.43	9.47
$Au(OH)^0 + Cl^- + Cl^0 + OH^0$	6.82	5.06	7.26	5.50
$AuCl(OH)_2^0 + Cl^0 + e^-$	6.50	7.98	6.72	8.20
$AuCl(OH)^0 + OH^- + Cl^0$	6.30	4.04	6.70	4.44
$AuCl_2(OH)^0 + OH^0 + e^-$	6.25	7.76	6.38	7.89
$AuCl^0 + Cl^- + 2\ OH^0$	6.20	4.34	6.50	4.62
$AuCl_2^0 + OH^- + OH^0$	6.15	3.93	6.44	4.25
$AuCl_2(OH)^0 + OH^-$	5.18	2.48	5.39	2.67
$Au(OH)_2^- + 2\ Cl^0$	4.77	4.37	5.20	4.80
$AuCl_2(OH)_2^0 + e^-$	4.64	6.38	4.68	6.48
$Au(OH)_2^0 + Cl^- + Cl^0$	4.37	2.93	4.75	3.34
$AuCl(OH)^0 + Cl^- + OH^0$	4.16	2.74	4.43	3.02
$AuCl(OH)^- + Cl^0 + OH^0$	**3.81**	**3.66**	**4.09**	**3.95**
$AuCl(OH)_2^0 + Cl^-$	3.28	1.39	3.46	1.56
$AuCl(OH)_2^- + Cl^0$	2.98	2.81	3.24	3.07
$AuCl_2^- + 2\ OH^0$	**2.85**	**2.98**	**2.99**	**3.12**
$AuCl_2(OH)^- + OH^0$	2.23	2.23	2.37	2.37

Table 9.3. Table of relative energies calculated using the PBE0 density functional and corresponding Boltzmann populations for isomers of the $AuCl_2(OH)_2^-$ ion.

	PBE0			
	relative energy [meV]		Boltzmann population	
isomer	gas phase	COSMO	gas phase	COSMO
cis-homo	1	9	0.96	0.71
cis-hetero	0	0	1.00	1.00
trans-homo	35	20	0.26	0.46
trans-hetero	74	23	0.06	0.42

Table 9.4. Table of calculated valence electron orbital energies for several d^8 square planar transition metal complexes. Energies have been calculated using density functional theory with the B3LYP density functional and a def2-TZVPP basis set. The calculations predict that all species should have the same relative ordering of the antibonding, metal-based d-orbitals as (x^2-y^2) > (*xz*),(*yz*) > (*xy*) > (z^2). This ordering is different than most predictions (see Chapter 6 and references therein). This suggests that the ordering is highly dependent upon the method used and is not simply due to the identity of the central transition metal. Additionally, it is important to note that the large number of ligand-based orbitals that have energies comparable to or above the energies of the metal-based *d*-orbitals for the gold complexes when compared to the other metals. As mentioned in the main text, this can be attributed to the increased ability of gold to accept electrons when compared to the other metals Pt and Pd, which could lead to stabilization of the metal-based orbitals.

$PtCl_4^{2-}$			$PdCl_4^{2-}$			$AuCl_4^{1-}$		
orbital	symmetry	energy [eV]	orbital	symmetry	energy [eV]	orbital	symmetry	energy [eV]
(x^2-y^2)	6 b_{1g}	6.326	(x^2-y^2)	6 b_{1g}	5.448	(x^2-y^2)	6 b_{1g}	-0.029
(*xz*),(*yz*)	3 e_g	2.324	(*xz*),(*yz*)	3 e_g	1.779	ligand	2 a_{2g}	-3.496
(*xy*)	3 b_{2g}	2.103	(*xy*)	3 b_g	1.515	(*xz*),(*yz*)	3 e_g	-3.754
(z^2)	7 a_{1g}	1.955	(z^2)	7 a_{1g}	1.515	(*xy*)	3 b_{2g}	-4.012
ligand	2 a_{2g}	1.403	ligand	2 a_{2g}	1.451	ligand	8 e_u	-4.077
ligand	8 e_u	0.886	ligand	8 e_u	0.955	ligand	2 b_{2u}	-4.171
ligand	2 b_{2u}	0.784	ligand	2 b_{2u}	0.824	ligand	3 a_{2u}	-4.859
ligand	3 a_{2u}	0.198	ligand	3 a_{2u}	0.235	ligand	7 e_u	-5.485
ligand	7 e_u	-0.284	ligand	7 e_u	-0.183	(z^2)	7 a_{1g}	-5.645
ligand	2 e_g	-0.286	ligand	2 e_g	-0.326	ligand	2 e_g	-7.238
$PtBr_4^{2-}$			$PdBr_4^{2-}$			$AuBr_4^{1-}$		
orbital	symmetry	energy [eV]	orbital	symmetry	energy [eV]	orbital	symmetry	energy [eV]
(x^2-y^2)	10 b_{1g}	5.358	(x^2-y^2)	10 b_{1g}	4.601	(x^2-y^2)	10 b_{1g}	-0.442
(*xz*),(*yz*)	6 e_g	1.771	ligand	4 a_g	1.374	ligand	4 a_{2g}	-3.131
(*xy*)	5 b_{2g}	1.488	(*xz*),(*yz*)	6 e_g	1.334	(*xz*),(*yz*)	6 e_g	-3.612
(z^2)	11 a_{1g}	1.368	(*xy*)	5 b_g	1.014	ligand	14 e_u	-3.712
ligand	4 a_{2g}	1.34	(z^2)	11 a_{1g}	0.977	ligand	4 b_{2u}	-3.818
ligand	14 e_u	0.808	ligand	14 e_u	0.874	(*xy*)	5 b_{2g}	-3.988
ligand	4 b_{2u}	0.689	ligand	4 b_{2u}	0.725	ligand	5 a_{2u}	-4.519
ligand	5 a_{2u}	0.075	ligand	5 a_{2u}	0.123	ligand	13 e_u	-5.175
ligand	13 e_u	-0.425	ligand	13 e_u	-0.316	(z^2)	11 a_{1g}	-5.731
ligand	5 e_g	-0.465	ligand	5 e_g	-0.525	ligand	5 e_g	-7.126

Table 9.5. Table of all allowed singlet excitation transitions of $AuCl_4^-$ within the approximate spectral range of our experiment. Values were calculated using TDDFT employing both the B3LYP and PBE0 functionals with a def2-TZVPP basis set.

B3-LYP		
Excitation Energy [eV]	Oscillator Strength [length rep.]	Symmetry
3.08	3.91E-04	a_{2u}
3.13	3.36E-02	e_u
5.18	6.68E-01	e_u
6.95	1.29E-01	e_u

PBE0		
Excitation Energy [eV]	Oscillator Strength [length rep.]	Symmetry
3.49	4.27E-04	a_{2u}
3.54	4.66E-02	e_u
5.60	7.23E-01	e_u
7.40	1.14E-02	e_u